

NORTHWESTERN UNIVERSITY

Noise Engineering and Mitigation in Superconducting Quantum Circuits

A DISSERTATION

SUBMITTED TO THE GRADUATE SCHOOL  
IN PARTIAL FULFILLMENT OF THE REQUIREMENTS

of the degree

DOCTOR OF PHILOSOPHY

Field of Physics

By

Ziwen Huang

EVANSTON, ILLINOIS

September 2021

© Copyright by Ziwen Huang 2021

All Rights Reserved

## ABSTRACT

Superconducting qubits are among the leading competitors in the race towards building the first full-fledged quantum computer. Using this platform, researchers have for the first time demonstrated computational capability that is beyond the reach of the current classical machines. (This achievement is nicknamed “*Quantum Supremacy*”.) Up to date, however, the performance of superconducting quantum processors still fails to fully satisfy the requirement for efficient and useful quantum computation, which is largely due to their decoherence induced by the environmental noise. The challenge posed by the noise motivates researchers to put intensive efforts into understanding, mitigating and even leveraging the noise that affects superconducting qubits.

In this thesis, we will discuss several strategies that we have developed recently for both noise engineering and mitigation in superconducting qubits. Specifically, we present a strategy based on the tunable coupling between a qubit and a noisy ancilla to universally stabilize the former in arbitrary single-qubit states. For noise mitigation, we propose a scheme based on *dynamical sweet spots* to protect superconducting qubits from the ubiquitous and detrimental  $1/f$  noise. Using this framework, we further introduce a novel qubit design, the *revolver qubit*, which is predicted to enjoy protection from both dephasing due to  $1/f$  noise and depolarization.

## **Acknowledgements**

I first acknowledge the teaching, guidance and support from my advisor, Professor Jens Koch. Over the past five years, he has kept a strict weekly schedule to meet with each of his students, including me. I really cherish the productive meetings with him, from where I learned not only about physics, but also about the code of doing good research and being a responsible researcher. Particularly, from him, I understand the importance of basing research on hard work and rigorous derivation, instead of on handwavy arguments and unproductive talking. Due to his training, I find myself sometimes mimic his role in my own brain when I think about a physics problem, questioning in extreme detail what I mean exactly by certain words. I believe that I will benefit a lot from this in my future research.

Next, I want to thank Professors James A. Sauls and Timothy Kovachy for joining the defense committee. I am grateful to Professor Sauls for recommending me for admission to Northwestern, without which none of my humble achievements would be possible. I took several of his classes, and I learned so much about superconductivity from him. I would like to thank Professor Kovachy for his participation and support during my prospectus and his insightful questions. I regret not having much interaction with him in person due to the ongoing pandemic, but I really cherish his wisdom and kindness through our zoom and email correspondence. I acknowledge the help and teaching from David I. Schuster and Andrew A. Houck. I have participated in several great projects under their supervision. They have helped a lot not only

in physics, but also in planning my future career. I also want to thank Professors Garg and Chandrasekhar, who have taught me a lot about condensed matter physics in their classes.

To my colleagues in the physics department: I would like to thank them for supporting me throughout my Ph.D. study. I really appreciate the friendship with Robert Regan, who has helped me from my first year with problems in both research and life. He is such a warmhearted friend who will wholeheartedly help you whenever there is trouble. I will never forget the days when we went for authentic tacos and played basketball. I still remember the days when Weiting Lin taught me how to drive very patiently. He has such a nice personality and he was never mad at me when I was a really bad driver. We had lots of good lunches at the Sargent dining hall, and we shared good moments of discussing quasi-particles.

I want to thank Jason He, Yuxin Wang and Qiming Wu for their companion over these years. With them, I explored many restaurants in Chicago, and we played many kinds of sport during these years. I am so blessed to have them to chat with whenever I need someone to talk to. Especially during the pandemic, their support and friendship have been priceless. I appreciate the many helpful discussions with my colleague Xinyuan You. When I have an idea or question about ongoing research, I usually first come to him for discussion, and he is always patient and helpful in sharing his perspectives. I appreciate the companionship with my colleague Daniel Weiss, who has taught me a lot about English writing and US culture. He is always good at cheering people up whenever he is in the office. I cherish the friendship with Brian Baker, Yunwei Lu, Peter Groszkowski, Andy Li, Vinh San Dinh, Sai Pavan Chitta and other current or former group members.

Outside Northwestern, I am blessed to have had the opportunity to collaborate with András Gyenis, Pranav Mundada, Andrei Vrajitoarea and Anjali Premkumar from the Houck research

lab at Princeton, and Yao Lu and Helin Zhang from the Schuster research lab at University of Chicago. They have taught me a lot about the real experimental issues, thanks to which I did not become a theorist living in his own world. I enjoy the collaboration with theorists from Northrop Grumman, David Ferguson and Rudolph J. Magyar, on the revolver project. I appreciate their insights into this project and the great research ideas they share with me.

To my friends: My roommate, Weihua Lei, has been a great support for me after we began to share an apartment. We have shared good stories with each other, and Friday dinners with him are always great times. I thank Lisa Wang for the trips and fun we had together in the early days of my Ph.D. I appreciate the many conversations with Yuezhi Xu in my first year, during which time I only had few friends around me. I want to thank my friends Bill Bi, Su Chen, Ran Chen, Xutong Chen, Ning Li, Rachel Li, Tianzhe Li, Zhizhong Li, Allen Lin, Yidan Ni, Michelle Shen, Yangfan Sui, Tiffany Sun, Yiqun Wang, Xinyan Wang, Bingcong Ye, Jian Yang, Yinting Yu, Grace Xie, and Wenyang Zhang. It has been great fun being with them playing all kinds of board games during the weekends. I had never imagined that I could be so lucky to have so many lovely friends around me, to keep me constantly reminded that there is still life beyond sometimes depressing research (most of the time research is great, though). I am grateful to Mr. and Mrs. Lin, Mr. and Mrs. Tong, and Mr. and Mrs. Ho from the Northwestern Chinese Christian Fellowship for their kind help throughout these years. With them, I have found another place to escape to. I appreciate the support and help from Bowen Zhao during the writing of this thesis, without which I would be driven mad by the tedious editing.

I finally thank my parents and sister for their silent support behind my Ph.D. study. Although they are on the other side of the Pacific, it would have been impossible for me to get to this point

without their understanding and steadfast support. I hope that I can spend more time with them after my graduation.

## List of Notations

Below, we list a number of symbols that are frequently used in this thesis.

Symbol	Description
$e$	Electron charge
$k_B$	Boltzmann constant
$\Phi_0$	Magnetic flux quantum
$\hat{H}_q(t)$	Hamiltonian of the system (qubit)
$\hat{H}_B$	Hamiltonian of the bath
$\hat{H}_I$	Hamiltonian of the system-bath interaction
$\mathcal{T}$	Time-ordering operator
$\hat{U}_q(t)$	System propagator defined by $\hat{U}_q(t) = \mathcal{T} \exp[-i \int_0^t \hat{H}_q(t') dt']$
$\hat{U}_B(t)$	Bath propagator defined by $\hat{U}_B(t) = \exp[-i \int_0^t \hat{H}_B dt']$
$\tilde{\rho}_q(t), \tilde{\rho}_B(t)$	Density operator of the system and bath in the interaction picture
$\tilde{H}_I(t)$	Interaction Hamiltonian in the interaction picture
$\hat{\mathcal{A}}_\alpha, \hat{\mathcal{B}}_\alpha$	System and bath operators describing the interaction between the system and the $\alpha$ th bath
$\tilde{\mathcal{A}}_\alpha(t), \tilde{\mathcal{B}}_\alpha(t)$	The above operators in the interaction picture
$\hat{\mathcal{A}}_\alpha(\omega)$	$\omega$ -frequency component of $\tilde{\mathcal{A}}_\alpha(t)$
$ w_j(t)\rangle, \epsilon_j$	$j$ th Floquet state and its quasi-energy
$ w_{j,n}(t)\rangle, \epsilon_{j,n}$	Redundant Floquet state and its quasi-energy, defined by $ w_{j,n}(t)\rangle =  w_j(t)\rangle \exp(-in\omega_d)$ and $\epsilon_{j,n} = \epsilon_j + n\omega_d$
$\epsilon_{01}$	The quasi-energy difference defined by $\epsilon_{01} = \epsilon_1 - \epsilon_0$
$S_{\alpha\beta}(\omega)$	Noise spectrum defined by $S_{\alpha\beta}(\omega) = \int_{-\infty}^{\infty} d\tau \exp(i\omega\tau) \langle \tilde{\mathcal{B}}_\alpha(\tau) \tilde{\mathcal{B}}_\beta(0) \rangle$
$\hat{\sigma}_{\pm,z}$	Pauli $+$ , $-$ , $z$ operators

$\hat{c}_{\pm,\phi}(t)$	Pauli $+$ , $-$ , $z$ operators defined in the Floquet basis [See Eq. (2.20)], which will be abbreviated as $\hat{c}_{\pm,\phi}$ if $t = 0$
$\hat{\sigma}, \hat{\eta}$	Qubit and bath operators through which the two-level system and the bath are coupled
$g_{k\mu}$	Fourier coefficient of the matrix elements of the noise operator in the Floquet basis [See Eq. (2.22)] ( $\mu = \pm, \phi$ )
$T_{\text{env}}$	Environmental temperature
$\gamma_{\pm}$	Excitation and decay rates
$\gamma_{\phi}$	Pure-dephasing rate
$T_1, T_{\phi}$	Depolarization and pure-dephasing times
$T_{2E}, T_{2R}$	Dephasing times obtained from echo and Ramsey experiments
$\omega_d$	Driving frequency
$A$	Driving amplitude
$\bar{\omega}_{k,\mu}$	Filter frequencies, defined in Eq. (2.21)
$T$	Driving period, defined by $T = 1/\omega_d$
$ g\rangle,  e\rangle$	Qubit ground and first excited state
$\Omega_{ge}$	Energy difference between the qubit states $ g\rangle$ and $ e\rangle$
$\sigma_{ge}, \sigma_{gg}, \sigma_{ee}$	Matrix elements of the operator $\hat{\sigma}$ in terms of the qubit energy states $ g\rangle$ and $ e\rangle$
$E_{C,L,J}$	Charging, inductive and Josephson energies of a superconducting qubit
$\hat{\phi}, \hat{n}$	Phase and charge operators of a superconducting qubit
$n_g$	Offset charge in a superconducting qubit
$\Phi_e, \phi_e$	External flux and its reduced version that penetrates the circuit loop, related by $\phi_e = 2\pi\Phi_e/\Phi_0$
$\omega_r, \omega_q$	Resonator and qubit frequencies
$\hat{a}, \hat{a}^\dagger, \hat{b}, \hat{b}^\dagger$	Lowering and Raising operators of two harmonic oscillators $a$ and $b$
$\chi$	Dispersive shift
$\kappa$	Resonator loss rate
$\phi_{\text{dc}}, \phi_{\text{ac}}$	DC and AC amplitudes defined by $\phi_e(t) = \phi_{\text{dc}} + \phi_{\text{ac}} \cos \omega_d t$
$\omega_{\text{ir}}$	Infrared cutoff introduced for regularizing $1/f$ noise spectrum
$\Delta, \Delta_m$	Gap size at the avoided crossing in the eigenenergy and quasi-energy spectrum of an undriven and driven qubit

$\mathcal{F}$	Function space of $T$ -periodic functions $f : \mathbb{R} \rightarrow \mathbb{C}^N$ ( $N$ is the dimension of the system Hilbert space)
$\bar{O}_q$	Operator defined in $\mathcal{F}$ , which is mapped to by the time-periodic operator $\hat{O}(t)$ defined in the original qubit Hilbert space
$ \bar{w}_{j,n}\rangle$	Vector in $\mathcal{F}$ , which corresponds to the Floquet state $ w_{j,n}(t)\rangle$
$\zeta^+, \zeta_1^-, \zeta_2^-$	Strength of coupling between the two qubits induced by the Revolver coupler, first shown in Eq. (4.29)
$ \psi_{\text{ins},j}(t)\rangle, E_{\text{ins},j}$	$j$ th instantaneous eigenstates and its instantaneous eigenenergy
$\vec{\lambda}$	Set of parameters that control a driven system
$\mathcal{K}$	Function space that contains $2\pi$ -periodic functions $f : \mathbb{R} \rightarrow \mathbb{C}^N$ ( $N$ is the dimension of the system Hilbert space)
$\hat{K}(t)$	Quasi-energy operator defined in $\mathcal{K}$
$ \Phi^{\mathcal{K}}(t)\rangle\rangle$	Time-dependent vector defined in $\mathcal{K}$
RWA	Abbreviation for “rotation wave approximation”
SQUID	Abbreviation for “superconducting quantum interference device”
DD	Abbreviation for “dynamical decoupling”
ODE	Abbreviation for “ordinary differential equation”

## Table of Contents

ABSTRACT	3
Acknowledgements	4
List of Notations	8
Table of Contents	11
List of Tables	15
List of Figures	16
Chapter 1. Introduction	18
Chapter 2. Quantum Master Equation	24
2.1. Secular Redfield Floquet master equation	24
2.2. Markovian approximation	31
2.3. Coherence times of a two-level system	32
Chapter 3. Introduction to the Transmon and Fluxonium Qubits	36
3.1. Transmon	36
3.2. Fluxonium	40
Chapter 4. Noise Engineering: Universal Stabilization of Single-Qubit States	46
4.1. Bath engineering and tunable coupler	46

	12
4.2. Model of the composite system	47
4.3. Photon conserving and non-conserving interaction	49
4.4. Excited-state stabilization	53
4.5. Stabilization in arbitrary mixed states along the $z$ -axis	55
4.6. Universal qubit stabilization strategies	58
4.7. Pure-state stabilization fidelities	63
4.8. Azimuthal angle and stabilization in arbitrary mixed state	68
4.9. Fast stabilization and critical damping	70
4.10. Circuit quantization	71
Chapter 5. Noise Mitigation: Driving Superconducting Qubits at Dynamical Sweet Spots	79
5.1. Protecting qubits from low-frequency noise	79
5.2. Two-level system subject to $1/f$ noise	82
5.3. Dynamical coherence times and sweet spots	84
5.4. Numerical calculation of dynamical coherence times	89
5.5. Relating dynamical sweet spots to extrema of the quasi-energy difference	92
5.6. Strong-drive limit	97
5.7. Weak-drive limit	100
5.8. Gap size and the width of $T_\phi$ peaks surrounding sweet-spot manifolds	102
5.9. Interpretation of coherence times in terms of filter functions	104
5.10. Conservation of the sum of filter weights	107
5.11. Gates and readout of a single Floquet qubit	109
5.12. Floquet two-qubit gates	112
5.13. Experimental demonstration of the proposed protection scheme	116

	13
Chapter 6. Noise Mitigation: The Revolver Qubit	118
6.1. Double protection from pure dephasing and depolarization	118
6.2. The revolving wavefunctions	121
6.3. Two heavy fluxonium qubits connected by a tunable coupler	122
6.4. Control pulses and potential	124
6.5. Methods to calculate the Floquet states	127
6.6. Noise channels and estimation of coherence times	130
6.7. Using symmetry to design the revolving pulses for $1/f$ noise cancellation	134
6.8. Coherence times	139
6.9. Circuit quantization	143
Chapter 7. Outlook	147
Appendix A. Rotating-Wave Approximation	149
A.1. RWA and Rabi oscillations	149
A.2. RWA in first-order ODEs	151
A.3. Numerical simulation	155
Appendix B. Unifying Other $1/f$ -noise Protection Schemes Under the Floquet Framework	158
B.1. General discussion	158
B.2. Dynamical sweet spots realized through qubit-frequency modulation	160
B.3. Dynamical sweet spots induced by on-resonance Rabi driving	161
B.4. Dynamical sweet spots realized by dynamical decoupling pulse sequences	163
Appendix C. Adiabatic Floquet Theory	165

	14
Appendix D. Born-Oppenheimer Approximation	171
D.1. General discussion	171
D.2. Toy model	178
Bibliography	181

## List of Tables

1.1	A comparison between superconducting and trapped-ion qubits on several important metrics.	20
4.1	Energy scales of circuit parameters used in Chapter 4.	73
5.1	Calculated dynamical coherence times for four example operating points.	90
6.1	Circuit parameters used for the simulation in Chapter 6.	146

## List of Figures

1.1	The evolution of the coherence times of superconducting qubits based on some of the start-of-the-art demonstrations over the last two decades.	21
1.2	A schematic showing the different roles of noise in quantum-information processing based on superconducting qubits.	22
3.1	Lumped-element circuit diagrams of the transmon and fluxonium qubits.	37
3.2	Numerically calculated spectra of Cooper pair boxes with respect to offset charge.	39
3.3	Energy spectrum and charge matrix element of a fluxonium qubit.	42
3.4	Schematic of the energy spectrum and wave functions of a fluxonium qubit operated close to half-integer flux.	43
3.5	The coherence times of a heavy fluxonium realized in a recent experiment.	45
4.1	Lumped-element diagrams describing two circuits where a qubit is coupled to a resonator.	48
4.2	Transmission measurement through the resonator which is coupled to the qubit.	51
4.3	Stabilization fidelity as a function of control parameters and resonator decay rate.	56
4.4	Ladder diagrams illustrating red- and blue-sideband couplings.	58
4.5	Stabilization fidelity as a function of stabilization angle, coupling strength and temperature.	64
4.6	Different damping behaviors characterizing the stabilization process.	72
5.1	Static and quasi-energy spectrum of undriven and driven fluxonium qubits.	80
5.2	Dynamical coherence time as a function of drive frequency $\omega_d$ and drive amplitude $A$ .	91
5.3	Sweet-spot manifolds embedded in the 3d parameter space.	97
5.4	Noise spectra and filter weights centered at the corresponding filter frequencies.	105
5.5	Concurrent gates for the Floquet qubit.	109

		17
5.6	Adiabatic mapping protocol for readout.	111
5.7	Simulation of a Floquet- $\sqrt{i}$ SWAP gate for two inductively coupled fluxonium qubits.	115
5.8	Theory prediction and experimental demonstration of the dephasing time at and away from the dynamical sweet spot in a flux-modulated fluxonium qubit.	117
6.1	A schematic that compares a revolver qubit with a heavy fluxonium.	120
6.2	Lumped-element circuit diagram of the revolver qubit.	124
6.3	Five snapshots of the time-dependent revolver potential, taken during the first half of a revolving period.	125
6.4	Instantaneous eigenenergies, potential landscape and Floquet states of one example revolver qubit.	130
6.5	Coherence times of a revolver qubit a function of the revolving frequency.	140
6.6	The time-dependent control fluxes and mutual coupling strength used in the simulation.	146
A.1	Numerically calculated error introduced by RWA.	156

## CHAPTER 1

### **Introduction**

Quantum bits (qubits) based on superconducting circuits have drawn significant research attention in recent decades, thanks to their potential of becoming building blocks of near-future quantum computers [1–3]. Compared with other competing architectures, superconducting-circuit devices enjoy convenient controllability via microwave signals [1, 3–7]. Furthermore, almost all building elements of a superconducting circuit are configurable, which offers a flexible tuning range of the qubit parameters (e.g., the qubit transition frequency) [8–11]; Fabricating many copies of a qubit is straightforward with this 2d solid-state platform, given the mature and economic fabrication techniques [1, 3–7]. Leveraging these advantages, the development of superconductor-based quantum-information processors has reached a milestone, by demonstrating a clear advantage of a superconducting quantum computer over classical supercomputers in the implementation of a specific quantum algorithm (often referred to as “quantum supremacy”) [12].

To date, however, a number of challenges remain for building a full-fledged quantum computer based on superconducting qubits. One imminent problem is that environmental noise considerably restricts the qubits’ coherence times and gate fidelities [3, 13, 14]. The reason is traced back to the relatively strong electromagnetic interaction between superconducting circuits and the environment, which is a double-edged sword [10]. On one hand, strong interactions make it easier to control and manipulate the qubit states. (Typically, single-qubit gates take  $\sim 5$  ns, and two-qubit gates take  $\sim 50$  ns [5–7]). On the other hand, strong interactions induce

increased qubit decoherence in superconducting devices [10, 13]. Especially, imperfections in the material bulk and on the many interfaces of the device (metal-to-air, metal-to-substrate, substrate-to-air, etc.) may interact with the qubit degree of freedom uncontrollably [11], yielding limited coherence times in many widely-used superconducting qubits. Based on the most recent research results, the coherence times of superconducting qubits can currently reach 1 ms [3, 15–17]. (In several experiments [18–20], qubit depolarization times well exceed 1 ms, but dephasing times are still limited to the order of  $10 \mu\text{s}$ ). The ratio of qubit coherence time to the typical duration of a qubit gate is still considered low ( $10^3$ – $10^4$ ) [8]. Largely limited by decoherence, the fidelity of two-qubit gates, which is usually considered one important metric for assessing the performance of a qubit platform, is still below 99.9% on superconducting qubits [3, 21–23]. Quantum error correction for large-scale superconducting circuits is still beyond our reach, partly due to the limited coherence times and gate fidelities. These problems place superconducting qubits, although one of the leading competitors, in the noisy intermediate-scale quantum (NISQ) era [3, 24]. To help readers understand the advantages and disadvantages of the superconducting qubits in a more quantitative manner, in TABLE 1.1 we directly compare several important metrics of superconducting qubits and trapped-ion qubits, another leading and well established competitor.

Earlier works have identified multiple relevant noise channels, including dielectric loss [26–28], charge noise [13, 29], flux noise [30, 31], critical current fluctuations [32], photon-shot noise [33, 34], quasi-particle tunneling [35, 36], etc. To date, methods to eliminate some or all of these noise channels have yet to be discovered, but researchers have made tremendous progress in mitigating noise, specifically by optimizing qubit designs [37–41], improving materials [16, 28, 42], and inventing new control protocols [43–46]. We showcase a list of noticeable advances

Table 1.1. A comparison between superconducting and trapped-ion qubits on several important metrics. The range of parameters shown in the table entries indicate the typical values from some state-of-the-art experiments, as summarized in recent reviews [3, 8]. Approximate ranges are meant to give the readers a sense of their difference in magnitude. \*This number has been increased to 66 according to a recent preprint [12]. \*\*This number has been updated to 32 according to IonQ’s recent news [25].

	Superconducting qubit	Trapped-ion qubit
Coherence time	$10^{-2} - 1$ ms	$10^{-1} - 10^3$ s
Single-qubit gate infidelity	$10^{-4} - 10^{-2}$	$10^{-6} - 10^{-3}$
Single-qubit gate duration	1 – 10 ns	1– 10 $\mu$ s
Two-qubit gate infidelity	$10^{-3} - 10^{-2}$	$10^{-3} - 10^{-2}$
Two-qubit gate duration	10 – $10^3$ ns	1 – $10^3$ $\mu$ s
Largest size of fully controlled systems	53*	20**

in these directions in the following. Toward the optimization of circuit configurations, Koch *et al.* [37] and Manucharyan *et al.* [47] proposed the designs of the transmon and fluxonium qubits, which are especially used to tackle the harmful  $1/f$  charge noise. To date, these two types of qubits are still leading in coherence times over all other variants of superconducting qubit [15–17]. (Recently, Somoroff *et al.* have demonstrated over 1 ms  $T_1$  and  $T_2$  in a fluxonium qubit [15].) Beside these two types of qubits, a number of novel qubit designs, usually referred to as *protected qubits*, have gained increased research momentum due to their potentially much enhanced coherence times [20, 38, 41, 48, 49]. Noticeably, the first *zero-pi* qubit, originally proposed by Brooks *et al.* [50], has been manufactured by Gyenis *et al.* [20] and exhibited a long depolarization time as well as a favorable dephasing time. Toward the improvement of materials, Place *et al.* have shown that replacing niobium by tantalum as the superconducting metal can reduce the microwave loss at metal surfaces and significantly improve the transmon relaxation time to 0.3 ms [16]. Following this work, Wang *et al.* recently have demonstrated 0.5 ms  $T_1$  by improving metal processing [17]. On control protocols, schemes based on continuous drives and

pulse sequences are developed to especially mitigate the ubiquitous  $1/f$  noise [45, 46, 51–55]. Among them, the demonstrations of the dynamical decoupling technique and dynamical-sweet-spot operation have both raised the dephasing time by at least an order of magnitude [46, 51, 56]. All the efforts combined have continuously pushed the coherence times of superconducting qubits to new levels. We use Fig. 1.1 to demonstrate the trend of these improvements over the last two decades.

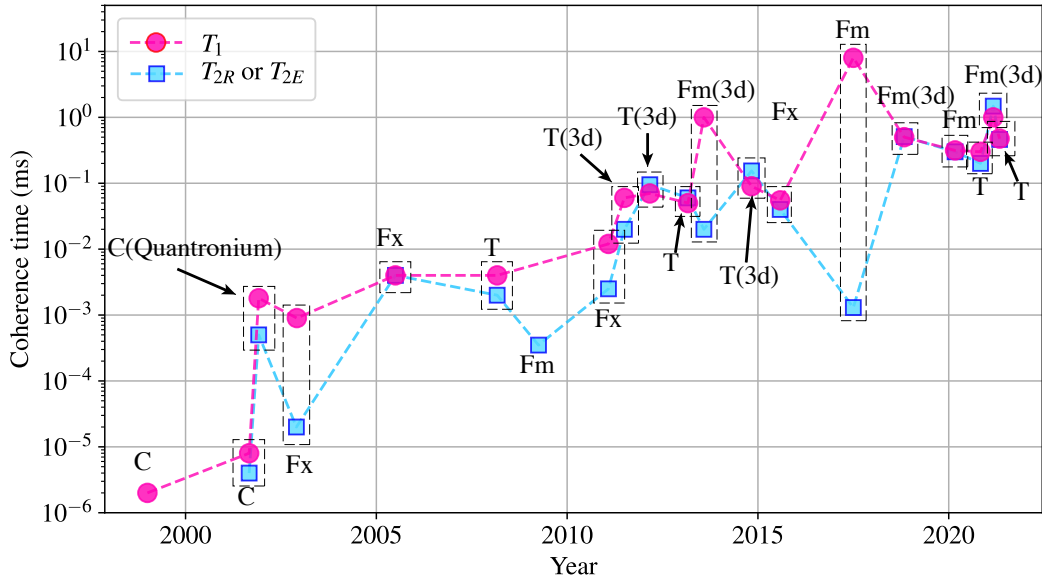


Figure 1.1. The evolution of the coherence times of superconducting qubits based on start-of-art demonstrations over the last two decades. Most of the data are obtained by the courtesy and permission of M. Kjaergaard. Some additional data reflects the progress after the publication of Ref. [3], showing the experimental measurements from Refs. [15–19, 28, 29, 40, 47, 51, 57–66]. Note that in this plot, we only showcase the results of superconducting qubits in the narrow sense, i.e., the Josephson-junction based qubits. We acknowledge that researchers have also made remarkable progress in hybrid qubits and cavity-based qubits [67–77]. The dephasing-time data shown in this plot are obtained by Ramsey or echo measurement. We use “C”, “T”, “Fx” and “Fm” to abbreviate the charge, transmon, flux and fluxonium qubits.

The discussion above has been centered around the downside of noise and mitigation strategies. However, it would not only be unrealistic but also unwise to think of eliminating all noise

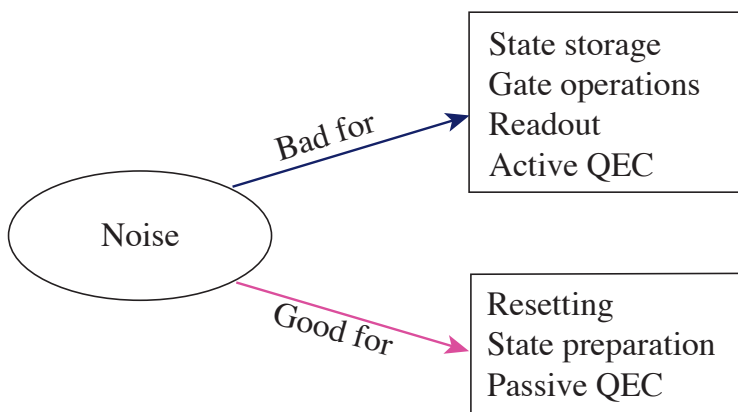


Figure 1.2. A schematic showing the different roles of noise in quantum information processing based on superconducting qubits.

channels. In fact, the engineered energy loss in the superconducting circuits is crucial for the initialization and measurement of the qubit states [78]. Beyond the simplest applications, many research groups have also explored using carefully designed qubit-environment coupling to design or optimize quantum control and noise protection protocols. For example, researchers have used noise engineering to realize state cooling, arbitrary state stabilization and autonomous error correction [70, 78–84]. The last application has been a research hot spot in quantum information processing based on bosonic qubits, where much enhanced coherence has been observed using such passive correction schemes [70, 80, 84, 85]. In short, carefully tuned noise can render qubits insensitive to the unwanted and unavoidable noise. Fig. 1.2 summarizes the discussion above.

Both positive and negative roles of noise have placed it in the spotlight of research on superconducting qubits. This motivates the theme of this thesis: developing strategies to not only mitigate harmful effects of noise, but also leverage it to the advantage of quantum

information processing with superconducting qubits. In the following, we will give an outline of this thesis.

In Chapter 2, we introduce in detail the quantum master equation, which is a useful tool for describing qubit state evolution in an open system. We particularly focus on the Floquet version of this equation, which deals with a periodically driven system. One can reduce this equation to one that describes an undriven system by replacing the time-periodic Hamiltonian by a time-independent one. In Chapter 3, we review in more detail the development of two aforementioned superconducting qubits, namely, the transmon and fluxonium qubits. They are the workhorses behind the research that will be presented in this thesis. In Chapter 4, we first introduce our progress on noise engineering. We present in detail our theory and experimental work on the universal stabilization of single-qubit states, with a tunable coupler tailoring the interaction between the qubit and the noisy bath. In Chapter 5, we turn to the direction of noise mitigation, and introduce a novel noise-protection scheme using the dynamical version of qubit sweet spots. We develop the connection between such sweet spots and the quasi-energy extrema of the Floquet states. In Chapter 6, we extend our single-qubit system to a composite one, and introduce the concept of a *revolver qubit*. Using this dynamically encoded qubit, we could achieve double protection from both depolarization and pure dephasing. In the appendices, we present some details about rotating wave approximation, Born-Oppenheimer approximation, adiabatic Floquet theory and discussion of other  $1/f$  noise protection schemes.

## CHAPTER 2

**Quantum Master Equation****2.1. Secular Redfield Floquet master equation**

The quantum master equation is a widely-used tool for simulating an open quantum system. In this section, we first focus on a more general scenario, where a time-periodically driven system is coupled to a large bath, to derive the Floquet quantum master equation [86, 87]. This equation lays the basis for the discussion in Chapter 5 and 6. By removing the time dependence in the Hamiltonian, the equation will naturally reduce to the usual master equation describing an undriven system.

We start the derivation by writing the Hamiltonian that describes the total system, which is composed of the subsystem of interest, the bath and their coupling, as

$$\hat{H} = \hat{H}_q(t) + \hat{H}_B + \hat{H}_I. \quad (2.1)$$

Above, the qubit Hamiltonian is periodic in time, i.e.,  $\hat{H}_q(t + T) = \hat{H}_q(t)$ , where  $T$  denotes the driving period. We restrict our discussion to the case where  $\hat{H}_B$  and  $\hat{H}_I$  are both time-independent, although the scenario where either or both of them vary with time could also be of interest [46, 88]. To approach, we need information about the closed-system dynamics governed only by Hamiltonian  $\hat{H}_q(t)$ , which can be easily derived if we know the Floquet states and their

quasi-energies. By solving the Floquet equation,

$$\left[ \hat{H}_q(t) - i \frac{\partial}{\partial t} \right] |w_j(t)\rangle = \epsilon_j |w_j(t)\rangle, \quad (2.2)$$

we obtain the Floquet states  $|w_j(t)\rangle$  with corresponding quasi-energies  $\epsilon_j$ . Note that the solution of  $|w_j(t)\rangle$  is required to be time-periodic with the same period  $T$ . Using the solutions, we can straightforwardly express the closed-system propagation operator as

$$\begin{aligned} \hat{U}_q(t, 0) &= \mathcal{T} \exp \left[ -i \int_0^t \hat{H}_q(t') dt' \right] \\ &= \sum_j |\psi^F(t)\rangle \langle \psi^F(0)|, \end{aligned} \quad (2.3)$$

with  $|\psi^F(t)\rangle \equiv |w_j(t)\rangle \exp(-i\epsilon_j t)$ , and  $\mathcal{T}$  is the time-ordering operator. Beside the propagator for the system, we also define the bath propagator  $\hat{U}_B(t, 0) = \exp[-i \int_0^t \hat{H}_B dt']$ . The two of them combined give us the unperturbed propagator of the full system  $\hat{U}_0(t, 0) = \hat{U}_q(t, 0) \hat{U}_B(t, 0)$ . The density operator in the interaction picture, defined by  $\tilde{\rho}(t) \equiv \hat{U}_0^\dagger(t) \rho(t) \hat{U}_0(t)$  [here  $\rho(t)$  denotes the density operator in the lab frame] satisfies the von Neumann equation

$$\frac{d\tilde{\rho}(t)}{dt} = -i[\tilde{H}_I(t), \tilde{\rho}(t)], \quad (2.4)$$

where  $\tilde{H}_I(t) = \hat{U}_0(t)^\dagger \hat{H}_I \hat{U}_0(t)$ . The next two steps are standard [86]: we first integrate the two sides of Eq. (2.4) and obtain

$$\tilde{\rho}(t) = \tilde{\rho}(0) - i \int_0^t ds [\tilde{H}_I(s), \tilde{\rho}(s)]; \quad (2.5)$$

then we insert Eq. (2.5) back into the right-hand side of Eq. (2.4) and trace over the bath degrees of freedom, to arrive at

$$\frac{d\tilde{\rho}_q(t)}{dt} = - \int_0^t ds \text{Tr}_B [\tilde{H}_I(t), [\tilde{H}_I(s), \tilde{\rho}(s)]] . \quad (2.6)$$

Here, we define  $\tilde{\rho}_q(t) \equiv \text{Tr}_B \tilde{\rho}(t)$ .

In principle, we could insert Eq. (2.5) into the von Neumann equation iteratively. However, such an operation will only over-complicate the problem, especially when the system-bath coupling is considered weak. Here, we introduce the first approximation.

*Born approximation.*— If the system-bath interaction is sufficiently weak, and the size of the bath is sufficiently large, the dynamics of the system only negligibly affects the bath. In this situation, we can safely neglect the correlation between the system and bath, and approximate the total density operator as  $\tilde{\rho}(s) \approx \tilde{\rho}_q(s) \otimes \tilde{\rho}_B$  on the right-hand side of Eq. (2.6), where  $\tilde{\rho}_B$  describes the thermal equilibrium state of the bath (still in the interaction picture). This will yield an integro-differential equation, which is still not sufficiently simplified.

After the replacement of  $\tilde{\rho}(s)$  by  $\tilde{\rho}_q(s) \otimes \tilde{\rho}_B$ , the von Neumann equation for  $\tilde{\rho}_q(t)$  has no dynamics of the bath degree of freedom anymore. The new problem is that, the evolution of the system's density operator depends on its full history, which makes this equation numerically challenging to solve. We further assume that the decay time of the bath correlation is much shorter compared to that of the system. In this case, the bath correlation function already approaches zero before  $\tilde{\rho}_q$  significantly changes. In this situation, the integration over  $s$  where  $\tilde{\rho}_q(s)$  differs significantly from  $\tilde{\rho}_q(t)$  will minimally contribute to the whole integral, which allows us to further replace  $\tilde{\rho}_q(s) \otimes \tilde{\rho}_B$  by  $\tilde{\rho}_q(t) \otimes \tilde{\rho}_B$ . After this, we finally obtain an ordinary differential equation that is local in time. The approximation described here is also considered

part of the Markovian approximation in literature [86]. Note that the system-bath correlation could be important if the system-bath coupling is not sufficiently weak, or the size of the bath is not sufficiently large [89].

By completing these steps, we arrive at the equation governing the evolution of the partially traced density operator in the interaction picture,

$$\frac{d\tilde{\rho}_q(t)}{dt} = - \int_0^t d\tau \text{Tr}_B [\tilde{H}_I(t), [\tilde{H}_I(t-\tau), \tilde{\rho}_q(t) \otimes \tilde{\rho}_B]], \quad (2.7)$$

where  $s$  is replaced by  $t - \tau$ . This equation is called the Redfield equation. One caveat of this equation is that it does not always conserve positivity of the density matrix, especially under a strong system-bath coupling. This problem will be later discussed in more detail after we make an appropriate secular approximation. For this approximation, the information about the Floquet states and quasi-energies will be required. Up to the step of Eq. (2.7), the derivation is not different from that of an undriven system given in many textbooks.

To prepare for the secular approximation, we first expand the lab-frame interaction Hamiltonian as

$$\hat{H}_I = \sum_{\alpha} \hat{\mathcal{A}}_{\alpha} \otimes \hat{\mathcal{B}}_{\alpha}, \quad (2.8)$$

where  $\hat{\mathcal{A}}_{\alpha}$  only acts on the system and  $\hat{\mathcal{B}}_{\alpha}$  only acts on the bath. We can require  $\hat{\mathcal{A}}_{\alpha}$  and  $\hat{\mathcal{B}}_{\alpha}$  to be traceless (if they are not traceless, we can take out the trace and incorporate that part with  $\hat{H}_q$  or  $\hat{H}_B$ ). In the interaction picture, they are transformed to  $\tilde{\mathcal{A}}_{\alpha}(t) = \hat{U}_q^{\dagger}(t, 0) \hat{\mathcal{A}}_{\alpha} \hat{U}_q(t, 0)$  and  $\tilde{\mathcal{B}}_{\alpha}(t) = \hat{U}_B^{\dagger}(t, 0) \hat{\mathcal{B}}_{\alpha} \hat{U}_B(t, 0)$ . Toward the secular approximation, it is important to identify the fast-rotating terms in the differential equation. For this purpose, we resolve the different

frequency components of  $\tilde{\mathcal{A}}_\alpha(t)$  by using Eq. (2.3) to expand  $\tilde{\mathcal{A}}_\alpha(t)$  as

$$\begin{aligned}\tilde{\mathcal{A}}_\alpha(t) &= \sum_{jj'} \langle w_{j'}(t) | \hat{\mathcal{A}}_\alpha | w_j(t) \rangle \exp[-i(\epsilon_j - \epsilon_{j'})t] |w_j(0)\rangle \langle w_{j'}(0)| \\ &= \sum_{jj'k} \mathcal{A}_{\alpha jj'k} \exp[-i(\epsilon_j - \epsilon_{j'} + k\omega_d)t] |w_j(0)\rangle \langle w_{j'}(0)|,\end{aligned}\quad (2.9)$$

where

$$\mathcal{A}_{\alpha jj'k} \equiv \frac{1}{T} \int_0^T dt \langle w_j(t) | \hat{\mathcal{A}}_\alpha | w_{j'}(t) \rangle \exp(ik\omega_d t) \quad (2.10)$$

is the  $k$ th Fourier component of the time-periodic function  $\langle w_j(t) | \hat{\mathcal{A}}_\alpha | w_{j'}(t) \rangle$ . We further define  $\bar{\omega}_{jj'k} \equiv \epsilon_j - \epsilon_{j'} + k\omega_d$  for later convenience (these frequencies are called the filter frequencies). Some filter frequencies are identical, for example,  $\bar{\omega}_{jjk} = \bar{\omega}_{j'j'k}$  for any  $j, j' = 0, 1, \dots, N$ . It is convenient to define a set that contains all different filter frequencies  $F = \{\omega | \omega = \bar{\omega}_{jj'k} \text{ for all applicable } j, j', k\}$ . Using this notation, we expand

$$\tilde{\mathcal{A}}_\alpha(t) = \sum_{\omega \in F} \hat{\mathcal{A}}_\alpha(\omega) \exp(-i\omega t), \quad (2.11)$$

where the coefficient  $A_\alpha(\omega)$  is derived as

$$\tilde{\mathcal{A}}_\alpha(\omega) = \sum_{j,j',k \ni \bar{\omega}_{jj'k}=\omega} \tilde{\mathcal{A}}_{\alpha jj'k} |w_j(0)\rangle \langle w_{j'}(0)|. \quad (2.12)$$

We insert Eq. (2.9) into (2.7), and find

$$\begin{aligned}\frac{d\tilde{\rho}_q(t)}{dt} &= \sum_{\alpha,\beta} \sum_{\omega,\omega' \in F} \exp[i(\omega' - \omega)t] \Gamma_{\alpha\beta}^+(\omega) \\ &\quad \times \left( \hat{\mathcal{A}}_\beta(\omega) \tilde{\rho}_S(t) \hat{\mathcal{A}}_\alpha^\dagger(\omega') - \hat{\mathcal{A}}_\alpha^\dagger(\omega') \hat{\mathcal{A}}_\beta(\omega) \tilde{\rho}_S(t) \right) + \text{H.c.},\end{aligned}\quad (2.13)$$

where we define

$$\begin{aligned}
\Gamma_{\alpha\beta}^+(\omega, t) &= \int_0^t d\tau \exp[-i\omega(\tau - t)] \langle \tilde{\mathcal{B}}_\alpha(t) \tilde{\mathcal{B}}_\beta(\tau) \rangle \\
&= \int_0^t d\tau \exp(i\omega\tau) \langle \tilde{\mathcal{B}}_\alpha(\tau) \tilde{\mathcal{B}}_\beta(0) \rangle \quad (\text{variable change } t - \tau \rightarrow \tau) \\
&= \int_{-\infty}^{\infty} \frac{du}{2\pi} S_{\alpha\beta}(u) \int_0^t \exp[i(\omega - u)\tau] d\tau \\
&= \int_{-\infty}^{\infty} \frac{du}{2\pi} S_{\alpha\beta}(u) t \operatorname{sinc} \left[ \frac{(\omega - u)t}{2} \right] \exp \left[ \frac{i(\omega - u)t}{2} \right], \tag{2.14}
\end{aligned}$$

and  $S_{\alpha\beta}(\omega) = \int_{-\infty}^{\infty} d\tau \exp(i\omega\tau) \langle \tilde{\mathcal{B}}_\alpha(\tau) \tilde{\mathcal{B}}_\beta(0) \rangle$ .

*Secular approximation.*— We assume that for any pair of filter frequencies  $(\omega, \omega')$  that belong to F, if they are not exactly the same and  $\hat{\mathcal{A}}_\alpha(\omega)$  and  $\hat{\mathcal{A}}_\alpha(\omega')$  is finite, their difference  $|\omega - \omega'|$  is always sufficiently large compared with the inverse of the time we are interested in (this time is usually the system decay time). In this scenario, the rotating-wave approximation allows us to neglect the terms in Eq. (2.13) with  $\omega \neq \omega'$ . (See detailed discussion of RWA in Appendix A.) If the assumption about the filter frequencies accidentally fails, we need to find another strategy to carry out the secular approximation.

Let us assume that the above assumptions hold. The approximated equation can still be further simplified, using the following two facts, namely  $S_{\alpha\beta}(u) = S_{\beta\alpha}^*(u)$  and  $\operatorname{sinc}[(\omega - u)t/2] \exp[i(\omega - u)t/2] + \text{C.c.} = 2\operatorname{sinc}[(\omega - u)t]$ . After this step, we finally have

$$\begin{aligned}
\frac{d\tilde{\rho}_q(t)}{dt} &= \sum_{\alpha,\beta} \sum_{\omega} \Gamma_{\alpha\beta}(\omega, t) \left( \hat{\mathcal{A}}_\beta(\omega) \tilde{\rho}_q(t) \hat{\mathcal{A}}_\alpha^\dagger(\omega) - \frac{1}{2} \hat{\mathcal{A}}_\alpha^\dagger(\omega) \hat{\mathcal{A}}_\beta(\omega) \tilde{\rho}_q(t) - \frac{1}{2} \tilde{\rho}_q(t) \hat{\mathcal{A}}_\alpha^\dagger(\omega) \hat{\mathcal{A}}_\beta(\omega) \right) \\
&\quad - \sum_{\alpha,\beta} \sum_{\omega} \left( \int_{-\infty}^{\infty} \frac{du}{2\pi} S_{\alpha\beta}(u) t \operatorname{sinc} \left[ \frac{(\omega - u)t}{2} \right] \sin \left[ \frac{(\omega - u)t}{2} \right] \right) \times i [\hat{\mathcal{A}}_\alpha^\dagger(\omega) \hat{\mathcal{A}}_\beta(\omega), \tilde{\rho}_q(t)], \tag{2.15}
\end{aligned}$$

where

$$\Gamma_{\alpha\beta}(\omega, t) \equiv 2 \int_{-\infty}^{\infty} \frac{du}{2\pi} S_{\alpha\beta}(u) t \operatorname{sinc}[(\omega - u)t]. \quad (2.16)$$

Eq. (2.15) is the secular Floquet Redfield equation we have aimed for. We have two comments before we proceed to the application of this equation. First, the last line of Eq. (2.15) contains terms that are referred to as the Lamb shift. Researchers have experimentally studied the Lamb shift in superconducting qubits induced by their coupling to a transmission line [90, 91]. As usual, we will omit these terms in the following discussion. Our second comment is that, in the definition Eq. (2.16),  $t \operatorname{sinc}[(\omega - u)t]$  serves as a filter function over the noise spectrum  $S_{\alpha\beta}(u)$ . This function is peaked at  $u = \omega$ , with the peak width given by  $2\pi/t$ . Therefore, the filter function peak will grow narrower for longer times  $t$ .

At the end of this section, we briefly demonstrate how to reduce this equation for an undriven system. In fact, the scenario of a static system is only a special case of that of a periodic drive. Naturally, the eigenstates and eigenenergies derived from the time-independent Hamiltonian of the static system are also the Floquet states and the quasi-energies. We only need to replace  $|w_0(t)\rangle$  and  $\epsilon_j$  by the eigenstate  $|j\rangle$  and eigenenergy  $E_j$  in Eq. (2.3), which gives the propagator

$$\hat{U}_q(t) = \sum_{jj'} |j\rangle \langle j| \exp(-iE_j t). \quad (2.17)$$

The most noteworthy difference between the driven and undriven problems is that, for the latter case the component  $\mathcal{A}_{\alpha jj'k}$  with  $k \neq 0$  vanishes, since now the eigenstates are constant over time. The filter frequencies will just take the values of  $E_j - E_{j'}$ .

## 2.2. Markovian approximation

When the bath's correlation time is much shorter compared with the time of interest, we are allowed to make another import approximation, the Markovian approximation.

In terms of the noise power and the filter function, the previous statement is reworded as follows. A short bath correlation time implies that  $\langle \tilde{\mathcal{B}}_\alpha(t) \tilde{\mathcal{B}}_\beta(0) \rangle$  decays quickly with time, such that the time domain the correlation function has a narrow peak width, which we denote as  $\tau_R$ . Then in the frequency domain, the peak width will be contrarily broad, approximately  $2\pi/\tau_R$ . Recall that the filter function peak width is given by  $2\pi/t$ . Therefore, if the time of interest, which is usually the system decay time, is much longer than the bath correlation time, the filter function cannot resolve the variation in  $S(u)$  due to a much broader peak width. This fact allows us to replace the filter function by a Dirac delta function, which corresponds to replacing  $t$  by  $\infty$  in Eq. (2.16).

This step yields the Floquet Markovian master equation,

$$\frac{d\tilde{\rho}_q(t)}{dt} = \sum_{\alpha,\beta} \sum_{\omega} S_{\alpha,\beta}(\omega) \left( \hat{\mathcal{A}}_\beta(\omega) \tilde{\rho}_q(t) \hat{\mathcal{A}}_\alpha^\dagger(\omega) - \frac{1}{2} \hat{\mathcal{A}}_\alpha^\dagger(\omega) \hat{\mathcal{A}}_\beta(\omega) \tilde{\rho}_q(t) - \frac{1}{2} \tilde{\rho}_q(t) \hat{\mathcal{A}}_\alpha^\dagger(\omega) \hat{\mathcal{A}}_\beta(\omega) \right). \quad (2.18)$$

Note that the terms corresponding to the Lamb shift have been neglected here. We need to point out that in a number of experiments, especially those where  $1/f$  noise is an important contributor to the qubit decoherence, using the Markovian master equation will not give us the correct description of the evolution of the qubit's density matrix.

### 2.3. Coherence times of a two-level system

In this last section of the chapter, we present a concrete example where we apply the Floquet master equation to estimate qubit coherence time. We will finally arrive at expressions of the qubit depolarization and pure-dephasing rates, given that the system is coupled to a Markovian noise source where the Markovian master equation is applicable. The treatment of a system coupled to a non-Markovian noise source will be delayed to Chapter 5 when we discuss dynamical sweet spots.

We first specify the Hamiltonian in Eq. (2.1) that governs the evolution of this system. We assume that  $\hat{H}_q(t)$  is a time-periodic Hamiltonian describing a driven two-level system, and the qubit-bath coupling is given by  $\hat{H}_I = \hat{\sigma}\hat{\eta}$ , where  $\hat{\sigma}$  and  $\hat{\eta}$  are qubit and bath operators, respectively. To derive the propagator  $\hat{U}_q(t)$ , we use the Hamiltonian  $\hat{H}_q(t)$  to solve for the Floquet states and quasi-energies. Since the dimension of the Hilbert space is 2, we only have two independent Floquet states denoted by  $|w_j(t)\rangle$  ( $j = 0, 1$ ). In the interaction picture, the qubit-bath coupling is  $\tilde{H}_I(t) = \hat{U}_0^\dagger(t)\hat{H}_I\hat{U}_0(t)$ , where  $\hat{U}_0(t) = \hat{U}_q(t)\hat{U}_B(t)$ ,  $\hat{U}_q(t) = \sum_{j=0,1} |w_j(t)\rangle\langle w_j(0)| \exp(-i\epsilon_j t)$ , and  $\hat{U}_B(t) = \exp(-i\hat{H}_B t)$ . The interaction term can be further expressed as  $\tilde{H}_I(t) = \tilde{\sigma}(t)\tilde{\eta}(t)$ , where  $\tilde{\sigma}(t) = U_q^\dagger(t)\hat{\sigma}\hat{U}_q(t)$  and  $\tilde{\eta}(t) = U_B^\dagger(t)\hat{\eta}\hat{U}_B(t)$ .

The expansion in Eq. (2.9) is specified by

$$\tilde{\sigma}(t) = \sum_{k \in \mathbb{Z}, \mu = \pm, \phi} g_{k\mu} \hat{c}_\mu(0) \exp(-i\bar{\omega}_{k\mu} t). \quad (2.19)$$

Here, we define the Floquet counterparts of the Pauli matrices by

$$\begin{aligned}\hat{c}_+(t) &= |w_1(t)\rangle\langle w_0(t)|, \\ \hat{c}_-(t) &= |w_0(t)\rangle\langle w_1(t)|, \\ \hat{c}_\phi(t) &= |w_1(t)\rangle\langle w_1(t)| - |w_0(t)\rangle\langle w_0(t)|.\end{aligned}\tag{2.20}$$

The frequencies  $\bar{\omega}_{k,\mu}$  appearing in Eq. (2.19) are the filter frequencies defined in Section 2.1, namely

$$\bar{\omega}_{k\pm} = \mp\epsilon_{01} + k\omega_d, \quad \bar{\omega}_{k\phi} = k\omega_d.\tag{2.21}$$

Furthermore, the Fourier-transformed coupling matrix elements are given by

$$\begin{aligned}g_{k\pm} &= \frac{\omega_d}{2\pi} \int_0^{2\pi/\omega_d} dt e^{ik\omega_d t} \text{Tr}_q [\hat{\sigma} \hat{c}_\mp(t)], \\ g_{k\phi} &= \frac{\omega_d}{4\pi} \int_0^{2\pi/\omega_d} dt e^{ik\omega_d t} \text{Tr}_q [\hat{\sigma} \hat{c}_\phi(t)],\end{aligned}\tag{2.22}$$

where  $\text{Tr}_q$  is the partial trace over the qubit degrees of freedom.

Inserting Eq. (2.19) into Eq. (2.15), we find the secular Redfield equation for this two-level system

$$\frac{d\tilde{\rho}_q(t)}{dt} = \sum_{\mu=\pm,\phi} \zeta_\mu \left[ \int_{-\infty}^{\infty} d\omega F_\mu(\omega, t) S(\omega) \right] \mathbb{D}[\hat{c}_\mu] \tilde{\rho}_q(t),\tag{2.23}$$

where

$$F_\mu(\omega, t) = \zeta_\mu^{-1} \sum_k \pi^{-1} t \text{sinc}[(\omega - \bar{\omega}_{k\mu})t] |g_{k\mu}|^2\tag{2.24}$$

denotes the filter functions from Section III,  $\mathbb{D}[\hat{L}]\tilde{\rho}_q = \hat{L}\tilde{\rho}_q\hat{L}^\dagger - (\hat{L}^\dagger\hat{L}\tilde{\rho}_q + \tilde{\rho}_q\hat{L}^\dagger\hat{L})/2$  is the usual damping superoperator, and  $S(\omega) = \int_{-\infty}^{\infty} dt e^{i\omega t} \text{Tr}_B[\tilde{\eta}(t)\tilde{\eta}(0)\tilde{\rho}_B]$  is the noise spectrum. We have further introduced the abbreviations  $\zeta_{\pm} \equiv 1$  and  $\zeta_{\phi} \equiv 1/2$ , and used  $\hat{c}_{\mu}(0) \rightarrow \hat{c}_{\mu}$ .

The simplified Redfield equation (2.23) is reminiscent of the Lindblad form, and includes three distinct terms  $\mu = \pm$  and  $\mu = \phi$  that describe relaxation, excitation and pure dephasing of the Floquet qubit. However, in place of fixed rates associated with the individual jump terms, Eq. (2.23) still involves time-dependent rate coefficients given by

$$K_{\mu}(t) = \int_{-\infty}^{\infty} d\omega F_{\mu}(\omega, t)S(\omega). \quad (2.25)$$

This  $t$ -dependent integral implies that the instantaneous decay rates are also time-dependent in general, unless the noise spectrum is exactly flat. Note that  $K_{\mu}(t)$  is not guaranteed to be positive. Although  $S(\omega)$  is positive for all frequencies  $\omega$  [86], the function  $t \text{sinc}[(\omega - \bar{\omega}_{k_{\mu}})t]$  can take on negative values. Therefore, the secular Redfield equation we have derived still does not in general satisfy the Lindblad form, which implies that the density matrix obtained from this equation is not strictly guaranteed to be positive. Fortunately, we only rarely encounter cases of equation yields non-positive density matrices. Furthermore, certain choices of  $S(\omega)$  and  $F_{\mu}(\omega, t)$  will yield  $K_{\mu}(t) > 0$  for relevant times  $t$ . For example, if the noise spectrum is regular and the time we are interested in is sufficiently long, the narrowly peaked filter function  $t \text{sinc}[(u - \omega)t]$  cannot well resolve the variation in the noise spectrum. Under this condition,  $K_{\mu}(t)$  will be positive, given that  $\int_{-\infty}^{\infty} t \text{sinc}[(u - \omega)t]d\omega = \pi$  is positive. (We have verified this numerically using a couple of examples.)

If we further assume a short bath correlation time, we can carry out the Markovian approximation by taking  $t \rightarrow \infty$  in Eq. (2.25), and arrive at the two-level-system version of

Eq. (2.18)

$$\frac{d\tilde{\rho}_q(t)}{dt} = \sum_{k \in \mathbb{Z}, \mu = \pm, \phi} |g_{k\mu}|^2 S(\bar{\omega}_{k\mu}) \mathbb{D}[\hat{c}_\mu] \tilde{\rho}_q(t). \quad (2.26)$$

This form allows one to directly read off the resulting rates which are given by  $\gamma_\pm = \sum_k |g_{k\mu}|^2 S(\bar{\omega}_{k\pm})$  and  $\gamma_\phi = \sum_k 2|g_{k\phi}|^2 S(\bar{\omega}_{k\phi})$ .

To help the reader connect these equations to more familiar results, we next briefly show how the Floquet decoherence rates reduce to the ones for an undriven two-level system. The static qubit Hamiltonian is given by  $\hat{H}_q = \Omega_{ge} \hat{\sigma}_z / 2$ , where  $\Omega_{ge}$  denotes the qubit transition frequency, and  $\hat{\sigma}_z$  is defined by  $|e\rangle\langle e| - |g\rangle\langle g|$ . This choice yields,

$$g_{k-} = \sigma_{ge} \delta_{0,k}, \quad g_{k+} = \sigma_{eg} \delta_{0,k}, \quad g_{k\phi} = \frac{1}{2} (\sigma_{ee} - \sigma_{gg}) \delta_{0,k}$$

$$\bar{\omega}_{0\pm} = \mp \Omega_{ge} \quad \bar{\omega}_{0\phi} = 0.$$

Here, we define  $\sigma_{jj'} \equiv \langle j' | \hat{\sigma} | j \rangle$ . Finally, we find

$$\gamma_\pm = |\sigma_{ge}|^2 S(\mp \Omega_{ge}),$$

$$\gamma_\phi = |\sigma_{ee} - \sigma_{gg}|^2 S(0) / 2, \quad (2.27)$$

which replicates the usual results derived using Fermi's golden rule.

## CHAPTER 3

### Introduction to the Transmon and Fluxonium Qubits

In this section, we present a short introduction to two of the most successful superconducting qubits, namely, the transmon and fluxonium qubits. Both of these qubits are leading in qubit performance, especially in coherence times and gate fidelities. More importantly, we particularly choose to introduce these two qubit variants because these two types of qubits provide the hardware on which we base our following research work.

Our very short review does not pursue an experimental perspective with detailed discussion of the circuit's architectural layout, fabrication and control and readout techniques. We will rather focus on the lumped-element models of these qubits, and especially address the topic of qubit coherence times, which is in line with the theme of this thesis. We acknowledge that most of the simulations shown below are assisted by the python toolbox `scqubits` developed by Koch, Groszkowski and collaborators.

#### 3.1. Transmon

The transmon qubit is a derivative of an earlier qubit design – the Cooper pair box [29, 57, 92–95]. In 1999, Nakamura *et al.* first observed coherent oscillations in this type of qubit [57]. We show the lumped-element circuit diagram of the Cooper-pair box in Fig. 3.1 (a). The standard circuit quantization procedure yields the following qubit Hamiltonian

$$\hat{H}_t = 4E_C(\hat{n} - n_g)^2 - E_J \cos(\hat{\varphi}). \quad (3.1)$$

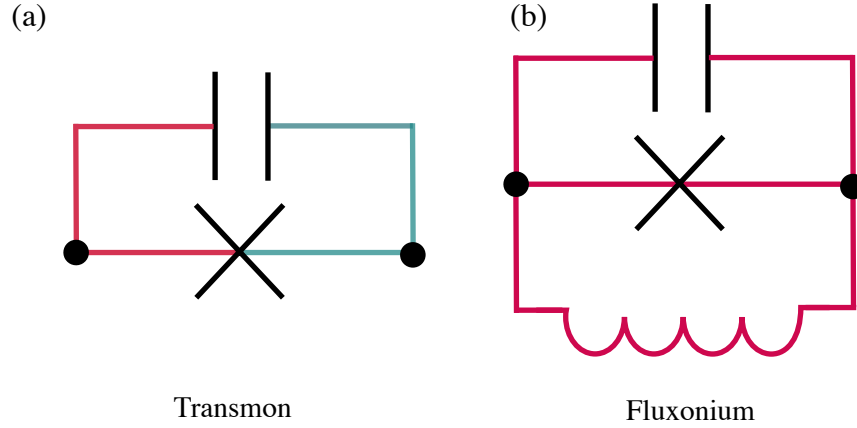


Figure 3.1. Lumped-element circuit diagrams of the transmon and fluxonium qubits. The different coloring in the diagrams indicates the separate superconducting islands in these circuits. (We imagine that we have a linear geometric inductor in the fluxonium circuit.) Because of different circuit topology, the transmon circuit consists of two islands weakly linked by a Josephson junction, while the fluxonium has no separate island.

Above,  $E_C = e^2/2C$  denotes the qubit charging energy ( $C$  is the total capacitance across the junction), and  $E_J$  is the Josephson energy related to the junction. The Cooper pair box can usually be controlled by a gate voltage, which allows us to tune the parameter  $n_g$  in Eq. (3.1). As shown in Fig. 3.1, the Cooper pair box has two separate islands, connected only by a weak junction. Since the Josephson junction can only tunnel electrons in pairs (called Cooper pairs), the charge operator  $\hat{n}$ , which describes the number of Cooper pairs transferred between the islands, only takes discrete eigenvalues. Meanwhile,  $\hat{\phi}$  is a periodic operator that denotes the gauge invariant phase difference between the two islands. The commutation relation of this pair of operators is  $[e^{\pm i\hat{\phi}}, \hat{n}] = \pm e^{\pm i\hat{\phi}}$ .

Before the proposal of the transmon qubit, researchers mostly explored the Cooper-pair boxes in the charge-qubit regime ( $E_C \simeq E_J$ ) [29, 57, 95]. In this regime, the qubit enjoys large anharmonicity, especially at  $n_g = 1/2$ , as shown in Fig. 3.2 (a). However, the benefit of anharmonicity comes at the cost of strong noise sensitivity, especially to  $1/f$  charge noise. The

interaction of the qubit with this noise source can be modeled as fluctuations of the gate charge  $n_g$ . In the charge-qubit regime, the variation of the transition energies with respect to different charge offset  $n_g$ , which we call the charge dispersion, is significant as shown in Fig. 3.2 (a), which makes the qubit especially sensitive to this type of noise.

Researchers have found optimal working points to suppress the qubit's first-order charge dispersion to zero [95]. We can easily check in Fig. 3.2 that at the "sweet spot"  $n_g = 0.5$ , the linear energy dispersion equals zero, i.e.,  $\partial\Omega_{ge}/\partial n_g = 0$ . Indeed, in Ref. [13], researchers have observed over an order of magnitude improvement of  $T_2$  by tuning the gate charge to the sweet spot. However, the coupling strength between the qubit and  $1/f$  charge noise source is so strong that the fluctuations induced by  $1/f$  charge noise (and quasi-particle tunneling) constantly moves the qubit off the sweet spot [37]. In this situation, suppressing the linear charge dispersion is not enough. These effects limited the pure-dephasing time of charge qubits at the sweet spot to the order of  $1 \mu\text{s}$  [13, 95]. The spectrum shown in Fig. 3.2 (a) is simulated using the same circuit parameters as in Ref. [95].

In 2007, Koch *et al.* found that, going to the limit of  $E_J \gg E_C$  exponentially suppresses the charge dispersion of a Cooper-pair box [37], which motivates the design of the transmon qubit. To see this, we simulate the energy spectrum of an experimentally realized transmon qubit in Ref. [61], with  $E_J/E_C = 70$ . The energy dispersion in this parameter regime is exponentially suppressed, which offers the transmon excellent insensitivity to charge noise. The cost is that the transmon qubit has a much smaller anharmonicity compared with that of the charge qubit (the anharmonicity is approximated by  $-E_C$  in the  $E_J \gg E_C$  limit). Fortunately, the reduction is only polynomial compared with the exponential suppression of the charge dispersion [37].

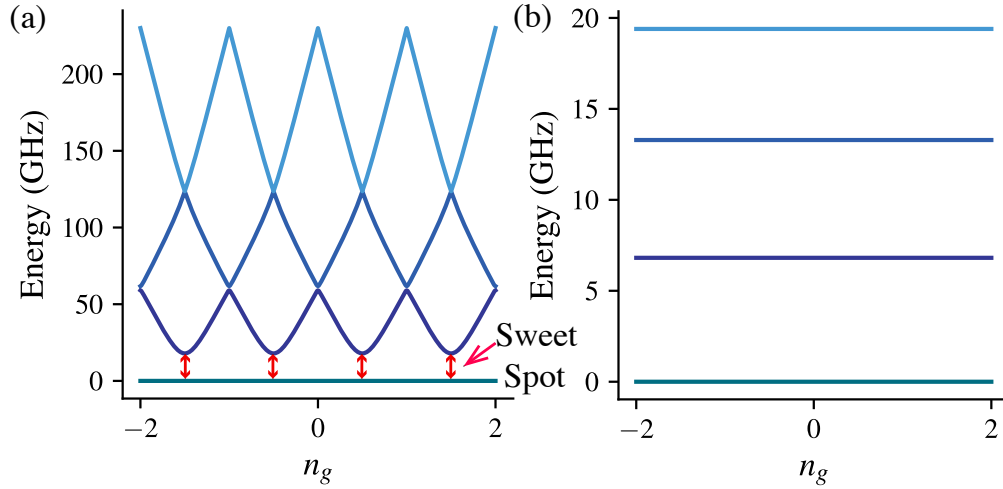


Figure 3.2. Numerically calculated spectra of Cooper pair boxes with respect to offset charge from two experiments [61, 95]. (a) shows the results for a Cooper pair box with  $E_J/E_C = 1.27$ , which yields significant charge dispersion. The double-headed arrows indicate the locations of the sweet spots used in Ref. [95]. (b) shows the spectrum of a transmon with  $E_J/E_C = 70$ , which yields almost flat energy levels as a function of the offset charge  $n_g$ .

Increasing the ratio of  $E_J/E_C$  is usually realized by adding a shunting capacitor across the two islands separated by the Josephson junction, to reduce the effective charging energy of the Cooper pair box. By optimizing the size and shape of the shunting capacitors to reduce the participation at the lossy surfaces, researchers have significantly reduced the surface loss in the transmon qubit, which helps improve the transmon depolarization time [3, 11, 16, 27, 28]. Probably because of the much improved coherence times and relatively simple circuit structure, the transmon qubit is today's most widely-used superconducting qubit not only in academia but also in industry.

### 3.2. Fluxonium

The strategy of sacrificing qubit anharmonicity for longer coherence times has enabled a series of important experiments on quantum information processing using the transmon qubits [4, 23, 82, 96–98]. However, the limited anharmonicity also causes trouble to quantum information processing in a larger qubit network, especially to the implementation of multi-qubit gates [4].

To avoid the trade-off relation between qubit anharmonicity and charge-noise sensitivity, we need a circuit that is beyond the framework of Cooper pair boxes. One alternative strategy to add an inductor across the junction, instead of shunting the charge qubit by a capacitor. This idea gives us the design of a fluxonium qubit, which was first proposed by Manucharyan *et al.* [47]. The lumped-element fluxonium circuit is shown in Fig. 3.1 (b), whose Hamiltonian is

$$\hat{H}_f(n_g, \phi_e) = 4E_C(\hat{n} - n_g)^2 - E_J \cos \hat{\varphi} + \frac{1}{2}E_L(\hat{\varphi} + \phi_e)^2, \quad (3.2)$$

where  $E_L = (\Phi_0/2\pi)^2/L$  is the inductive energy of the fluxonium,  $L$  denotes the linear inductance, and  $\Phi_0$  is the flux quantum. Note that a new control parameter  $\phi_e = 2\pi\Phi_e/\Phi_0$  is introduced to the Hamiltonian, which denotes the reduced flux that penetrates the fluxonium loop.

Different from capacitive shunting, introducing an inductor to the circuit abruptly changes the circuit topology. As illustrated in Fig. 3.1, the fluxonium circuit does not have separate islands (considering an ideal geometric inductor). Given the new circuit topology, the charge operator  $\hat{n}$  no longer takes on discrete eigenvalues. Also, the phase operator  $\hat{\varphi}$ , which now describes the phase difference across the inductor, is no longer periodic. Both of the operators take on continuous eigenvalues from  $-\infty$  to  $\infty$ . The new boundary conditions imply that the

conjugate pair now satisfies the commutation relation  $[\hat{\varphi}, \hat{n}] = i$ , which is similar to that satisfied by the position and momentum operators of an elementary particle.

The new commutation relation renders the fluxonium spectrum independent of  $n_g$  [99]. To see this, we first define a unitary transformation  $\hat{U}_g(n_g) = \exp(-in_g\hat{\varphi})$ , and then transform the Hamiltonian according to it. We find  $\hat{U}_g(n_g) \hat{n} \hat{U}_g^\dagger(n_g) = \hat{n} + n_g$ , and  $\hat{U}_g \hat{\varphi} \hat{U}_g^\dagger(n_g) = \hat{\varphi}$ , therefore,  $\hat{U}_g(n_g) \hat{H}_f(n_g, \phi_e) \hat{U}_g^\dagger(n_g) = \hat{H}_f(0, \phi_e)$ . This relation reveals that the DC offset in  $n_g$  does not modify the qubit's eigenenergies at all. Because of this, the fluxonium qubit can be considered intrinsically protected from dephasing by  $1/f$  charge noise. Such protection scheme is not available to Cooper-pair boxes due to a different commutation relation.

The special commutation relation also leads to a useful relation between the charge and phase matrix elements

$$\begin{aligned} \langle j | \hat{n} | j' \rangle &= (-i) \times \frac{1}{8E_C} \langle j | [\hat{\varphi}, \hat{H}_f] | j' \rangle \\ &= (-i) \times \frac{1}{8E_C} (E_{j'} - E_j) \langle j | \hat{\varphi} | j' \rangle. \end{aligned} \quad (3.3)$$

(We have already set  $n_g = 0$  since this parameter is irrelevant for a fluxonium.) This relation will be of interest when we discuss the revolver qubit in Chapter 6. Note that Eq. (3.3) does not hold for transmon qubits or Cooper pair boxes in general.

Compared with the transmon qubit, the fluxonium has three circuit parameters to tune. Particularly, it allows us to choose parameters that yield much larger anharmonicity than the transmon, while still maintaining charge-noise insensitivity. However, the cost of introducing the additional inductor is that the junction and the inductor closes the circuit loop, leaving the fluxonium qubit subject to fluctuations of the penetrating flux  $\phi_e$ . The noise spectrum that

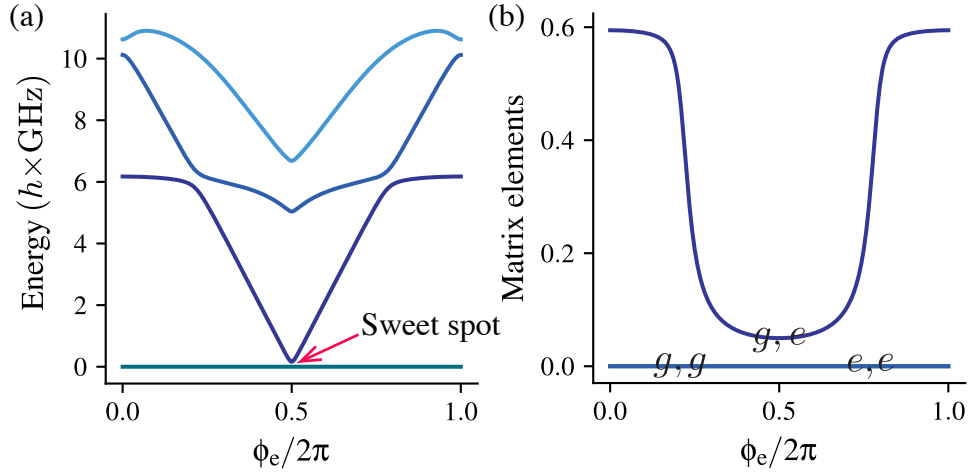


Figure 3.3. Energy spectrum and charge matrix element of a fluxonium qubit. (a) shows the fluxonium spectrum as a function of the external flux. The red arrow points to the sweet spot at  $\phi_e = \pi$ . (b) presents the charge matrix elements as a function of flux. We can observe that there is a dip of the off-diagonal matrix element around the aforementioned sweet spot. We use the circuit parameters of the qubit in Ref. [15], which has coherence times over 1 ms at the sweet spot.

characterizes such fluctuations also has a  $1/f$  behavior at low frequencies. We can observe the relatively strong flux dispersion of the fluxonium qubit in Fig. 3.3. Fortunately, it has been found that the typical amplitude of flux fluctuations ( $\sim 10^{-6} \Phi_0$ ) is much weaker than that for charge ( $\sim 10^{-4} e$ ) [100]. The relatively weak noise amplitude renders the  $1/f$  flux noise's higher-order contribution to decoherence subdominant compared with that from several other noise channels. Because of this, sweet-spot operation by biasing the penetrating flux for a vanishing derivative of energy difference has proven to be impressively successful in improving the dephasing time of a fluxonium qubit [see Fig. 3.5 (b) for experimental evidence] [40, 66].

To date, the most favorable fluxonium working point is probably the sweet spot at half-integer flux quantum [15, 40, 66, 101]. At that sweet spot, i.e.,  $\phi_e = \pi$ , the fluxonium qubit is to the first order insensitive to the low-frequency flux noise. (There is also interesting physics

with the flux slightly away from the sweet spot, which we will sketch in the next paragraph.) We list a couple of possible advantages of operating the fluxonium at this sweet spot rather than at  $\phi_e = 0$ . First, at this particular sweet spot, the off-diagonal charge matrix element  $\langle g|\hat{n}|e\rangle$  is small, which potentially leads to less capacitive loss [15] [See Fig. 3.3(b) for the matrix element's magnitude over different fluxes]. Second, quasi-particle tunneling minimally contribute to fluxonium depolarization at  $\phi_e = \pi$  [102]. Essentially, we find that the matrix element  $\langle g|\sin(\hat{\varphi}/2)|e\rangle$  reaches zero at the half-integer sweet spots. Third, the fluxonium usually has large anharmonicity at the sweet spots with half-integer flux quantum [see spectrum in Fig. 3.3 (a)]. One disadvantage may be that the frequency is too low for qubit operations including initialization, gates, and readout. However, Zhang *et al.* have demonstrated several strategies to solve these problems [66].

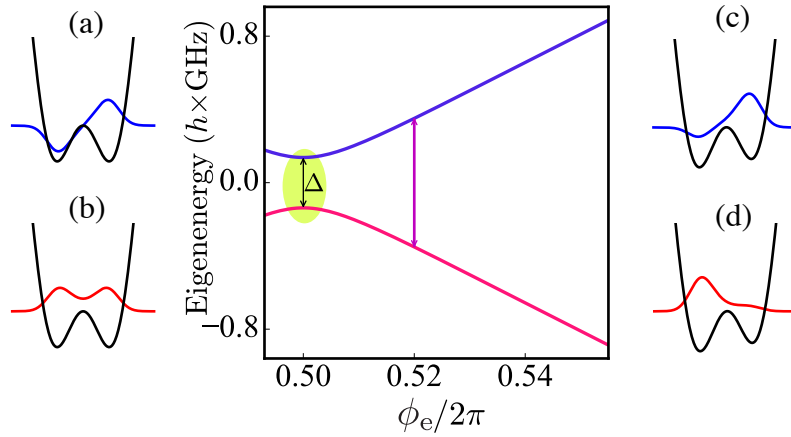


Figure 3.4. Schematic of the energy spectrum and wave functions of a fluxonium qubit operated close to half-integer flux. The central plot shows the spectrum around  $\phi_e = \pi$ . On the sides, we plot the wave functions of fluxonium at two different fluxes: (a) and (b) show the wavefunctions of the ground and first excited states at the sweet spot, i.e.,  $\phi_e = \pi$ ; (c) and (d) plot those at  $\phi_e = 0.52 \times 2\pi$ . (We use  $\Delta$  to denote the fluxonium splitting at the sweet spot.)

Interestingly, even in the small vicinity of that sweet spot, the qubit coherence times can differ characteristically [66]. To help illustrate this, we draw the spectrum and wavefunctions with the control flux located in the aforementioned flux range. Away from the flux sweet spot, the qubit has wavefunctions with disjoint support, as shown in Fig. 3.4 (c) and (d). This leads to a suppression of the off-diagonal matrix elements  $\langle g|\hat{\varphi}|e\rangle$ , relevant for relaxation and excitation, and hence to a relatively long depolarization time. The pure-dephasing time will be short, on the other hand, since the flux dispersion  $\partial\Omega_{ge}/\partial\phi_{dc}$  is significant away from the flux sweet spot (see the central plot of Fig. 3.4). At the flux sweet spot ( $\phi_e = \pi$ ), the situation changes: disjointness of eigenfunctions is lost, and depolarization times are correspondingly shorter. Since the flux dispersion  $\partial\Omega_{ge}/\partial\phi_{dc}$  vanishes at the sweet spot, the qubit is less sensitive to  $1/f$  noise, resulting in much longer pure-dephasing times. The behavior of coherence times described above is clearly observed in a recent experiment [66].

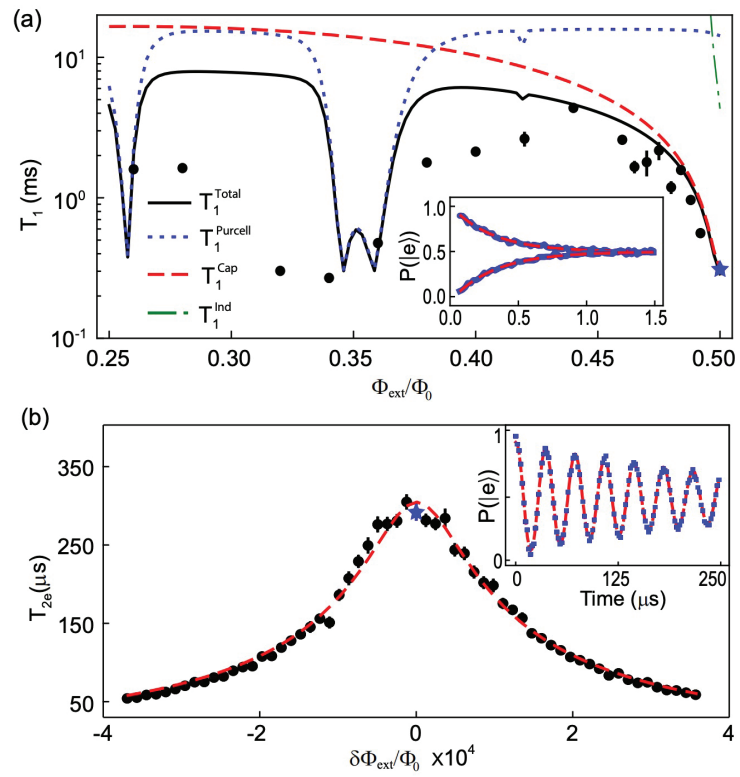


Figure 3.5. The coherence times of a heavy fluxonium realized in Ref. [66]. (a) and (b) show the measurement of depolarization and dephasing times (by echo experiments), respectively. Insets in (a) and (b) show the population decay from the excited state and an echo measurement, both at the sweet spot.

## CHAPTER 4

**Noise Engineering: Universal Stabilization of Single-Qubit States****4.1. Bath engineering and tunable coupler**

In this chapter, we focus on the positive roles of noise. As a recap of the discussion in Chapter 1, dissipation in superconducting elements plays an essential role in qubit operations including initialization, state preparation and autonomous quantum error correction [78–83, 85, 104–106].

The simplest example is probably the ground-state initialization of a qubit whose energy splitting is much larger than the temperature. In this case, nature willingly does us the favor of cooling the qubit to the ground state. However, nature cannot help us with the reset of qubits with a smaller splitting, or the preparation of qubit states other than the ground state. Bath engineering is a technique developed to solve these problems [66, 79, 83]. An early impressive demonstration of this [79] shows that the engineering of the coupling between the qubit and the bath can counteract unwanted thermal noise in a flux qubit and reduce the effective temperature as much as 100 times. The stabilization in a qubit's excited state is later achieved by carefully engineering the qubit-resonator coupling and adding another drive [106]. In 2012, Murch *et al.* [82] demonstrated a scheme which can stabilize arbitrary single-qubit states.

In the meantime, the application of tunable couplers in superconducting qubits also attracted a significant amount of research effort [22, 96, 103, 107–115]. Couplers are widely used to tune

---

Author contribution: This chapter summarizes the work published in Refs. [96, 103]. Ziwen Huang provided theoretical support for the experiment shown in in [96], and carried out the majority of the calculations and simulations in [103].

the coupling strength between two quantum elements (e.g., between two qubits, or between one qubit and one resonator). They are particularly useful for readout and two-qubit gates [21, 22, 108, 109, 111, 112, 115, 116]. Recently, researchers have carried out a series of experiments using this technique to demonstrate two-qubit gates in transmon qubits with state-of-the-art fidelities [21, 22].

The convenient tuning of the coupling strength motivates us to consider whether we can apply the tunable coupling technique in bath engineering to provide alternatives or even improve the previous qubit stabilization schemes.

## 4.2. Model of the composite system

This thought motivated our collaborators and us to explore qubit stabilization schemes that employ tunable couplers. In Ref. [96], our collaborators experimentally demonstrated a scheme for stabilizing a transmon qubit in an arbitrary superposition state, for which we provided theoretical support. Following this work, we further explore theoretically alternative stabilization schemes for higher stabilization fidelities, and investigate more carefully the stabilization time [103]. Different from the earlier experimental work, the theory project focused on stabilizing a fluxonium qubit.

In Fig. 4.1, we show the diagrams of the lumped-element circuits that we use for qubit stabilization in these two references. A full analysis of the circuit and a detailed derivation of the circuit Hamiltonian is lengthy, therefore we decide to relocate them to later parts of this chapter. In the first few sections, we will focus on the effective and much simplified Hamiltonian that describes the coupled qubit and resonator, with the coupler integrated out. The effective model is essential identical for the two circuits.

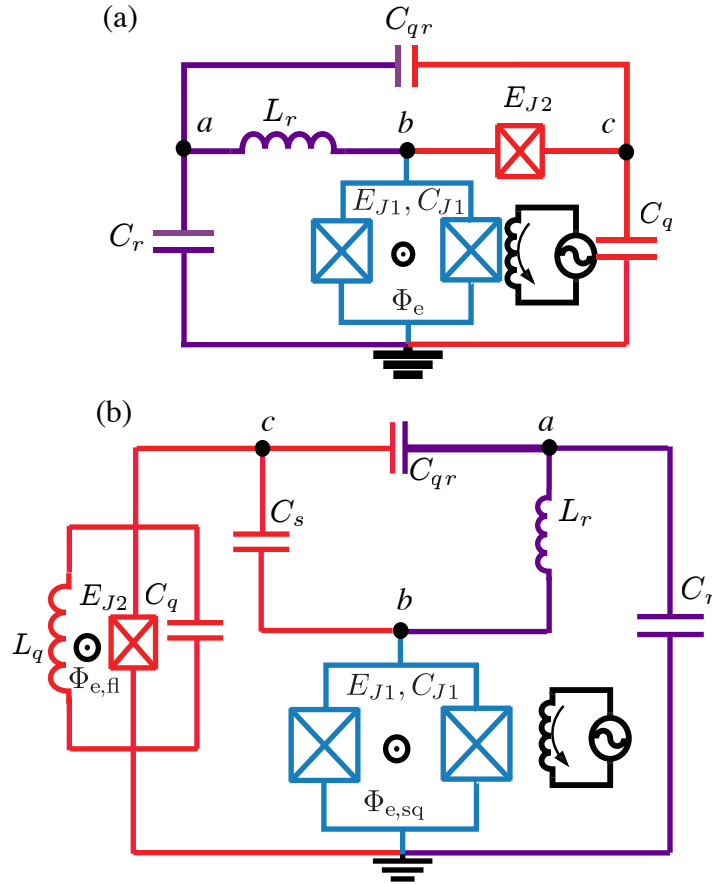


Figure 4.1. Lumped-element diagrams for circuits used in Ref. [96] and [103]. The different coloring indicates different components of the circuit. In both diagrams, elements in red coloring belong to the qubit degree of freedom, those in blue belong to the coupler mode, and the purple elements form the resonator. The three nodes are denoted by  $a, b$  and  $c$ .

In fact, both of the circuits in (a) and (b) share the “qubit-coupler-resonator” structure, where the coupler has a much higher excitation energy, such that only the ground state of the coupler mode will be occupied. The high-energy coupler only serves as a passive mediator. Adiabatic elimination of this mode can be carried out by either Born-Oppenheimer approximation or Schrieffer-Wolff transformation truncated to leading order, and the resulting effective Hamiltonian only has the resonator and qubit modes. For the purpose of qubit state stabilization,

the resonator is designed to be much lossier than the qubit. The static coupling between the two active elements is dispersive, since the detuning between the qubit and resonator is much larger than the coupling strength. Importantly, such coupling will introduce dispersive shifts to the qubit. To see this, we further adiabatically eliminate the static coupling, and find the Hamiltonian in the dressed basis

$$\hat{H}_{\text{eff}} = \omega_r \hat{a}^\dagger \hat{a} + \omega_q \hat{\sigma}^+ \hat{\sigma}^- - \chi \hat{\sigma}_z \hat{a}^\dagger \hat{a} + g(t) (\hat{a}^\dagger + \hat{a}) (\hat{\sigma}^+ + \hat{\sigma}^-), \quad (4.1)$$

where  $\hat{a}$  ( $\hat{a}^\dagger$ ) and  $\hat{\sigma}^-$  ( $\hat{\sigma}^+$ ) correspond to the lowering (raising) operators for the resonator and qubit, respectively. The third Pauli operator  $\sigma_z$  is related to the lowering and raising operators by  $\hat{\sigma}_z = 2\hat{\sigma}^+ \hat{\sigma}^- - 1$ . The coefficient  $\chi$  is the dispersive shift between the qubit and resonator modes. We use  $g(t)$  to denote the effective coupling strength between the two active elements.

### 4.3. Photon conserving and non-conserving interaction

To prepare for the discussion of state stabilization, we first introduce the two key building blocks of our stabilization schemes, the photon conserving and non-conserving coupling between the qubit and resonator. In Refs. [96, 103] we refer to them as the red- and blue-sideband coupling. These two types of coupling can be activated by modulating the coupling strength  $g(t)$  at the qubit-resonator difference or sum frequencies. This will become evident after we move to an appropriate rotating frame.

First, we study the case  $g(t) = 2g\epsilon_R \cos(\omega_d t)$  with the modulation frequency given by  $\omega_d = |\omega_r - \omega_q|$  to activate the photon-conserving or red-sideband coupling. (The factor 2 is used to simplify the notation in the following discussion.) The rotating-frame transformation is defined by the time-dependent unitary  $\hat{U}_{\text{rot}} = \exp[i\omega_r \hat{a}^\dagger \hat{a} t + i\omega_q \hat{\sigma}^+ \hat{\sigma}^- t]$ , and the effective Hamiltonian

(4.1) is transformed by

$$\begin{aligned}\tilde{H}_{\text{nonRWA}} &= \hat{U}(t)\hat{H}_{\text{eff}}\hat{U}^\dagger(t) + i\dot{\hat{U}}(t)\hat{U}^\dagger(t) \\ &= g\epsilon_R(\hat{a}e^{-i\omega_r t} + \text{H.c.})(\hat{\sigma}^- e^{-i\omega_q t} + \text{H.c.})(e^{i\omega_d} + \text{H.c.}) - \chi\hat{\sigma}_z\hat{a}^\dagger\hat{a}.\end{aligned}\quad (4.2)$$

In the parameter regime  $g\epsilon_R, \chi \ll 2\omega_d, |\omega_r + \omega_q - \omega_d|, |\omega_r + \omega_q + \omega_d|$ , we are allowed to neglect all oscillatory terms above, and only keep the following

$$\tilde{H}_{\text{eff}} = g\epsilon_R(\hat{a}\hat{\sigma}^+ + \hat{a}^\dagger\hat{\sigma}^-) - \chi\hat{\sigma}_z\hat{a}^\dagger\hat{a}.\quad (4.3)$$

The first term is the red-sideband coupling that we referred to previously. The second term, i.e., the dispersive shift, is not particularly useful here and should be made small. This specific type of coupling brings states  $|m+1, e\rangle$  and  $|m, g\rangle$  into resonance. Here  $m$  stands for the photon occupation number in the resonator and  $g$  and  $e$  denote the qubit ground and first excited state.

To activate the blue-sideband coupling, we instead choose  $g(t) = 2g\epsilon_B \cos \omega_d t$ , where  $\omega_d = \omega_r + \omega_q$  (disregarding the dispersive shift term). The rotating-frame transformation is the same as before, but the fast-rotating terms to neglect are different. The effective Hamiltonian in this case is given by

$$\tilde{H}_{\text{eff}} = g\epsilon_B(\hat{a}^\dagger\hat{\sigma}^+ + \hat{a}\hat{\sigma}^-) - \chi\hat{\sigma}_z\hat{a}^\dagger\hat{a}.\quad (4.4)$$

In this case, the states  $|m, g\rangle$  and  $|m+1, e\rangle$  are brought into resonance (again disregarding the dispersive shift term).

Ref. [96] presents the experimental evidence of these two type of couplings by measuring the resonator's transmission signal with an extra weak probing tone applied to the resonator.

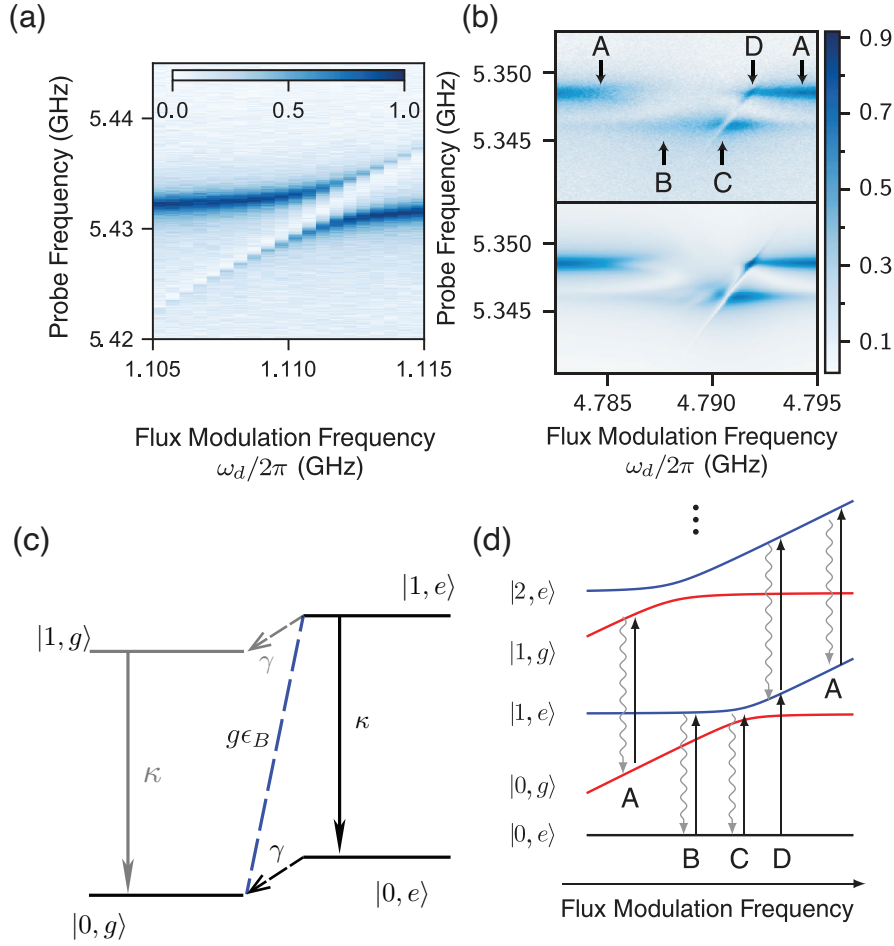


Figure 4.2. Transmission measurement through the resonator in the circuit shown in the top plot of Fig. 4.1. The figures are adapted from the Ref. [96]. (a) and (b) present transmission signals with the red- and blue-sideband coupling turned on, respectively. The lower half of (b) shows the numerical simulation of the transmission data using the effective Hamiltonian 4.4. (c) presents a four-level diagram to illustrate how the system population is trapped in state  $|1, e\rangle$  in (b). (d) uses a more complicated level diagram to explain the novel structure in (b) with an extra probing turned on.

We show the transmission data in Fig. 4.2 and explain in detail the roles played by these two different types of interaction.

In (a), the red-sideband coupling is activated, which hybridizes  $|0, e\rangle$  and  $|1, g\rangle$ . We observe a typical vacuum Rabi splitting, showing transitions from  $|0, g\rangle$  to  $(|0, e\rangle \pm |1, g\rangle)/\sqrt{2}$ . Repeating

the same measurement with the blue-sideband coupling turned on yields characteristically different structures of resonance bands. The features shown in Fig.4.2 (b) can be understood conceptually by considering the energy level diagram of the qubit-resonator system. We first focus only on the blue-sideband coupling, using Fig. 4.2 (c). The figure shows the relevant energy eigenstates and processes leading to coherent and incoherent transitions among them. For the stabilization scheme which we will discuss later to work, the blue-sideband coupling strength  $g\epsilon_B$  and resonator dissipation rate  $\kappa$  are chosen to be much larger than the qubit decay and dephasing rates  $\gamma, \gamma_\phi$ . To assess the dynamics of the system, consider a quantum trajectory starting in the ground state  $|0, g\rangle$ . The blue-sideband coupling quickly shifts occupation amplitude to the state  $|1, e\rangle$  on the timescale  $\sim (g\epsilon_B)^{-1}$ . The  $|1, e\rangle$  state will typically lose its photon in a short time  $\sim \kappa^{-1}$  and thus enter the target state  $|0, e\rangle$ . Relative to the timescales involved so far, qubit decay is slow. Whenever the qubit induces the system to return to the ground state  $|0, g\rangle$ , the described process starts over, thus making  $|0, e\rangle$  the state predominantly occupied during the dynamics. In other words, the system will be stabilized in  $|0, e\rangle$ .

Given such a stable state, the weak probing tone will excite the transition between  $|0, e\rangle$  to a pair of hybridized states  $(|1, e\rangle \pm |0, g\rangle)/\sqrt{2}$  [see points C on Fig. 4.1(d)]. The hybridization is again due to the activated blue-sideband coupling. The excitation frequency is approximately  $\omega_r - \chi$ , shifted down by the ac-Stark shift. If the blue-sideband coupling is not activated, then the dominant transition is from the ground state, i.e.,  $|0, g\rangle$ , to the state  $|1, g\rangle$ , corresponding to the transition frequency  $\omega_r + \chi$ ,  $2\chi$  higher than that for the previous resonance [see points A on Fig. 4.1(d)]. There are other interesting structures shown in this figure, such as point D, but we decide to omit here. Interested readers are directed to Ref. [96] for more details.

#### 4.4. Excited-state stabilization

Based on our discussion in the last section, the resonance in the transmission signal shown in Fig. 4.2 (b) provides clear evidence of the success of excited state stabilization. This idea was first proposed in Ref. [106], and has been implemented in experiments [96, 106]. Meanwhile, it was not clear to us how high the stabilization fidelity would be using this scheme. A method to calculate this fidelity is particularly useful for the optimization of the reset operations. In the following discussion, we will study how the fidelity is determined by the loss rates and coupling strength.

For our analytic treatment, we neglect population in  $|1, g\rangle$ , since quick photon decay is expected to prevent occupation amplitude to build up in this state. We thus consider the dynamics of the system in the subspace spanned by  $|0, g\rangle$ ,  $|0, e\rangle$  and  $|1, e\rangle$ . The evolution of the system, at zero temperature, is governed by the Lindblad master equation,

$$\frac{d\tilde{\rho}}{dt} = -i[\tilde{H}_{\text{eff}}, \tilde{\rho}] + \kappa \mathbb{D}[\hat{a}]\tilde{\rho} + \gamma \mathbb{D}[\hat{\sigma}^-]\tilde{\rho} + \frac{\gamma_\phi}{2} \mathbb{D}[\hat{\sigma}_z]\tilde{\rho}, \quad (4.5)$$

where we truncate the rotating-frame density matrix  $\tilde{\rho}$  and all other operators to the three levels of relevance. In the equation above, the damping superoperator is defined by  $\mathbb{D}[\hat{L}]\tilde{\rho} = (2\hat{L}\tilde{\rho}\hat{L}^\dagger - \hat{L}^\dagger\hat{L}\tilde{\rho} - \tilde{\rho}\hat{L}^\dagger\hat{L})/2$ . We assess the stabilization performance by calculating the state fidelity for the qubit's excited state,  $\mathcal{F}_z = \sqrt{\langle e|\tilde{\rho}_q|e\rangle}$ , where  $\tilde{\rho}_q$  is the qubit's reduced density matrix. By solving for the steady state,  $d\tilde{\rho}/dt = 0$ , we obtain an analytical expression for this stabilization fidelity:

$$\mathcal{F}_z = \sqrt{1 - \left[ \frac{2g\epsilon_B}{\kappa} + \left( \frac{1}{2}\kappa + \gamma_\phi \right) \frac{1}{g\epsilon_B} \right] C}, \quad (4.6)$$

where

$$\begin{aligned}
C &= \text{Im}[\langle 0, g | \rho | 1, e \rangle] \\
&= \left[ \frac{2g\epsilon_B}{\gamma} + \frac{2g\epsilon_B}{\kappa} + \left( \frac{1}{2}\kappa + \gamma_\phi \right) \frac{1}{g\epsilon_B} \right]^{-1}.
\end{aligned} \tag{4.7}$$

The detailed derivation of Eq. (4.6) is postponed to Section 4.7 where we discuss the fidelity of stabilization in an arbitrary pure state. Here we focus on the expression itself and discuss the dependence of the fidelity on different parameters.

In the parameter regime that we are interested in, the coupling strength  $g\epsilon_B$  and resonator decay rate  $\kappa$  are much larger than the qubit decoherence rates  $\gamma$  and  $\gamma_\phi$ . Such regime enables one to obtain the more compact approximation

$$\mathcal{F}_z \approx \sqrt{1 - \left[ \frac{2g\epsilon_B}{\kappa} + \frac{\kappa}{2g\epsilon_B} \right] \frac{\gamma}{2g\epsilon_B}}. \tag{4.8}$$

For given qubit dissipation rates, we can optimize the state fidelity by tuning the resonator dissipation rate  $\kappa$  and modulation strength  $g\epsilon_B$ . First, considering fixed  $\kappa$ , the fidelity increases monotonically with  $g\epsilon_B$  and approaches an upper limit set by  $\lim_{g\epsilon_B \rightarrow \infty} \mathcal{F}_z = \sqrt{1 - \gamma/\kappa}$ . For fixed  $g\epsilon_B$ , Eq. (4.8) shows that the fidelity approximately reaches its maximum for  $\kappa = 2g\epsilon_B$ , namely

$$\max_{\kappa > 0} \mathcal{F}_z \approx \sqrt{1 - \frac{\gamma}{g\epsilon_B}}. \tag{4.9}$$

Fig. 4.3 (a) shows numerical results for the fidelity as a function of  $g\epsilon_B$  and  $\kappa$ , obtained by a full simulation of the steady state based on Eq. (4.4). We find that high stabilization fidelities

exceeding 99.5% can be reached with realistic parameters. The optimum condition  $\kappa = 2g\epsilon_B$  is shown as the dashed line in the  $\kappa$ - $g\epsilon_B$  plane, which yields the maximum fidelity values.

We note from Eq. (4.8) that larger resonator decay rates will ultimately suppress the stabilization fidelity when  $\kappa > 2g\epsilon_B$ . This fact can be understood when considering the system dynamics at the level of quantum trajectories: fast resonator decay leads to frequent jumps projecting the system state to a quantum state with definite photon number – an effect similar to that of repeated projective measurements of the resonator’s occupation number. For a large resonator decay rate, the coherent evolution between states  $|0, g\rangle$  and  $|1, e\rangle$  will thus be persistently interrupted, trapping the system in  $|0, g\rangle$  through the quantum Zeno effect. Therefore, exceedingly large resonator decay rates will ultimately slow down the increase of the magnitudes of population in state  $|1, e\rangle$  and  $|0, e\rangle$ , which will lead to lower stabilization fidelities.

#### 4.5. Stabilization in arbitrary mixed states along the $z$ -axis

A combination of both red and blue-sideband couplings enables the stabilization of mixed states centered on the  $z$ -axis of the Bloch sphere. With the two types of coupling turned on, the effective Hamiltonian is

$$\tilde{H}_{\text{eff}} = g\epsilon_B(\hat{a}^\dagger \hat{\sigma}^+ + \hat{a} \hat{\sigma}^-) + g\epsilon_R(\hat{a}^\dagger \hat{\sigma}^- + \hat{a} \hat{\sigma}^+) - \chi \hat{\sigma}_z \hat{a}^\dagger \hat{a}. \quad (4.10)$$

As depicted in Fig. 4.4 (a), the interactions between states now become more complicated, since the three-level approximation is no longer appropriate. Different from blue-sideband coupling, red-sideband coupling promotes amplitude transfer between states  $|m, e\rangle$  and  $|m+1, g\rangle$  and may thus allow the system to access states with more than one photon inside the resonator.

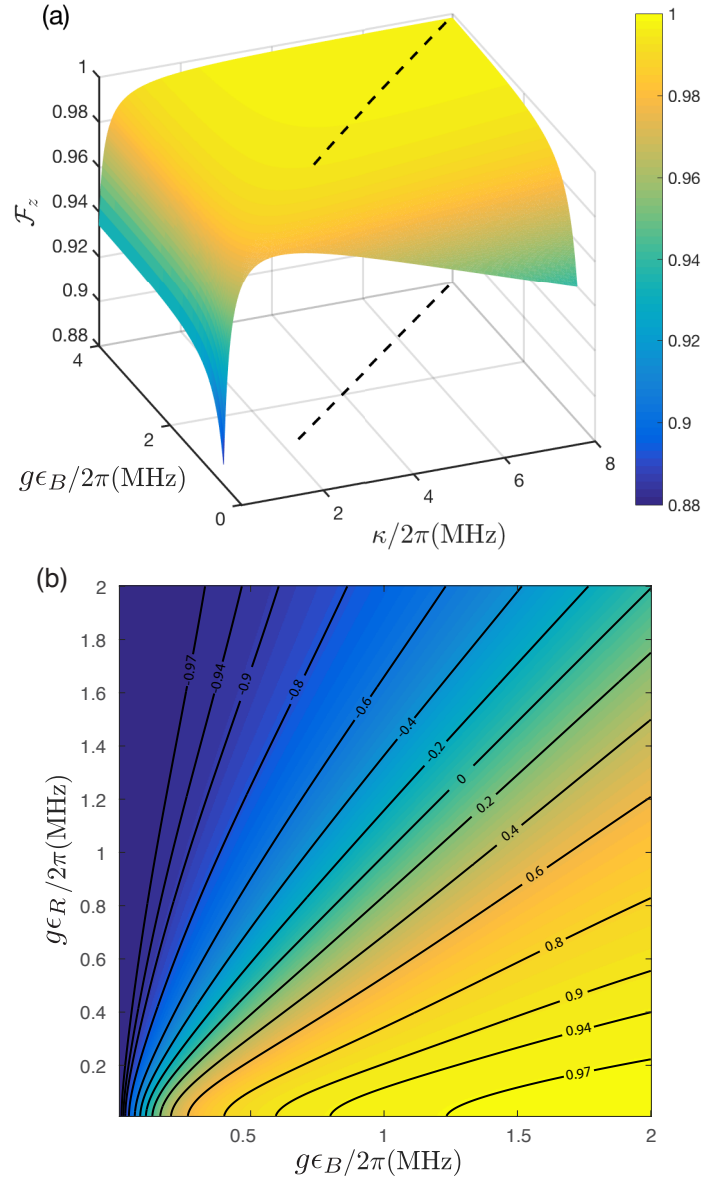


Figure 4.3. (a) Fidelity for stabilization in the excited state  $|e\rangle$ , as a function of resonator dissipation rate  $\kappa$  and blue-sideband coupling strength  $g\epsilon_B$ . The dotted line is the approximated maximum line from Eq. (4.8). (Qubit dissipation rates are chosen as  $\gamma = \gamma_\phi = 0.1$  MHz.) (b) Expectation of  $\hat{\sigma}_z$  for different  $g\epsilon_R$  and  $g\epsilon_B$ , see Eq. (4.10), with a fixed  $\kappa/2\pi = 4$  MHz. All results shown assume  $\chi/2\pi = 0.5$  MHz and a temperature of 15 mK.

The particular qubit mixed state which is stabilized now depends on the magnitudes and relative phases of the red- and blue-sideband coupling. We fully characterize this mixed state by computing the ensemble averages  $\langle \hat{\sigma}_{x,y,z} \rangle$ , and discuss their dependence on the couplings strengths. The ensemble average of  $\hat{\sigma}_z$  in the non-equilibrium steady state is shown in Fig. 4.3 (b) as a function of the modulation strengths  $g\epsilon_R$  and  $g\epsilon_B$ , using a fixed resonator decay rate. On average, the qubit acquires a larger portion of the excited state  $|e\rangle$  for increasing  $\epsilon_B/\epsilon_R$ , and a larger portion of the ground state  $|g\rangle$  for decreasing  $\epsilon_B/\epsilon_R$ . We note that the plot is approximately symmetric under exchange of  $g\epsilon_R$  and  $g\epsilon_B$  and, simultaneously, transforming  $\hat{\sigma}_z$  to  $-\hat{\sigma}_z$ . Indeed, if we momentarily neglect the slow qubit dissipation, then the Lindblad master equation becomes invariant under interchange of  $\hat{\sigma}^-$  with  $\hat{\sigma}^+$ , and  $\epsilon_R$  with  $\epsilon_B$ . The qubit will be stabilized into a mixed state with equal weights of  $|e\rangle$  and  $|g\rangle$  with  $\langle \hat{\sigma}_z \rangle \approx 0$ , when  $g\epsilon_R$  equals  $g\epsilon_B$ . This symmetry breaks down when sideband coupling strengths become so small that qubit dissipation rates and the spurious ac-Stark shift cannot be neglected anymore.

Our numerical simulations show that ensemble averages of  $\hat{\sigma}_x$  and  $\hat{\sigma}_y$  vanish in the steady state. This can be understood as follows. Based on Fig. 4.4 (a), we can divide the system into two groups of states,

1.  $|0, g\rangle, |1, e\rangle, |2, g\rangle, |3, e\rangle \dots$
2.  $|0, e\rangle, |1, g\rangle, |2, e\rangle, |3, g\rangle \dots$

The generation of coherent qubit superposition states of  $|e\rangle$  and  $|g\rangle$  would require hybridization of system states  $|m, e\rangle$  and  $|m, g\rangle$  with the same resonator occupation number  $m$ . However, red- and blue-sideband couplings can only hybridize states within each of the two groups, which

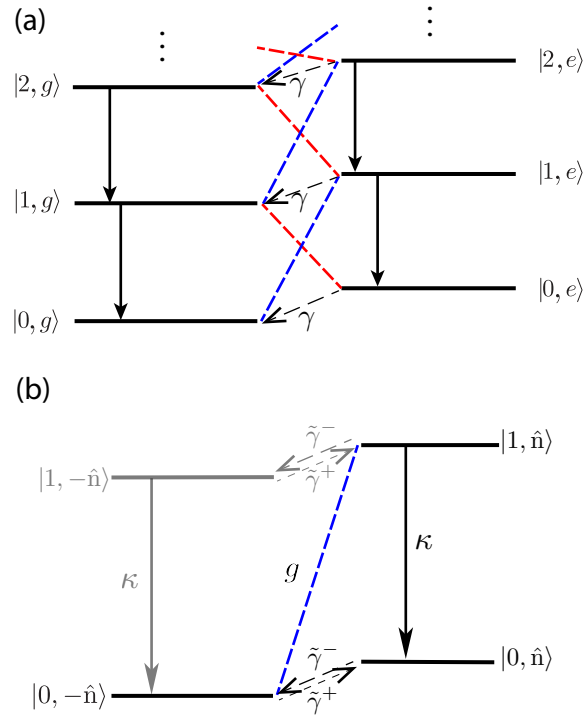


Figure 4.4. (a) Ladder diagram with both red- and blue-sideband coupling turned on. System states with different total photon numbers are interconnected by these two types of interaction. (b) Diagram of the arbitrary-axis stabilization scheme. With  $\kappa \gg \tilde{\gamma}^-, \tilde{\gamma}^+$ , the population in  $|1, -\hat{n}\rangle$  can be safely neglected, and the system is stabilized in  $|0, \hat{n}\rangle$ . In both of these plots, the red- and blue-dashed lines represent the connection between states induced by the red- and blue-sideband coupling. The solid-black arrows indicate the fast resonator loss, while the dashed arrows describe the slow qubit loss.

excludes superpositions of  $|m, e\rangle$  and  $|m, g\rangle$ . (Even if the initial state should present a nonzero matrix element  $\langle m, e | \rho | m, g \rangle$ , decoherence processes will effectively erase any such coherence.)

#### 4.6. Universal qubit stabilization strategies

So far, we have discussed stabilization of the qubit in states along the  $z$ -axis of the Bloch sphere. It is desirable to generalize this scheme to stabilization along an arbitrary axis through the Bloch sphere. Toward this goal, our collaborators proposed and demonstrated one scheme

in Refs. [96]. Following that work, we introduce a more sophisticated method which is aimed for higher stabilization fidelities and shorter stabilization times [103].

We point out that the strategies provided in these two references are crucially different. The first chooses a simpler experimental implementation with only the blue-sideband coupling activated, together with a resonant qubit Rabi drive. In the later theory work, we leverage two modulation tones to activate both red- and blue-sideband coupling. We show that the access to both types of coupling offers more flexibility in designing a fast and high-fidelity stabilization scheme over all target states. In the following, we will only sketch the method used in Ref. [96], but lay more emphasis on the strategy used in the theory paper.

In the simpler stabilization method used in Ref. [96], a near-resonance Rabi drive has been added on the qubit, which yields a modified rotating-frame Hamiltonian

$$\tilde{H}_{\text{eff},B} = \frac{1}{2}\Omega_R\hat{\sigma}_x + \frac{1}{2}\Omega_z\hat{\sigma}_z + g\epsilon_B(\hat{a}^\dagger\hat{\sigma}^+ + \hat{a}\hat{\sigma}^-) - \chi\hat{\sigma}_z\hat{a}^\dagger\hat{a}. \quad (4.11)$$

Here,  $\Omega_R$  is the Rabi drive strength,  $\Omega_z = \omega_q - \omega_R$  is the small detuning between the Rabi drive and the qubit frequency ( $\omega_R$  is the Rabi drive frequency). In the rotating frame, the eigenstates of the Rabi-driven qubit, given by the Hamiltonian  $(\Omega_R\hat{\sigma}_x + \Omega_z\hat{\sigma}_z)/2$ , are the superpositions of the bare eigenstates given by  $|\tilde{g}\rangle = \cos(\tilde{\theta}/2)|g\rangle - \sin(\tilde{\theta}/2)|e\rangle$  and  $|\tilde{e}\rangle = \sin(\tilde{\theta}/2)|g\rangle + \cos(\tilde{\theta}/2)|e\rangle$ . Here, the angle  $\tilde{\theta} = \arccos(\Omega_z/\Omega_R)$  depends on the drive detuning and Rabi strength. The change of the qubit eigenstates in the rotating frame certainly affects the stabilization target state. This scheme can be described by the diagram in Fig. 4.2 (c), with the replacement of  $|m, g(e)\rangle$  by  $|m, \tilde{g}(\tilde{e})\rangle$ . If so, the stabilization target state is  $|\tilde{g}\rangle$ , which is different from the excited state without the Rabi drive. (The exact mechanism is much more complicated than the

description given above. We choose to omit the detailed discussion of this, but only direct our readers to the Supplementary Information of Ref. [96].)

This simple method has led to a successful demonstration of universal stabilization of the single-qubit states, with a fidelity for all sampled stabilization angles over 80%. But this scheme is not convenient for the stabilization of states in the vicinity of the  $|g\rangle$  state. Specifically, the effective two-photon pumping rate drops to zero when  $|\tilde{g}\rangle$  approaches the real ground state  $|g\rangle$ . Also, the time required for this stabilization scheme is not optimized. In the following, we will present another scheme with both blue- and red-sideband interactions turned on, which is aimed to solve the issues raised above.

The scheme we introduce in Ref. [103] is a natural generalization to qubit stabilization along an arbitrary axis through the Bloch sphere. Before launching into a detailed discussion, we first employ the convention that the qubit excited state  $|e\rangle$  resides at the north pole of the Bloch sphere. The axis specified by the unit vector  $\hat{\mathbf{n}}$  has polar and azimuthal angles  $\theta$  and  $\phi$ , respectively, with the pure qubit states  $|\pm \hat{\mathbf{n}}\rangle$  located at the two points where the axis intercepts the Bloch sphere. Explicitly, the two pure states are given by

$$\begin{aligned} |\hat{\mathbf{n}}\rangle &= \sin \frac{\theta}{2} |g\rangle + e^{-i\phi} \cos \frac{\theta}{2} |e\rangle, \\ |-\hat{\mathbf{n}}\rangle &= -e^{-i\phi} \sin \frac{\theta}{2} |e\rangle + \cos \frac{\theta}{2} |g\rangle. \end{aligned} \quad (4.12)$$

Points along the axis  $\hat{\mathbf{n}}$  in the interior of the Bloch sphere represent mixed states composed of  $|\hat{\mathbf{n}}\rangle$  and  $|-\hat{\mathbf{n}}\rangle$ , as usual.

We start by presenting how to stabilize the qubit in the pure state  $|\hat{\mathbf{n}}\rangle$  on the Bloch sphere. Inspired by Fig. 4.2 (c), we aim for a Hamiltonian of the form

$$\hat{H}_{\hat{\mathbf{n}}B} = g\epsilon(\hat{a}^\dagger \hat{\sigma}_{\hat{\mathbf{n}}}^+ + \hat{a} \hat{\sigma}_{\hat{\mathbf{n}}}^-), \quad (4.13)$$

analogous to Eq. (4.4). Here,  $\hat{\sigma}_{\hat{\mathbf{n}}}^\pm$  are defined via  $\hat{\sigma}_{\hat{\mathbf{n}}}^\pm |\mp \hat{\mathbf{n}}\rangle = |\pm \hat{\mathbf{n}}\rangle$ . For the special case of  $\theta = 0$ , Hamiltonian (4.13) reduces to the blue-sideband coupling. We call this Hamiltonian an effective blue-sideband coupling for state  $|\hat{\mathbf{n}}\rangle$ , as it couples the system states  $|m + 1, \hat{\mathbf{n}}\rangle$  to  $|m, -\hat{\mathbf{n}}\rangle$ .

As before, we require the resonator decay rate  $\kappa$  and the coupling strength  $g\epsilon$  to be much greater than the qubit dissipation rates. As shown in Fig. 4.4 (b), the effective blue-sideband coupling for axis  $\hat{\mathbf{n}}$  opens up a decay channel from  $|0, -\hat{\mathbf{n}}\rangle$  to  $|0, \hat{\mathbf{n}}\rangle$  via hybridization of  $|0, -\hat{\mathbf{n}}\rangle$  and  $|1, \hat{\mathbf{n}}\rangle$  and fast resonator decay from  $|1, \hat{\mathbf{n}}\rangle$  to  $|0, \hat{\mathbf{n}}\rangle$ . Relative to these fast dynamics, qubit relaxation and dephasing are slow, leading to infrequent transitions between the states  $|m, \hat{\mathbf{n}}\rangle$  and  $|m, -\hat{\mathbf{n}}\rangle$ . The resulting effective rates are given by [96]

$$\begin{aligned} \tilde{\gamma}^- &= \gamma \cos^4 \frac{\theta}{2} + \frac{\gamma_\phi}{2} \sin^2 \theta, \\ \tilde{\gamma}^+ &= \gamma \sin^4 \frac{\theta}{2} + \frac{\gamma_\phi}{2} \sin^2 \theta, \\ \tilde{\gamma}_\phi &= \frac{\gamma}{2} \sin^2 \theta + \gamma_\phi \cos^2 \theta, \end{aligned} \quad (4.14)$$

where  $\tilde{\gamma}^\mp$  are the transition rates from qubit state  $|\hat{\mathbf{n}}\rangle$  to  $|\mp \hat{\mathbf{n}}\rangle$  (and reverse), and  $\tilde{\gamma}_\phi$  is the effective dephasing rate. Since all three are much smaller than the resonator decay rate  $\kappa$  and sideband coupling strength  $g\epsilon$ , the effective decay from  $|0, -\hat{\mathbf{n}}\rangle$  to  $|0, \hat{\mathbf{n}}\rangle$  dominates the dynamics and thus stabilizes the qubit in the state  $|\hat{\mathbf{n}}\rangle$ .

We next show how to generate the desired Hamiltonian in Eq. (4.13) with our circuit-QED device. We first expand  $\hat{\sigma}_{\hat{\mathbf{n}}}^{\pm}$  in the Pauli matrix basis as

$$\begin{aligned}\hat{\sigma}_{\hat{\mathbf{n}}}^{\pm} &= \exp\left(-i\frac{\phi}{2}\hat{\sigma}_z\right)\exp\left(-i\frac{\theta}{2}\hat{\sigma}_y\right)\hat{\sigma}^{\pm}\exp\left(i\frac{\theta}{2}\hat{\sigma}_y\right)\exp\left(i\frac{\phi}{2}\hat{\sigma}_z\right) \\ &= \frac{1}{2}\hat{\sigma}^{\pm}(\cos\theta+1)e^{\mp i\phi} + \frac{1}{2}\hat{\sigma}^{\mp}(\cos\theta-1)e^{\pm i\phi} - \frac{1}{2}\hat{\sigma}_z(\sin\theta).\end{aligned}\quad (4.15)$$

For simplicity (and without loss of generality) we set the azimuthal angle  $\phi = 0$  and defer the discussion of nonzero  $\phi$  to the subsequent subsection. This way, we can plug the expression of  $\sigma_{\hat{\mathbf{n}}}^{\pm}$  into Eq. (4.13) to obtain

$$\begin{aligned}\hat{H}_{\hat{\mathbf{n}}B} &= \frac{1}{2}g\epsilon(\cos\theta-1)(\hat{a}^{\dagger}\hat{\sigma}^{-} + \hat{a}\hat{\sigma}^{+}) \\ &\quad + \frac{1}{2}g\epsilon(\cos\theta+1)(\hat{a}^{\dagger}\hat{\sigma}^{+} + \hat{a}\hat{\sigma}^{-}) \\ &\quad - \frac{1}{2}g\epsilon\sin\theta(\hat{a}^{\dagger} + \hat{a})\hat{\sigma}_z.\end{aligned}\quad (4.16)$$

Here,  $\hat{H}_{\hat{\mathbf{n}}B}$  denotes the effective blue-sideband coupling for state  $|\hat{\mathbf{n}}\rangle$ . This Hamiltonian is a combination of the red- and blue-sideband couplings, as well as a longitudinal coupling between the qubit and the resonator [117]. The latter can be generated by switching on a Rabi drive,

$$\hat{H}_d = \xi(\hat{\sigma}^{-}e^{i\omega_r t} + \hat{\sigma}^{+}e^{-i\omega_r t}),\quad (4.17)$$

driving the qubit at the resonator frequency  $\omega_r$  with strength  $\xi$ . This drive gives rise to a longitudinal coupling of the form

$$\hat{H}'_d = -g'\xi(\hat{a}^{\dagger} + \hat{a})\hat{\sigma}_z,\quad (4.18)$$

written in the dressed basis of the appropriate rotating frame. (We have dropped several fast-oscillating terms here.) We will discuss in Section 4.10.

Therefore, the Hamiltonian in Eq. (4.16) can be generated by tuning the strengths of the red- and blue-sideband couplings as well as the Rabi drive to match

$$\begin{aligned} g\epsilon_R &= \frac{1}{2}g\epsilon(\cos\theta - 1), \\ g\epsilon_B &= \frac{1}{2}g\epsilon(\cos\theta + 1), \\ g'\xi &= \frac{1}{2}g\epsilon\sin\theta, \end{aligned} \tag{4.19}$$

respectively.

#### 4.7. Pure-state stabilization fidelities

Using the scheme proposed above, we next show by analytical and numerical calculation that, with realistic experimental parameters, this scheme yields high stabilization fidelities over all polar angle  $\theta$ . Specifically, for a sideband coupling strength of  $g\epsilon/2\pi = 2$  MHz and resonator decay rate of  $\kappa = 2g\epsilon$ , we can obtain state fidelities for  $|\hat{\mathbf{n}}\rangle$  of up to 99.5%, see Fig.4.5 (a). The results are obtained using Eq. (4.5), with  $\hat{H}_{\text{eff}}$  replaced by Eq. (4.13). (the dispersive shift is also added for completeness.)

Similarly, we base our discussion of stabilization fidelity and time on a three-level model shown in Fig. 4.4(b). Specifically, we neglect residual population of state  $|1, -\hat{\mathbf{n}}\rangle$  and confine the dynamics of the system to a subspace spanned by  $|0, -\hat{\mathbf{n}}\rangle$ ,  $|0, \hat{\mathbf{n}}\rangle$  and  $|1, \hat{\mathbf{n}}\rangle$ . In the case of arbitrary-state stabilization, the stabilization dynamics is effectively described by the Lindblad

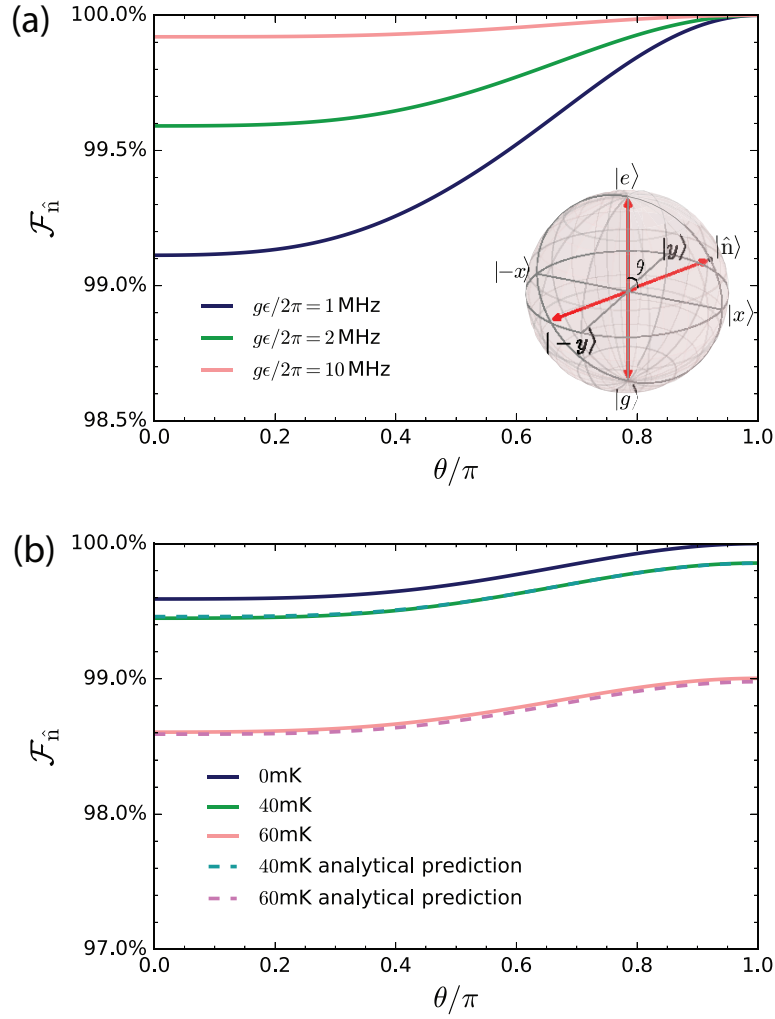


Figure 4.5. (a) Stabilization fidelity for states along an axis  $\hat{n}$  in the  $x$ - $z$  plane, as a function of the polar angle  $\theta$  (see in subplot). The three curves depict results for different strengths of the effective blue-sideband coupling. (Temperature and resonator decay rate are chosen as  $T_{\text{env}} = 15$  mK,  $\kappa/2\pi = 4$  MHz.) (b) Dependence of the fidelity on temperature, using  $\kappa/2\pi = 2g\epsilon/2\pi = 4$  MHz. Dashed curves show the analytical prediction from Eq. (4.25). In both graphs, we choose  $\gamma = 0.1$  MHz,  $\gamma_\phi = 0.1$  MHz and  $\chi/2\pi = 0.5$  MHz. Excitation energies for the resonator and qubit are set to 4.89 GHz and 5.99 GHz, respectively.

master equation

$$\begin{aligned} \frac{d\tilde{\rho}}{dt} = & -i[\hat{H}_{\text{eff}}, \tilde{\rho}] + \kappa \mathbb{D}[\hat{a}]\tilde{\rho} \\ & + \tilde{\gamma}^- \mathbb{D}[\hat{\sigma}_{\hat{\mathbf{n}}}^-]\tilde{\rho} + \tilde{\gamma}^+ \mathbb{D}[\hat{\sigma}_{\hat{\mathbf{n}}}^+]\tilde{\rho} + \frac{\tilde{\gamma}_\phi}{2} \mathbb{D}[\hat{\sigma}_{\hat{\mathbf{n}}}] \tilde{\rho}, \end{aligned} \quad (4.20)$$

where  $\hat{H}_{\text{eff}}$  refers to Eq. (4.13), and  $\hat{\sigma}_{\hat{\mathbf{n}}}$  is defined as  $\hat{\sigma}_{\hat{\mathbf{n}}} = 2\hat{\sigma}_{\hat{\mathbf{n}}}^+ \hat{\sigma}_{\hat{\mathbf{n}}}^- - 1$ . The decoherence rates  $\tilde{\gamma}^-$ ,  $\tilde{\gamma}^+$  and  $\tilde{\gamma}_\phi$  were defined in Eq. (4.14). The time evolution of the density matrix  $\tilde{\rho}$  can be described in terms of four key components:

$$\begin{aligned} \frac{d\tilde{\rho}_{11}}{dt} &= -2g\epsilon C + \tilde{\gamma}^- \tilde{\rho}_{22} - \tilde{\gamma}^+ \tilde{\rho}_{11}, \\ \frac{d\tilde{\rho}_{22}}{dt} &= \kappa \tilde{\rho}_{33} - \tilde{\gamma}^- \tilde{\rho}_{22} + \tilde{\gamma}^+ \tilde{\rho}_{11}, \\ \frac{d\tilde{\rho}_{33}}{dt} &= 2g\epsilon C - \kappa \tilde{\rho}_{33}, \\ \frac{dC}{dt} &= g\epsilon(\tilde{\rho}_{11} - \tilde{\rho}_{33}) - \left(\frac{1}{2}\kappa + \frac{1}{2}\tilde{\gamma}^+ + \tilde{\gamma}_\phi\right)C. \end{aligned} \quad (4.21)$$

Here,  $\tilde{\rho}_{11}$ ,  $\tilde{\rho}_{22}$  and  $\tilde{\rho}_{33}$  give the probability amplitudes for the states  $|0, -\hat{\mathbf{n}}\rangle$ ,  $|0, \hat{\mathbf{n}}\rangle$  and  $|1, \hat{\mathbf{n}}\rangle$ , and  $C = \text{Im}[\langle 0, -\hat{\mathbf{n}}|\tilde{\rho}|1, \hat{\mathbf{n}}\rangle]$ . Due to the constraint  $\tilde{\rho}_{11} + \tilde{\rho}_{22} + \tilde{\rho}_{33} = 1$ , only three of these four equations are independent. Except for  $\langle 0, -\hat{\mathbf{n}}|\tilde{\rho}|1, \hat{\mathbf{n}}\rangle$ , other off-diagonal components of the density matrix do not affect the evolution of  $\tilde{\rho}_{ii}$  ( $i = 1, 2, 3$ ). These elements will decay to zero when the qubit is stabilized in state  $|0, \hat{\mathbf{n}}\rangle$ , i.e., when  $\tilde{\rho}_{22} \approx 1$ .

By setting all time derivatives in Eq. (4.21) to zero, we obtain an exact expression for the stabilization fidelity:

$$\mathcal{F}_{\hat{\mathbf{n}}} = \sqrt{1 - \left[ \frac{2g\epsilon}{\kappa} + \left( \frac{1}{2}\kappa + \frac{1}{2}\tilde{\gamma}^+ + \tilde{\gamma}_\phi \right) / g\epsilon \right] C}, \quad (4.22)$$

where

$$C = \frac{\tilde{\gamma}^- / (\tilde{\gamma}^+ + \tilde{\gamma}^-)}{\frac{2g\epsilon}{\kappa} + \frac{2g\epsilon}{\tilde{\gamma}^+ + \tilde{\gamma}^-} \left(1 + \frac{\tilde{\gamma}^-}{\kappa}\right) + \left(\frac{1}{2}\kappa + \frac{1}{2}\tilde{\gamma}^+ + \tilde{\gamma}_\phi\right) \frac{1}{g\epsilon}}. \quad (4.23)$$

The approximate result for the stabilization fidelity of the qubit excited state  $|e\rangle$ , given in Eq. (4.6), is recovered by taking  $\tilde{\gamma}^+ = 0$  and  $\tilde{\gamma}^- = \gamma$ . Similar to the approximation given in Eq. (4.8), if the coupling strength and resonator decay rate are much larger than the qubit decoherence rates, i.e.,  $g\epsilon, \kappa \gg \tilde{\gamma}^+, \tilde{\gamma}^-, \tilde{\gamma}_\phi$ , the stabilization fidelity can be further approximately given by

$$\mathcal{F}_{\hat{\mathbf{n}}} = \sqrt{\langle \hat{\mathbf{n}} | \tilde{\rho}_q | \hat{\mathbf{n}} \rangle} \approx \sqrt{1 - \left[ \frac{2g\epsilon}{\kappa} + \frac{\kappa}{2g\epsilon} \right] \frac{\tilde{\gamma}^-}{2g\epsilon}}. \quad (4.24)$$

The most important difference between this equation and Eq. (4.8) may be that the qubit decay rate in the latter is replaced by  $\tilde{\gamma}^-$  in the former, which is defined in Eq. (4.14). The conclusions we have reached about the fidelity maximum can be easily generalized to the stabilization in an arbitrary state.

The discussion above does not include possible thermal excitation in the qubit and the resonator. Within the same approximation described, we can further predict the stabilization fidelity at finite temperatures, and confirm that our scheme is robust to realistic levels of thermal excitations. The approximate relation between the stabilization fidelity and temperature is given by

$$\mathcal{F}_{\hat{\mathbf{n}}}(T_{\text{env}}) \approx \sqrt{\mathcal{F}_{\hat{\mathbf{n}}}^2(0) - \exp(-\hbar\omega_r/k_B T_{\text{env}}) \rho_{22}^{(0)}}}. \quad (4.25)$$

where  $\mathcal{F}_{\hat{\mathbf{n}}}(T_{\text{env}})$  denotes the state fidelity of  $|\hat{\mathbf{n}}\rangle$  obtained at temperature  $T_{\text{env}}$ . The quantity  $\rho_{22}^{(0)}$  represents the occupation probability for the state  $|0, \hat{\mathbf{n}}\rangle$  at zero temperature, and is very close to 1 in our scheme.

The influence of temperature can be assessed by a perturbative treatment within the three-level model. For finite temperatures, we add the terms  $\kappa_{\text{th}} \mathbb{D}[\hat{a}^\dagger]\rho$  and  $\gamma_{\text{th}} \mathbb{D}[\sigma^+]\rho$  to the Lindblad master equation (4.20), where  $\kappa_{\text{th}} = \kappa \exp(-\hbar\omega_r/k_B T_{\text{env}})$  and  $\gamma_{\text{th}} = \gamma \exp(-\hbar\omega_q/k_B T_{\text{env}})$ . In the low-temperature limit ( $\kappa_{\text{th}} \ll \kappa$  and  $\gamma_{\text{th}} \ll \gamma$ ), we maintain  $\langle 0, \hat{\mathbf{n}}|\rho|0, \hat{\mathbf{n}}\rangle \approx 1$ . Further, for  $\omega_r \sim \omega_q$  and  $\gamma \ll \kappa$ , we also have  $\gamma_{\text{th}} \ll \kappa_{\text{th}}$ . As a result, we expect the leading corrections due to thermal excitations to be given by the excitation from  $|0, \hat{\mathbf{n}}\rangle$  to  $|1, \hat{\mathbf{n}}\rangle$  at rate  $\kappa_{\text{th}}$ . We treat the term that describes such thermal excitation as perturbation, and solve for  $\tilde{\rho}_{ii}(i = 1, 2, 3)$  and  $C$  to leading orders. We denote the  $p$ th order solutions by  $\tilde{\rho}_{ii}^{(p)}(i = 1, 2, 3)$  and  $C^{(p)}$ . The zeroth- and first-order corrections to our zero-temperature solutions obey:

$$\begin{aligned} 0 &= -2g\epsilon C^{(1)} + \tilde{\gamma}^- \tilde{\rho}_{22}^{(1)} - \tilde{\gamma}^+ \tilde{\rho}_{11}^{(1)}, \\ 0 &= \kappa_{\text{th}} \tilde{\rho}_{22}^{(0)} + 2g\epsilon C^{(1)} - \kappa \tilde{\rho}_{33}^{(1)}, \\ 0 &= g\epsilon(\tilde{\rho}_{11}^{(1)} - \tilde{\rho}_{33}^{(1)}) - \left(\frac{1}{2}\kappa + \frac{1}{2}\tilde{\gamma}^+ + \gamma_\phi\right)C^{(1)}. \end{aligned} \quad (4.26)$$

With  $g\epsilon$  and  $\kappa$  far exceeding the qubit dissipation rates, we can infer from the first equation that  $C^{(1)}$  should be much smaller than  $\tilde{\rho}_{11}^{(1)}$  and  $\tilde{\rho}_{22}^{(1)}$ , and thus can be neglected in the second and third equation. As a result, we find the relation

$$\tilde{\rho}_{11}^{(1)} \approx \tilde{\rho}_{33}^{(1)} \approx \frac{\kappa_{\text{th}}}{\kappa} \tilde{\rho}_{22}^{(0)}, \quad (4.27)$$

shown in Eq. (4.25).

The above expression shows that, to leading order, the influence of finite temperatures is directly determined by the comparison between resonator excitation energy  $\hbar\omega_r$  and thermal excitation energy  $k_B T_{\text{env}}$ . We can thus suppress the influence of temperature by using a resonator with sufficiently large frequency while preserving the parameters of the qubit. Results shown in Fig. 4.5(b) confirm that our scheme is robust with respect to thermal fluctuations at realistic operating temperatures and practical circuit parameters.

#### 4.8. Azimuthal angle and stabilization in arbitrary mixed state

So far, we have set the phases of the modulation and drive tones to zero at  $t = 0$ , i.e.,  $g(t) = 2g\epsilon_R \cos(|\omega_r - \omega_q|t) + 2g\epsilon_B \cos(|\omega_r + \omega_q|t)$  and  $\hat{H}_d(t) = \xi[\hat{\sigma}^- \exp(i\omega_r t) + \text{C.c.}]$ . This special choice only enables stabilization in the  $\phi = 0$  plane. To generalize this and stabilize states with arbitrary azimuthal angle  $\phi$ , detailed control of the phases is needed. We shall denote the phases of the three tones at time  $t$  by

$$P_n = \omega_n t + \nu_n, \quad (4.28)$$

where  $n = 1, 2$  stand for red- and blue-sideband modulation tones, and  $n = 3$  for the Rabi drive tone. For the latter, we set  $\nu_3 = 0$  without loss of generality. The choice of the three frequencies, i.e.,  $\omega_1 = |\omega_r + \omega_q|$ ,  $\omega_2 = |\omega_r - \omega_q|$ , and  $\omega_3 = \omega_r$ , yields the relations  $\omega_1 + \omega_2 = 2\omega_3$  and  $\omega_2 - \omega_1 = 2\omega_q$ . In the dressed bases of the appropriately rotating frame, the effective Hamiltonian in the presence of all three drives is then given by

$$\begin{aligned} \hat{H} = & g\epsilon_1(\hat{a}^\dagger \hat{\sigma}^- e^{-i\nu_1} + \text{H.c.}) + g\epsilon_2(\hat{a}^\dagger \hat{\sigma}^+ e^{-i\nu_2} + \text{H.c.}) \\ & - \frac{g'\xi}{\Delta}(\hat{a}^\dagger + \hat{a})\hat{\sigma}_z. \end{aligned} \quad (4.29)$$

Calculation shows that by tuning the strengths and phases of the three tones the Hamiltonian in Eq. (4.29) can indeed generate the effective blue-sideband Hamiltonian

$$\hat{H}_{\hat{\mathbf{n}}B} = g\epsilon(\hat{a}^\dagger \hat{\sigma}_{\hat{\mathbf{n}}}^+ + \text{H.c.}), \quad (4.30)$$

if the drive strengths and phases satisfy the following conditions. First, the three phases from Eq. (4.28) must obey

$$P_1 + P_2 - 2P_3 = \nu_1 + \nu_2 = 0. \quad (4.31)$$

This relation reduces to one among the initial phases due to the frequency match among the three tones, i.e.,  $\omega_1 + \omega_2 = 2\omega_3$ . Second, for the azimuthal angle  $\phi$ , we require

$$(P_2 - P_1)/2 - \omega_q t = (\nu_2 - \nu_1)/2 = \phi. \quad (4.32)$$

Since  $\omega_2 - \omega_1 = 2\omega_q$ , the azimuthal angle is simply determined by the initial phases of the modulation tones,  $\nu_1$  and  $\nu_2$ . Third, the strengths of the three tones must meet the conditions of Eq. (4.19) to set the desired polar angle  $\theta$ .

Above, we have devised a method to stabilize the qubit in an arbitrary pure state. To complete the task of full universal stabilization, we still hope to stabilize in any mixed state inside the Bloch sphere. Toward this goal, one can in addition generate an effective red-sideband coupling for  $|\hat{\mathbf{n}}\rangle$ , defined as  $\hat{H}_{\hat{\mathbf{n}}R} = g\epsilon(\hat{a}^\dagger \hat{\sigma}_{\hat{\mathbf{n}}}^- + \hat{a} \hat{\sigma}_{\hat{\mathbf{n}}}^+)$ . (Note that with  $\hat{\sigma}_{\hat{\mathbf{n}}}^\pm = \hat{\sigma}_{-\hat{\mathbf{n}}}^\mp$ , we have  $\hat{H}_{\hat{\mathbf{n}}R} = \hat{H}_{-\hat{\mathbf{n}}B}$ .) A combination of  $\hat{H}_{\hat{\mathbf{n}}B}$  and  $\hat{H}_{\hat{\mathbf{n}}R}$  can then stabilize the qubit in a mixed state of  $|\hat{\mathbf{n}}\rangle$  and  $|-\hat{\mathbf{n}}\rangle$ , similar to our previous discussion and results in Figs. 4.4(a) and 4.3(b). In other words, we can stabilize the qubit in a state corresponding to an arbitrary point along the axis defined by  $\hat{\mathbf{n}}$ .

With the discussion in the previous sections, we claim that our scheme can effectively stabilize the qubit in any pure and mixed state, i.e., at any point on and inside the Bloch sphere, at will.

#### 4.9. Fast stabilization and critical damping

The time needed for stabilizing the qubit in a desired pure state is crucial for applications such as fast qubit initialization and reset. The timescale for pure-state stabilization is mainly set by  $g\epsilon$  and  $\kappa$ . To make this statement more quantitative, we follow the dynamics of the axis  $\hat{\mathbf{n}}$  stabilization scheme as described by the Lindblad master equation in Eq. (4.21). Neglecting the population amplitude associated with  $|1, -\hat{\mathbf{n}}\rangle$ , the stabilization process can be approximately described by the following set of differential equations:

$$\begin{aligned}\frac{d\tilde{\rho}_{33}}{dt} &= 2g\epsilon C - \kappa\rho_{33}, \\ \frac{d\tilde{\rho}_{11}}{dt} &= -2g\epsilon C, \\ \frac{dC}{dt} &= g\epsilon(\tilde{\rho}_{11} - \tilde{\rho}_{33}) - \frac{1}{2}\kappa C.\end{aligned}\tag{4.33}$$

These three first-order differential equations can be turned into a third-order differential equation for  $\tilde{\rho}_{11}$ ,

$$\frac{d^3\tilde{\rho}_{11}}{dt^3} + \frac{3}{2}\kappa\frac{d^2\tilde{\rho}_{11}}{dt^2} + (4g^2\epsilon^2 + \frac{1}{2}\kappa^2)\frac{d\tilde{\rho}_{11}}{dt} + 2\kappa g^2\epsilon^2\tilde{\rho}_{11} = 0,\tag{4.34}$$

with an associated characteristic equation

$$\left(\lambda + \frac{1}{2}\kappa\right)(\lambda^2 + \kappa\lambda + 4g^2\epsilon^2) = 0.\tag{4.35}$$

Similar to the classical damped harmonic oscillator, the stabilization process can be under-damped, critically-damped, or over-damped, depending on the nature of the roots of Eq. (4.35). Critically-damped stabilization occurs for  $\kappa = 4g\epsilon$ , at which point all three roots of Eq. (4.35) become real. Resonator dissipation rates deviating from this working point lead to under-damped or over-damped stabilization instead. For a fixed resonator dissipation rate, different sideband coupling strengths can also lead to all three damping types.

Fig. 4.6 shows the stabilization processes for different coupling strengths  $g\epsilon$  at fixed  $\kappa$ , for stabilizing the qubit in its excited state  $|e\rangle$  and in the superposition  $|x\rangle = \frac{1}{\sqrt{2}}(|e\rangle + |g\rangle)$ . As  $g\epsilon$  is decreased, we find behavior characteristic of the three damping types. Compared with critically-damped stabilization, a slightly under-damped case may help the system reach the steady state faster, since the tiny oscillations, arising from complex roots of Eq. (4.35), are almost negligible as evidenced by numerical simulations. For our chosen system parameters, we find that  $g\epsilon \approx \kappa/2.6$  yields the quickest stabilization.

The stabilization time is set by  $2/\kappa$  which is the characteristic time for the critically-damped stabilization process. With realistic parameters, as chosen for Fig. 4.6, the stabilization can be completed within around 100 ns.

#### 4.10. Circuit quantization

In this last section, we derive the effective Hamiltonian from the circuit presented in Fig. 4.1 (b). We direct the reader to Ref. [96] for the analysis of the first circuit. This circuit contains a fluxonium qubit (red), a resonator (purple) and a SQUID (blue) which serves as a coupler. Based on standard quantization procedure, the Lagrangian that describes the circuit of interest

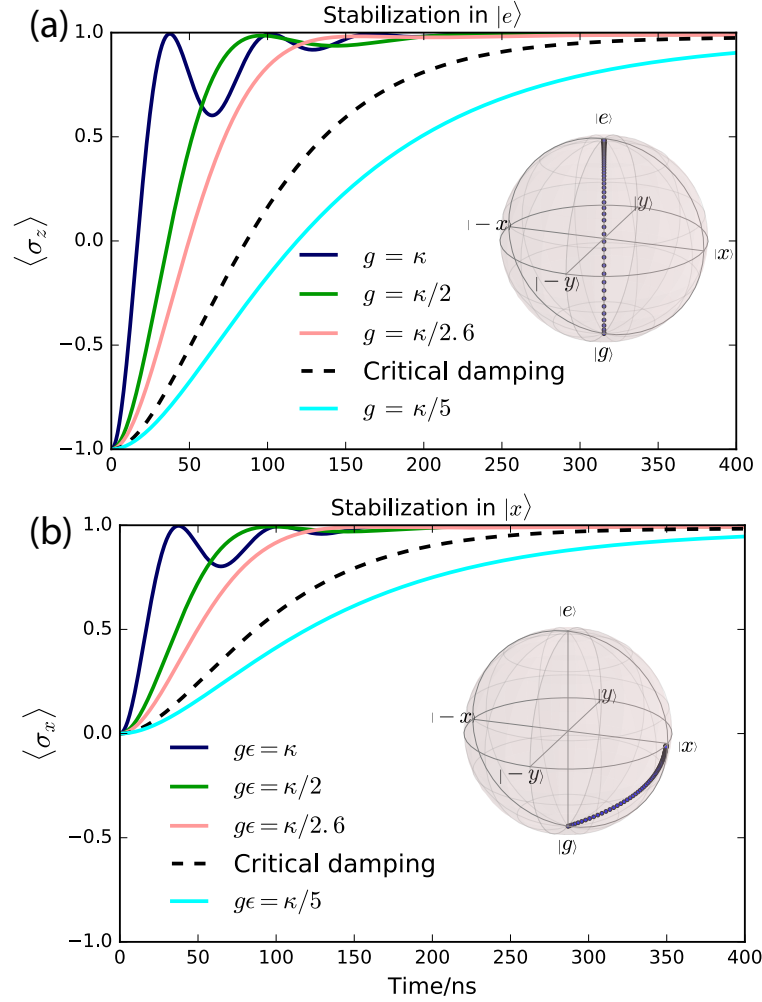


Figure 4.6. Stabilization processes in time domain. The qubit is initialized in the ground state. Shown is the expectation of  $\langle \hat{\sigma}_{\hat{n}} \rangle$  when targeting (a) the excited state and (b) state  $|x\rangle$ . The insets show the stabilization dynamics in terms of  $\rho(t)$ . ( $\kappa/2\pi$  is set to 8 MHz,  $T_{\text{env}} = 15$  mK,  $\gamma = 0.1$  MHz,  $\gamma_{\phi} = 0.1$  MHz, and  $\chi/2\pi = 0.5$  MHz.)

is given by

$$\begin{aligned}
 L = & \frac{1}{2}C_r\dot{\Phi}_a^2 + \frac{1}{2}C_{J1}\dot{\Phi}_b^2 + \frac{1}{2}C_s(\dot{\Phi}_b - \dot{\Phi}_c)^2 + \frac{1}{2}C_q\dot{\Phi}_c^2 \\
 & + \frac{1}{2}C_{qr}(\dot{\Phi}_a - \dot{\Phi}_c)^2 - \frac{1}{2L_r}(\Phi_a - \Phi_b)^2 - \frac{1}{2L_q}\Phi_c^2 \\
 & + E_{J2} \cos\left(2\pi\frac{\Phi_c + \Phi_{e,\text{fl}}}{\Phi_0}\right) + E_{J1\text{eff}}(t) \cos\frac{2\pi\Phi_b}{\Phi_0}.
 \end{aligned} \tag{4.36}$$

The SQUID loop's Josephson energy  $E_{J1\text{eff}}(t) = 2E_{J1} \cos[\phi_{\text{sq}}(t)/2]$  is tuned by the reduced external flux  $\phi_{\text{sq}}(t) = 2\pi\Phi_{e,\text{sq}}(t)/\Phi_0$  which is modulated around its DC value using two modulation tones, i.e.,  $\phi_{\text{sq}}(t) = \bar{\phi}_{\text{sq}} - d_R \cos \omega_1 t - d_B \cos \omega_2 t$ , with  $d_1, d_2 \ll 1$ . As long as modulation amplitudes for the external flux remain small, we can expand  $E_{J1\text{eff}}(t)$  into its DC value and a small time-varying part,

$$E_{J1\text{eff}}(t) = E_{J1\text{eff}}^{(0)} + E'_{J1\text{eff}}(t), \quad (4.37)$$

where  $E_{J1\text{eff}}^{(0)}$  is the time-average of  $E_{J1\text{eff}}(t)$ .  $E'_{J1\text{eff}}(t)$  can be approximated as

$$E'_{J1\text{eff}}(t) \approx (2\epsilon_R \cos \omega_1 t + 2\epsilon_B \cos \omega_2 t) E_{J1\text{eff}}^{(0)}, \quad (4.38)$$

where  $2\epsilon_n \approx \sin(\varphi_e/2)d_n/2$  ( $n = R, B$ ). (In this definition of  $\epsilon_n$ , a factor of 2 is included for more convenient notation in the main text.) The Hamiltonian can be obtained from Eq. (4.36) by a Legendre transformation.

The coupler mode only serves a passive role by tuning the coupling between the resonator and qubit. For this purpose, we choose the energy scales of the relevant circuit parameters as listed in Table 4.1. By design, the Josephson energy  $E_{J1\text{eff}}^{(0)}$  is the largest energy scale so that the coupler mode  $b$  has excitation energies far exceeding those of the qubit and resonator. The

Table 4.1. Energy scales of circuit parameters used in this chapter.

Parameters	Energy Scale
$E_{J1\text{eff}}^{(0)}/2\pi$	$\sim 1000$ GHz
$E_{Lr}/2\pi$	$\sim 50$ GHz
$E_{J2}/2\pi$	$\sim 10$ GHz
$E_c/2\pi$	$\sim 4$ GHz
$E_{Lq}, E_{ac}, E_{bc}/2\pi$	$\sim 300$ MHz
$E_a, E_b/2\pi$	$\sim 100$ MHz

potential energy of the mode  $b$  is dominated by the term  $-E_{J1\text{eff}}^{(0)} \cos \hat{\varphi}_b$  and, since  $E_{J1\text{eff}}^{(0)} \gg E_b$ , low-lying wave functions will be localized around  $\varphi_b = 0$ . The corresponding oscillator length is given by  $(8E_b/E_{J1\text{eff}}^{(0)})^{1/4} \ll 1$ . We approximate the Hamiltonian by a second-order expansion in  $\hat{\varphi}_b$  which gives

$$\begin{aligned}
\hat{H} = & \left[ 4E_b \hat{n}_b^2 + \frac{1}{2} (E_{Lr} + E_{J1\text{eff}}(t)) \hat{\varphi}_b^2 \right] \\
& + \left[ 4E_c \hat{n}_c^2 - E_{J2} \cos(\hat{\varphi}_c + \phi_{\text{fl}}) + \frac{E_{Lq}}{2} \hat{\varphi}_c^2 \right] \\
& + \left[ 4E_a \hat{n}_a^2 + \frac{E_{Lr}}{2} \hat{\varphi}_a^2 \right] + E_{ac} \hat{n}_a \hat{n}_c + E_{bc} \hat{n}_b \hat{n}_c \\
& - E_{Lr} \hat{\varphi}_a \hat{\varphi}_b.
\end{aligned} \tag{4.39}$$

In terms of annihilation and creation operators for the  $a$  and  $b$  modes as well as eigenstates  $\{|j\rangle\}$  of the  $c$  (qubit) mode, the Hamiltonian can be rewritten in the form

$$\begin{aligned}
\hat{H} \approx & \Omega_a \hat{a}^\dagger \hat{a} + \Omega_b \hat{b}^\dagger \hat{b} + \sum_j E_j |j\rangle \langle j| \\
& + i(\hat{a}^\dagger - \hat{a}) \sum_{j,k} (g_{a;jk} |j\rangle \langle k| + \text{H.c.}) \\
& + i(\hat{b}^\dagger - \hat{b}) \sum_{j,k} (g_{b;jk} |j\rangle \langle k| + \text{H.c.}) \\
& + \Omega_{ab} (\hat{a}^\dagger + \hat{a})(\hat{b}^\dagger + \hat{b}) + \Omega_{\text{mod}}(t) (\hat{b}^\dagger + \hat{b})^2.
\end{aligned} \tag{4.40}$$

Here,  $\Omega_a$  and  $\Omega_b$  are the excitation energies of the resonator and coupler, and  $E_j$  is the energy of fluxonium eigenstate  $|j\rangle$ . We design  $\Omega_b$  to be the largest excitation energy among the three degrees of freedom, setting  $\Omega_b \sim 2\pi \times 20$  GHz and  $\Omega_a, E_1 - E_0 \sim 2\pi \times 5$  GHz.  $\Omega_{ab}$  is the

coupling strength between the resonator and coupler due to the  $\hat{\varphi}_a \hat{\varphi}_b$  term in Eq. (4.39). The coupling strengths between the qubit and resonator ( $g_{a;jk}$ ) or coupler ( $g_{b;jk}$ ) are due to terms involving  $\hat{n}_a \hat{n}_b$  and  $\hat{n}_b \hat{n}_c$  in Eq. (4.39). These coefficients are given by

$$\begin{aligned}\Omega_{ab} &= E_L \left[ \frac{2E_a}{E_L} \right]^{\frac{1}{4}} \left[ \frac{2E_b}{E_L + E_{J1\text{eff}}^{(0)}} \right]^{\frac{1}{4}}, \\ g_{a;jk} &= E_{ac} \langle j | \hat{n}_c | k \rangle \left[ \frac{E_{Lr}}{32E_a} \right]^{\frac{1}{4}}, \\ g_{b;jk} &= E_{bc} \langle j | \hat{n}_c | k \rangle \left[ \frac{E_{Lr} + E_{J1\text{eff}}^{(0)}}{32E_b} \right]^{\frac{1}{4}}.\end{aligned}\quad (4.41)$$

All of them are small quantities compared with the excitation energies of the three modes, and can be treated perturbatively.  $\Omega_{\text{mod}}(t) = \sqrt{2E_b/(E_L + E_{J1\text{eff}}^{(0)})} E'_{J1\text{eff}}(t)$  denotes the strength of the time-dependent modulation on the coupler mode.

Since the coupler remains in its ground state, we may eliminate it adiabatically from the Hamiltonian. To this end, we adopt a Bogoliubov transformation [118] removing the static coupling term between resonator and coupler. As a result of the transformation, the coefficients of the remaining terms in Eq. (4.40) will be shifted. Second, a Schrieffer-Wolff transformation [37, 119, 120] decoupling the qubit from the other two modes is applied. Switching to the new dressed basis, all static couplings among the three modes are removed. The coupler's annihilation operator  $\hat{b}$  is transformed into

$$\hat{b} \rightarrow \hat{b} - \frac{\Omega_{ab}}{\Delta_{ab}} \hat{a} - \frac{\Omega_{ab}}{\Sigma_{ab}} \hat{a}^\dagger + \sum_{j,k} \frac{ig_{b;kj}}{\Delta_{b;kj}} |j\rangle \langle k|, \quad (4.42)$$

where  $\Delta_{ab} = \Omega_b - \Omega_a$ ,  $\Sigma_{ab} = \Omega_a + \Omega_b$ ,  $\Delta_{b;kj} = \Omega_b - (E_k - E_j)$ . The time-dependent modulation term  $\Omega_{\text{mod}}(t)(\hat{b}^\dagger + \hat{b})^2$  is transformed, to leading order, into

$$\Omega_{\text{mod}}(t) \left[ (\hat{b} + \hat{b}^\dagger) + \eta_a(\hat{a} + \hat{a}^\dagger) + \sum_{jk} (\eta_{jk}|j\rangle\langle k| + \text{H.c.}) \right]^2,$$

where  $\eta_a \approx -2\Omega_b\Omega_{ab}/(\Omega_b^2 - \Omega_a^2)$ , and

$$\eta_{jk} \approx \frac{ig_{b;kj}}{\Delta_{b;kj}} - \frac{ig_{b;jk}}{\Delta_{b;jk}}.$$

With this, we finally obtain the effective Hamiltonian

$$\begin{aligned} \hat{H} = & \Omega_a \hat{a}^\dagger \hat{a} + \sum_j E_j |j\rangle\langle j| \\ & + \sum_j \chi_{a,j} \hat{a}^\dagger \hat{a} |j\rangle\langle j| + \sum_j \kappa_j |j\rangle\langle j| \\ & + \Omega_{\text{mod}}(t) \left[ \eta_a^2 (\hat{a} + \hat{a}^\dagger)^2 + \left( \sum_{jk} \eta_{jk} |j\rangle\langle k| + \text{H.c.} \right)^2 \right] \\ & + 2\Omega_{\text{mod}}(t) \eta_a (\hat{a}^\dagger + \hat{a}) \left( \sum_j \eta_{jk} |j\rangle\langle k| + \text{H.c.} \right), \end{aligned} \quad (4.43)$$

describing the resonator and qubit modes only, where  $\chi_{a,j}$  and  $\kappa_j$  stand for the dispersive shifts and the Lamb shifts to the qubit [119]. When approximating the fluxonium qubit as a two-level

system, we recover the Hamiltonian in Eq. (4.1), with the coefficients given by

$$\begin{aligned}\omega_r &= \Omega_a + \frac{\chi_{a,0} + \chi_{a,1}}{2}, \\ \omega_q &= (E_1 + \kappa_1) - (E_0 + \kappa_0), \\ \chi &= \frac{\chi_{a,0} - \chi_{a,1}}{2}.\end{aligned}\tag{4.44}$$

In Eq. (4.43), the second to last line introduces small oscillations in the resonator and qubit energies, but can be neglected within the rotating-wave approximation. Terms in the last line of Eq. (4.43) give rise to time-dependent coupling between the resonator and qubit, and lead to the expression of  $g(t)$ . The magnitude  $g$  of that coupling is given by

$$g = 2\eta_a\eta_{01}E_{J_{1\text{eff}}}^{(0)}\sqrt{\frac{2E_b}{E_L + E_{J_{1\text{eff}}}^{(0)}}}.\tag{4.45}$$

Slight modulation of the fluxonium's reduced penetrating flux,  $\phi_{\text{fl}}(t) = d_3 \cos \omega_3 t$ , yields the Rabi drive in Eq. (4.17). To see this, we approximate <sup>1</sup>

$$\cos(\hat{\varphi}_c + \phi_{\text{fl}}(t)) \approx \cos \hat{\varphi}_c - d_3 \cos \omega_3 t \sum_{jk} f_{jk} |j\rangle\langle k|,$$

where  $f_{jk} = \langle j | \sin \hat{\varphi}_c | k \rangle$ . In the dressed basis, this drive gives terms involving  $(\hat{a}^\dagger + \hat{a})|0\rangle\langle 0|$  and  $(\hat{a}^\dagger + \hat{a})|1\rangle\langle 1|$ , leading to the longitudinal coupling in Eq. (4.18). The coefficient  $g'$  in Eq. (4.18) is given by

$$g' = \frac{\alpha_0 - \alpha_1}{2f_{01}},\tag{4.46}$$

---

<sup>1</sup>Actually, the choice of the circuit element with which we group the time-dependent flux  $\phi_{\text{fl}}(t)$  is an important question, which has been discussed in detail in Refs. [121, 122]. Fortunately, both choices will lead to linear drive terms. The existence of these terms has been confirmed by two recent experiments [46, 66].

where

$$\begin{aligned}\alpha_0 &= \sum_j f_{j0} \left( -\frac{ig_{a;0j}}{\Delta_{a;0j}} \right) - f_{0j} \left( -\frac{ig_{a;j0}}{\Delta_{a;j0}} \right), \\ \alpha_1 &= \sum_j f_{j1} \left( -\frac{ig_{a;1j}}{\Delta_{a;1j}} \right) - f_{1j} \left( -\frac{ig_{a;j1}}{\Delta_{a;j1}} \right),\end{aligned}\tag{4.47}$$

and  $\Delta_{a;jk} = \Omega_a - (E_j - E_k)$ .

In conclusion, we and our collaborators present stabilization schemes based on tunable couplers. These schemes enable us to prepare qubits in an arbitrary superposition state, and potentially also in an arbitrary mixed state. In the theory work, we also investigate the time required for qubit stabilization, and conclude that high-fidelity stabilization can be completed within 100 ns using realistic noise and circuit parameters. Our work could provide useful tools for applications including qubit initialization, resetting, and autonomous quantum error correction.

## CHAPTER 5

**Noise Mitigation: Driving Superconducting Qubits at Dynamical Sweet Spots****5.1. Protecting qubits from low-frequency noise**

The last chapter has presented a scheme where noise is used to the advantage of quantum control, specifically, stabilization of arbitrary quantum state. Starting from this chapter, we discuss strategies to mitigate noise present in superconducting qubits.

Our first focus is the ubiquitous low-frequency noise. This type of noise has been a limiting factor for dephasing times of many solid-state based qubits [13, 18, 19, 29, 31, 37, 40, 48, 51, 53–55, 63, 66, 76, 123–143]. Superconducting qubits especially suffer from  $1/f$  charge and flux noise [13, 18, 19, 29, 31, 37, 40, 51, 53–55, 63, 66, 76, 123–130]. A conventional way to improve dephasing times is to operate the qubit at so-called sweet spots [13, 37, 40, 66, 125]. These sweet spots correspond to extrema of the qubit’s transition frequency [13], see Fig. 5.1(a) for an example. Another established method for improving dephasing times is dynamical-decoupling (DD) [44, 51, 144–147], which is well-known in the context of NMR echo sequences [148–150], and has been successfully applied to superconducting qubits [44, 51].

---

Author contribution: This chapter is mainly based on the theory work published in Ref. [45], where the majority of the calculations and simulations were carried out by Ziwen Huang. The last section reflects some of the experimental results published in [46], which Ziwen Huang contributed to by providing theoretical support.

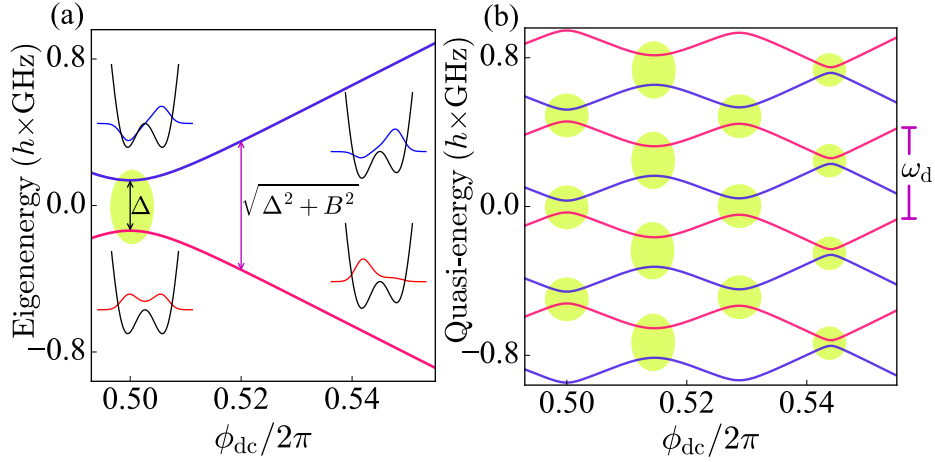


Figure 5.1. (a) Static fluxonium spectrum as a function of magnetic flux. Insets show the qubit eigenfunctions at the sweet spot and slightly away from it ( $\phi_{dc}/2\pi = 0.52$ ). The parameters used are:  $E_C/h = 0.5$  GHz,  $E_J/h = 4.0$  GHz and  $E_L/h = 1.3$  GHz for the capacitive, Josephson and inductive energy, respectively. (b) Quasi-energy spectrum of the driven qubit for flux  $\phi_{ac}/2\pi = 0.028$  and drive frequency  $\omega_d/2\pi = 490$  MHz. The highlighted regions in both panels mark the flux sweet spots. The drive produces numerous dynamical sweet spots at different DC flux values, as opposed to only one in the static case.

Generalizing the concept of static sweet spots, we propose a qubit protection protocol based on *dynamical* sweet spots [53–55, 130–132]. Inspired by static sweet-spot operation and dynamical decoupling, this protocol employs a periodic drive to mitigate the dephasing usually induced by  $1/f$  noise. Utilizing Floquet theory, we show that dynamical sweet spots represent extrema in the qubit’s quasi-energy difference, and [Fig. 5.1(b)]. Notably, dynamical sweet spots are generally not isolated points, but rather form extended sweet-spot manifolds in parameter space. The multi-dimensional nature of dynamical sweet spots provides additional freedom to tune qubit properties such as the transition frequency while maintaining dynamical protection. We show that dynamical sweet-spot operation can simultaneously yield both long depolarization ( $T_1$ ) and pure-dephasing times ( $T_\phi$ ).

This protection scheme can also be interpreted as a continuous version of DD [151]. Here, the sequences of ultra-short pulses widely used in many DD experiments are replaced by a periodic drive on the qubit, which is much easier to realize experimentally. In addition to earlier explorations in this direction [13, 43, 52–55, 130–135, 152, 153], we here provide a systematic and general framework for locating dynamical sweet-spot manifolds in the control parameter space. This framework is general enough to cover a variety of qubit systems beyond the specific example discussed here, and can be adapted to different types of drives as well as noise environments. Indeed, some of the previously developed protection schemes [13, 43, 52–55, 130, 131, 152, 153] based on qubit-frequency modulation or on-resonant Rabi drives, can be understood as special limits of the framework presented here (see Appendix B). The theoretical approach we develop allows us not only to predict the improvement of pure-dephasing times, but also to assess how dynamical depolarization times are affected by the driving. In an experimental paper [46] following our theory work, the theoretical proposals are demonstrated to lead to a significant improvement in the dephasing time of a flux-modulated fluxonium qubit.

In the following sections, we consider the superconducting fluxonium qubit a platform for illustrating the dynamical-protection protocol. To simplify the problem, we first demonstrate how to model a fluxonium as a two-level system. Then, focusing on this two-level system, we discuss the dynamical coherence times and sweet spots using the framework developed in Chapter 2. Following the discussion of qubit coherence, we turn to gate operations and readout of this qubit.

## 5.2. Two-level system subject to $1/f$ noise

Fluxonium qubits biased close to half-integer flux, as also pointed out in Chapter 3, exhibit attractive properties including increased coherence times as compared to other superconducting qubits [18, 19, 40, 46, 66, 102]. However, this sweet spot is point-like, and the qubit regains sensitivity to  $1/f$  flux noise when the external flux is tuned slightly away from the half-integer point [18, 19, 40, 66, 76, 129]. This sensitivity leads to increased pure dephasing of the fluxonium qubit.

Our protection scheme is based on introducing a modulation of the external flux close to the static sweet spot, i.e.,  $\phi_e(t) = \phi_{ac} \cos(\omega_d t) + \phi_{dc}$ . Here,  $\phi_e = 2\pi\Phi_e/\Phi_0$  denotes the reduced external flux,  $\Phi_0$  is the flux quantum, and  $\phi_{ac}$ ,  $\phi_{dc}$  are its AC modulation amplitude and DC offset, respectively. The flux-modulated fluxonium is described by the following Hamiltonian [121]

$$\hat{H}_{q,\text{full}}(t) = 4E_C \hat{n}^2 + \frac{1}{2} E_L [\hat{\phi} + \phi_e(t)]^2 - E_J \cos \hat{\phi}, \quad (5.1)$$

where  $\phi_e(t) = \phi_{dc} + \phi_{ac} \cos(\omega_d t)$ . The strong anharmonicity of the fluxonium allows us to reduce this system to an effective two-level model. We next derive such simplified model by appropriate truncation of the full fluxonium Hamiltonian.

The static eigenenergies  $\Omega_l$  and corresponding eigenstates  $|l\rangle$  ( $l = g, e, f, \dots$ ) are obtained by diagonalizing  $\hat{H}_{q,\text{full}}$ , and depend on the DC flux component  $\phi_{dc}$ . We will refer to the specific solutions at the static sweet spot  $\phi_{dc} = \pi$  by  $\Omega_{\pi,l}$  and  $|l\rangle^\pi$ . These eigenstates, expressed in the phase basis, have alternating parities (for example,  $|g\rangle^\pi$  and  $|e\rangle^\pi$  have even and odd parities respectively).

To avoid leakage into higher fluxonium states under flux modulation, we choose fluxonium parameters resulting in a large anharmonicity at half-integer flux,  $\Omega_{\pi,f} - \Omega_{\pi,e} \gg \Omega_{\pi,e} - \Omega_{\pi,g}$ . If we limit the external flux  $\phi_e(t)$  to values in the vicinity of  $\phi_{dc} = \pi$ , and avoid resonance with the  $e - f$  transition,  $\omega_d \ll \Omega_{\pi,f} - \Omega_{\pi,e}$ , then Eq. (5.1) can be approximated by the effective two-level Hamiltonian

$$\hat{H}_q(t) = \frac{\Delta}{2} \hat{\sigma}_x + \left( A \cos \omega_d t + \frac{B}{2} \right) \hat{\sigma}_z, \quad (5.2)$$

where  $\Delta = \Omega_{\pi,e} - \Omega_{\pi,g}$ ,  $A = E_L \phi_{ac} \varphi_{ge}^\pi$ ,  $B = 2E_L (\phi_{dc} - \pi) \varphi_{ge}^\pi$ , and  $\varphi_{ge}^\pi = |\langle g |^\pi \hat{\phi} | e \rangle^\pi|$ . Different from the usual convention, we define the Pauli matrices as,

$$\hat{\sigma}_x = |e\rangle^\pi \langle e|^\pi - |g\rangle^\pi \langle g|^\pi, \quad \hat{\sigma}_z = |g\rangle^\pi \langle e|^\pi + |e\rangle^\pi \langle g|^\pi, \quad (5.3)$$

which is a common choice in the context of flux qubits [154, 155].

The resulting eigenenergies of the static qubit ( $\phi_{ac} = 0$ ) are plotted in Fig. 5.1 (a) as a function of  $\phi_{dc}$ . The full Hamiltonian including the qubit-bath coupling is given by  $\hat{H} = \hat{H}_q(t) + \hat{H}_B + \hat{H}_I$ , where  $\hat{H}_B$  and  $\hat{H}_I$  denote the Hamiltonian of the bath and the qubit-bath interaction. We consider two major noise sources that often limit fluxonium coherence times:  $1/f$  flux noise and dielectric loss [19, 40, 66, 76, 127, 128]. The fluxonium's interaction with the  $1/f$  flux noise source can be modeled as mutual inductance between the fluxonium's inductor and the bath, hence the coupling to the noise is via the qubit operator  $\hat{\phi}$ . Experimental results are further consistent with dielectric noise coupling to the qubit's phase operator [19, 40, 66, 76, 128]. Note that operator  $\hat{\phi}$  only couples states with different parities. Therefore, based on Eq. (5.3), it is projected to  $\hat{\sigma}_z$  in the two-level subspace, which results in the  $\hat{H}_I$  used in our model. The corresponding interaction Hamiltonian thus takes the form  $\hat{H}_I = (\hat{\eta}_f + \hat{\eta}_d) \hat{\sigma}_z$ , where  $\hat{\eta}_f$  and  $\hat{\eta}_d$

are the bath operators through which  $1/f$  flux noise and dielectric loss are induced. The noise spectra characterizing these channels are given by <sup>1</sup>

$$S_f(\omega) = \mathcal{A}_f^2 |\omega/2\pi|^{-1}, \quad S_d(\omega) = \alpha(\omega, T_{\text{env}}) \mathcal{A}_d(\omega/2\pi)^2. \quad (5.4)$$

Here,  $\alpha(\omega, T_{\text{env}}) = |\coth(\omega/2k_B T_{\text{env}}) + 1|/2$  is a thermal factor,  $k_B$  and  $T_{\text{env}}$  denote the Boltzmann constant and temperature, and  $\mathcal{A}_f$  and  $\mathcal{A}_d$  denote the noise amplitudes.

### 5.3. Dynamical coherence times and sweet spots

As reference for our discussion of dynamical coherence times, we first briefly review the static coherence times of the undriven qubit. Based on our discussion in Section 2.3, the decoherence rates depend on the matrix elements of the qubit operator coupling to the noise as well as the noise spectra. For a non-singular noise spectrum  $S(\omega)$ , the rates for relaxation, excitation and pure dephasing are

$$\gamma_{\mp} = |\sigma_z^{ge}|^2 S(\pm\Omega_{ge}), \quad (5.5)$$

$$\gamma_{\phi} = |\sigma_z^{ee} - \sigma_z^{gg}|^2 S(0)/2. \quad (5.6)$$

Here,  $\Omega_{ge} = \sqrt{\Delta^2 + B^2}$  the corresponding eigenenergy difference, and  $\sigma_z^{ll'} \equiv \langle l | \hat{\sigma}_z | l' \rangle$  ( $l, l' = g, e$ ) the relevant matrix elements. (Since these matrix elements will appear rather frequently, we choose to introduce this slightly more compact notation.) The quantity  $|\sigma_z^{ee} - \sigma_z^{gg}|$  governing the pure-dephasing rate  $\gamma_{\phi}$  turns out to be proportional to the flux dispersion of the eigenenergy difference  $|\partial\Omega_{ge}/\partial\phi_{\text{dc}}|$ , in agreement with the well-known proportionality  $\gamma_{\phi} \propto (\partial\Omega_{ge}/\partial\phi_{\text{dc}})^2$

<sup>1</sup>At low frequencies  $\omega \ll k_B T_{\text{env}}$ , the asymmetry in the spectrum is negligible, and a symmetric  $1/f$  noise spectrum may be used.

[13, 37]. For the realistic noise spectrum  $S(\omega) = S_d(\omega) + S_f(\omega)$ , however, there is a divergence at  $\omega = 0$  from the  $1/f$  flux noise. In this case, our evaluation of dephasing times includes careful consideration of frequency cutoffs, see Refs. [13, 37, 38, 55].

To make a quantitative comparison of coherence times between the driven and undriven qubits, we use realistic circuit and noise parameters to show numerical calculated coherence times (see Table 5.1 caption for our specific choice of parameters). Away from the flux sweet spot, the qubit has wavefunctions with disjoint support [insets of Fig. 5.1(a)]. This leads to a suppression of the coefficient  $|\sigma_z^{ge}|^2$  relevant for relaxation and excitation, and hence to a relatively long depolarization time of  $T_1 = 770 \mu\text{s}$ . The pure-dephasing time of  $T_\phi = 0.88 \mu\text{s}$  is rather short, on the other hand, since the flux dispersion  $\partial\Omega_{ge}/\partial\phi_{\text{dc}}$  is significant away from the flux sweet spot. At the flux sweet spot, the situation changes: disjointness of eigenfunctions is lost, and depolarization times are correspondingly shorter,  $T_1 = 360 \mu\text{s}$ . Since the flux dispersion  $\partial\Omega_{ge}/\partial\phi_{\text{dc}}$  vanishes at the sweet spot, the qubit is less sensitive to  $1/f$  noise, resulting in a pure-dephasing time exceeding 10 ms [40, 41], limited only by second-order contributions from  $1/f$  flux noise. <sup>2</sup>

When including a periodic drive acting on the qubit, the analysis of coherence times must be modified. Based on an open-system Floquet theory [86, 87], the coherence times are most conveniently characterized in the basis formed by the qubit's Floquet states. The quasi-energies  $\epsilon_j$  and time-periodic Floquet states  $|w_j(t)\rangle$  of the driven qubit, labeled by index  $j$ , are the counterparts of the ordinary eigenstates and eigenenergies in the undriven case [86, 154–156].

---

<sup>2</sup>In realistic settings, the pure-dephasing times will be limited by other sources including photon shot noise, critical current noise, etc [33, 62, 142, 143].

They are obtained as solutions of the Floquet equation

$$\left[ \hat{H}_q(t) - i \frac{\partial}{\partial t} \right] |w_j(t)\rangle = \epsilon_j |w_j(t)\rangle. \quad (5.7)$$

In the absence of noise, the evolution operator  $\hat{U}_q(t, 0) = \sum_{j=0,1} |w_j(t)\rangle \langle w_j(0)| \exp(-i\epsilon_j t)$  governs the evolution of the driven qubit. As a result, the population in each Floquet state remains invariant, while the relative phase accumulates at a rate given by the quasi-energy difference  $\epsilon_{01} \equiv \epsilon_1 - \epsilon_0$ . In the following, we will use the framework presented in Chapter 5 to study the coherence times of this periodically driven qubit. This framework is based on a secular Redfield equation, which can definitely capture the effect from a non-Markovian noise source. Note that it is only applicable if the system coupling to the noise bath is sufficiently weak, such that the higher-order effect from the noise, especially the  $1/f$  noise, can be safely neglected. Since the noise amplitude of  $1/f$  flux noise is considered much weaker compared with its charge counterpart [100], we believe that our assumption is valid.

The central elements that used in that framework are the matrix elements and noise frequencies relevant for the decoherence. We note that they differ crucially from those of the undriven qubit. This difference can be clearly understood using the language of filter functions. We first investigate a case with a sufficiently flat noise spectrum  $S(\omega)$  (certainly no singularity is present in this spectrum). In this case, the decoherence rates are given by

$$\gamma_\mu = \int_{-\infty}^{\infty} F_\mu(\omega, t) S(\omega) d\omega, \quad (5.8)$$

where  $F_\mu(\omega, t)$  is the filter function and  $t$  should be taken to infinity, defined in Eq. (2.24). (Due to the nonexponential decay for  $1/f$  noise, the relationship between rate and filter function has

to be modified [127]). Here,  $\mu = \mp, \phi$  denotes the different noise channels corresponding to relaxation, excitation and pure dephasing.

For the undriven qubit,  $F_\mu(\omega, t)$  is strongly peaked at the filter frequencies  $\omega = \pm\Omega_{ge}$  and  $\omega = 0$ . The integrated peak areas, referred to as weights, are given by the quantities  $|\sigma_z^{ge}|^2$ ,  $|\sigma_z^{eg}|^2$  and  $|\sigma_z^{ee} - \sigma_z^{gg}|^2/2$  associated with the three noise channels. By contrast, for the driven qubit,  $F_\mu(\omega) \sim \sum_k |g_{k\mu}|^2 \delta(\omega - \bar{\omega}_{k\mu})$  develops additional sideband peaks, resulting in filter frequencies  $\bar{\omega}_{k\mp} = \pm\epsilon_{01} + k\omega_d$  and  $\bar{\omega}_{k\phi} = k\omega_d$  ( $k \in \mathbb{Z}$ ). The corresponding weights are  $|g_{k\mp}|^2$  and  $2|g_{k\phi}|^2$ . These coefficients are defined in Eq. (2.22), but for the readers' convenience, we show the definitions again

$$\begin{aligned} g_{k\pm} &= \frac{\omega_d}{2\pi} \int_0^{2\pi/\omega_d} dt e^{ik\omega_d t} \text{Tr}_q [\hat{\sigma}_z \hat{c}_\mp(t)], \\ g_{k\phi} &= \frac{\omega_d}{4\pi} \int_0^{2\pi/\omega_d} dt e^{ik\omega_d t} \text{Tr}_q [\hat{\sigma}_z \hat{c}_\phi(t)]. \end{aligned} \quad (5.9)$$

This yields the explicit expression of the decoherence rates given below Eq. (2.26).

The simple estimation based on Eq. (5.8) does not apply to the case where the noise spectrum has divergence. Specifically, the spectrum we consider,  $S(\omega)$ , diverges at  $\omega = 0$ , while it is relatively flat at other frequencies. Our strategy to treat such spectrum is sketched as follows. Away from zero frequency, the filter function still behaves like a  $\delta$  function, therefore the treatment is the same as before. Since filter frequencies for depolarization  $\bar{\omega}_{k\pm}$  are away from 0, the resulting expressions of  $\gamma_\pm$  is the same.

The appearance of a zero filter frequency for dephasing motivates us to separate the integral

$$K_\phi(t) = \int_{-\infty}^{\infty} d\omega F_\phi(\omega, t) S(\omega). \quad (5.10)$$

into a low-frequency and a high-frequency part. We focus on the low-frequency part first, which is given by

$$I(t) = 2|g_{0\phi}|^2 \int_{-\pi/t}^{\pi/t} d\omega \frac{t}{\pi} \text{sinc}(\omega t) S_f(\omega), \quad (5.11)$$

where the integration range is set by the peak width  $2\pi/t$ . To regularize the logarithmic divergence of this integral, we employ infrared cutoffs  $\pm\omega_{\text{ir}}$  [13, 38, 55, 129]. The cutoff is of the order of 1 Hz [129], much smaller than the inverse of the measurement time. In this case, the integral can be approximated by

$$I(t) \approx 8\mathcal{A}_f^2 t |\ln \omega_{\text{ir}} t| |g_{0\phi}|^2. \quad (5.12)$$

For the integral over the remaining high-frequency range, the  $\delta$ -function approximation is again valid. After combining the low and high-frequency contributions, the approximated  $K_\phi(t)$  is a time-dependent function, given by

$$K_\phi(t) \approx I(t) + 2 \sum_{k \neq 0} |g_{k\phi}|^2 S(\bar{\omega}_{k\phi}). \quad (5.13)$$

According to this,  $K_\phi(t)$  is reminiscent of a time-dependent rate for pure dephasing that grows linearly in time (up to logarithmic corrections). Consequently, the off-diagonal elements of the density matrix do not follow an exponential decay. Instead, the decay is given by

$$\tilde{\rho}_{q,01} \sim \exp \left[ -4\mathcal{A}_f^2 |g_{0\phi}|^2 t^2 |\ln \omega_{\text{ir}} t| - \sum_{k \neq 0} 2|g_{k\phi}|^2 S(\bar{\omega}_{k\phi}) t \right], \quad (5.14)$$

which is a product of a Gaussian (again, up to logarithmic corrections) and pure exponential. (Note that to estimate the pure-dephasing rate, the contribution of depolarization to the decay of  $\tilde{\rho}_{q,01}$  is excluded in the expression above.) Based on the  $1/e$  decay time, we obtain

$$\gamma_\phi \simeq \mathcal{A}_f |2g_{0\phi}| \sqrt{|\ln \omega_{ir} t_m|} + \sum_{k \neq 0} 2|g_{k\phi}|^2 \mathcal{S}(\bar{\omega}_{k\phi}), \quad (5.15)$$

as a simple approximation bounding the pure-dephasing rate from above. Here,  $t_m$  is the characteristic measurement time; a representative value of the factor  $\sqrt{|\ln \omega_{ir} t_m|}$  found in a recent experiment [129] is close to 4.

Finally, we arrive at the decoherence rates

$$\gamma_\mp = \sum_{k \in \mathbb{Z}} |g_{k\mp}|^2 \mathcal{S}(k\omega_d \pm \epsilon_{01}), \quad (5.16)$$

$$\gamma_\phi = \mathcal{A}_f |2g_{0\phi}| \sqrt{|\ln \omega_{ir} t_m|} + \sum_{k \neq 0} 2|g_{k\phi}|^2 \mathcal{S}(k\omega_d), \quad (5.17)$$

It is instructive to mention that the expressions for the dynamical rates [Eqs. (5.16) and (5.17)] reduce to the rates obtained for the static case when the drive is switched off ( $A = 0$ ). To see this, note that the Floquet states are time-independent for  $A = 0$ . As a result, the filter weights vanish for  $k \neq 0$  [see, for example, Eq. (2.22)]. The remaining quantities to be identified are simply:  $\pm\Omega_{ge} \leftrightarrow \bar{\omega}_{0\mp}$ ,  $0 \leftrightarrow \bar{\omega}_{0\phi}$ , and  $|\sigma_z^{ge}|^2$ ,  $|\sigma_z^{eg}|^2$ ,  $|\sigma_z^{ee} - \sigma_z^{gg}|^2/2 \leftrightarrow |g_{0\mp}|^2$  and  $2|g_{0\phi}|^2$ .

#### 5.4. Numerical calculation of dynamical coherence times

We numerically calculate the dynamical coherence times as a function of drive frequency and amplitude, for a flux bias fixed close to the half-integer point. Results of pure-dephasing times

are presented in Fig. 5.2 (a), and show broad regions where  $T_\phi = \gamma_\phi^{-1}$  remains close to the value of the undriven qubit, but also exhibit well-defined maxima where pure-dephasing times exceed 1 ms. (This value is based on the noise sources included in our analysis, but may ultimately be limited by other noise channels.) Fig. 5.2(b) shows the corresponding depolarization times  $T_1 = (\gamma_+ + \gamma_-)^{-1}$ . While there are point-like dropouts of  $T_1$  for certain drive parameters, the majority of the predicted  $T_1$ 's are well over  $100 \mu\text{s}$ . Table 5.1 summarizes the coherence times for two example working points ① and ② aligned with local maxima of  $T_\phi$ . The pure-dephasing times for both points exceed 1 ms, much longer than those of the undriven qubit. The depolarization times at those two points are around  $500 \mu\text{s}$ , which are favorable compared to the static sweet-spot value.

The regions where  $T_\phi$  becomes maximal, form curves in the plane spanned by the drive frequency and amplitude, with distinct behavior in the two regimes of weak driving,  $A \ll \Omega_{ge}$  [bottom of Fig. 5.2(a)], and strong driving,  $A \gtrsim \Omega_{ge}$  [top of Fig. 5.2(a)]. These curves are

Table 5.1. Calculated coherence times for four operating points. Without a drive and operated away from the sweet spot ( $\delta\phi_{\text{dc}} = 0.02$ ), the qubit has the longest  $T_\phi$  but the shortest  $T_1$ . At the sweet spot, this behavior reverses: the static  $T_1$  reaches maximum values, but  $T_\phi$  becomes relatively short. By comparison, Floquet operation at dynamical sweet spots yields  $T_1$  and  $T_\phi$  values that do not exceed the static maximal values, but are well above the minimal ones. [Underlying parameter choices: The noise amplitudes used are  $\mathcal{A}_d = \pi^2 \tan \delta_C |\varphi_{ge}^\pi|^2 / E_C$  and  $\mathcal{A}_f = 2\pi\delta_f E_L |\varphi_{ge}^\pi|$ , where  $\varphi_{ge}^\pi = \langle g | \hat{\phi} | e \rangle$  is evaluated at  $\phi_{\text{dc}}/2\pi = 0.5$ , and  $\hat{\phi}$  is the phase operator. We assume the loss tangent  $\tan \delta_C = 1.1 \times 10^{-6}$ , flux-noise amplitude  $\delta_f = 1.8 \times 10^{-6}$ , and a temperature of 15 mK. The noise parameters used here are typical for recent fluxonium experiments, see e.g., Ref. [40, 66].]

Working points	$T_1$ ( $\mu\text{s}$ )	$T_\phi$ ( $\mu\text{s}$ )
Away from the static sweet spot	<b>770</b>	0.88
Dynamical sweet spot ①	590	1200
Dynamical sweet spot ②	490	1750
Static sweet spot	360	<b>&gt; 10<sup>4</sup></b>

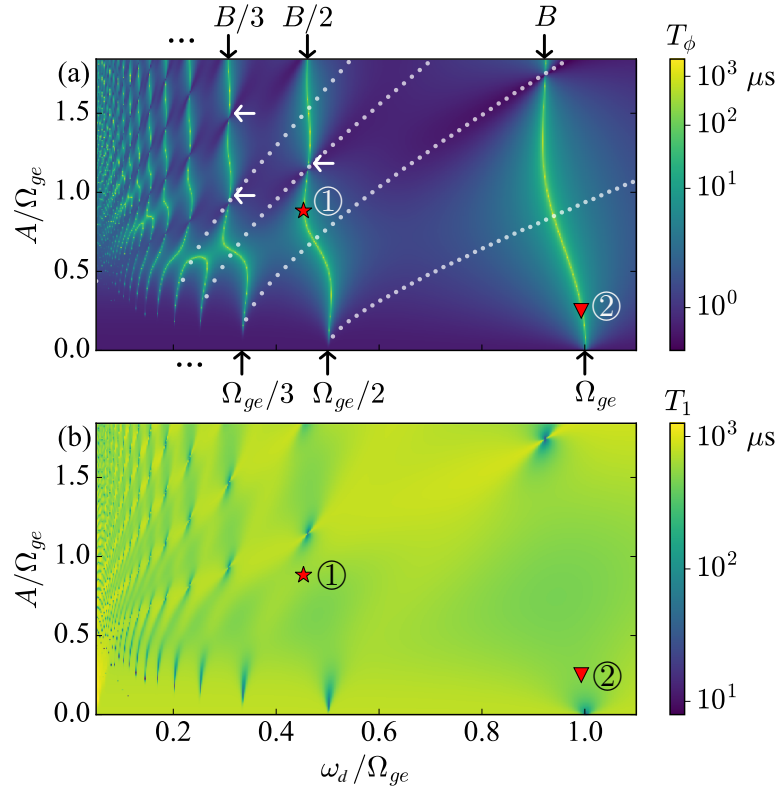


Figure 5.2. (a) Dynamical pure-dephasing time  $T_\phi$  (color-coded) as a function of drive frequency  $\omega_d$  (horizontal axis) and drive amplitude  $A$  (vertical axis). Results are calculated via Eq. (5.17) for flux  $\delta\phi_{\text{dc}}/2\pi = 0.02$ . The curves visible by their bright-yellow coloring are the dynamical sweet spots characterized by large  $T_\phi$ . In the weak ( $A \ll \Omega_{ge}$ ) and strong drive limit ( $A \gtrsim \Omega_{ge}$ ) these curves asymptotically line up with  $\omega_d = \Omega_{ge}/m$  and  $\omega_d = B/m$  (black arrows). The curves formed by the dynamical sweet spots are interrupted by cuts marked by white arrows. The overlaid white dotted curves depict the AC dynamical sweet spots corresponding to  $\partial\epsilon_{01}/\partial\phi_{\text{ac}} = 0$ . (b) Depolarization time  $T_1$  calculated by Eq. (5.16). The majority of the obtained  $T_1$  values are at the order of  $500 \mu\text{s}$ , except for point-like dropouts shown by the dark-blue coloring. The red star and triangle specify the dynamical sweet spots ① and ②. The noise parameters used for the calculation are given in the caption of Table 5.1.

the cross-sections of the sweet-spot manifolds at a fixed DC flux value  $\delta\phi_{\text{dc}}$ , see Fig. 5.2(c).

The curves of maximal pure-dephasing times show simple asymptotic behavior in these two limits, where they approach fixed-frequency intercepts in the  $A$ - $\omega_d$  plane. In the strong-drive limit, these curves are interrupted by cuts (see white arrows) where the width of the peak in

$T_\phi(\omega_d)|_{A=\text{const}}$  goes to zero. No such cuts are present in the weak-drive regime; rather, the peak width gradually decreases as drive amplitude  $A$  is lowered.

This behavior of pure-dephasing times of the driven qubit can be explained and approximated analytically using Floquet theory. In the next few sections, we will introduce in detail an analytical framework to solve the Floquet equation, based on which we use perturbation theory to understand the band-like structures of calculated  $T_1$  and  $T_\phi$  shown in Fig. 5.2.

### 5.5. Relating dynamical sweet spots to extrema of the quasi-energy difference

Away from dynamical sweet manifolds,  $T_\phi$  is limited by contributions from the (regularized) pole of the  $1/f$  spectrum, see the first term on the right-hand side of Eq. (5.17). Thus, we have  $\gamma_\phi \propto |g_{0\phi}|$ . The dynamical sweet spots then correspond to the operating points where  $|g_{0\phi}|$  vanishes. Finding the condition for  $|g_{0\phi}| = 0$  is then crucial for understanding the high- $T_\phi$  structure in Fig. 5.1 (a). For this goal, we prove a key relation,

$$\frac{\partial \epsilon_{01}}{\partial \phi_{\text{dc}}} \propto |g_{0\phi}|, \quad (5.18)$$

i.e., the dynamical flux-noise sensitivity given by the flux dispersion of the Floquet quasi-energy difference. We emphasize that this result is analogous to the more familiar case of the undriven qubit, where the pure-dephasing rate is proportional to the static flux dispersion  $\partial \Omega_{ge} / \partial \phi_{\text{dc}}$ , with quasi-energies replaced by eigenenergies.

Toward the proof of Eq. (5.18), we first note that in solving the Floquet equation (5.7), solutions  $|w_j(t)\rangle$  are required to be time-periodic in  $2\pi/\omega_d$ . Each such wavefunction can be considered an element in the vector space  $\mathcal{F}$  of  $2\pi/\omega_d$ -periodic functions of the type  $f : \mathbb{R} \rightarrow \mathbb{C}^2$ . The basis vectors of  $\mathcal{F}$  can be chosen to be  $|f_{\sigma,k}(t)\rangle = |\sigma\rangle \exp(-ik\omega_d t)$ , where  $|\sigma = z^\pm\rangle$

are the eigenvectors of the operator  $\hat{\sigma}_z$  and  $k \in \mathbb{Z}$ . In this basis, the Floquet state  $|w_j(t)\rangle$  has the decomposition

$$|w_j(t)\rangle = \sum_{k \in \mathbb{Z}} \sum_{\sigma = z^\pm} u_{j\sigma k} |\sigma\rangle e^{-ik\omega_d t}, \quad (5.19)$$

which is the Fourier expansion of  $|w_j(t)\rangle$  with  $u_{j\sigma k}$  as Fourier coefficients. It is useful to define an inner product for elements of  $\mathcal{F}$  via the time average of their product over one drive period. Based on this definition, the basis  $\{|f_{\sigma,k}(t)\rangle\}$  is orthonormal, since

$$\frac{\omega_d}{2\pi} \int_0^{2\pi/\omega_d} dt \langle f_{\sigma,k}(t) | f_{\sigma',k'}(t) \rangle = \delta_{\sigma\sigma'} \delta_{kk'}. \quad (5.20)$$

The decomposition (5.19) maps the periodic function  $|w_j(t)\rangle \in \mathcal{F}$  to a vector  $\vec{\mathbf{u}}_j \in \mathcal{V} = \mathbb{C}^2 \otimes \mathbb{C}^\infty$ . Here, the basis vectors  $|f_{\sigma,k}(t)\rangle$  of  $\mathcal{F}$  are mapped to the canonical unit vectors,  $(\vec{\mathbf{u}})_{\sigma',k'} = \delta_{\sigma\sigma'} \delta_{kk'}$ , which we also denote by  $|\sigma, k\rangle$ . Following this basis change, the Floquet state Eq. (5.19) is now represented as a vector in  $\mathcal{V}$ ,

$$|\vec{w}_j\rangle = \sum_{\sigma = z^\pm} \sum_{k \in \mathbb{Z}} u_{j\sigma k} |\sigma, k\rangle. \quad (5.21)$$

Applying the basis change to the Floquet equation, one finds that it converts to an ordinary eigenvalue problem. To carry out this step, we consider the two operators  $\hat{H}_q(t)$  and  $-i\partial/\partial t$  acting on  $|w_j(t)\rangle$  on the left-hand side of Eq. (5.7). Both of them map basis functions  $|f_{\sigma,k}(t)\rangle$  to other time-periodic functions in  $\mathcal{F}$ , and hence correspond to matrices acting on elements in

$\mathcal{V}$ . Specifically, we have

$$\begin{aligned}\hat{H}_q(t)|f_{\sigma,k}(t)\rangle &= \sum_{\sigma,\sigma'=z^\pm} \sum_{k'\in\mathbb{Z}} h_{\sigma'\sigma k'} |f_{\sigma',k+k'}(t)\rangle, \\ -i\frac{\partial}{\partial t}|f_{\sigma,k}(t)\rangle &= -k\omega_d |f_{\sigma,k}(t)\rangle,\end{aligned}\tag{5.22}$$

where

$$h_{\sigma'\sigma k'} = \frac{\omega_d}{2\pi} \int_0^{2\pi/\omega_d} dt e^{ik'\omega_d t} \langle \sigma' | \hat{H}_q(t) | \sigma \rangle.$$

Using Eq. (5.22), we can easily express the matrices representing  $\hat{H}_q(t)$  and  $-i\partial/\partial t$  as

$$\begin{aligned}\bar{H}_q &= \sum_{\sigma,\sigma'=z^\pm} \sum_{k,k'\in\mathbb{Z}} h_{\sigma'\sigma k'} |\sigma', k+k'\rangle \langle \sigma, k|, \\ \bar{\Lambda} &= - \sum_{\sigma=z^\pm} \sum_{k\in\mathbb{Z}} k\omega_d |\sigma, k\rangle \langle \sigma, k|.\end{aligned}\tag{5.23}$$

With this the Floquet equation takes on the form

$$\bar{H}|\bar{w}_j\rangle = \epsilon_j |\bar{w}_j\rangle,\tag{5.24}$$

where  $\bar{H} = \bar{H}_q + \bar{\Lambda}$ .

Solving this eigenvalue equation yields an infinite number of eigenvectors and corresponding eigenvalues (quasi-energies). The structure of this equation is such that any given eigenpair  $|\bar{w}_j\rangle$ ,

$\epsilon_j$  generates an infinite set of solutions defined via

$$|\bar{w}_{j,n}\rangle = \sum_{\sigma=z^\pm} \sum_{k \in \mathbb{Z}} u_{j\sigma,k} |\sigma, k-n\rangle,$$

$$\epsilon_{j,n} = \epsilon_j + n\omega_d \quad (n \in \mathbb{Z}). \quad (5.25)$$

Reverting back to the function space  $\mathcal{F}$ , the above states have the form  $|w_{j,n}(t)\rangle = |w_j(t)\rangle \exp(-in\omega_d t)$ . Accordingly, at the level of the underlying Hilbert space of quantum states, only two of these states ( $j = 0, 1$ ) are linearly independent.

In the following, we employ this Floquet framework to the specific Hamiltonian (5.2). For this analysis, it is useful to provide explicit expressions for the transformed  $\bar{H}_q$  from  $\hat{H}_q(t)$ .  $\hat{H}_q(t)$  involves three distinct operations:  $\hat{\sigma}_x$ ,  $\hat{\sigma}_z$ , and  $\hat{\sigma}_z \cos \omega_d t$  which are all valid linear operators on the function space  $\mathcal{F}$ . Applying again the basis transformation that led from Eq. (5.22) to Eq. (5.23), these operators are transformed to the following matrices in the  $|\sigma, k\rangle$  basis:

$$\bar{\sigma}_x = \sum_{k \in \mathbb{Z}} |z^+, k\rangle \langle z^-, k| + |z^-, k\rangle \langle z^+, k|,$$

$$\bar{\sigma}_z = \sum_{k \in \mathbb{Z}} |z^+, k\rangle \langle z^+, k| - |z^-, k\rangle \langle z^-, k|, \quad (5.26)$$

$$\bar{\sigma}_{z,d} = \frac{1}{2} \sum_{k'=\pm 1} \sum_{k \in \mathbb{Z}} |z^+, k+k'\rangle \langle z^+, k| - |z^-, k+k'\rangle \langle z^-, k|.$$

The resulting  $\bar{H}_q$  can then be compactly written as

$$\bar{H}_q = \frac{\Delta}{2} \bar{\sigma}_x + \left( A \bar{\sigma}_{z,d} + \frac{B}{2} \bar{\sigma}_z \right). \quad (5.27)$$

After these preparations, we establish the relation between the derivative  $\partial \epsilon_{01} / \partial B \sim \partial \epsilon_{01} / \partial \phi_{dc}$  and the coefficients  $g_{k\mu}$ . We consider a small perturbation affecting the Floquet

Hamiltonian (5.27) of the type  $\bar{H}_q \rightarrow \bar{H}_q + \delta B \bar{\sigma}_z/2$ . The first-order correction to the quasi-energy difference  $\epsilon_{01}$  is given by

$$\delta\epsilon_{01}^{(1)} = \frac{\delta B}{2} (\langle \bar{w}_1 | \bar{\sigma}_z | \bar{w}_1 \rangle - \langle \bar{w}_0 | \bar{\sigma}_z | \bar{w}_0 \rangle). \quad (5.28)$$

Making use of the definition of  $\bar{\sigma}_z$  in Eq. (5.26) and the inner product, we find

$$\langle \bar{w}_j | \bar{\sigma}_z | \bar{w}_{j'} \rangle = \frac{\omega_d}{2\pi} \int_0^{2\pi/\omega_d} dt \langle w_j(t) | \hat{\sigma}_z | w_{j'}(t) \rangle, \quad (5.29)$$

and thus arrive at the identity

$$\delta\epsilon_{01}^{(1)} = \frac{\delta B}{2} \times \frac{\omega_d}{2\pi} \int_0^{2\pi/\omega_d} dt \text{Tr}_q [\hat{\sigma}_z \hat{c}_z(t)] = \delta B g_{0\phi}, \quad (5.30)$$

where the last step uses the definition of  $g_{0\phi}$  from Eq. (5.9). We thus conclude that  $\partial\epsilon_{01}/\partial B = g_{0\phi}$ .

Back to the  $T_\phi$ -plot in Fig. 5.2, now we confirm that the maximal  $T_\phi$  corresponds to the extrema of the qubit's quasi-energy difference. We will later see that these extrema generically occur at avoided crossings in the extended quasi-energy spectrum [Fig. 5.1 (b)]. The latter, analogous to the extended Brillouin zone in spatially periodic systems, consists of the extended set of quasi-energies  $\epsilon_{j,n} = \epsilon_j + n\omega_d$  ( $n \in \mathbb{Z}$ ) [86, 154, 157]. This extended spectrum shows numerous avoided level crossings, and hence a multitude of regions of maximal  $T_\phi$ . These operation points are called *dynamical sweet spots*; see Refs. [53, 131, 132] for previous studies of this concept. Here, we specifically use this term to refer to the working points where the derivative of  $\epsilon_{01}$  with respect to the noise parameter vanishes. As shown in Fig. 5.2(a), these spots form a set of curves with maximal  $T_\phi$  in the  $A$ - $\omega_d$  plane. Once we account for the additional

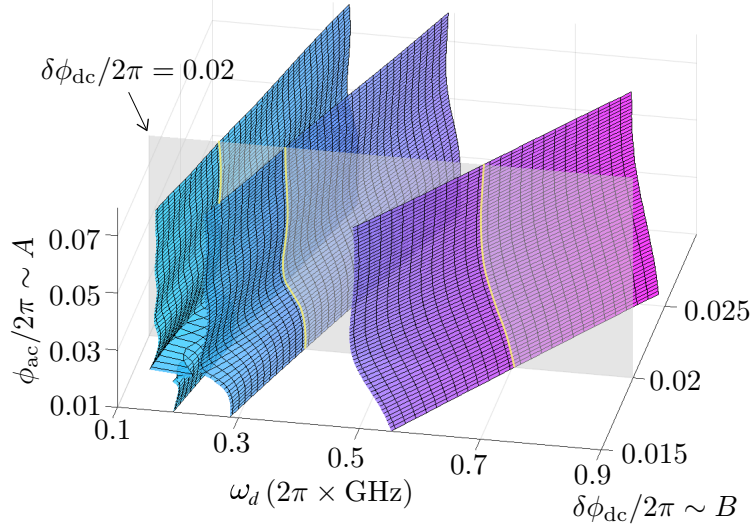


Figure 5.3. Sweet-spot manifolds embedded in the 3d parameter space, with axes corresponding to  $\omega_d$ ,  $\delta\phi_{dc}$  and  $\phi_{ac}$ . The semi-transparent plane given by  $\delta\phi_{dc}/2\pi = 0.02$ , intersects the manifolds and thus yields the sweet-spot curves shown in (a) as cross-sections (bright-yellow coloring).

perpendicular axis representing  $B$ , we find that each curve is the cross-section of a continuous surface of sweet spots, which we refer to as a sweet-spot manifold [see Fig. 5.3].

In the next section, we predict the locations of sweet spots in the limits of weak and strong drive, by treating either the drive  $A \cos \omega_d t \hat{\sigma}_z$  or the transverse qubit Hamiltonian  $\Delta \hat{\sigma}_x/2$  perturbatively.

## 5.6. Strong-drive limit

In this and the following sections, we locate the avoided crossings in the quasi-energy spectrum, in the strong-drive ( $A \gtrsim \Omega_{ge}$ ) and weak-drive ( $A \ll \Omega_{ge}$ ) limit. We further employ perturbation theory to estimate the gap sizes of avoided crossings, which are closely related to the stability of the dynamical sweet spots.

In the strong-drive limit, we treat the first term  $\bar{V} = \Delta\bar{\sigma}_x/2$  in (5.27) perturbatively while  $\bar{H}_0 = \bar{H} - \bar{V}$  acts as the unperturbed Hamiltonian. The exact eigenstates and eigenvalues of  $\bar{H}_0$  are [154, 156, 158, 159].

$$|\bar{w}_{\pm,n}^{(0)}\rangle = \sum_{k \in \mathbb{Z}} J_k \left( \mp \frac{A}{\omega_d} \right) |z^{\pm}, k - n\rangle, \quad (5.31)$$

$$\epsilon_{\pm,n} = \pm B/2 + n\omega_d.$$

Here, we have chosen to adjust notation according to  $j = 0, 1 \rightarrow \pm$  which helps keep expressions in the following more compact, but should not be confused with the notation  $z^{\pm}$ . Whenever the drive frequency matches  $\omega_d = B/m$  ( $m \in \mathbb{N}$ ), one finds that the unperturbed quasi-energies  $\epsilon_{+,n}$  become  $\epsilon_{-,n+m}$  degenerate. This degeneracy is lifted when including corrections of first order in  $\Delta$ , thus generating avoided crossings. At the center of these avoided crossings, the derivative of the quasi-energy difference vanishes, which results in dynamical sweet spots. Given the condition pointed out above, it is straightforward to see that resulting sweet spots asymptotically line up with vertical intercepts  $\omega_d = B/m$ , as shown in Fig. 5.2(a)

We next focus on the width the the sweet manifolds. The width of maxima in  $T_{\phi}(\omega_d)$  is significant for the issue of parameter deviations: the wider the maximum, the larger is the robustness of the coherence-time increase with respect to small detunings from the dynamical sweet spot. (We give more details about this claim in the last section of this chapter, i.e., Section 5.8) Perturbation theory yields

$$\Delta_m^{(1)} = 2|\langle \bar{w}_{+,0}^{(0)} | \bar{V} | \bar{w}_{-,m}^{(0)} \rangle| = \Delta |\langle \bar{w}_{+,0}^{(0)} | \bar{\sigma}_x | \bar{w}_{-,m}^{(0)} \rangle|.$$

To proceed, we convert the Floquet states back into the time domain via

$$|w_{\pm,n}^{(0)}(t)\rangle = \exp\left(\mp i \frac{A}{\omega_d} \sin \omega_d t + in\omega_d t\right) |z^{\pm}\rangle. \quad (5.32)$$

(Note that Eqs. (5.31) and (5.32) are related through the Jacobi-Anger expansion.) This enables the evaluation of the leading-order gap size:

$$\begin{aligned} \Delta_m^{(1)} &= \Delta \left| \frac{\omega_d}{2\pi} \int_0^{2\pi/\omega_d} dt \langle w_{+,0}^{(0)}(t) | \hat{\sigma}_x | w_{-,m}^{(0)}(t) \rangle \right| \\ &= \Delta \left| J_m \left( \frac{2A}{\omega_d} \right) \right|. \end{aligned} \quad (5.33)$$

Whenever  $\Delta_m^{(1)} = 0$ , i.e.,  $2A/\omega_d$  is one of the roots of the Bessel function  $J_m$ , the width goes to zero and the sweet-spot curve is interrupted with a cut.

The dropouts of  $T_1$  visible in Fig. 5.2(b) are similarly related to the vanishing gap size of the avoided crossings. If the gap opening of the avoided crossing, i.e., the quasi-energy difference of the qubit at the dynamical sweet spot becomes smaller, the terms  $|g_{0\mp}|^2 S(\pm\epsilon_{01})$  in Eq. (5.16) rapidly increase in magnitude as the regularized divergence of  $S(\omega)$  is sampled. In other words, the low-frequency  $1/f$  noise significantly suppresses the dynamical  $T_1$  whenever  $\epsilon_{01}$  vanishes. Therefore, the low- $T_1$  features observed in Fig. 5.2(b) match the locations of strong narrowing of the maximal  $T_\phi$  regions in Fig. 5.2(a) ( $\Delta_m \rightarrow 0$ ), including the discussed cuts in the strong-drive limit, as well as the gradual narrowing in the weak-drive limit. In our example, the widths of  $T_\phi$  peaks surrounding the sweet-spot manifolds are generally sufficiently wide and, hence, gap sizes sufficiently large, such that  $1/f$  flux noise does not limit the dynamical  $T_1$ .

### 5.7. Weak-drive limit

In the weak-drive limit ( $A \ll \Omega_{ge}$ ), we instead treat the drive-related term  $\bar{V} = A \bar{\sigma}_{z,d}$  perturbatively. The unperturbed eigenvalues and eigenstates of  $\bar{H}_0 = \bar{H} - \bar{V}$  are given by

$$|\bar{w}_{\pm,n}^{(0)}\rangle = \cos \frac{\theta}{2} |z^{\pm}, -n\rangle \pm \sin \frac{\theta}{2} |z^{\mp}, -n\rangle, \quad (5.34)$$

$$\epsilon_{\pm,n} = \pm \Omega_{ge}/2 + n\omega_d. \quad (5.35)$$

These are closely related to the eigenstates and eigenvalues of the undriven qubit. Here, we employ the definitions  $\theta = \tan^{-1}(\Delta/B)$ , and  $\Omega_{ge} = \sqrt{\Delta^2 + B^2}$ .

Whenever the drive frequency obeys  $\omega_d = \Omega_{ge}/m$  ( $m \in \mathbb{N}$ ), the quasi-energies  $\epsilon_{+,n} = \epsilon_{-,n+m}$  become degenerate. Again, this degeneracy is lifted by the perturbation  $\bar{V}$ , and thus avoided crossings are generated. As a result, the sweet spots observed towards the bottom of Fig. 5.2(a) asymptotically take the form of vertical lines at drive frequencies set by  $\omega_d = \Omega_{ge}/m$ . This width of the maximal is proportional to the gap size of the avoided crossing and given by  $\Delta_m \approx A^m |\sin \theta \cos^{m-1} \theta| / \omega_d^{m-1} (m-1)!$  in the weak-drive limit, where  $\theta = \tan^{-1}(\Delta/B)$ . We next show in detail how this expression is derived.

For  $m = 1$ , the calculation resembles the one for the strong-drive limit and results in a leading-order gap size of

$$\Delta_{m=1}^{(1)} = 2 |\langle \bar{w}_{+,0}^{(0)} | \bar{V} | \bar{w}_{-,1}^{(0)} \rangle| = A |\sin \theta|. \quad (5.36)$$

The calculation of the gap sizes for  $m > 1$  requires higher-order degenerate perturbation theory, which we perform using Brillouin-Wigner expansion. This approach converts Eq. (5.24) into a reduced equation that only involves the degenerate eigenvector pair  $|\bar{w}_{+,0}^{(0)}\rangle$  and  $|\bar{w}_{-,m}^{(0)}\rangle$ .

To facilitate the derivation of the reduced equation, we define the projection operators

$$\bar{P} = |\bar{w}_{+,0}^{(0)}\rangle\langle\bar{w}_{+,0}^{(0)}| + |\bar{w}_{-,m}^{(0)}\rangle\langle\bar{w}_{-,m}^{(0)}|$$

and  $\bar{Q} = \hat{\mathbb{1}} - \bar{P}$ , which project vectors in  $\mathcal{V}$  onto the degenerate subspace, and onto the subspace orthogonal to it, respectively. Here,  $\hat{\mathbb{1}}$  is the identity operator on  $\mathcal{V}$ . According to Brillouin-Wigner theory, the two exact eigenvectors  $|\bar{w}_j\rangle$  with quasi-energy  $\epsilon_j$  obey the equation

$$\bar{H}_{\text{deg}}|\bar{w}_j\rangle = \epsilon_j|\bar{w}_j\rangle, \quad (5.37)$$

where

$$\bar{H}_{\text{deg}} = \bar{P}(\bar{V} + \bar{V}\bar{T}\bar{V} + \bar{V}\bar{T}\bar{V}\bar{T}\bar{V} + \dots)\bar{P}, \quad (5.38)$$

and

$$\bar{T} = \frac{\bar{Q}}{\epsilon_j - \bar{H}_0}. \quad (5.39)$$

Note that despite its appearance, Eq. (5.37) is not an ordinary eigenvalue problem, since both sides contain the eigenvalue  $\epsilon_j$ . It is possible to find a solution for the eigenvalues iteratively. To avoid excessive notation, we focus on the  $j = 0$  eigenvalue and omit unnecessary subscripts in the following. In the first iteration, we insert the unperturbed quasi-energy  $\epsilon^{(0)} = \epsilon_{+,0}$  into the left-hand side of Eq. (5.37), and solve for  $\epsilon^{(1)}$  on the right-hand side. Using the new quasi-energy approximation, we then repeat these steps to include higher-order corrections. With this

procedure, we find that, to leading order in  $A$ , the gap size is given by

$$\Delta_m \approx |\sin \theta \cos^{m-1} \theta| \frac{A^m}{(m-1)! \omega_d^{m-1}}. \quad (5.40)$$

For decreasing drive strength  $A$ , the width narrows with  $\sim A^m$  consistent with the behavior observed in Fig. 5.2(a).

We made a final remark before we move to the next section. Recent experimental evidence points to the relevance of additional noise in the AC drive amplitude [46, 53–55, 130]. While the magnitude and power spectrum of this noise are not well established, it is useful to note that there exist simultaneous sweet spots for the DC and AC flux amplitude,  $\partial \epsilon_{01} / \partial \phi_{dc} = \partial \epsilon_{01} / \partial \phi_{ac} = 0$ . These doubly-sweet spots correspond to intersection points of the white dotted curves ( $\partial \epsilon_{01} / \partial \phi_{ac} = 0$ ) and the underlying DC sweet-spot curves obtained for  $\partial \epsilon_{01} / \partial \phi_{dc} = 0$  [see Fig. 5.2(a)]<sup>3</sup>. Depending on the magnitude of this AC noise, we expect such doubly-sweet spots to form the optimal working points.

### 5.8. Gap size and the width of $T_\phi$ peaks surrounding sweet-spot manifolds

In short section, we establish the relation between the gap size  $\Delta_m$  and the width of the  $T_\phi$  peaks along the drive-frequency axis surrounding sweet-spot manifolds. We derive this relation only for the strong-drive limit; the derivation for the weak-drive limit is analogous.

Generically, the pure-dephasing rate of a Floquet qubit is likely to be dominated by the  $1/f$  noise contributions away from sweet spots. In our case, that noise correspond to flux noise which limits the system, whenever the derivative of the quasi-energy difference with respect to

---

<sup>3</sup>The stability of the doubly sweet spots with respect to the DC flux bias can be estimated by the second derivative of the quasi-energy difference. We have verified numerically that our protection scheme does not significantly deteriorate the sweet-spot stability.

flux is nonzero,  $\partial\epsilon_{01}/\partial B \neq 0$ . Under these conditions, Eq. (5.17) implies that  $T_\phi$  is inversely proportional to  $|\partial\epsilon_{01}/\partial B|$ . Therefore, to find the drive-frequency width of the  $T_\phi$  peaks, it is useful to first explore how  $|\partial\epsilon_{01}/\partial B|$  depends on  $\omega_d$ .

For a dynamical sweet spot in the strong-drive limit,  $A_0 \gg \Omega_{ge}$ , the drive parameters satisfy  $\omega_{d,m} = B_0/m$ . At the sweet spot, the quasi-energy derivative vanishes,  $\partial\epsilon_{01}/\partial B = 0$ . Let us consider values  $B$  and  $\omega_d$  in the vicinity of the sweet-spot point given by  $B_0$  and  $\omega_{d,m}$ . Using Eq. (5.31), we see that the Hamiltonian in the relevant subspace is

$$\begin{aligned} \bar{H} &= \bar{H}_0 + \bar{V} \\ &= \epsilon_{+,0} |\bar{w}_{+,0}^{(0)}\rangle \langle \bar{w}_{+,0}^{(0)}| + \epsilon_{-,m} |\bar{w}_{-,m}^{(0)}\rangle \langle \bar{w}_{-,m}^{(0)}| + \Delta\bar{\sigma}_x/2, \end{aligned} \quad (5.41)$$

which results in the quasi-energy difference

$$\epsilon_{01} \approx \sqrt{\Delta_m^2 + (B - m\omega_d)^2}. \quad (5.42)$$

The derivative of  $\epsilon_{01}$  with respect to  $B$  is thus

$$\frac{\partial\epsilon_{01}}{\partial B} \approx \frac{B - m\omega_d}{\epsilon_{01}}. \quad (5.43)$$

Since we are interested in the width of the sweet manifold along the  $\omega_d$ -axis, we set  $B = B_0$ , and consider variations of  $\omega_d$  around  $\omega_{d,m}$ . As a function of  $\omega_d$ , the derivative  $|\partial\epsilon_{01}/\partial B|$  takes on its minimum value of zero at  $\omega_d = \omega_{d,m}$ . Away from this sweet spot,  $|\partial\epsilon_{01}/\partial B|$  has an upper bound of 1, which is reached asymptotically in the limit  $m|\omega_d - \omega_{d,m}| \gg \Delta_m$ . Based on this, we can use the full width at half minimum (FWHM) of  $|\partial\epsilon_{01}/\partial B|$  as an estimate of the peak width of  $T_\phi$ . The condition  $|\partial\epsilon_{01}/\partial B| = 1/2$  for reaching the half-minimum value, results in the

equation

$$\frac{m|\omega_d - \omega_{d,m}|}{\sqrt{\Delta_m^2 + m^2(\omega_d - \omega_{d,m})^2}} = \frac{1}{2}. \quad (5.44)$$

The corresponding two solutions  $\omega_d^{(1,2)}$  yield the FWHM  $|\omega_d^{(2)} - \omega_d^{(1)}|$ . Due to the dependence of  $\Delta_m$  on  $\omega_d$  involving a Bessel function [Eq. (5.33)], the above equation (5.44) is transcendental. We can obtain analytical approximations as follows. We rewrite Eq. (5.44) in the form  $\sqrt{3}m|\omega_d - \omega_{d,m}| = \Delta_m$ , and expanding the latter in  $\omega_d$  around  $\omega_{d,m}$ . The result of this is another transcendental equation, in which the problematic Bessel function term can, however, be neglected if  $\partial\Delta_m/\partial\omega_d \ll \sqrt{3}m$  holds. We have verified the validity of this inequality for our parameters numerically, and this way finally obtain the approximate FWHM

$$\Delta\omega_{\text{FWHM}} = 2\Delta_{m,0}/\sqrt{3}m, \quad (5.45)$$

where  $\Delta_{m,0} = \Delta|J_m(2A_0/\omega_{d,m})|$ .

### 5.9. Interpretation of coherence times in terms of filter functions

We observe that, although the obtained dynamical  $T_1$  and  $T_\phi$  times in the sweet manifolds do not exceed the maximal values at the two static working points (see Table 5.1), they are well above the corresponding static minimal values. To understand this behavior, it is instructive to interpret the decoherence rates in terms of the sampling of the noise spectrum by the filter function [Eq. (5.8)]. For that purpose, Fig. 5.4 shows the noise spectrum  $S(\omega)$  along with information characterizing the filter function  $F_\mu(\omega)$  in terms of the relevant filter frequencies and weights. The noise spectrum (black curve) is peaked at  $\omega = 0$  due to the  $1/f$  flux

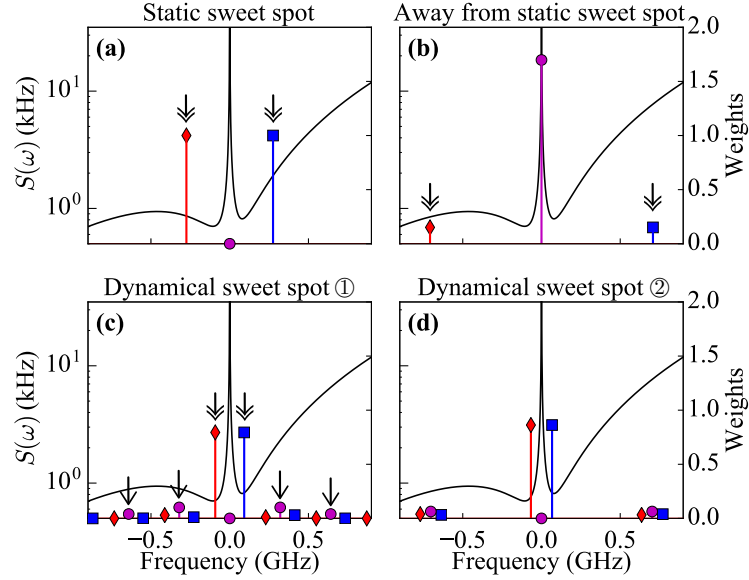


Figure 5.4. Noise spectra and filter weights centered at the corresponding filter frequencies. The panels refer to four different working points: (a) the static sweet spot, (b) static operation away from the sweet spot ( $\phi_{dc}/2\pi = 0.52$ ), (c)-(d) dynamical sweet-spot operation at the working points ① and ②. The symbols represent relaxation (blue squares), excitation (red diamonds), and pure dephasing (purple dots). The noise spectrum is plotted concurrently in (a)-(d). The positions of filter frequencies and the associated filter weights determine which components of the noise spectrum contribute significantly to the rates  $\gamma_{\pm}$  and  $\gamma_{\phi}$  [see Eqs. (5.16) and (5.17)]. (See the main text for the discussion of filter frequencies marked by arrows.)

noise; away from that peak, dielectric loss dominates. For each filter frequency, the value of the corresponding filter weight is shown and marked by symbols distinguishing between depolarization and pure-dephasing channels. While there are only three filter frequencies in the static case, the dynamical case in principle produces an infinite number of filter frequencies  $\bar{\omega}_{k\mu}$ . The appearance of additional filter frequencies corresponds to the sampling of the noise spectral density at sideband frequencies, a point previously discussed for weakly driven systems in Refs. [52, 152, 153].

We first interpret the behavior of pure-dephasing times. The weight related to filter frequency  $\bar{\omega}_{0\phi}$  is suppressed to zero for both static and dynamical sweet spots [see Fig. 5.4(a),(c),(d)], but is large for the working point away from sweet spot [see Fig. 5.3(a) and (b)]. This weight reflects the qubit's sensitivity to  $1/f$  flux noise. Therefore, the  $T_\phi$  times at the sweet spots (both static and dynamical) are significantly longer than the one at the non-sweet spot. Compared with  $T_\phi$  at the static sweet spot, the dynamical sweet spots exhibit somewhat lower values of  $T_\phi$ . This is related to the small but nonzero pure-dephasing weights at filter frequencies  $\bar{\omega}_{k\phi} \neq 0$ , absent for static sweet spots. Figure 5.4(c) illustrates this for the working point ①, where the relevant weights resulting in the dynamical  $T_\phi \approx 1$  ms are marked by single-headed arrows. (The same reasoning applies to the other working point ②.)

The behavior of depolarization times  $T_1$  at and away from sweet spots is reversed relative to that of  $T_\phi$ . Specifically,  $T_1$  is longest at the static *non-sweet spot*, where disjoint support of wave functions leads to the strongly suppressed weights marked by double-headed arrows in Fig. 5.4(b). By contrast, depolarization weights for *sweet spots* [both static and dynamical, Figs. 5.4(a),(c)] are not subject to this suppression and produce correspondingly lower  $T_1$ . [The  $T_1$  trend obtained from the analysis of weight suppression is partially offset by the fact that  $S(\omega)$  is filtered at different frequencies in the sweet-spot vs. non-sweet-spot case.] Next, the comparison shows that the static depolarization time at the sweet spot is smaller than the dynamical  $T_1$ . The reason for this can be traced to the difference in filter frequencies and corresponding magnitudes of the noise power spectrum, see Fig. 5.4(a) vs. (c). In the static case, the filter frequencies for depolarization are  $\pm\Omega_{ge}$ , and  $S(\pm\Omega_{ge})$  is relatively large compared to the dynamical case in 5.4(c) where the dominant contributions arise from  $S(\bar{\omega}_{0\pm})$ . Indeed, these latter contributions

closely match the minima of the noise power spectrum – a situation which can be established simply by tuning the drive parameters.

### 5.10. Conservation of the sum of filter weights

Inspection of Tab. 5.1 reveals a trend of  $T_1$  and  $T_\phi$  being anti-correlated: larger  $T_1$  tend to coincide with smaller  $T_\phi$  and vice versa. This trend originates from the conservation of the cumulative filter weight,

$$(W_+ + W_-) + W_\phi = 2, \quad (5.46)$$

where  $W_\pm = \sum_k |g_{k\pm}|^2$  governs depolarization and  $W_\phi = \sum_k 2|g_{k\phi}|^2$  pure dephasing. Below we provide a short proof of this conservation law.

Since the law does not only apply to the noise operator  $\hat{\sigma}_z$ , for a more general interest, this proof will not be limited to this specific variable. We assume a more abstract system-bath interaction  $\hat{H}_I = \hat{\sigma}\hat{\eta}$ . Without loss of generality, we take the qubit coupling operator  $\hat{\sigma}$  in  $\hat{H}_I = \hat{\sigma}\hat{\eta}$  to be traceless with eigenvalues  $\pm 1$ . (Any trace contribution renormalizes the bath Hamiltonian, and the scale factor rendering the eigenvalues  $\pm 1$  can be absorbed into  $\hat{\eta}$ .) Employing the decomposition of the identity in terms of the Floquet states,  $\hat{\mathbb{1}} = \sum_{j=0,1} |w_j(t)\rangle\langle w_j(t)|$ , and making use of Eqs. (2.20) and (5.9), we find

$$\begin{aligned} \text{Tr}_q(\hat{\sigma}^2) &= \text{Tr}_q(\hat{\sigma}\hat{\mathbb{1}}\hat{\sigma}\hat{\mathbb{1}}) = \sum_{j,j'=0,1} |\langle w_j(t)|\hat{\sigma}|w_{j'}(t)\rangle|^2 \\ &= \frac{1}{2} \left| \text{Tr}_q[\hat{\sigma}\hat{c}_z(t)] \right|^2 + \sum_{\mu=\pm} \left| \text{Tr}_q[\hat{\sigma}\hat{c}_\pm(t)] \right|^2 \\ &= \sum_{\mu=\pm,\phi} \zeta_\mu^{-1} \left| \sum_{k\in\mathbb{Z}} g_{k\mu} e^{-ik\omega_d t} \right|^2 = 2. \end{aligned} \quad (5.47)$$

(The definitions of  $\zeta_{\pm} \equiv 1$  and  $\zeta_{\phi} \equiv 1/2$  are consistent with those in Section 2.3.) Time averaging this expression over one drive period  $2\pi/\omega_d$  finally yields the claimed conservation rule

$$W_+ + W_- + W_{\phi} = \sum_{k \in \mathbb{Z}} \left( |g_{k+}|^2 + |g_{k-}|^2 + 2|g_{k\phi}|^2 \right) = 2. \quad (5.48)$$

We further note that Eq. (5.48) also imposes a constraint on the filter functions, namely

$$\sum_{\mu=\pm,\phi} \int_{-\infty}^{\infty} d\omega F_{\mu}(\omega, t) = 2. \quad (5.49)$$

Increases in depolarization weights thus go along with decreases in the pure-dephasing weight, creating a tendency for trade-off between depolarization and dephasing which is exact only in the special case of white noise. This conservation rule is analogous to the sum rule that emerges in the context of dynamical decoupling [51, 145]. It is crucial that the conservation rule applies to filter weights rather than the rates. This enables one to manipulate the distribution of weights and filter frequencies to our advantage, putting the largest weights at or near minima in the noise spectrum.

For simplicity, our discussion has been based exclusively on a two-level approximation of the fluxonium qubit. In general, the presence of higher qubit levels can induce leakage to states outside the computational subspace. This concern is less significant for qubits with relatively large anharmonicity like the fluxonium circuit considered here. Through numerical calculations including higher levels, we have confirmed that this leads to quantitative changes of the dynamical decoherence rates above, but does not affect the results reported above qualitatively.

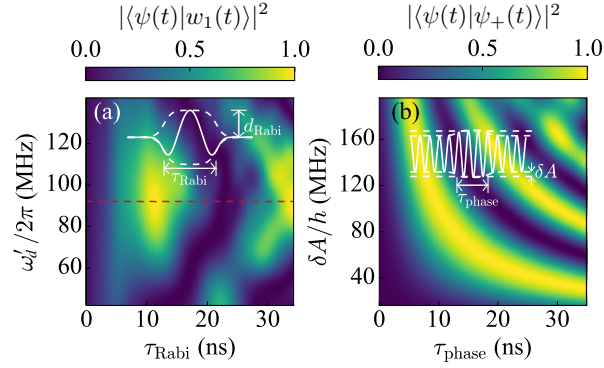


Figure 5.5. Concurrent gates for the Floquet qubit. (a) Adding a secondary pulse (inset) to the Floquet drive induces Rabi oscillations, which are sufficient for implementing  $X$  gate operations. The plot shows the final population in Floquet eigenstate  $|w_1(t)\rangle$  as a function of pulse duration  $\tau_{\text{Rabi}}$  and carrier frequency  $\omega'_d$ , for the initial state  $|w_0(t)\rangle$ . Full Rabi oscillations are observed when the secondary drive frequency matches the quasi-energy difference  $\epsilon_{01}$  (dashed line) (b) Phase gates can be realized by a temporary increase in the Floquet drive strength (inset). The change in drive strength modulates the quasi-energy and thus enables phase gates such as  $S(\pi/2)$  and  $T(\pi/4)$ . The plot shows the final population in  $|\psi_+(t)\rangle$ , as a function of the pulse duration  $\tau_{\text{phase}}$  and the drive amplitude variation  $\delta A$ , with the qubit initialized in  $|\psi_-(t)\rangle$  (see main text for definition for  $|\psi_{\pm}(t)\rangle$ ).

### 5.11. Gates and readout of a single Floquet qubit

The above results suggest that use of the driven Floquet states as computational qubit states can be advantageous due to the long coherence times reached at the dynamical sweet spots. We refer to this dynamically protected qubit as the *Floquet qubit*, which belongs to the broader class of *dressed-state qubits*. A host of previous work has studied gate operations on such dynamically encoded qubits [133, 134, 160–162]. Here, we specifically discuss how to maintain dynamical-sweet-spot operation while performing gates in order to maximize protection from  $1/f$  noise. In the following, we show that Floquet qubits can easily be integrated into gate and readout protocols necessary for quantum-information processing.

### 5.11.1. Single-qubit gates

We show that we can realize direct single-qubit gates on the Floquet qubit. For example,  $X$  and  $\sqrt{X}$  gates can be realized by inducing Rabi oscillations among Floquet eigenstates. This is accomplished by applying an additional pulse with carrier frequency  $\omega'_d \approx \epsilon_{01}$ , duration  $\tau_{\text{Rabi}}$ , and maximal amplitude  $d_{\text{Rabi}}$ , see inset of Fig. 5.5(a). We verify the presence of Rabi oscillations numerically by simulating the time evolution for the working point ①. For a fixed initial state  $|w_0(t)\rangle$ , the final population of  $|w_1(t)\rangle$  shows oscillatory behavior as a function of  $\tau_{\text{Rabi}}$  and  $\omega'_d$ , see Fig. 5.5(a). Full Rabi cycles only occur when  $\omega'_d$  matches  $\epsilon_{01}$ . Computation of the gate fidelities for the examples of  $X$  and  $\sqrt{X}$  gates yields a value of 99.99% in both cases.

Single-qubit phase gates can be implemented by modulating the quasi-energy difference  $\epsilon_{01}$  through a temporary increase  $\delta A$  of the drive amplitude [see inset of Fig. 5.5(b)]. This modifies the dynamical phase acquired over the gate duration  $\tau_{\text{phase}}$ , enabling  $S$  and  $T$  gates, for example. For numerical verification, we initialize the qubit in one of the Floquet superposition states  $|\psi_{\pm}(t)\rangle = [ |w_0(t)\rangle \pm |w_1(t)\rangle e^{-i\epsilon_{01}t} ] / \sqrt{2}$  (equator of the Bloch sphere) and monitor the population in the orthogonal state as a function of  $\tau_{\text{phase}}$  and  $\delta A$ . The observed oscillations [Fig. 5.5(b)] in this population indicates that the computational states accumulate a relative phase as expected. The computed fidelity for  $S$  ( $\pi/2$ ) and  $T$  ( $\pi/4$ ) gates realized both exceed 99.99%.

### 5.11.2. Readout

Floquet states can be adiabatically mapped [155, 163] to the eigenstates of the driven qubit by slowly ramping down the flux modulation, provided that gaps in the quasi-energy spectrum are

sufficiently large. Interested readers can find our detailed discussion on this topic in Appendix C.

For  $\textcircled{1}$ , Fig. 5.6(a) shows that quasi-energy gaps do not close as  $A$  is decreased to 0, thus enabling the adiabatic state transfer. We verify this mapping numerically by simulating the closed-system evolution with either of the driven Floquet qubit eigenstates  $|w_{0(1)}(t)\rangle$  as the initial state and a smooth ramp-down of duration  $t_{\text{ramp}}$ . Fig. 5.6(b) shows the calculated population in the undriven qubit eigenstates  $|g(e)\rangle$  as a function of time. The resulting state-transfer fidelity is high for ramp times of the order of tens of ns, (99.6% for  $t_{\text{ramp}} = 30$  ns). Conventional dispersive readout techniques, applicable to fluxonium qubits [18, 19, 40, 66, 76], can then be employed subsequently in order to infer the original dynamical state.

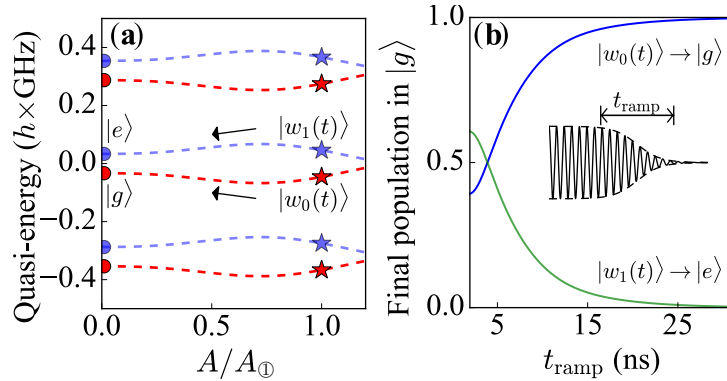


Figure 5.6. Adiabatic mapping protocol for readout. (a) shows the quasi-energy spectrum as a function of  $A$  (from 0 to  $A_{\textcircled{1}}$ ), with Floquet drive frequency fixed at  $\omega_{d\textcircled{1}}$ . ( $A_{\textcircled{1}}$  and  $\omega_{d\textcircled{1}}$  are the drive parameters at working point  $\textcircled{1}$ .) Red and blue star symbols mark the two Floquet states at the point  $\textcircled{1}$ , whereas dots of the same color represent the states  $|g\rangle$  and  $|e\rangle$  of the undriven fluxonium. An adiabatic mapping from Floquet states to static qubit eigenstates can be realized with a sufficiently slow switch-off of the drive from  $A_{\textcircled{1}}$  to 0, given the nonzero gap between the quasi-energies. (b) Simulation of the adiabatic mapping achieved by continuously switching off the drive (ramp-down in inset). The final population in  $|g\rangle$  is plotted as a function of the ramp time  $t_{\text{ramp}}$ , with the qubit initiated in  $|w_0(t)\rangle$  (blue) or  $|w_1(t)\rangle$  (green). The results confirm the feasibility of an adiabatic mapping with high fidelity, thus enabling readout of the Floquet states.

In future work, it may be interesting to explore alternative readout protocols similar to the one presented in [66]. In an extension of that scheme, a higher fluxonium level that produces a large dispersive shift on the readout resonator would be excited conditionally, based on the occupied computational Floquet state.

## 5.12. Floquet two-qubit gates

The fact that dynamical sweet spots form entire manifolds in the control-parameter space provides sufficient flexibility to perform two-qubit gates among Floquet qubits without ever giving up the dynamical protection. Thanks to the one-to-one relation between quasi-energies and Floquet states on one hand, and ordinary eigenenergies and eigenstates on the other hand, it is possible to transfer existing protocols for two-qubit gates to the case of Floquet qubits. In the following, we present a protocol for implementing a  $\sqrt{i}$ SWAP gate between two Floquet qubits, again based on flux-modulated fluxonium qubits. Related protocols for implementing two-qubit gates with dynamical protection have been discussed for slightly different systems involving either near-adiabatic parametric modulation of the qubit frequency [53–55, 131] or requiring a tunable coupler between qubits [115, 164]. The two-qubit gate proposed here is designed for the protected Floquet regime discussed above. It is compatible with direct driving of the qubit and circumvents the need for tunable coupling, thus providing a relatively simple scheme for future experimental realization.

### 5.12.1. Analytical description

A simple method of implementing  $\sqrt{i}$ SWAP gates, for example among two transmon qubits, consists of bringing the pair of weakly coupled qubits into resonance for a certain gate duration.

For two Floquet qubits, we show that  $\sqrt{i\text{SWAP}}$  gates can be realized in a similar manner by tuning the quasi-energy differences into and out of resonance. An important advantage of the Floquet two-qubit gate is the ability to keep both qubits within the dynamical sweet manifolds for the complete duration of the gate, thus reducing the error due to the qubits' coupling to  $1/f$  noise.

We establish this Floquet-gate protocol for a composite system of two coupled fluxonium qubits, each of which is flux-modulated, described by

$$\hat{H}_{LR} = \hat{H}_L(t) + \hat{H}_R(t) + \hat{H}_I. \quad (5.50)$$

Here,  $\hat{H}_L(t)$  and  $\hat{H}_R(t)$  denote the Hamiltonians of the two periodically driven fluxonium qubits, and  $\hat{H}_I$  is the time-independent coupling between them. The flux-modulation frequencies associated with the two qubits are given by  $\omega_d^L$  and  $\omega_d^R$ , respectively. As appropriate for a fluxonium with large anharmonicity, we may simplify the description by truncating the Hilbert space to a two-level subspace. We propose to induce the necessary qubit-qubit interaction  $\hat{H}_I$  via a mutual inductance between the two fluxonium loops. In this case, the coupling term takes the form  $\hat{H}_I = J\hat{\sigma}_z^L\hat{\sigma}_z^R$ , with  $J$  denoting the coupling strength. For later convenience, we introduce the abbreviation  $\hat{H}_0(t) = \hat{H}_L(t) + \hat{H}_R(t)$  for the bare qubit Hamiltonian.

When the two Floquet qubits are in resonance, i.e., their quasi-energies are degenerate, the static coupling induces excitation swapping between the Floquet states (rather than between bare qubit eigenstates). To describe this process, we move to the interaction picture using the time-dependent unitary  $\hat{U}_0(t) = \mathcal{T} \exp[-i \int_0^t \hat{H}_0(t') dt'] = \hat{U}_q^L(t) \otimes \hat{U}_q^R(t)$ . Here,  $\hat{U}_q^{L(R)}(t) = \sum_{j=0,1} |w_j^{L(R)}(t)\rangle \langle w_j^{L(R)}(0)| \exp[-i\epsilon_j^{L(R)}t]$ , and  $|w_j^{L(R)}(t)\rangle$  and  $\epsilon_j^{L(R)}$  denote the  $j$ th Floquet state and corresponding quasi-energy of the left (right) qubit. In this interaction picture, the

Hamiltonian is given by

$$\begin{aligned}\tilde{H}_{\text{LR}}(t) &= J \hat{U}_0^\dagger(t) \hat{\sigma}_z^L \hat{\sigma}_z^R \hat{U}_0(t) \\ &= J \sum_{k,k' \in \mathbb{Z}} \sum_{\mu, \mu' = \pm, \phi} g_{k\mu}^L g_{k'\mu'}^R \hat{c}_\mu^L \hat{c}_{\mu'}^R \exp\left[-i(\bar{\omega}_{k\mu}^L + \bar{\omega}_{k'\mu'}^R)t\right],\end{aligned}\quad (5.51)$$

where  $\bar{\omega}_{k\mu}^{L(R)}$  and  $g_{k\mu}^{L(R)}$  are the filter frequencies and the Fourier coefficients of the  $\hat{\sigma}_z^{L(R)}$ 's matrix elements in the Floquet basis, associated with the left (right) qubit, respectively. The operators  $\hat{c}_\mu^{L(R)}$  denote the Pauli matrices defined in the Floquet basis (see Section 5.3 for details).

Following the conventional strategy, we perform a  $\sqrt{i\text{SWAP}}$  gate by bringing the Floquet qubits into resonance ( $\epsilon_{01}^L = \epsilon_{01}^R$ ) through a suitable change of the drive parameters. After rotating-wave approximation, the effective Hamiltonian at the degeneracy point reduces to

$$\tilde{H}' = J g_{0+}^L g_{0-}^R \hat{c}_+^L \hat{c}_-^R + \text{h.c.}, \quad (5.52)$$

which is the flip-flop interaction necessary for the  $\sqrt{i\text{SWAP}}$  gate. We note that the term proportional to  $g_{0\phi}^L g_{0\phi}^R \hat{c}_\phi^L \hat{c}_\phi^R$  corresponds to an unwanted ZZ interaction between Floquet qubits. This term exactly vanishes as soon as at least one of the qubits is at a dynamical sweet spot where  $g_{0\phi}^{L,R} = 0$  [Eq. (5.18)].

Based on the full interaction Hamiltonian (5.51), we next verify numerically that this simple strategy indeed yields high-fidelity two-qubit gates.

### 5.12.2. Numerical simulation

To construct our  $\sqrt{i\text{SWAP}}$  gate, we first identify appropriate drive parameters for sweet-spot operation and for bringing the qubits into and out of resonance. Fig. 5.7(a) and (b) show the

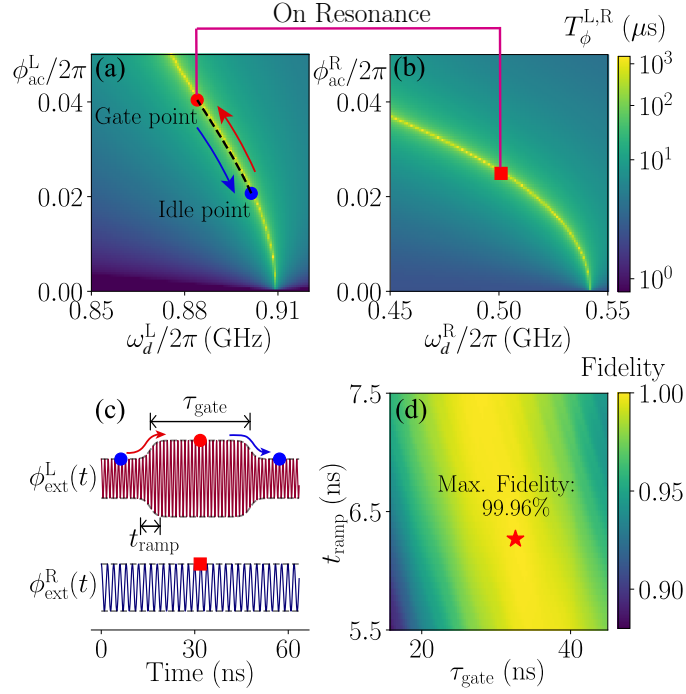


Figure 5.7. Simulation of a Floquet- $\sqrt{i}$ SWAP gate for two inductively coupled fluxonium qubits. (a) and (b) show the dynamical sweet manifolds corresponding to the two driven fluxonium qubits, at given DC flux biases. The red and blue dots in (a) indicate the gate and idle points for the left fluxonium, which is tuned along the path marked by the black-dashed curve. The red square in (b) represents the operating point for the right fluxonium qubit. (c) shows the drive pulses realizing this gate operation with  $\tau_{wait}$  and  $t_{ramp}$  denoting gate duration and ramp time, respectively. (d) depicts the calculated gate fidelity as a function of ramp time and gate duration, where the red star marks the position of maximal gate fidelity. (Parameters are as follows: left fluxonium –  $E_C^L/h = 1.2$  GHz,  $E_J^L/h = 6.0$  GHz; right fluxonium –  $E_C^R/h = 1.0$  GHz,  $E_J^R/h = 4.1$  GHz, and  $E_L^R/h = 0.7$  GHz. The interaction strength is set by  $J/h = 4.8$  MHz. The DC fluxes are fixed to  $\phi_{dc}^{L(R)}/2\pi = 0.529(0.520)$ , and noise parameters are the same as in Table 5.1.)

relevant sweet-spot manifolds for the two fluxonium qubits. Within these manifolds, the quasi-energy difference  $\epsilon_{01}^{L,R}$  varies continuously, making it possible to establish degeneracy of the two Floquet qubit quasi-energies,  $\epsilon_{01}^L = \epsilon_{01}^R$ . In the example we selected, the right qubit is maintained at a fixed dynamical sweet spot [Fig. 5.7(b), red square] while the left qubit can be tuned within

its sweet-spot manifold from an idle point (blue dot) into resonance at the gate point (red dot) and back [Fig. 5.7(a)].

The detailed pulse shapes of the drives enacting the gate are shown in Fig. 5.7(c). For the left fluxonium qubit, amplitude and frequency of the flux modulation are adjusted in a way to smoothly tune the qubit from its idle point to the gate point (within the ramp time  $t_{\text{ramp}}$ ). Pulse shaping allows one to choose a path (black-dashed curve) that keeps the Floquet qubit within the sweet manifold [Fig. 5.7(a)]. After leaving the qubit at the gate point for a suitable waiting time  $\tau_{\text{wait}}$ , the drive parameters are tuned back to the idle point. We calculate the  $\sqrt{i\text{SWAP}}$ -gate fidelity by an open-system simulation of this composite system (again taking into account of  $1/f$  flux noise and dielectric loss). The results in Fig. 5.7(d) show a broad region of gate parameters  $\tau_{\text{wait}}$  and  $t_{\text{ramp}}$  with high gate fidelities up to 99.96%. (The discussion of the effect of stray two-qubit interactions at the idle point is beyond the scope of this paper, but see Refs. [22, 97, 98, 115, 116] for mitigation strategies.)

### 5.13. Experimental demonstration of the proposed protection scheme

In a following experimental paper [46], our theoretical results are demonstrated to lead to a 40-fold improvement in the dephasing time of a flux-modulated fluxonium qubit. The longest dynamical dephasing time measured is  $23 \pm 5 \mu\text{s}$ , which is located at the dark spot in Fig. 5.8(b).

Crucially, the sweet-spot curves in Fig. 5.2 shrink to points, since the low-frequency fluctuation of  $\phi_{\text{ac}}$  also significantly affect the qubit dephasing time. Therefore, the experimental sweet spot only occurs if both  $\partial\epsilon_{01}/\partial\phi_{\text{dc}}$  and  $\partial\epsilon_{01}/\partial\phi_{\text{ac}}$  vanish.

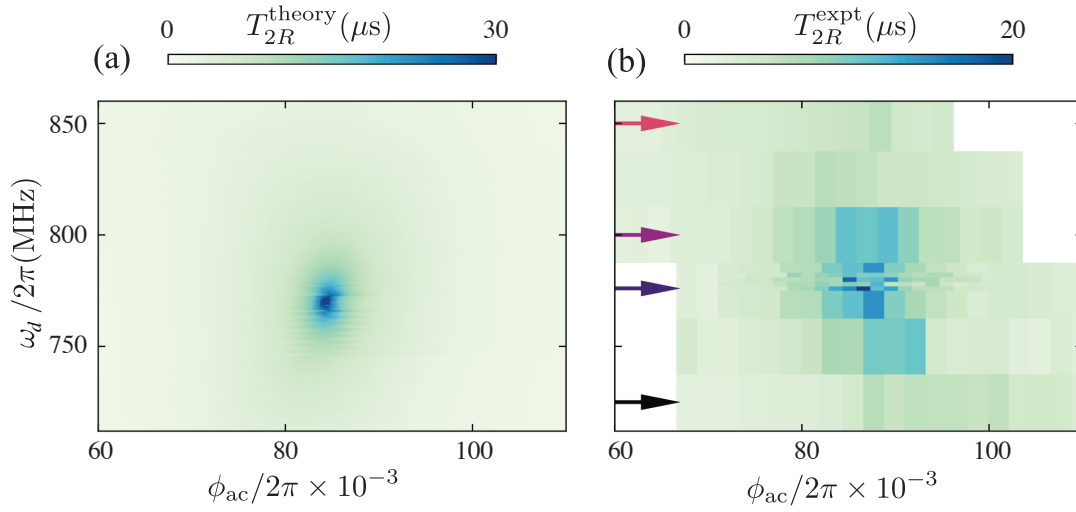


Figure 5.8. Theory prediction and experimental demonstration of the dephasing time at and away from the dynamical sweet spot in a flux-modulated fluxonium qubit. The figure is adapted from our companion experimental paper [46]. The fluxonium used in that experiment are characterized by the following parameters:  $E_C/h = 1.17$  GHz,  $E_L/h = 0.54$  GHz and  $E_J/h = 2.65$  GHz. The DC flux is set at  $\phi_{dc}/2\pi = 0.451$ .

## CHAPTER 6

**Noise Mitigation: The Revolver Qubit****6.1. Double protection from pure dephasing and depolarization**

In the previous chapter, we have focused on using a drive to protect a superconducting qubit from low-frequency noise. The concept of dynamical sweet spots has extended the conventional protection schemes, which are based on static sweet spots, to a much broader regime. Although both the static and dynamical methods have successfully reduced the qubit dephasing from low-frequency noise [40, 46, 66], these strategies do not specifically deal with qubit depolarization [45].

Since a good quantum information processor should possess both long depolarization and dephasing times, a strategy that can protect superconducting qubits simultaneously from both depolarization and pure dephasing is in high demand. The ideal way to minimize qubit depolarization is to engineer disjoint support between the two computational states of qubits [18–20, 38]. Specifically, assuming that the qubit is coupled to a depolarization noise source by operator  $\hat{O}$ , we can minimize the relaxation and thermal excitation of the qubit if we suppress the matrix element  $|\langle g|\hat{O}|e\rangle|$ .

However, disjoint support of qubit states and the sweet-spot operation are not always compatible with each other [see our discussion of a driven two-level system in Section 5.10]. A simple example is the heavy fluxonium. When operated away from the sweet spot, the fluxonium has

---

Author contribution: This chapter summarizes results from an unpublished project Ziwen Huang has worked on recently. Jens Koch, David I. Schuster, Rudolph J. Magyar and David Ferguson have also contributed to this work.

long  $T_1$  due to the exponentially suppressed depolarization matrix element ( $\sim 10$  ms [18, 19]), but  $1/f$  noise strongly dephases it at these working points ( $T_2 \sim 1$   $\mu$ s) [see discussion in Section 3.2]. On the contrary, when the penetrating flux is tuned to half a flux quantum ( $\Phi_e = \Phi_0/2$ ), the qubit is maximally insensitive to the low-frequency flux noise, but the suppression of off-diagonal matrix element  $|\langle g|\hat{O}|e\rangle|$  no longer remains.

The double protection of qubits from depolarization and pure dephasing requires not only clever control schemes, but also novel hardware design. Toward this direction, several qubit designs have been proposed, with some of them already experimentally realized [20, 38, 41, 48–50, 165]. For example, in the *zero-pi* circuit [20, 38, 50], the two computational states can be both disjoint and operated at a flux sweet spot. Using this qubit, researchers have achieved over 1.5 ms  $T_1$  and over 25  $\mu$ s  $T_2$  (measured using the standard single  $\pi$ -pulse echo sequence), which clearly demonstrates the feasibility of a double protection scheme. However, many such protected qubits pose challenging requirements on the circuit hardware for their full protection. Up to date, there has not been an experiment on such qubits that demonstrates a longer coherence time (considering both  $T_1$  and  $T_2$ ) than that of the most recent transmon and fluxonium qubits [15, 16].

The research efforts mentioned above are mainly focused on operating the qubits at static sweet spots. The combination of the dynamical version of sweet-spot and disjoint-support protection in a superconducting qubits has yet to be explored, which leaves the question open about whether this alternative option can yield more favorable  $T_1$  and  $T_\phi$  and/or lower the requirement on the hardware side. In the following sections, we will describe our efforts on the first proposal of such qubit. We will start from an abstract model to sketch the mechanism of this scheme. After this, we will introduce a physical realization of the revolver qubit, using a

pair of coupled heavy fluxonium qubits. Finally, we will analyze the coherence times based on realistic noise models.

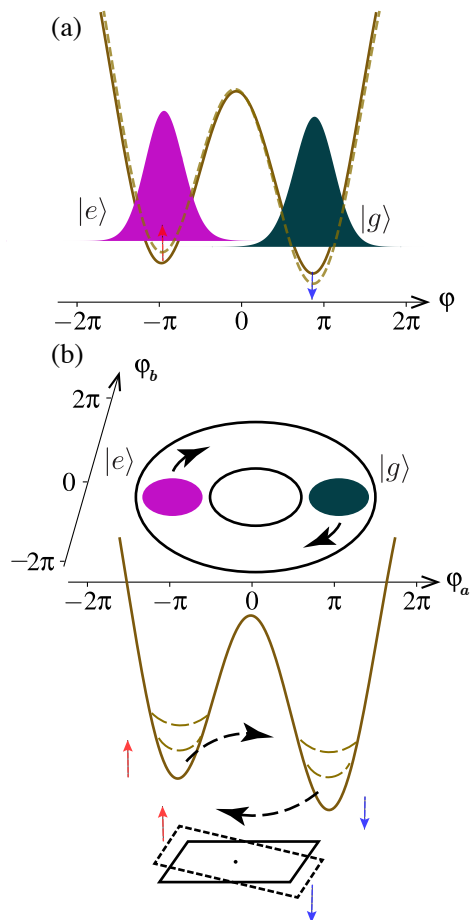


Figure 6.1. A schematic that compares a revolver qubit with a heavy fluxonium. (a) shows the potential of a heavy fluxonium whose flux is biased slightly away from half flux quantum. The wavefunctions of the ground and first excited states are plotted in dark green and pink, respectively. The solid brown curve shows the fluxonium potential, while the dashed one indicates how the potential is shifted by flux noise. (b) sketches the wavefunctions and 2d potential for the proposed revolver qubit. The dark green and pink circles represent the wavefunctions of the ground and the first excited states that are intended to rotate circularly. The 2d potential at one snapshot is plotted in brown. The inset at the bottom shows how the potential landscape is affected by noise. See main text for detailed explanation.

## 6.2. The revolving wavefunctions

We first sketch the basic idea behind a revolver qubit. From an abstract perspective, an ideal revolver qubit is imagined to have two computational wavefunctions that are always disjoint and rotate circularly in a 2d potential plane. In this way, the qubit is certainly protected from depolarization. Meanwhile, the rotation of the wavefunctions may suppress low-frequency noise induced dephasing.

To have a more intuitive picture, it is useful to compare the revolver qubit with a heavy fluxonium qubit. We illustrate this comparison in Fig. 5.1. To start with, the two lowest eigenstates of a heavy fluxonium, whose external flux is parked slightly away from half a flux quantum, have disjoint support [see Fig. 5.1 (a)]. Although the disjoint support of the qubit wavefunctions yields a low depolarization rate, the qubit at this operating point is sensitive to the low-frequency fluctuations in the penetrating flux. To see this, imagine that the noise introduces a small perturbation  $\delta\phi_e$  in the external flux, which distorts the potential (as shown with the black-dashed line in Fig. 6.1) [see fluxonium Hamiltonian in Eq. (3.2)]. To first order in this small perturbation, the energies of the eigenstate on the left and on the right get shifted upward and downward, respectively, due to the change of the depth of the wells. This results in a shift in the energy difference between the two eigenstates (the value is approximated by  $2\pi E_L \delta\phi_e$  to leading order). These random shifts cause strong dephasing of the qubit, especially if the fluctuations have a  $1/f$  type of spectrum.

Rotating wavefunctions circularly, as shown in Fig. 6.1 (b), could suppress the energy shift described above. To see this, consider that the lowest energy states  $|g(t)\rangle$  and  $|e(t)\rangle$  derived using the time-varying Hamiltonian, can move in a circle. In fact, the computational basis should be formed by two of the Floquet states of the periodically modulated system, which will only

be identical to the instantaneous eigenstates if the system evolution is perfectly adiabatic. [as shown in Fig. 6.1 (b)]. In the 2d case, the perturbation introduced by the noise tilts the 2d potential to be lower toward one direction [see the bottom inset of Fig. 6.1 (b)]. Without loss of generality, we assume that the perturbation is proportional to  $\delta\phi_{e,a}\hat{\phi}_a$ . This perturbation term will still shift the energies of the instantaneous eigenstates. However, the averaged energy shift,

$$\delta\Omega_{ge,\text{avg}} \propto \delta\phi_{e,a} \times \frac{1}{T} \int_0^T dt [\langle e(t)|\hat{\phi}_a|e(t)\rangle - \langle g(t)|\hat{\phi}_a|g(t)\rangle],$$

will be zero if the wavefunctions rotate circularly at a constant speed. (Here,  $T$  is the revolving period.) Then, if the revolving period  $T$  is sufficiently short such that  $\delta\phi_{e,a}$  does not vary significantly over one revolving period, the averaged energy shift  $\delta\Omega_{ge,\text{avg}}$  will be approximately zero. In this way, the computational states of the qubit enjoy disjoint support while gaining protection from  $1/f$  noise.

However, the ideal picture where the two wavefunctions rotate circularly is not straightforward to realize with superconducting qubits. In the next section, we will introduce how to use a simple circuit to mimic the strategy described above.

### 6.3. Two heavy fluxonium qubits connected by a tunable coupler

Certainly, we cannot use a single fluxonium to create a two-dimensional potential. A naive way to increase the dimension of the potential is to double the number of the fluxonium qubits. The rotation of the potential wells as shown in Fig. 6.1 (b) requires interaction between the two fluxonium qubits. One can check that, if there is no interaction, we can still tune the fluxonium fluxes such that the deepest well rotates (although not circularly), but the second-deepest well will not “tango” with the deepest one as shown in Fig. 6.1 (b). Therefore, introducing interaction

between the two fluxonium qubits is necessary for realizing a revolver qubit. The interaction should also be tunable and time-dependent, so that the qubit state does not always favor one diagonal over the other during one revolving period.

In Fig. 6.2, we show one exemplar circuit that fulfills the requirements described above, which will be the platform for our following discussion. In this circuit, the two fluxonium qubits are connected by a SQUID, which mediates the interaction between the two qubits. The analysis of this circuit is slightly involved, therefore we relocate it to Section 6.9, and only sketch the derivation here. We first follow the standard circuit quantization technique [166] to derive the full Hamiltonian of this circuit. Following this step, we use the Born-Oppenheimer approximation to adiabatically eliminate the high-energy coupler mode (see Appendix D for details about this approximation). This approximation yields effective interaction between the two fluxonium qubits, and the coupling strength depends on the coupler control fluxes. The final effective Hamiltonian is then given by

$$\hat{H}_{\text{eff}} = \hat{H}_{\text{slow}} + \zeta^+ [\hat{\varphi}_a + \hat{\varphi}_b]^2 + \zeta_1^- (\phi_{J,c}, \phi_{e,c}) [\hat{\varphi}_a - \hat{\varphi}_b] + \zeta_2^- (\phi_{J,c}, \phi_{e,c}) [\hat{\varphi}_a - \hat{\varphi}_b]^2, \quad (6.1)$$

where

$$\hat{H}_{\text{slow}} = \left[ 4E_{C_a} \hat{n}_a^2 + \frac{E_{L_a}}{2} (\hat{\varphi}_a + \phi_{e,a})^2 - 2E_{J_a} \cos\left(\frac{\phi_{J,a}}{2}\right) \cos \hat{\varphi}_a + (a \rightarrow b) \right]. \quad (6.2)$$

Readers can find detailed definitions of all coefficients in Section 6.9. We specifically point out that the coefficients  $\zeta_1^-$  and  $\zeta_2^-$  are controlled by the reduced fluxes  $\phi_{J(e),c} = 2\pi\Phi_{J(e),c}/\Phi_0$ . One important note is that we should design the circuit such that we can tune  $\zeta_2 \equiv \zeta^+ - \zeta_2^-$  to either positive and negative values during a revolving period, to equally favor the two diagonals.

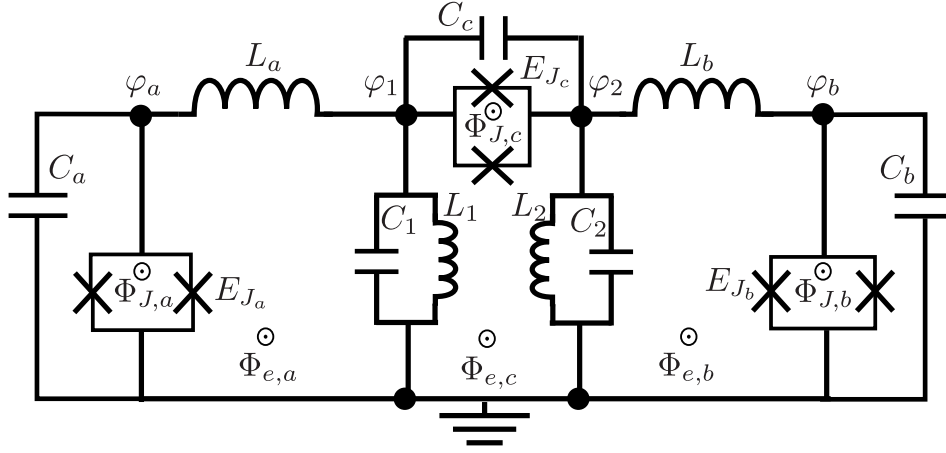


Figure 6.2. Lumped-element circuit diagram of the revolver qubit. This circuit contains two fluxonium qubits which are connected by a coupler SQUID. The symbols shown in the figure are explained as follows. We use  $E_{J_q}$  ( $q = a, b, c$ ) to denote the Josephson energy of each junction in the SQUID that belongs to fluxonium  $a$ ,  $b$  and the coupler  $c$ . Similarly,  $C_q$  ( $q = a, b, c$ ) represents the effective capacitance across the three SQUIDs. The inductance of the four inductors are denoted by  $L_a$ ,  $L_b$ ,  $L_1$  and  $L_2$ . We assume that there are also capacitors that shunt the inductors  $L_1$  and  $L_2$ , whose capacitances are denoted by  $C_1$  and  $C_2$ , respectively. The symbols  $\Phi_{J,q}$  and  $\Phi_{e,q}$  denote the effective control fluxes threading the SQUID loops and the fluxonium/coupler loops.

If so,  $\zeta_2$  should be tunable through zero. In the following, we will fix  $\phi_{e,c}$  to zero such that  $\zeta_1^- = 0$ .

Focusing on the effective Hamiltonian (6.1), in the next section we will discuss one scheme to mimic the revolving potential in Fig. 6.1 (b).

#### 6.4. Control pulses and potential

It is challenging to use the model described by Hamiltonian (6.1) to exactly emulate the circular rotation of the potential wells shown in Fig. 6.1. However, by tuning the barrier height and the mutual coupling strength, we find it possible to let the deepest two wells periodically move along the four sides of a square in the potential plane.

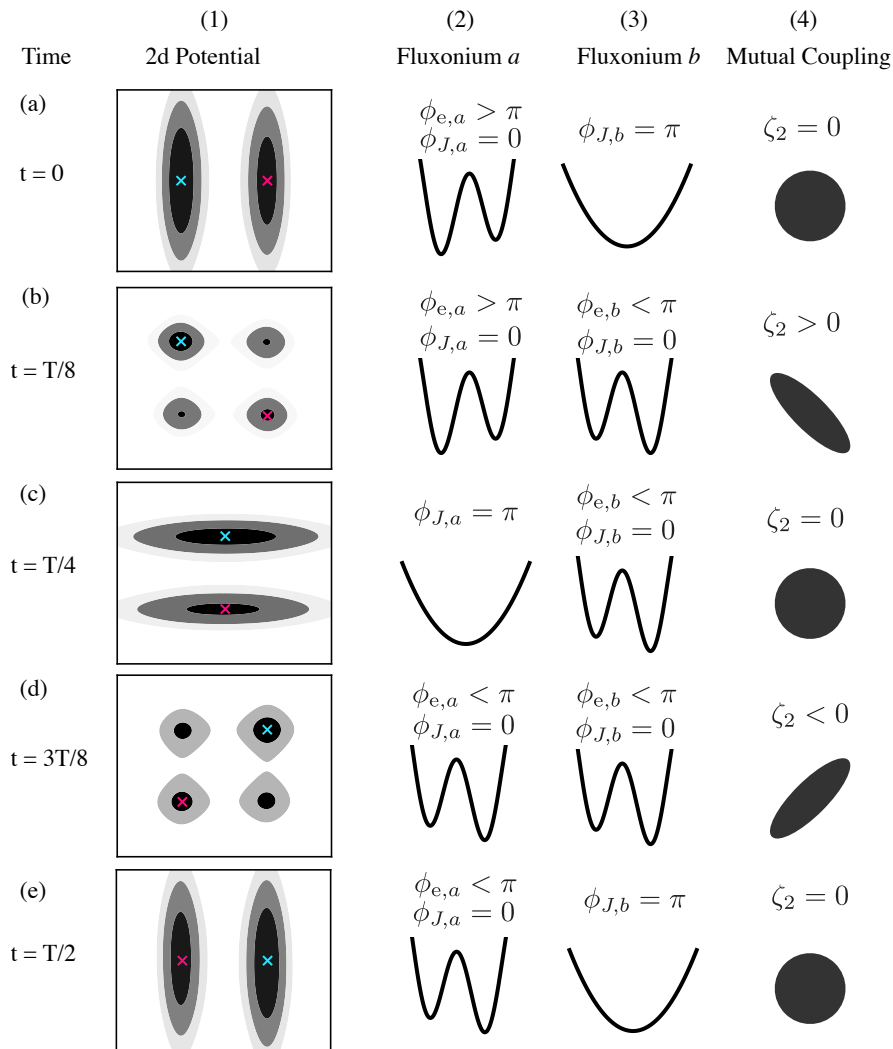


Figure 6.3. Five snapshots (a)-(e) of the time-dependent revolver potential, from the first half of a revolving period. Column (1) shows the two-dimensional potential at different times. The blue and red crosses indicate the locations of the deepest and the second-deepest potential wells, respectively. The columns (2)-(4) demonstrate how to realize the potential structures shown in column (1). The curves shown in (2) and (3) are the corresponding single-fluxonium potentials of the left and right fluxonium qubits, with the choices of  $\phi_{J,a(b)}$  and  $\phi_{e,a(b)}$  given on the side. In column (4), we use ellipses and circles to indicate the sign of the mutual coupling. An ellipse whose long axis is along the “/” or “\” diagonal indicate the direction with lower potential energy, while a circle means zero coupling.

We sketch the scheme we use to realize the trajectory in Fig. 6.3. (We only show half of the revolving period due to constraint of the page size. The second half is easy to infer based on the first half.) Using this figure, we also explain in detail how we tune the control fluxes and how the potential wells travel accordingly during one revolving period.

First, we take a look at the chosen starting point (a). The potential has a two-well structure at this point, which can be realized by tuning  $\phi_{e,b}$  to  $\pi$  while  $\phi_{e,a}$  to 0, such that  $E_{J_b,\text{eff}} = 2E_{J_b} \cos(\phi_{e,b})$  vanishes but  $E_{J_a,\text{eff}}$  takes its maximal value. Also, both  $\phi_{e,a}$  and  $\phi_{e,b}$  are kept close to  $\pi$ . This particular choice of control fluxes yields a degenerate double-well potential. To ensure that there is always one well that is deeper than the others, we intend to let the left well lie slightly lower than the right one, by tuning  $\phi_{e,a}$  slightly away from  $\pi$ . The respective single-fluxonium potential is sketched in the second and third columns of Fig. 6.3. No mutual coupling is needed at this point.

Our next move is to rotate the deepest two wells clockwise to the corners. Toward this goal, we tune  $E_{J_b,\text{eff}}$  as well as the mutual coupling  $\zeta_2$ . During this process, we ramp  $\phi_{J,b}$  from  $\pi$  towards 0, such that at the time  $t = T/8$  ( $T$  is the whole revolving period), there exist four nearly degenerate wells. We need to ensure that the two wells along the “/” diagonal have higher energy. To achieve this, we set  $\zeta_2 > 0$  such that the “\” diagonal is lower than “/” in terms of potential energy. Together with the tuning of  $\zeta_2$ , we also carefully choose the tilting fluxes  $\phi_{e,a}$  and  $\phi_{e,b}$  to ensure that the deepest well has no degeneracy, as shown in the plots in (b,2) and (b,3).

After understanding the first two steps, readers can follow the steps (c)-(e) more easily. To further rotate the deepest wells clockwise, this time we tune  $E_{J_a,\text{eff}}$  to zero, and make the potential energy lower in the upper part of  $\varphi_a$ - $\varphi_b$  plane. We will see the four-well structure

again in (d) and then go back to the double-well landscape in (e). At snapshot (e), the deepest well is on the right, opposite its position shown in (a). This means that the revolver qubit has completed half of the whole revolving period. In the following steps, the deepest well will move in the lower half of the plane and finally come back to its starting point as shown in (a), while the second deepest one will travel in the upper half of the potential plane.

This scheme can roughly mimic the rotation depicted in Fig. 6.1. Up to this point, we have primarily discussed the potential rather than the wavefunctions. The rotating potential wells do not necessarily “drag” the wavefunctions (Floquet states) with them. Therefore, we should further confirm that the computational states, i.e., the Floquet states, do rotate as we wish. In the next section, we will discuss numerical methods to solve for the computational Floquet states.

### 6.5. Methods to calculate the Floquet states

For a periodically driven quantum system, the natural choice of the computational basis should be the Floquet states, since the qubit populations in these states will stay unchanged if no noise or additional control is present. Furthermore, they are important for estimating the dynamical coherence times of the driven qubit, based on our work in Chapter 5. Therefore, solving for the Floquet states of the revolver qubit is an indispensable step for any quantitative study of the revolver qubit’s coherence.

For efficient numerical computation of the Floquet states, it is crucial to choose a proper basis, with which the Hilbert space can be safely truncated to a lower dimension without significantly affecting the accuracy. We find it convenient to use the instantaneous eigenstates to form that basis [167]. The reason is that, since the plasmonic energies of the two fluxonium qubits are designed to have much higher energies than the revolving frequency, the occupation in those

much higher states should be negligible. In this case, the instantaneous eigenstates with much higher energies can be omitted in the calculation.

The details of this calculation are given as follows. We first solve for the instantaneous eigenstates  $|\psi_{\text{ins},j}(t)\rangle$  and eigenenergies  $E_{\text{ins},j}(t)$  of the time-periodic Hamiltonian  $\hat{H}_{\text{eff}}(t)$ . Specifically, they satisfy  $\hat{H}_{\text{eff}}(t)|\psi_{\text{ins},j}(t)\rangle = E_{\text{ins},j}(t)|\psi_{\text{ins},j}(t)\rangle$ . Using them, we perform a rotating-frame transformation, which is defined by

$$\hat{U}_{\text{ins}}(t) = \sum_j |\psi_{\text{ins},j}(t)\rangle \langle \psi_{\text{ins},j}(0)|. \quad (6.3)$$

Note that  $|\psi_{\text{ins}}(t)\rangle$  and  $\hat{U}_{\text{ins}}(t)$  are not uniquely defined, since the phases of states  $|\psi_{\text{ins},j}(t)\rangle$  at different times are arbitrary. For an efficient numerical calculation, we require this unitary to be (a) differentiable in time, and (b) periodic in  $T$ . The second requirement ensures that the period of the Hamiltonian in the new frame stays unchanged, important for finding the proper Floquet states. We are always able to find such a basis if the variation of the Hamiltonian is continuous and if there is no degeneracy in the instantaneous energy spectrum. The unitary that satisfies these requirements, however, is still not unique: a transformation on one allowed  $|\psi_{\text{ins}}(t)\rangle$ ,  $|\psi_{\text{ins},j}(t)\rangle \rightarrow |\psi_{\text{ins},j}(t)\rangle \exp[i\tilde{\chi}_j(t)]$ , yields another unitary that satisfies the aforementioned requirements, where the phase function  $\tilde{\chi}_j(t)$  only needs to be differentiable and periodic. In practice, we should choose a transformation such that the transformed Hamiltonian has the minimal variation in time, which is the most beneficial for numerical simulation.

In one of such frames, the effective Hamiltonian becomes

$$\begin{aligned}
\tilde{H}_{\text{eff}}(t) &= \hat{U}_{\text{ins}}^\dagger(t) \hat{H}_{\text{eff}}(t) \hat{U}_{\text{ins}}(t) + i\dot{\hat{U}}_{\text{ins}}^\dagger(t) \hat{U}_{\text{ins}}(t) \\
&= \sum_j E_{\text{ins},j}(t) |\psi_{\text{ins},j}(0)\rangle \langle \psi_{\text{ins},j}(0)| + i \sum_{jj'} \langle \dot{\psi}_{\text{ins},j}(t) | \psi_{\text{ins},j'}(t) \rangle |\psi_{\text{ins},j}(0)\rangle \langle \psi_{\text{ins},j'}(0)|.
\end{aligned}
\tag{6.4}$$

We can check that  $\tilde{H}_{\text{eff}}(t)$  is indeed periodic since  $\hat{U}_{\text{ins}}(t)$  and  $\dot{\hat{U}}_{\text{ins}}(t)$  share the same periodicity with  $\hat{H}_{\text{eff}}(t)$ . We group the terms in the first sum as the adiabatic Hamiltonian  $\hat{H}_{\text{adiab}}(t)$  and those in the second as the diabatic part  $\hat{H}_{\text{diab}}(t)$ . Obviously, if the revolving frequency is extremely low and  $\hat{H}_{\text{diab}}(t) \rightarrow 0$ , we find that the Floquet states for this Hamiltonian approach the qubit's instantaneous eigenstates.

Based on our previous assumption regarding the fluxonium plasmonic energies, the population in the plasmonic states with high excitation energies should be negligible for a sufficiently low revolving frequency. In this case, we should be allowed to truncate the Hilbert space to a relevant dimension, which makes the calculation of the Floquet states and corresponding quasi-energies efficient.

Before we launch into further details, we want to give the reader a glance at the Floquet states of a revolver qubit calculated using this method, which along with the time-dependent potential are shown in Fig. 6.4. The plots of the Floquet states certainly demonstrate the disjoint support over the whole revolving period. As designed, the two Floquet states move around the four sides of a square. In the following sections, we will discuss quantitatively how the merry-go-round behavior of the Floquet states indeed improves the coherence times.

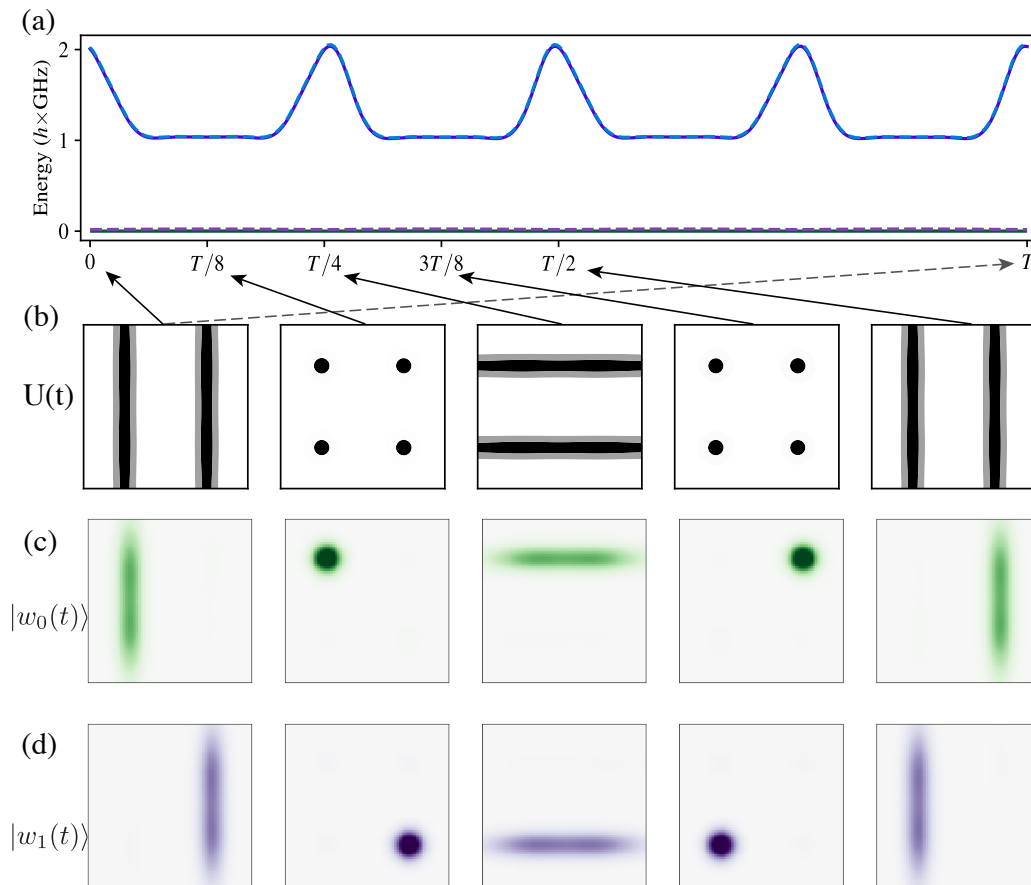


Figure 6.4. Instantaneous eigenenergies, potential landscape and Floquet states of one example revolver qubit. (a) shows the lowest four instantaneous eigenenergies over the revolving period. It is difficult to distinguish between the energies of states in the lowest and second-lowest eigenstate pairs due to the tiny splitting ( $\sim \text{MHz}$ ). (b) shows five snapshots of the potential energy at  $t = 0, T/8, T/4, 3T/8, T/2$ . (c) and (d) present the wavefunctions of the two computational Floquet states in the phase representation, at the aforementioned times.

## 6.6. Noise channels and estimation of coherence times

The first step towards calculating the coherence times is to model the system-noise coupling. In Chapter 1, we mentioned that multiple types of noise sources have been identified as causing

qubit decoherence. Since the revolver qubit we study is still based on the fluxonium qubit, we focus on the noise types that are particularly important for this specific type of qubit [40, 66].

*I/f flux noise.* – Different from a single fluxonium, the revolver circuit shown in Fig. 6.2 has six independent loops. Because of this, we should in principle consider six flux noise sources, which affect the qubit by inducing fluctuations of the external fluxes:  $\phi_{e,q} \rightarrow \phi_{e,q} + \delta\phi_{e,q}$  and  $\phi_{J,q} \rightarrow \phi_{J,q} + \delta\phi_{J,q}$  ( $q = a, b, c$ ). These fluctuations perturb the Hamiltonian (6.1), by adding the sum of the following terms:

$$E_{L_a} \delta\phi_{e,a} \hat{\varphi}_a, \quad E_{L_b} \delta\phi_{e,b} \hat{\varphi}_b, \quad (6.5)$$

$$E_{J_a} \sin[\phi_{J,a}(t)/2] \cos \hat{\varphi}_a \delta\phi_{a,J}, \quad E_{J_b} \sin[\phi_{J,b}(t)/2] \cos \hat{\varphi}_b \delta\phi_{b,J}, \quad (6.6)$$

$$[\partial\zeta_1^- / \partial\phi_{J,c}] \delta\phi_{J,c} (\hat{\varphi}_a - \hat{\varphi}_b), \quad [\partial\zeta_2^- / \partial\phi_{J,c}] \delta\phi_{J,c} (\hat{\varphi}_a - \hat{\varphi}_b)^2, \quad (6.7)$$

$$[\partial\zeta_1^- / \partial\phi_{e,c}] \delta\phi_{e,c} (\hat{\varphi}_a - \hat{\varphi}_b), \quad [\partial\zeta_2^- / \partial\phi_{e,c}] \delta\phi_{e,c} (\hat{\varphi}_a - \hat{\varphi}_b)^2. \quad (6.8)$$

Among these many perturbation terms, we particularly focus on the ones in the first three lines. The last two, which are related to the fluctuations of  $\phi_{e,c}$ , are less important if we always fix  $\phi_{e,c}$  at its sweet spot  $\phi_{e,c} = 0$ . The noise spectra associated with the fluctuations in  $\phi_{e,q}$  and  $\phi_{J,q}$  ( $q = a, b, c$ ) are defined by

$$S_{e_q}(\omega) = \int_{-\infty}^{\infty} dt e^{i\omega t} \langle \delta\phi_{e,q}(t) \phi_{e,q}(0) \rangle$$

and similarly for  $S_{J_q}(\omega)$ .

*Capacitive loss.* – We consider two fluxonium qubits each coupled capacitively to a noise source. The interaction terms describing such coupling are given by  $\hat{n}_a \hat{\eta}_{\text{cap},a}$  and  $\hat{n}_b \hat{\eta}_{\text{cap},b}$ , where the noise spectra associated with the operator  $\hat{\eta}_{\text{cap},a(b)}$  are denoted by  $S_{n_{a(b)}}(\omega)$ . To evaluate

the decoherence rates contributed by the capacitive noise, we need to first calculate the charge operator's matrix elements. We find that these matrix elements can be conveniently obtained using the phase matrix elements. In fact, if the only capacitive energy terms in Eq. (6.1) are  $4E_{C_a}\hat{n}_a^2$  and  $4E_{C_b}\hat{n}_b^2$ , we can relate the charge and phase matrix elements in terms of the Floquet states by the following relation:

$$\begin{aligned}
n_{a(b),jj'}^{\text{F}}(t) &\equiv \langle w_j(t) | \hat{n}_{a(b)} | w_{j'}(t) \rangle \\
&= \frac{1}{8E_{C_{a(b)}}} \langle w_j(t) | [\hat{\varphi}_{a(b)}, \hat{H}_{\text{eff}}(t)] | w_{j'}(t) \rangle \\
&= \frac{1}{8E_{C_{a(b)}}} \langle w_j(t) | \hat{\varphi}_{a(b)} \hat{H}_{\text{eff}}(t) - \hat{H}_{\text{eff}}(t) \hat{\varphi}_{a(b)} | w_{j'}(t) \rangle \\
&= \frac{1}{8E_{C_{a(b)}}} \langle w_j(t) | \hat{\varphi}_{a(b)} \left[ i \frac{\overrightarrow{\partial}}{\partial t} + \epsilon_{j'} \right] - \left[ -i \frac{\overleftarrow{\partial}}{\partial t} + \epsilon_j \right] \hat{\varphi}_{a(b)} | w_{j'}(t) \rangle \\
&= \frac{1}{8E_{C_{a(b)}}} \times \left[ i \frac{\partial}{\partial t} \varphi_{a(b),jj'}^{\text{F}}(t) + (\epsilon_{j'} - \epsilon_j) \varphi_{a(b),jj'}^{\text{F}}(t) \right]. \tag{6.9}
\end{aligned}$$

where we also define  $\varphi_{a(b),jj'}^{\text{F}}(t) \equiv \langle w_j(t) | \hat{\varphi}_{a(b)} | w_{j'}(t) \rangle$ , and  $\omega_d$  denotes the modulation frequency. (Note that the arrows indicate which object that the time derivative acts on.) According to this equation, the Fourier coefficients of  $n_{a(b),jj'}^{\text{F}}(t)$  and  $\varphi_{a(b),jj'}^{\text{F}}(t)$ , denoted by  $n_{a(b),jj',k}^{\text{F}}$  and  $\varphi_{a(b),jj',k}^{\text{F}}$  are related by

$$n_{a(b),jj',k}^{\text{F}} = \frac{1}{8E_{C_{a(b)}}} (k\omega_d + \epsilon_{j'} - \epsilon_j) \varphi_{a(b),jj',k}^{\text{F}}. \tag{6.10}$$

This is reminiscent of Eq. (3.3), which relates the charge and phase matrix elements in terms of the eigenstates of the undriven fluxonium. Eq. (6.10) allows us to calculate the contribution from capacitive noise and flux noise with the same set of phase matrix elements.

Using the noise assumptions we have made above, we are ready to give the expressions of revolver decoherence rates via the Floquet framework discussed in Chapter 5. The dynamical  $\gamma_1$  and  $\gamma_\phi$  contributed by noise channel  $\varsigma$  are

$$\begin{aligned}\gamma_{1,\varsigma} &= \sum_k \sum_{\pm} |g_{\varsigma,k,\pm}|^2 \mathcal{S}_\varsigma(\mp\epsilon_{01} + k\omega_d), \\ \gamma_{\phi,\varsigma} &= \sum_k \frac{1}{2} |2g_{\varsigma,k,\phi}|^2 \mathcal{S}_\varsigma(k\omega_d),\end{aligned}\quad (6.11)$$

where  $g_{\varsigma,k,\pm(\phi)}$  is the Fourier coefficient of the matrix element of the noise operator related to the  $\varsigma$  noise channel ( $\varsigma = e_a, e_b, e_c, J_a, J_b, J_c, n_a, n_b$ ).

The definitions of  $g_{\varsigma,k,\pm(\phi)}$  is very similar to that in Eq. (2.22), except that some of the noise operators are time-dependent. We use the noise channel  $\varsigma = J_a$  as an example. The noise operator associated with the fluctuations  $\delta\phi_{J,a}$  is  $E_{J_a} \sin[\phi_{J,a}(t)/2] \cos(\hat{\varphi}_a)$ . For this noise channel,  $g_{J_a,k,\pm(\phi)}$  is given by

$$\begin{aligned}g_{J_a,k,\pm} &= \frac{\omega_d}{2\pi} \int_0^{2\pi/\omega_d} dt e^{ik\omega_d t} \text{Tr}_q \left[ E_{J_a} \sin[\phi_{J,a}(t)/2] \cos \hat{\varphi}_a \hat{c}_\mp(t) \right], \\ g_{J_a,k,\phi} &= \frac{\omega_d}{4\pi} \int_0^{2\pi/\omega_d} dt e^{ik\omega_d t} \text{Tr}_q \left[ E_{J_a} \sin[\phi_{J,a}(t)/2] \cos \hat{\varphi}_a \hat{c}_\phi(t) \right].\end{aligned}\quad (6.12)$$

The definitions of  $\hat{c}_\pm(t)$  and  $\hat{c}_\phi(t)$  are analogous to Eq. (2.20).

According to Eq. (6.10), we can rewrite the expression of the decoherence rate contributed by the capacitive loss in terms of the phase matrix elements. For convenience, we group the coefficients on the right-hand side of Eq. (6.10) with the noise spectrum  $S_{n_{a(b)}}(\omega)$ , and define

the effective noise spectra

$$S_{n_{a(b)},\varphi}(\omega) = \left( \frac{1}{8E_{C,a(b)}} \right)^2 \omega^2 S_{n_{a(b)}}(\omega). \quad (6.13)$$

This relation will be useful when we analyze the different contributions to the total decoherence rates.

The successful implementation of the revolver qubit requires us to maximally suppress the sum of the decoherence rates contributed by all these noise channels. Particularly, the mitigation of the hazardous  $1/f$  noise is crucial for an enhanced coherence time, considering how this type of noise limits coherence times of a heavy fluxonium. In the next section, we will use the Floquet framework to develop strategies to mitigate this type of noise in the revolver qubit.

### 6.7. Using symmetry to design the revolving pulses for $1/f$ noise cancellation

For a heavy fluxonium, the static sweet spot is extremely narrow, which means that one needs to fine tune the control flux to observe the optimal coherence time. Analogously, the mitigation of low-frequency noise in a revolver qubit requires a careful design of control pulses. In the following, we will demonstrate how two symmetries satisfied by the Hamiltonian and the Floquet states are particularly useful for mitigating  $1/f$  noise, which will guide us in designing the control pulses.

*Mitigating “odd noise”.*— We can characterize the  $1/f$  flux noise channels that the revolver qubit is subject to as “odd” and “even” based on how their noise operators transform under a point-reflection transformation. To describe this transformation, we define a reflection operator  $\hat{P}$ , which satisfies  $\hat{P}|\varphi_a, \varphi_b\rangle = |-\varphi_a, -\varphi_b\rangle$ . [Here,  $|\varphi_a, \varphi_b\rangle$  is the simultaneous eigenstate of  $\hat{\varphi}_a$  and  $\hat{\varphi}_b$ , satisfying  $\hat{\varphi}_{a(b)}|\varphi_a, \varphi_b\rangle = \varphi_{a(b)}|\varphi_a, \varphi_b\rangle$ .] We list a few important relations that  $\hat{P}$

satisfies

$$\hat{P}\hat{P}^\dagger = \hat{\mathbb{1}}, \quad \hat{P}^\dagger \hat{n}_{a,b} \hat{P} = -\hat{n}_{a,b}, \quad \hat{P}^\dagger \hat{\varphi}_{a,b} \hat{P} = -\hat{\varphi}_{a,b}.$$

We call a noise operator  $\hat{O}$  and the noise coupled through it “odd” (“even”) if  $\hat{O}$  satisfies the relation  $\hat{P}^\dagger \hat{O} \hat{P} = (\mp) \hat{O}$ .

We first focus on the “odd” noise, which we can mitigate if we require the Hamiltonian to satisfy one special dynamical symmetry. This symmetry requires  $\hat{P} \hat{H}_{\text{eff}}(t + T/2) \hat{P}^\dagger = \hat{H}_{\text{eff}}(t)$ . If this relation holds, a similar symmetry will be satisfied by the resulting Floquet states, which leads to the suppression of certain noise matrix elements. To see this, we start from writing the Floquet equation,

$$\left[ \hat{H}_{\text{eff}}(t) - i \frac{\partial}{\partial t} \right] |w_j(t)\rangle = \epsilon_j |w_j(t)\rangle. \quad (6.14)$$

This is an eigenvalue equation. For a more convenient description, we define an enlarged Hilbert space, which is the tensor product of (a) the Hilbert space of the qubit and (b) a function space that contains square-integrable functions  $f : [0, T) \rightarrow \mathbb{C}$ , which have periodic boundary conditions. Rigorously, the new Hilbert space is defined by  $\mathcal{F} = \mathcal{H} \otimes L_2(S^1, t)$ , where  $\mathcal{H}$  is the qubit Hilbert space and  $L_2(S^1, t)$  stands for the function space containing square-integrable functions whose domain is a circle  $S^1$  with length  $T$ , and codomain is  $\mathbb{C}$ . To avoid the confusion about objects defined in these two different Hilbert space, we add a bar (“ $\bar{\phantom{x}}$ ”) over the symbols denoting the operators and vectors defined in the enlarged Hilbert space (such as  $|\bar{w}_j\rangle$  and  $\bar{H}$  which will appear below). The basis vectors spanning this enlarged Hilbert space form the set  $\{|\varphi_a, \varphi_b\rangle \otimes |t\rangle | \varphi_a, \varphi_b \in \mathbb{R}, t \in [0, T)\}$ . Here,  $|t\rangle$  is an improper vector defined by  $|t\rangle = \sum_{n \in \mathbb{Z}} e^{int} |n\rangle$ , where  $|n\rangle$  is an element in  $L_2(S^1, t)$  that maps  $t$  to  $e^{-int}/\sqrt{T}$ . The vector  $|t\rangle$

is improper because it is not normalizable (similar to the position and momentum eigenstate of an elementary particle), but this notation is convenient for expressing the Hamiltonian and wavefunctions.

In terms of this new Hilbert space, the Floquet equation (6.14) is equivalent to an eigenvalue problem of the operation <sup>1</sup>

$$\bar{H} = \int_0^T dt \hat{H}_{\text{eff}}(t) \otimes |t\rangle\langle t| - i\mathbb{1}_q \otimes \int_0^T dt \int_0^T dt' \left[ \frac{\partial}{\partial t'} \delta(t' - t) \right] |t\rangle\langle t'|.$$

To discuss the symmetry of the Hamiltonian  $\bar{H}$ , we define two operations in this enlarged Hilbert space,

$$\begin{aligned} \bar{P}|\varphi_a, \varphi_b, t\rangle &= |-\varphi_a, -\varphi_b, t\rangle, \\ \bar{T}|\varphi_a, \varphi_b, t\rangle &= \left| \varphi_a, \varphi_b, t + T/2 \pmod{T} \right\rangle, \end{aligned} \quad (6.15)$$

which correspond to a point-reflection transformation of a wavefunction in the phase representation, and a time displacement, respectively. These linear operations satisfy  $[\bar{P}, \bar{T}] = 0$ ,  $\bar{P}^2 = \bar{P}\bar{P}^\dagger = \mathbb{1}$ ,  $\bar{T}^2 = \bar{T}\bar{T}^\dagger = \mathbb{1}$ . The symmetry that  $\hat{H}_{\text{eff}}(t)$  satisfies is translated into the following relation  $\bar{P}\bar{T}\bar{H}\bar{T}^\dagger\bar{P}^\dagger = \bar{H}$ , or  $[\bar{H}, \bar{P}\bar{T}] = 0$ . Then, if the quasi-energy spectrum is non-degenerate, each Floquet state should be an eigenstate of  $\bar{P}\bar{T}$ . Since  $\bar{P}\bar{T}\bar{P}\bar{T} = \hat{\mathbb{1}}$ , the eigenvalues of  $\bar{P}\bar{T}$  have to be  $\pm 1$ , therefore  $\bar{P}\bar{T}|\bar{w}_j\rangle = \pm|\bar{w}_j\rangle$ . Equivalently, the time-parametrized wavefunctions satisfy  $\hat{P}|w_j(t + T/2)\rangle = \pm|w_j(t)\rangle$ .

<sup>1</sup>The delta function is here defined by  $\delta(t' - t) = \sum_{k \in \mathbb{Z}} e^{-ik\omega_d(t'-t)} / T$ .

Such symmetry ensures the vanishing of  $\int_0^T dt \langle w_j(t) | \hat{O} | w_j(t) \rangle$ , if  $\hat{O}$  is an odd noise operator.

This can be verified as follows

$$\begin{aligned}
\int_0^T dt \langle w_j(t) | \hat{O}(t) | w_j(t) \rangle &= \int_0^{T/2} dt \langle w_j(t) | \hat{O} | w_j(t) \rangle + \int_{T/2}^T dt \langle w_j(t) | \hat{O}(t) | w_j(t) \rangle \\
&= \int_0^{T/2} dt \langle w_j(t) | \hat{P}^\dagger \hat{P} \hat{O} \hat{P}^\dagger \hat{P} | w_j(t) \rangle + \int_{T/2}^T dt \langle w_j(t) | \hat{\phi}_{a,b} | w_j(t) \rangle \\
&= - \int_0^{T/2} dt \langle w_j(t + T/2) | \hat{O} | w_j(t + T/2) \rangle \\
&\quad + \int_{T/2}^T dt \langle w_j(t) | \hat{O} | w_j(t) \rangle = 0.
\end{aligned} \tag{6.16}$$

Examining the definitions in Eq. (6.12), one can verify that the vanishing of this integral yields  $g_{\zeta,0,\phi} = 0$ . Looking back at Eq. (6.11), we find that this further results in the vanishing of the sampling weight at zero frequency in the  $1/f$  noise spectrum.

Therefore, if the Hamiltonian satisfies this dynamical symmetry, the revolver qubit should be insensitive to the low-frequency flux fluctuations described by Eq. (6.5). Fortunately, such a Hamiltonian is relatively straightforward to realize by carefully designing the control pulses. Note that if the noise operator is time-dependent, one can check that this protection scheme still works if the time-dependent noise operator  $\hat{O}(t)$  satisfies  $\hat{P} \hat{O}(t) \hat{P}^\dagger = \hat{O}(t + T/2)$ .

*Mitigating “even noise”.* – The noise operators given in Eq. (6.5)-(6.8) are not all “odd” – for example,  $E_{J_a} \sin[\phi_{J,a}(t)/2] \cos \hat{\phi}_a$  in Eq. (6.6) is an “even” noise operator and is also time-dependent. The mechanism discussed above will fail in mitigating noise coupled to the qubit through such operators.

One can mitigate this type of noise by enforcing another approximate symmetry of the Floquet states. Specifically, we require  $|w_0(t)\rangle \approx e^{i\tilde{\chi}(t)} \hat{P} |w_1(t)\rangle$  [ $\tilde{\chi}(t)$  is an unimportant phase]. More

rigorously, the Floquet states should satisfy  $|\langle w_0(t)|\hat{P}|w_1(t)\rangle| \approx 1$  at any time  $t$ . If this relation holds, we find

$$\begin{aligned}
& \langle w_0(t)|\hat{O}(t)|w_0(t)\rangle - \langle w_1(t)|\hat{O}(t)|w_1(t)\rangle \\
&= \langle w_0(t)|\hat{P}^\dagger\hat{P}\hat{O}(t)\hat{P}^\dagger\hat{P}|w_0(t)\rangle - \langle w_1(t)|\hat{O}(t)|w_1(t)\rangle \\
&= \langle w_0(t)|\hat{P}^\dagger\hat{O}(t)\hat{P}|w_0(t)\rangle - \langle w_1(t)|\hat{O}(t)|w_1(t)\rangle \approx 0.
\end{aligned} \tag{6.17}$$

As a result, the integral of the first line in this equation over one revolving period is also close to zero, which further yields  $g_{\zeta,0,\phi} \approx 0$ .

Our device, which is based on two heavy fluxonium qubits, can be used to conveniently realize such an approximate symmetry among Floquet states. If we choose the circuit parameters and control pulses such that the two lowest and almost degenerate potential wells are only slightly different in their depth, the lowest two instantaneous eigenstates will satisfy  $|e(t)\rangle \approx \hat{P}|g(t)\rangle$  [see Fig. 6.1 (a) for the wavefunctions of a heavy fluxonium]. According to the discussion surrounding Eq. (6.4), the Floquet states approach the instantaneous eigenstates if we modulate the fluxes at a sufficiently low revolving frequency. If so,  $|w_0(t)\rangle$  and  $|w_1(t)\rangle$  will also satisfy a similar symmetry as long as we keep the state evolution mostly adiabatic. We can see the point-reflection symmetry between  $|w_0(t)\rangle$  and  $|w_1(t)\rangle$  clearly in Fig. 6.4 (c) and (d).

In the next section, we will present results of the coherence times for the revolver qubit, whose circuit parameters and control pulses are designed according to the findings discussed above.

## 6.8. Coherence times

The findings discussed in the last section give us useful instructions on designing the revolver qubit and the control pulses. After some trials, we find several successful schemes which yield favorable coherence times. Here, we will only present the results of one example to showcase the competitive coherence times in a revolver qubit. The detailed control pulses and circuit parameters can be found in the Section 6.9.

The depolarization and pure-dephasing times of the revolver qubit are plotted in Fig. 6.5 (a) and (b), as a function of the revolving frequency. We observe that the dynamical  $T_1$ 's of this qubit at different frequencies are mostly of the order of 1 second, thanks to the disjoint support between the two Floquet states. Different from the situation for a heavy fluxonium, the revolver qubit maintains a favorable  $T_\phi$ , which is of the order of 1 millisecond, due to the operation at dynamical sweet spots. In Fig. 6.5 (a) and (b), we use red stars to mark an example working point, where the qubit is predicted to have 812 ms  $T_1$  and 1.08 ms  $T_\phi$ . In both (a) and (b), we observe peculiar dips and spikes, which we believe are given by stray resonances between the modulation tones and transitions from the lowest two instantaneous eigenstates to higher ones. If we disregard the strange dips and spikes, we find that the pure-dephasing time appears to saturate for  $\omega_d/2\pi \gtrsim 50$  MHz.

We turn to Fig. 6.5 (b) and (c) to better understand such saturation. In (b), we plot the inverse of the pure-dephasing rates contributed by the fluctuation of  $\delta\phi_{e_{a(b)}}$  and the dielectric noise that is capacitively coupled to the qubit in brown and purple, respectively. These are the two noise channels that we find contribute the most to the pure dephasing of the qubit. For higher  $\omega_d$ , although  $1/f$  flux noise contributes less to pure dephasing, the capacitive noise contributes more. The opposite trends of these two curves can be explained using the ‘‘lollipop’’ plot [see

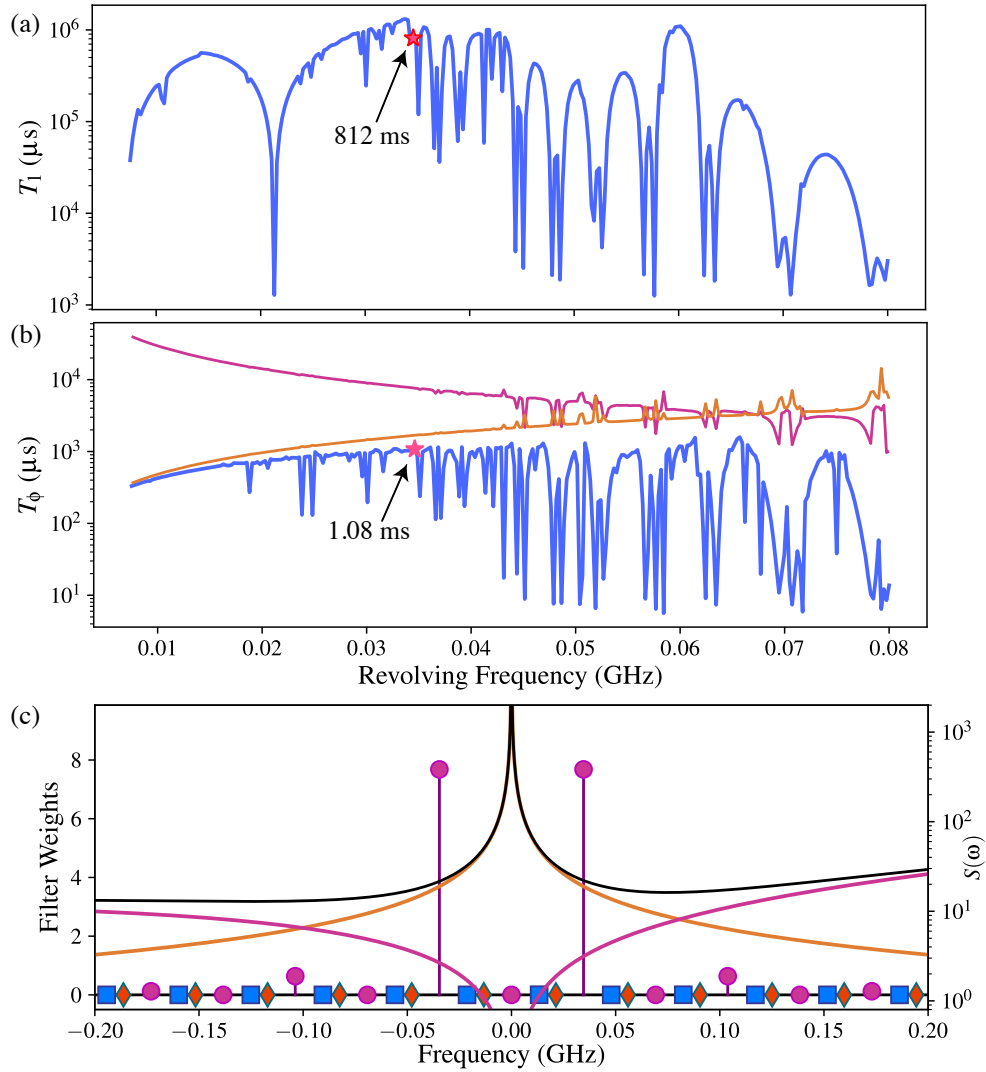


Figure 6.5. Coherence times of a revolver qubit as a function of the revolving frequency. (a) and (b) show the depolarization and pure-dephasing times of the revolver qubit, respectively. In both (a) and (b), the red star marks the position of an example working point. (b) also plots the inverse of the decoherence rates contributed by the low-frequency fluctuations of  $\phi_{e,a(b)}$  and dielectric noise sources that are coupled through the operator  $\hat{n}_{a(b)}$ , in brown and purple, respectively. In (c), the magnitudes of the filter weights related to  $\zeta = e_a$  and  $n_a$  are centered at the corresponding filter frequencies. We also plot the noise spectrum of the capacitive loss (purple coloring),  $S_{n_a, \phi}(\omega)$  and the  $1/f$  flux noise (brown coloring),  $S_{e_a}(\omega)$ . We make similar assumptions about the noise magnitudes as stated in the caption of Fig. 5.1.

Fig. 5.4 for a similar plot]. We show one such plot in Fig. 6.5 (c) which corresponds to the example working point marked by the red stars in (a) and (b). To focus on the most important noise sources, we only show the filter weights related to the low-frequency fluctuations of  $\phi_{e,a}$  and the capacitive loss coupled through  $\hat{n}_a$ . (The contributions from the noise sources affecting the “ $b$ ” mode are identical to those for “ $a$ ”, if we assume a symmetric circuit.) The relation we have derived in Eq. (6.10) allows us to conveniently use the phase matrix elements to evaluate the contributions from capacitive noise. On top of them, we show the noise spectra  $S_{e_a}(\omega)$  and  $S_{n_a,\phi}(\omega)$  [defined in Eq. (6.13)].

We observe that, the weights related to depolarization are negligible, due to the disjoint support between the two Floquet states. The largest filter weights instead belong to pure dephasing, and the corresponding sampling frequencies are the revolving frequencies  $\pm\omega_d$ . Since the noise spectrum of the  $1/f$  noise decays rapidly with an increasing sampling frequency, the qubit is indeed less sensitive to  $1/f$  noise if we revolve the Floquet states sufficiently fast. This is reminiscent of the effect of dynamical decoupling. Different from the case of  $1/f$  flux noise, the noise power describing capacitive noise becomes stronger at a higher frequency. Therefore, increasing  $\omega_d$  makes the qubit on one hand less sensitive to the  $1/f$  flux noise, on the other hand more susceptible to the capacitive noise. The opposite trends of the contributions from  $1/f$  flux noises and dielectric loss finally yield the saturation of the pure-dephasing times. To see this, we also plot the sum noise power spectrum by a solid black curve in Fig. 6.5 (c). As one can observe, the rapid decrease of the noise power is replaced by a slow increase when the sampling frequency exceeds  $\sim 50$  MHz. Because of this behavior of the sum noise power,  $T_\phi$  as a function of  $\omega_d$  has a maximal value around  $\omega_d \approx 50$  MHz.

To conclude the main discussion of this chapter, we predict by one example that the revolver qubit can have extremely long  $T_1$  together with also excellent  $T_\phi$ . However, we have not yet found an example that predicts a much longer coherence time than that of the state-of-the-art fluxonium qubit [15]. We point out that there is still plenty of space for further improvement of the coherence times. The technique of quantum optimal control [168] could help in this direction. With this technique, we can optimize the control pulses such that the resulting filter functions can give the qubit minimal decoherence rate given the noise spectra. Furthermore, the special combination of second-level  $T_1$  and millisecond-level  $T_\phi$  is rarely seen in the research field of superconducting circuit. This combination makes the revolver qubit especially interesting as a candidate for the biased-noise qubit [169, 170]. Specifically, the dephasing errors in such qubits dominates over all the other types of errors. The situation of biased noise could be advantageous (as compared to unbiased noise) in the context of implementing quantum error correction.

### 6.9. Circuit quantization

The Lagrangian of this circuit, whose generalized coordinates are the combination of node fluxes:  $\varphi_a, \varphi_b, \varphi_+ \equiv (\varphi_1 + \varphi_2)/2, \varphi_- \equiv \varphi_2 - \varphi_1$ , is given by

$$\begin{aligned}
\mathcal{L} = & \frac{C_a}{2} \left( \frac{\Phi_0}{2\pi} \right)^2 \dot{\varphi}_a^2 + \frac{C_b}{2} \left( \frac{\Phi_0}{2\pi} \right)^2 \dot{\varphi}_b^2 + \frac{C_c}{2} \left( \frac{\Phi_0}{2\pi} \right)^2 \dot{\varphi}_-^2 \\
& - \left( \frac{\Phi_0}{2\pi} \right)^2 \left[ \frac{(\varphi_a - \varphi_+ + \varphi_-/2)^2}{2L_a} + \frac{(\varphi_b - \varphi_+ - \varphi_-/2)^2}{2L_b} \right] \\
& + \frac{1}{2} \left( \frac{\Phi_0}{2\pi} \right)^2 [C_1(\dot{\varphi}_+ - \dot{\varphi}_-/2)^2 + C_2(\dot{\varphi}_+ + \dot{\varphi}_-/2)^2] \\
& - \left( \frac{\Phi_0}{2\pi} \right)^2 \frac{(\varphi_+ + \varphi_-/2)^2}{2L_1} - \left( \frac{\Phi_0}{2\pi} \right)^2 \frac{(\varphi_+ - \varphi_-/2)^2}{2L_2} \\
& + 2E_{J_a} \cos(\phi_{J,a}/2) \cos(\varphi_a - \phi_{e,a}) + 2E_{J_b} \cos(\phi_{J,a}/2) \cos(\varphi_b - \phi_{e,b}) \\
& + 2E_{J_c} \cos(\phi_{J,c}/2) \cos(\varphi_- + \phi_{e,c}).
\end{aligned} \tag{6.18}$$

A Legendre transformation and the following quantization give us the Hamiltonian

$$\begin{aligned}
\hat{H}_{\text{full}} = & \left[ 4E_{C_a} \hat{n}_a^2 + \frac{E_{L_a}}{2} (\hat{\varphi}_a + \phi_{e,a})^2 - 2E_{J_a} \cos\left(\frac{\phi_{J,a}}{2}\right) \cos(\hat{\varphi}_a - \phi_{e,a}) + (a \rightarrow b) \right] \\
& + 4E_{C_+} \hat{n}_+^2 + 4E_{C_-} \hat{n}_-^2 + \frac{E_L}{2} \left( \hat{\varphi}_+^2 + \frac{\hat{\varphi}_-^2}{4} \right) - 2E_{J_c} \cos\left(\frac{\phi_{J,c}}{2}\right) \cos(\hat{\varphi}_- + \phi_{e,c}) \\
& - E_{L_a} \hat{\varphi}_a (\hat{\varphi}_+ + \hat{\varphi}_-/2) - E_{L_b} \hat{\varphi}_b (\hat{\varphi}_+ - \hat{\varphi}_-/2),
\end{aligned} \tag{6.19}$$

where  $\hat{\varphi}_q$  and  $\hat{n}_q$  denote the promoted phase and charge operators. They satisfy  $[\hat{\varphi}_q, \hat{n}_{q'}] = \delta_{qq'}$  ( $q, q' = a, b, c$ ). Above, we have assumed symmetric parameters for a simpler treatment, i.e.,  $C_1 = C_2, C_a = C_b, L_1 = L_2, L_a = L_b$ , and  $E_{J_a} = E_{J_b}$ . The coefficients denote the effective

capacitive and inductive energies

$$E_{C_{a(b)}} = \frac{e^2}{2C_{a(b)}}, \quad E_{C_-} = \frac{e^2}{2C_J + C_1/2 + C_2/2}, \quad E_{C_+} = \frac{e^2}{2C_1 + 2C_2},$$

$$E_{L_{a(b)}} = \left(\frac{\Phi_0}{2\pi}\right)^2 \frac{1}{L_{a(b)}}, \quad E_L = \left(\frac{\Phi_0}{2\pi}\right)^2 \left(\frac{1}{L_a} + \frac{1}{L_1} + \frac{1}{L_b} + \frac{1}{L_2}\right), \quad E_{L_{a(b)}} = \left(\frac{\Phi_0}{2\pi}\right)^2 \frac{1}{L_{a(b)}}.$$

The quantum system governed by Hamiltonian (6.19) is described by four degrees of freedom. Meanwhile, the revolver qubit we have in mind only has two modes. We intend to make the remaining two have much higher excitation energy and only mediate the interaction between the former pair. In this situation, we can reduce the full model to a simpler one by proper approximations. One crucial tool useful for this derivation is the Born-Oppenheimer approximation. More discussion of this type of approximation can be found in Appendix D. Here, we will list the important steps.

STEP 1: Separating the low-energy and high-energy modes. The  $\varphi_+$  and  $\varphi_-$  modes are designed to have much higher excitation energies compared with those of  $\varphi_a$  and  $\varphi_b$ . We refer to the former pair as the high-energy modes and the latter pair as the low-energy ones. The first step is to separate the Hamiltonian into the high-energy and low-energy parts, where the former is given by

$$\begin{aligned} \hat{H}_{\text{high}} = & 4E_{C_+}\hat{n}_+^2 + 4E_{C_-}\hat{n}_-^2 + \frac{E_L}{2} \left( \hat{\varphi}_+^2 + \frac{\hat{\varphi}_-^2}{4} \right) - E_{J_c} \cos\left(\frac{\phi_{J,c}}{2}\right) \cos(\hat{\varphi}_- + \phi_{e,c}) \\ & - E_{L_{\text{coup}}}(\varphi_a + \varphi_b)\hat{\varphi}_+ - \frac{1}{2}E_{L_{\text{coup}}}(\varphi_a - \varphi_b)\hat{\varphi}_-. \end{aligned} \quad (6.20)$$

Above, we use  $E_{L_{\text{coup}}}$  to replace  $E_{L_a}$  and  $E_{L_b}$  for convenience, since they have the equal value under the assumption of symmetric parameters. The remaining terms in Eq. (6.19) are grouped into  $\hat{H}_{\text{low}}$ .

STEP 2: Calculating the ground state energy of the high-energy modes. In the spirit of Born-Oppenheimer approximation, we treat the quantum operators of the low-energy modes,  $\hat{\varphi}_a$  and  $\hat{\varphi}_b$ , as classical variables in Eq. (6.20). The shift of the resulting eigenenergy of the ground state due to the variation of  $\varphi_a$  and  $\varphi_b$  will be added as a perturbation to the low-energy modes' Hamiltonian in the next step.

We choose the eigenenergies of the low-energy modes with  $\varphi_a = 0$  and  $\varphi_b = 0$  as an offset. The shift of the ground-state energy of the “+” mode, induced by nonzero  $\varphi_a$  and  $\varphi_b$ , is

$$\Delta E_{g,+}(\varphi_a, \varphi_b) = -\frac{E_{L\text{coup}}^2}{2E_L}(\varphi_a + \varphi_b)^2. \quad (6.21)$$

The calculation of the energy shift to the “-” mode is more complicated, since this degree of freedom is no longer harmonic. In fact, its Hamiltonian is identical to that of a fluxonium. If we design  $E_{L\text{coup}}$  to be much smaller than the excitation energies of the “-” mode, we can treat the term  $E_{L\text{coup}}(\varphi_a - \varphi_b)\hat{\varphi}_-$  perturbatively. The first and second-order corrections are given by

$$\Delta E_{g,-}^{(1)}(\varphi_a, \varphi_b) = -\frac{1}{2}E_{L\text{coup}}(\varphi_a - \varphi_b)\langle\psi_0^-|\hat{\varphi}_-|\psi_0^-\rangle, \quad (6.22)$$

$$\Delta E_{g,-}^{(2)}(\varphi_a, \varphi_b) = -\frac{1}{4}E_{L\text{coup}}^2(\varphi_a - \varphi_b)^2 \sum_{m \neq 0} \frac{|\langle\psi_0^-|\hat{\varphi}_-|\psi_m^-\rangle|^2}{E_m^- - E_0^-}. \quad (6.23)$$

Above, we use  $|\psi_m^-\rangle$  and  $E_m^-$  to denote the  $m$ th eigenstate and corresponding eigenenergy of the “-” mode, which are derived with both  $\varphi_a = \varphi_b = 0$ . For the convenience of the following discussion, we denote the coefficients associated with  $(\varphi_a - \varphi_b)$  and  $(\varphi_a - \varphi_b)^2$  as  $\zeta_1$  and  $\zeta_2$ , respectively. Obviously, these coefficients are mediated by the control flux  $\phi_{J,c}$  and  $\phi_{e,c}$ .

STEP 3: Deriving the effective Hamiltonian for the low-energy modes. The final step of this approximation is to add the shifted energy to the Hamiltonian, meanwhile recovering the

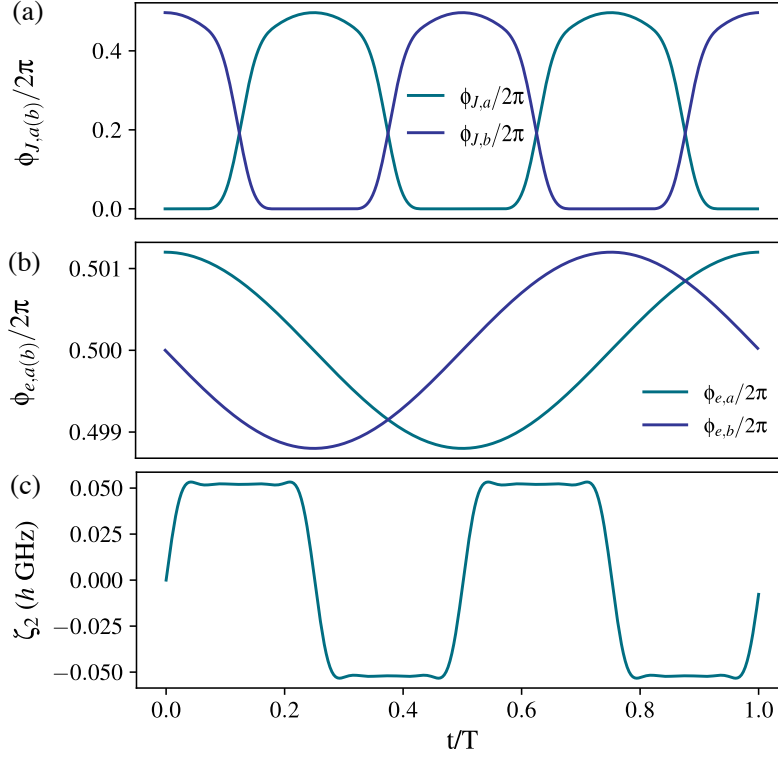


Figure 6.6. The time-dependent control fluxes and mutual coupling strength used in the simulation in Fig. 6.4 and 6.5.

quantum operators  $\hat{\varphi}_a$  and  $\hat{\varphi}_b$  from classical variables. After this step, we finally arrive at the effective Hamiltonian in Eq. (6.1).

Finally, we list the circuit parameters used for all the simulations shown above. The control

Table 6.1. Circuit parameters used for the simulation in this chapter.

Parameters	Energy
$E_{C_a}, E_{C_b}/2\pi$	4.3 GHz
$E_{L_a}, E_{L_b}/2\pi$	0.36 GHz
$E_{J_a}, E_{J_b}/2\pi$	$1.0 \times 10^2$ GHz
$E_{J_c}/2\pi$	5.0 GHz
$E_{C_-}/2\pi$	9.0 GHz
$E_L/2\pi$	1.4 GHz

pulses and engineered time-dependent mutual coupling are shown in Fig. 6.6.

## CHAPTER 7

### **Outlook**

In the late 20th century, quantum computation was more like a dream to scientists. Some even described quantum computing “a nightmare” for experimentalists, due to concerns about strong decoherence [171]. After decades of continuous efforts, these concerns have been partially addressed by significant improvements of coherence times in several quantum platforms. One of these is the superconducting-circuit platform [172].

The impressive progress in recent years toward building full-fledged quantum computers has brought our dream one step closer to reality. It has ignited the popularity of quantum computation not only among scientists, but also the public. However, despite all the hype created by the media about how powerful quantum computers can be and how close their arrival might be, we need to recognize that current quantum machines still cannot outperform widely-available classical computers in *useful* tasks. (Although some research has claimed quantum supremacy over classical computers [12, 111], it is still debatable whether the algorithm implemented in these experiments is useful.)

To fully realize the dream of quantum computing, experimentalists and theorists are still working hard to improve the performance of qubits. Specifically, researchers have invested tremendous efforts into improving materials, circuit designs and control protocols to enhance the control fidelities for superconducting qubits, as summarized in Chapter 1. In this thesis, we have introduced our own efforts which have been focused on designing state-preparation protocols, protecting qubits from low-frequency noise, and designing a noise-protected qubit.

Obviously, much more endeavors are still required. To contribute to this field more efficiently, it is necessary for us to look for directions that can further push the research frontier. Aside from popular topics already under intensive exploration, here are several directions we believe to be useful for advancing quantum information technologies with superconducting qubits: (a) Understanding how defects interact with the qubit modes from a more microscopic perspective, and how to adjust circuit designs, materials, and control protocols accordingly. (b) Exploring circuit architectures that can reduce the energy participation in the substrate and uncontrolled surfaces, such that dielectric loss can be mitigated. (c) Exploring junction types other than S-I-S junctions or, more broadly, seeking alternative high-coherence circuit elements that could provide the necessary nonlinearity.

Apart from quantum computation, quantum technologies may eventually help us solve other long-standing problems (such as the detection of dark matter, potentially). It will be exciting to witness the revolution that quantum machines will enable, both in our everyday life and in science. We hope that the work discussed in this thesis contributes to the development of future quantum technologies. We will conclude by one quote from John Heywood to encourage future exploration: *“Nothing is impossible to a willing heart.”*

## APPENDIX A

**Rotating-Wave Approximation**

The rotating-wave approximation (RWA) is an important tool for simplifying equations governing the evolution of closed or open quantum systems. We can find its applications in many places in quantum physics. In Chapter 2, we see that this approximation plays an essential role in deriving the Lindblad master equation. In this appendix, we will justify this approximation by deriving the error bound. We will start from the discussion of probably the simplest example, the Rabi oscillation, to give a concrete example where RWA is applied. Then, we will move to a more abstract level to justify it in a general first-order ordinary differential equation (ODE).

**A.1. RWA and Rabi oscillations**

The driven two-level system is a precious analytically-solvable model in quantum mechanics. When a two-level system is weakly driven by a single-tone drive, the population in both eigenstates goes through periodic oscillations. This phenomenon is described as the *Rabi oscillation*. RWA is essential for explaining such behaviors analytically, which allows us to neglect certain terms in the Schrödinger equation that are regarded as “fast-rotating”. We use this as an example to demonstrate how RWA is applied.

The weakly driven two-level system is governed by the Hamiltonian  $\hat{H}(t) = \hat{H}_0 + \hat{H}_d(t)$ , where

$$\begin{aligned}\hat{H}_0 &= \frac{\omega_q}{2} \hat{\sigma}_z, \\ \hat{H}_d(t) &= d_R \hat{\sigma}_x \cos \omega_d t,\end{aligned}\tag{A.1}$$

where  $\omega_q$  is the bare qubit transition frequency,  $d_R$  and  $\omega_d$  denote the drive strength and frequency respectively. We set the drive frequency on resonance with the qubit transition frequency, i.e.,  $\omega_d = \omega_q$ . We choose to solve the state-evolution of this quantum system in the interaction picture, using the von Neumann equation. The density operator in the interaction picture is defined as  $\tilde{\rho}(t) \equiv \hat{U}_0^\dagger(t) \rho(t) \hat{U}_0(t)$ , where  $\rho(t)$  is the density operator in the Schrödinger picture, and  $\hat{U}_0(t)$  is the propagator defined by  $\hat{U}_0(t) = \exp(-i\hat{H}_0 t)$ . Then  $\tilde{\rho}(t)$  satisfies the equation

$$\frac{d\tilde{\rho}(t)}{dt} = i[\tilde{H}_d(t), \tilde{\rho}(t)],\tag{A.2}$$

where,

$$\begin{aligned}\tilde{H}_d(t) &= U_0^\dagger(t) \hat{H}_d(t) \hat{U}_0(t) \\ &= \frac{d_R}{2} (\sigma^+ + \sigma^-) + \frac{d_R}{2} (\sigma^+ e^{2i\omega_q t} + \sigma^- e^{-2i\omega_q t}).\end{aligned}\tag{A.3}$$

Therefore,

$$\frac{d\tilde{\rho}(t)}{dt} = i \left[ \frac{d_R}{2} (\sigma^+ + \sigma^-), \tilde{\rho}(t) \right] + i \left[ \frac{d_R}{2} (\sigma^+ e^{2i\omega_q t} + \sigma^- e^{-2i\omega_q t}), \tilde{\rho}(t) \right].\tag{A.4}$$

The terms in the second square bracket on the right-hand side are regarded as fast-rotating terms, usually under the condition  $d_R \ll 2\omega_q$ . We will provide a rigorous justification on why this works in the next section. Here we provide an intuitive explanation of such a treatment: if the characteristic timescale of the variation of  $\tilde{\rho}(t)$  is much longer than the period  $2\pi/(2\omega_q)$ , the time-integration of the second term will be “averaged out” by the oscillatory coefficients  $\exp(\pm 2i\omega_q t)$ , which should only slightly contribute to the solution of  $\tilde{\rho}(t)$ . Based on Eq. (A.4), that timescale should be at the order of  $d_R^{-1}$ , hence the condition mentioned above. The justification of RWA discussed in the next section closely follows this line of thought.

After we neglect the second term in Eq. (A.4), the problem reduces to a constant-coefficient first-order ODE. It is straightforward to derive the equation for  $\rho_{00} - \rho_{11}$  using the simplified von Neumann equation, which is given by

$$\frac{d^2[\tilde{\rho}_{00}(t) - \tilde{\rho}_{11}(t)]}{dt^2} = -d_R^2[\tilde{\rho}_{00}(t) - \tilde{\rho}_{11}(t)]. \quad (\text{A.5})$$

Solving this equation yields the sinusoidal population oscillation of the qubit. The period of the Rabi cycle is thus given by  $2\pi/d_R$ . Numerical simulations have found excellent agreement between the solution obtained by the full model and that using Eq. (A.5).

## A.2. RWA in first-order ODEs

The problem of Rabi oscillations is not the only example where RWA is applied. Other examples include the derivation and simplification of Lindblad master equation [86]. In all these examples, we actually deal with first-order linear ODEs, where oscillatory terms that are regarded as fast-rotating are neglected to simplify the equation. For example, the von Neumann and Lindblad master equations can be converted to this form through a “vectorization” procedure.

For example, the density operator  $\rho(t)$  is converted to  $\vec{f} = [\rho_{00}, \rho_{01}, \rho_{10}, \rho_{11}]^T$  for a two-level system.

In general, we can formulate the full equations that describe these problems as

$$\frac{d\vec{f}(t)}{dt} = \sum_{\omega} e^{-i\omega t} \underline{V}_{\omega} \vec{f}(t), \quad (\text{A.6})$$

where  $\vec{f}$  is a  $n$ -dimensional vector, and  $\underline{V}_{\omega}$  denotes a time-independent  $n \times n$  matrix. Each  $\underline{V}_{\omega}$  is associated with an oscillatory coefficient  $e^{-i\omega t}$ . We impose another condition for Eq. (A.6) that is essential for the following derivation: for all relevant time  $t$ , the norm of Eq. (A.6) vector  $\vec{f}(t)$  is bounded, namely, there exists a positive value  $B$  that bounds vector  $\vec{f}(t)$  by the relation  $B > \|\vec{f}(t)\|$  for any relevant  $t$ . In general, it is not straightforward to derive what requirement  $\underline{V}_{\omega}$  should satisfy to ensure this condition. However, if the equation is used to describe the evolution of a density matrix under the equation which has the Lindblad form, we know that the norm of the vectorized density matrix is guaranteed to be bounded by 1. (Note that the von Neumann equation is a special case of the Lindblad master equation – the latter reduces to the former if we set the dissipation rates to zero.)

It is important to note that, if  $\vec{f}$  is bounded, then  $\underline{V}_{\omega} \vec{f}$  is also bounded according to the relation  $\|\underline{V}_{\omega} \vec{f}\| \leq \|\underline{V}_{\omega}\| \|\vec{f}\|$ . Here, the matrix norm is chosen to be the vector-induced norm with  $p = 2$ . In fact, this norm is identical to the largest singular value of  $\underline{V}_{\omega}$ , which we denote by  $S_{\omega}$ . Based on this fact, we can further prove that: If  $\underline{V}_{\omega} \vec{f}$  is bounded, then  $\|\vec{f}(t_2) - \vec{f}(t_1)\|/|t_2 - t_1|$  is bounded. As hinted in the last section, it is essential to find the characteristic timescale of the variation of the quantity  $\vec{f}(t)$ . For this goal, we evaluate  $\|\vec{f}(t_2) - \vec{f}(t_1)\|$ , which we find is

bounded by the relation

$$\|\vec{f}(t_2) - \vec{f}(t_1)\| = \left\| \int_{t_1}^{t_2} dt' \sum_{\omega} e^{-i\omega t'} \underline{V}_{\omega} \vec{f}(t') \right\| \leq \sum_{\omega} S_{\omega} B(t_2 - t_1) = DB(t_2 - t_1). \quad (\text{A.7})$$

Here we define  $D \equiv \sum_{\omega} S_{\omega}$ , which can be understood as the effective drive strength on the quantum or classical system. The variation timescale of  $\vec{f}(t)$  is lower-bounded by  $D^{-1}$ , since at  $\Delta t = t_2 - t_1 = D^{-1}$ , the variation of  $\vec{f}(t)$  is at most  $B$ .

Finally, using these two facts, we evaluate the error caused by RWA. As we have mentioned in the last section, if the oscillatory period of one term is much shorter than the variation timescale, the contribution of this term to  $\vec{f}(t) - \vec{f}(0)$  will be small. For example, we assume that there is one term on the right-hand side of Eq. (A.6) that is associated with a frequency  $|\omega^R| \gg D$ . We are tempted to throw that term away, but how different will  $\vec{f}(t)$  be if this term is neglected? We denote the solution of  $\vec{f}$  without that term as  $\vec{f}_{\text{RWA}}(t)$ . For convenience, we estimate the quantity  $\|\vec{f}(t) - \vec{f}_{\text{RWA}}(t)\|$  at  $t = NT$  with  $N \gg 1$  ( $T \equiv 2\pi/\omega^R$ ). The bound of this error is estimated by

$$\begin{aligned} \|\vec{f}(t) - \vec{f}_{\text{RWA}}(t)\| &= \left\| \int_0^t dt' e^{-i\omega^R t'} \underline{V}_{\omega^R} \vec{f}(t') \right\| \\ &\leq \sum_{j=0}^{N-1} \left\| \int_{jT}^{(j+1)T} dt' e^{-i\omega^R t'} \underline{V}_{\omega^R} \vec{f}(t') \right\| \\ &= \sum_{j=0}^{N-1} \left\| \int_{jT}^{(j+1)T} dt' e^{-i\omega^R t'} \underline{V}_{\omega^R} [\vec{f}(jT) + \vec{f}(t') - \vec{f}(jT)] \right\|. \end{aligned} \quad (\text{A.8})$$

Using the relation

$$\int_{jT}^{(j+1)T} dt' e^{-i\omega^R t'} \underline{V}_{\omega^R} \vec{f}(jT) = \underline{0}, \quad (\text{A.9})$$

we further show

$$\begin{aligned}
\|\vec{f}(t) - \vec{f}_{\text{RWA}}(t)\| &= \sum_{j=0}^{N-1} \left\| \int_{jT}^{(j+1)T} dt' e^{-i\omega^R t'} \underline{V}_{\omega^R} [\vec{f}(t') - \vec{f}(jT)] \right\| \\
&\leq \sum_{j=0}^{N-1} \int_{jT}^{(j+1)T} dt' \left\| \underline{V}_{\omega^R} [\vec{f}(t') - \vec{f}(jT)] \right\| \\
&\leq \sum_{j=0}^{N-1} \int_{jT}^{(j+1)T} dt' S_{\omega^R} \left\| [\vec{f}(t') - \vec{f}(jT)] \right\| \\
&\leq \sum_{j=0}^{N-1} \int_{jT}^{(j+1)T} dt' S_{\omega^R} DB(t' - jT) \\
&\leq \frac{1}{2} N S_{\omega^R} DBT^2 \leq \frac{1}{2} NB(DT)^2 = \frac{1}{2} t BD^2 T = \frac{\pi t BD^2}{\omega^R}. \tag{A.10}
\end{aligned}$$

Note that there may be smarter strategies to further decrease this bound. For example, we can use integration by parts to further reduce the error bound. But these methods will still yield a linear behavior of the bound.

How significant is this error? To answer this question, we estimate how much error is introduced at the characteristic timescale, which we assume is  $D^{-1}$ . Setting  $t = D^{-1}$  in Eq. (A.10) yields the error bound  $\pi B(D/\omega^R)$ . If we normalize  $\vec{f}$  so that  $B = 1$ , we prove that the error introduced by RWA is at most  $D/\omega^R$  at the characteristic timescale  $D^{-1}$ . Back to the example of a driven two-level system, the error from neglecting fast-rotating terms is at the order of  $d/\omega_d$  at a full Rabi period.

Above, the fast-rotating term we omit contains a constant  $\underline{V}_{\omega^R}$ . In practice, we sometimes also drop fast-rotating drive terms whose envelope is slowly varying, i.e.,  $\underline{V}_{\omega^R}$  could be weakly time-dependent. In this situation, the relation in Eq. (A.9) does not hold. However, if the

variation of  $\underline{V}_{\omega^R}(t)$  is sufficiently slow, the omission can still be justified, although we need to slightly increase the error bound.

To estimate the error bound in this case quantitatively, we first find the maximal norm of  $\underline{V}_{\omega^R}(t)$ , which is defined by  $S_\omega \equiv \max_t \|\underline{V}_{\omega^R}(t)\|$ . The slow variation of  $\underline{V}_{\omega^R}(t)$  implies that we can find  $\delta \ll 1$  such that

$$\frac{1}{T} \left\| \int_t^{t+T} dt' e^{-i\omega^R t'} \underline{V}_{\omega^R}(t) \right\| \leq \delta S_\omega, \quad (\text{A.11})$$

for all relevant time  $t$ . If so, we find

$$\begin{aligned} \|\vec{f}(t) - \vec{f}_{\text{RWA}}(t)\| &\leq \sum_{j=0}^{N-1} \left\| \int_{jT}^{(j+1)T} dt' e^{-i\omega^R t'} \underline{V}_{\omega^R}(t) [\vec{f}(t') - \vec{f}(jT)] \right\| \\ &\quad + \sum_{j=0}^{N-1} \left\| \int_t^{t+T} dt' e^{-i\omega^R t'} \underline{V}_{\omega^R}(t) \vec{f}(jT) \right\| \\ &\leq \frac{\pi t B D^2}{\omega^R} + t D B \delta. \end{aligned} \quad (\text{A.12})$$

The additional error also linearly grows with  $t$ , with a rate proportional to  $\delta$ .

### A.3. Numerical simulation

In this section, we evaluate the RWA-induced error numerically using a driven two-level system, to check how far the real error is from the bound derived above. If we calculate  $\|\vec{f}(t) - \vec{f}_{\text{RWA}}(t)\|$ , we will need to specify an initial state. To avoid the dependence of the calculated error on the initial state, here we instead evaluate the error caused to the propagator by RWA.

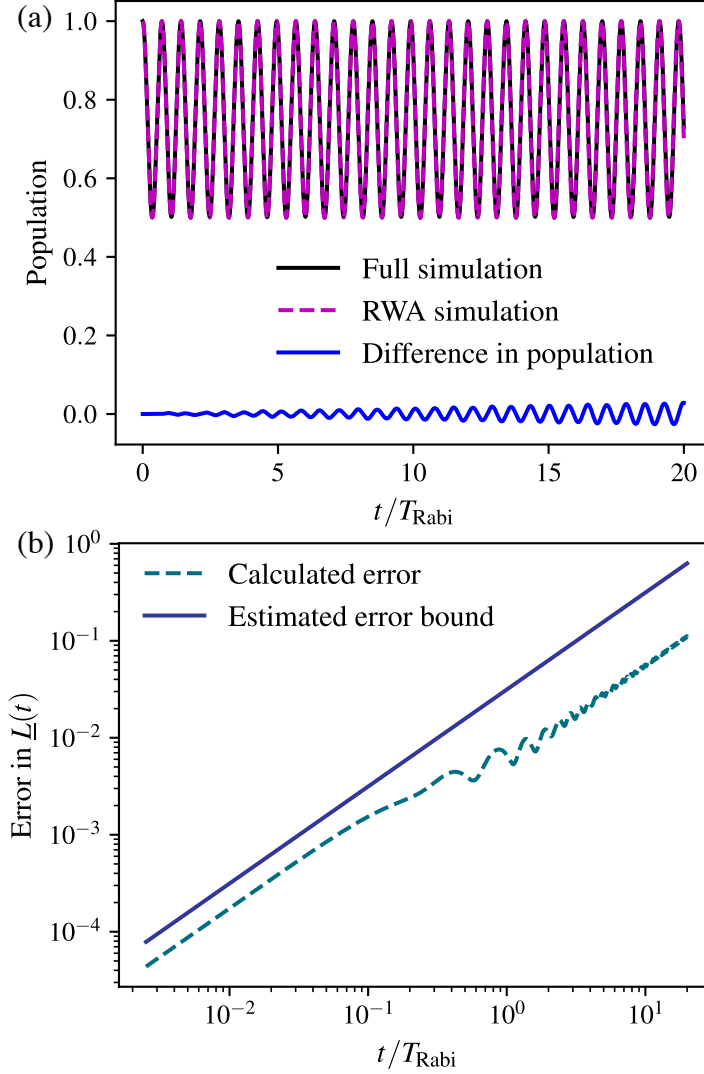


Figure A.1. Numerically calculated error introduced by RWA. (a) shows the evolution of the ground-state population of an off-resonantly driven two-level system, obtained with and without RWA. The difference is plotted in blue at the bottom of this figure. (b) shows the comparison between the estimated error bound derived in Eq. (A.12) and the calculated error,  $|\underline{L}(t) - \underline{L}_{\text{RWA}}(t)|$ . The simulation is based on the following choices of parameters:  $\omega_q = 1$ ,  $d_R = 1/200$ ,  $|\omega_q - \omega_d| = 1/200$ .

The operator  $\underline{L}(t)$  is one of fundamental matrices for the ODE (A.6), which specifically satisfies  $\underline{L}(0) = \underline{\mathbb{1}}$  and  $\det[\underline{L}(t)] \neq 0$ . This implies that  $\underline{L}(t)$  satisfies  $\vec{f}(t) = \underline{L}(t)\vec{f}(0)$  for an arbitrary initial state  $\vec{f}(0)$ . Estimating how much  $\underline{L}_{\text{RWA}}(t)$  deviates from  $\underline{L}(t)$  avoids the dependence of the choice of the initial state. We still assume that  $\|\underline{L}(t)\|$  is bounded at all times. For a Lindblad master equation,  $\underline{L}(t)$  is certainly bounded by 1. Note that this norm is still a vector induced one, which ensures the relation  $\|\underline{AB}\| \leq \|\underline{A}\| \|\underline{B}\|$ . This is important for the following result. By a similar procedure, we show that  $\|\underline{L}(t) - \underline{L}_{\text{RWA}}(t)\| \leq tB'D^2T/2$ , where  $B'$  stands for the bound of operator  $\underline{L}(t)$ .

The example we use is a simple two-level system that is driven off-resonantly. The Hamiltonian describing this system is the same as Eq. (A.1). Different from the discussion in Section A.1, here we add detuning to the drive frequency<sup>1</sup>. As we see in Fig. A.1, the error indeed grows roughly linearly with time, although the real error is far less than the estimated value given in Eq. (A.12).

We have arrived at a useful result about the error of RWA. However, we need to notice that all we have derived assumes sufficiently small coefficients of the terms on the right-hand side of Eq. (A.6). Sometimes we need to perform certain transformations on the given ODE to ensure this condition and perform RWA. Of course, there might be multiple choices of the transformations that can one can use to carry out RWA. Among them, some can give us simpler solutions after RWA, others may give more accurate results after the approximation.

---

<sup>1</sup>We point out that the RWA-induced error in the case where an on-resonance drive is applied appears to be much smaller compared with that with an off-resonant drive, probably due to certain symmetry in the former case. Here we will not further dig into this observation. We direct interested readers to Ref. [173].

## APPENDIX B

## Unifying Other $1/f$ -noise Protection Schemes Under the Floquet Framework

The discussion in the main text focuses on the connection between dynamical sweet spots and extrema of quasi-energy differences for the example of a driven fluxonium qubit. In this appendix, we first extend this connection to a general periodically driven qubit system, using a procedure similar to the one discussed in Section 5.3. Subsequently, we employ the Floquet framework to rephrase several previously developed protection schemes [13, 43, 52–55, 130, 131, 152, 153] as special limits of our theory.

### B.1. General discussion

We consider a periodically driven qubit described by an abstract Hamiltonian  $\hat{H}(\lambda, t)$ . Here,  $\lambda$  is a control parameter, and the Hamiltonian is time-periodic with period  $T = 2\pi/\omega_d$ , i.e.,  $\hat{H}(\lambda, t + T) = \hat{H}(\lambda, t)$ . (As in the main text,  $\omega_d$  denotes the drive frequency.) Due to environmental noise,  $\lambda$  is subjected to low-frequency fluctuations,  $\lambda(t) = \lambda_0 + \delta\lambda(t)$ . Here,  $\delta\lambda(t)$  captures the random fluctuations in  $\lambda$ . (Note that in this simple model, there is only a single noise channel.)

If the amplitude of the classical noise is sufficiently weak, then the original Hamiltonian may be expanded up to leading order in  $\delta\lambda(t)$  which yields the unperturbed qubit Hamiltonian

and the time-dependent perturbation

$$\hat{H}_q(t) = \hat{H}(\lambda_0, t), \quad \hat{H}_I(t) = \left. \frac{\partial \hat{H}(\lambda, t)}{\partial \lambda} \right|_{\lambda=\lambda_0} \delta\lambda(t), \quad (\text{B.1})$$

respectively. For convenience, we define  $\hat{\sigma}(t) \equiv [\partial \hat{H}(\lambda, t) / \partial \lambda]_{\lambda=\lambda_0}$ . The time-periodicity of the Hamiltonian renders  $\hat{\sigma}(t)$  time-periodic as well. While the example discussed in the main text leads to a constant  $\hat{\sigma}(t)$ , time dependence is present in other cases such as discussed in Refs. [53, 55]. With  $\hat{H}_q$  and  $\hat{H}_I$  specified, we are ready to employ the Floquet framework developed in Section 5.3, and calculate the pure-dephasing rate. The result is given by

$$\gamma_\phi = \sum_{k \in \mathbb{Z}} 2 |g_{k\phi}^\lambda|^2 S_\lambda(k\omega_d), \quad (\text{B.2})$$

where

$$g_{k\phi}^\lambda = \frac{1}{2T} \int_0^T dt e^{i\omega_d t} \text{Tr}_q [\hat{\sigma}(t) \hat{c}_\phi(t)], \quad (\text{B.3})$$

and  $S_\lambda(\omega) = \int_{-\infty}^{\infty} dt e^{i\omega t} \langle \delta\lambda(t) \delta\lambda(0) \rangle$  is the noise spectrum. As a regularized variant of the  $1/f$  noise, it is appropriate to consider a  $S_\lambda(\omega)$  that is strongly peaked at  $\omega = 0$ . For such a spectrum the pure-dephasing rate (B.2) of the qubit is generically dominated by the term  $2 |g_{0,\phi}^\lambda|^2 S_\lambda(0)$ . However, the pure dephasing rate can be decreased significantly by choosing a working point where  $g_{0,\phi}^\lambda = 0$ , thus eliminating the dominant contribution. In this case, weaker contributions of terms sampling the noise spectral density at non-zero frequencies will become relevant. These  $g_{0,\phi}^\lambda = 0$  working points are the *dynamical sweet spots*.

Based on a similar argument as in Section 5.5, we can prove that the condition  $g_{0,\phi}^\lambda = 0$  is closely related to the extrema of the quasi-energy difference, according to the relation

$$g_{0\phi}^\lambda = \frac{1}{2} \frac{\partial \epsilon_{01}}{\partial \lambda}. \quad (\text{B.4})$$

Setting both sides of Eq. (B.4) to zero establishes the connection between the dynamical sweet spots and the quasi-energy extrema.

In the following, we show how the theoretical framework outlined above can be used to understand noise protection schemes based on qubit frequency modulation and Rabi drives, as presented in Refs. [13, 43, 52–55, 130, 131, 152, 153].

## B.2. Dynamical sweet spots realized through qubit-frequency modulation

In Refs. [53–55, 130, 131], it is pointed out that qubit-frequency modulation can be harnessed for protecting a qubit from low-frequency noise. Such protection can be established by choosing modulation parameters for which the averaged, instantaneous transition frequency exhibits an extremum with respect to the noise parameter. Here, we confirm that the Floquet framework presented above indeed reproduces this condition in a certain limit.

We specifically consider the case of a frequency-modulated qubit using a purely longitudinal drive as discussed in Ref. [55]. The model Hamiltonian in this case is given by  $\hat{H}(\lambda, t) = \Omega_{ge}(\lambda, t)\hat{\sigma}_z/2$ , where  $\Omega_{ge}(\lambda, t)$  is the time-dependent instantaneous eigenenergy splitting, and  $\lambda$  is an external control parameter that determines the splitting. The unperturbed Hamiltonian and perturbation operator from Eq. (B.1) now take on the concrete form  $\hat{H}_q = \Omega_{ge}(\lambda_0, t)\hat{\sigma}_z/2$  and  $\hat{H}_I = [\partial\Omega_{ge}(\lambda, t)/\partial\lambda]|_{\lambda=\lambda_0}\delta\lambda(t)\hat{\sigma}_z/2$ . (We assume that  $\hat{H}_I$  is nonzero.) To phrase the calculation of decoherence rates in our previous Floquet language,

we obtain the unperturbed Floquet states and corresponding quasi-energies of the frequency-modulated qubit (in the absence of fluctuations  $\delta\lambda(t)$ ). The Floquet states read

$$|w_{0(1)}(t)\rangle = |g(e)\rangle \exp\left[\frac{i}{2} \int_0^t dt' (\Omega_{ge}(t') - \bar{\Omega}_{ge})\right], \quad (\text{B.5})$$

and the corresponding quasi-energies are given by  $\epsilon_{0(1)} = \bar{\Omega}_{ge}/2$ . Different from notation in the main text,  $|g(e)\rangle$  here denote the eigenstates of  $\sigma_z$ , and we have defined the averaged transition frequency  $\bar{\Omega}_{ge} = \int_0^T dt \Omega_{ge}(\lambda, t)/T$ . Within this model, the quasi-energy difference is evidently given by the averaged qubit transition frequency, i.e.,  $\epsilon_{01} = \bar{\Omega}_{ge}$ . According to Eq. (B.4), dynamical sweet spots now manifest whenever the time-averaged transition frequency vanishes,  $\partial\bar{\Omega}_{ge}/\partial\lambda = 0$ . This is in full agreement with the sweet-spot condition as formulated in Refs. [53–55, 130, 131].

The full expression of the pure-dephasing rate is calculated using Eq. (B.2), where the coefficients are given by

$$g_{k\phi}^\lambda = \frac{1}{2T} \int_0^T dt e^{ik\omega dt} \frac{\partial\Omega_{ge}(\lambda, t)}{\partial\lambda} \Big|_{\lambda=\lambda_0} = \frac{1}{2} \frac{\partial\Omega_{ge,k}}{\partial\lambda} \Big|_{\lambda=\lambda_0}. \quad (\text{B.6})$$

Here,  $\Omega_{ge,k}$  denotes the  $k$ th Fourier coefficient of the time-periodic transition frequency. We find that this result reproduces the one reported in Ref. [55].

### B.3. Dynamical sweet spots induced by on-resonance Rabi driving

It has been demonstrated that an on-resonance Rabi drive can dynamically decouple a qubit from low-frequency noise affecting its transition frequency [13, 43, 52, 152, 153]. Such decoupling is sometimes also referred to as *spin-locking* [13, 52]. In the following, we confirm

that this protection scheme can also be understood as an instance of the dynamical sweet-spot operation discussed in this paper.

Consider the Hamiltonian of a transversely driven qubit within RWA,

$$\hat{H}(\lambda, t) = \frac{\Omega_{ge}(\lambda)}{2} \hat{\sigma}_z + d_R (\hat{\sigma}^+ e^{-i\omega_d t} + \text{h.c.}), \quad (\text{B.7})$$

where  $d_R$  denotes the drive strength. As before,  $\lambda = \lambda_0 + \delta\lambda(t)$  is an external control parameter subjected to random fluctuations  $\delta\lambda$ . Note that, in contrast to the previous case, there is no separate modulation (AC component) of  $\Omega_{ge}$  here. Employing series expansion in  $\delta\lambda$ , the perturbation describing the effect of noise to leading order is  $\hat{H}_I = \delta\lambda(t) [\partial\Omega_{ge}(\lambda)/\partial\lambda]_{\lambda=\lambda_0} \hat{\sigma}_z/2$ . (We again assume operation away from static sweet spots, so that  $\hat{H}_I \neq 0$ .) To evaluate the decoherence rates, we need to invoke the Floquet states of the noise-free qubit, which are given by

$$\begin{aligned} |w_0(t)\rangle &= \cos \frac{\theta}{2} |g\rangle - \exp(-i\omega_d t) \sin \frac{\theta}{2} |e\rangle, \\ |w_1(t)\rangle &= \sin \frac{\theta}{2} |g\rangle + \exp(-i\omega_d t) \cos \frac{\theta}{2} |e\rangle, \end{aligned} \quad (\text{B.8})$$

where  $\theta = \tan^{-1}(d_R/\delta\Omega_{ge})$  and  $\delta\Omega_{ge} = \Omega_{ge}(\lambda) - \omega_d$ . The corresponding quasi-energies are given by  $\epsilon_{0(1)} = (\mp)\Omega_R/2$ , where  $\Omega_R = \sqrt{\delta\Omega_{ge}^2 + d_R^2}$  is the Rabi frequency. As a result, the quasi-energy difference for this model is given by the Rabi frequency, i.e.,  $\epsilon_{01} = \Omega_R$ . The dynamical sweet spots therefore obey the condition  $\partial\epsilon_{01}/\partial\lambda = \partial\Omega_R/\partial\lambda = 0$ , which implies  $\delta\Omega_{ge} = 0$ .

We further compare the explicit expressions of the depolarization and pure-dephasing rates derived within our framework with the results previously reported in the literature. We find for

these rates

$$\begin{aligned}\gamma_\phi &= \frac{1}{2} \left[ \left. \frac{\partial \Omega_{ge}(\lambda)}{\partial \lambda} \right|_{\lambda=\lambda_0} \cos \theta \right]^2 S_\lambda(0), \\ \gamma_\mp &= \frac{1}{4} \left[ \left. \frac{\partial \Omega_{ge}(\lambda)}{\partial \lambda} \right|_{\lambda=\lambda_0} \sin \theta \right]^2 S_\lambda(\pm \Omega_R),\end{aligned}\quad (\text{B.9})$$

which reproduce the results presented in Ref. [13].

#### B.4. Dynamical sweet spots realized by dynamical decoupling pulse sequences

We finally show that we can also interpret the dynamical decoupling (DD) scheme [145, 146, 149–151] as a special dynamical-sweet-spot operation. For simplicity, we consider a two-level system driven by an ideal DD pulse sequence. After moving to a rotating frame and apply the rotating-wave approximation, we find the Hamiltonian describing the driven two-level system

$$\hat{H}_0 = \frac{1}{2} f_{\text{DD}}(t) \hat{\sigma}_x + \frac{1}{2} \delta \omega_z \hat{\sigma}_z. \quad (\text{B.10})$$

Above,  $f_{\text{DD}}(t) = \sum_{j \in \mathbb{Z}} \pi \delta(t - jT)$ , and  $T$  is the interval between two DD pulses. To solve for the Floquet states and quasi-energies, we derive the propagator of the driven qubit in this rotating frame as

$$\hat{U}_0(t) = \exp \left[ -i \frac{1}{2} \delta \omega_z (t \% T) \hat{\sigma}_z \right] \left[ (-i \hat{\sigma}_x) \cdot \exp \left( -i \frac{1}{2} \delta \omega_z T \hat{\sigma}_z \right) \right]^{\lfloor \frac{t}{T} \rfloor}. \quad (\text{B.11})$$

Since the quasi-energies are closely related to the phases of the eigenvalues of the unitary at the end of one period, we first solve for its eigenvalues. Inserting  $t = T$  in the equation above,

we find

$$\begin{aligned}\hat{U}(T) &= -i \cos\left(\frac{1}{2}\delta\omega_z T\right) \hat{\sigma}_x + i \sin\left(\frac{1}{2}\delta\omega_z T\right) \hat{\sigma}_y \\ &= -i \left[ \cos\left(\frac{1}{2}\delta\omega_z T\right) \hat{\sigma}_x - \sin\left(\frac{1}{2}\delta\omega_z T\right) \hat{\sigma}_y \right].\end{aligned}\quad (\text{B.12})$$

The eigenvalues of this matrix are  $\pm i$ . Using the method presented in Ref. [174], we derive the quasi-energies of the two Floquet states as  $\epsilon_{0(1)} = (\mp)\omega_d/4$ . Surprisingly, the quasi-energy difference  $\epsilon_{01} = \omega_d/2$  is not  $\delta\omega_z$ -dependent. This implies that the qubit under an ideal DD pulse sequence has a extremely resilient sweet spot against the fluctuation of  $\delta\omega_z$ .

However, this conclusion has several caveats. Most obviously, it is not practical to engineer a sequence of delta pulses in reality. Any non-zero  $\delta\omega_z$  will lower the fidelity of a flip operation realized by a  $\pi$  pulse with finite width, which makes the unitary derived in Eq. (B.12) inaccurate. The rotating-wave approximation we have made will also break down for high driving power, and therefore counter-rotating terms must be included in Eq. (B.10).

## APPENDIX C

**Adiabatic Floquet Theory**

In this appendix, we discuss the adiabatic Floquet theory [163, 175], which is useful for the adiabatic mapping used in Refs. [46, 155].

For simplicity, we focus on a  $N$ -level system driven by a chirped single-tone pulse. Assume that this periodically driven system is controlled by a parameter set  $\vec{\lambda}$ . The time-dependent Hamiltonian corresponding to each  $\lambda$  is given by  $\hat{H}_F(\vec{\lambda}, \tau)$ . For the system we are interested in here,  $\vec{\lambda} = [\omega_d, A]$ , namely, the control parameters are the drive amplitude and frequency. For each  $\vec{\lambda}$ , the Hamiltonian  $\hat{H}_F(\vec{\lambda}, \tau)$  satisfies

$$\hat{H}_F(\vec{\lambda}, \tau + 2\pi/\lambda_1) = \hat{H}_F(\vec{\lambda}, \tau).$$

It has  $N$  independent Floquet states  $|w_j(\vec{\lambda}, \tau)\rangle$  with their quasi-energy  $\epsilon_j(\vec{\lambda})$ . They satisfy

$$\left[ \hat{H}_F(\vec{\lambda}, \tau) - i \frac{\partial}{\partial \tau} \right] |w_j(\vec{\lambda}, \tau)\rangle = \epsilon_j(\vec{\lambda}) |w_j(\vec{\lambda}, \tau)\rangle. \quad (\text{C.1})$$

We note that, the period of the Hamiltonian as well as the Floquet states depends on the first entry of  $\vec{\lambda}$ , namely,  $\lambda_1$ .

To ensure adiabaticity by slowly tuning  $\vec{\lambda}$ , we should require that the Hamiltonian family  $\hat{H}_F(\vec{\lambda}, \tau)$  and its quasi-energy spectrum  $\epsilon_j(\vec{\lambda})$  vary continuously with  $\vec{\lambda}$ . However, it is not straightforward to define the continuity of  $\hat{H}_F(\vec{\lambda}, \tau)$ , because the period of  $\hat{H}_F(\vec{\lambda}, \tau)$  changes for different  $\lambda_1$ . To rigorously define continuity, we introduce another  $\vec{\lambda}$ -dependent Hamiltonian,

which is a function of  $\theta$  instead of  $\tau$ :  $\hat{H}'_F(\vec{\lambda}, \theta) \equiv \hat{H}_F(\vec{\lambda}, \tau = \theta/\lambda_1)$ . Now, all  $\hat{H}'_F(\vec{\lambda}, \theta)$  have a fixed period  $2\pi$  in  $\theta$ . The proper definition of continuity is given by  $\hat{H}'_F(\vec{\lambda} + \delta\vec{\lambda}, \theta + \delta\theta)|_{\delta\vec{\lambda} \rightarrow 0, \delta\theta \rightarrow 0} \rightarrow \hat{H}'_F(\vec{\lambda}, \theta)$ . In the following, we will mainly use  $\hat{H}'_F(\vec{\lambda}, \theta)$  for clarity.

Using these preparations, we next study how the system evolves with slowly varying  $\vec{\lambda}$ . Assume that the parameter vector  $\vec{\lambda}$  varies slowly with time as a function  $\vec{\lambda}(t)$ . The system Hamiltonian at time  $t$  is

$$\hat{H}(t) = \hat{H}'_F\left(\vec{\lambda}(t), \theta = \int_0^t \lambda_1(t') dt'\right), \quad (\text{C.2})$$

where the form of the second entry mimics the phase accumulation according to the time-dependent frequency. The system state  $|\psi(t)\rangle$  evolves according to

$$\frac{d}{dt}|\psi(t)\rangle = -i\hat{H}(t)|\psi(t)\rangle. \quad (\text{C.3})$$

Note that the Hamiltonian  $\hat{H}(t)$  is in general not time periodic, therefore the standard Floquet analysis is not applicable.

In the following, we will prove that, if  $\vec{\lambda}$  varies sufficiently slow, the system still follows instantaneous Floquet states. Specifically, if adiabaticity holds, we will find our system in state  $\left|w_j\left(\vec{\lambda}(t), \tau = \int_0^t dt' \lambda(t')/\lambda_1(t)\right)\right\rangle$  if it is initiated in  $\left|w_j\left(\vec{\lambda}(0), \tau = 0\right)\right\rangle$ . To verify this, we need an extra dimension to make the Floquet formalism, where the periodic boundary condition is crucial, and a non-periodic Hamiltonian compatible with each other.

We first extend our previous Hilbert space by a tensor product of the previous one with another function space, which contains all square-integrable functions  $f : S^1 \rightarrow \mathbb{C}$ . Rigorously, the new Hilbert space is defined by  $\mathcal{K} = \mathcal{H} \otimes L_2(S^1, \theta)$ , where  $\mathcal{H}$  is the previous  $N$ -dimensional

Hilbert space and  $L_2(S^1, \theta)$  stands for the function space containing square-integrable functions whose domain is a circle  $S^1$  with length  $2\pi$ , and codomain is  $\mathbb{C}$ . A state in  $\mathcal{K}$  can be generally represented by  $|\Phi^{\mathcal{K}}\rangle\rangle = \int_0^{2\pi} d\theta \sum_j \Phi_j(\theta) |j\rangle \otimes |\theta\rangle$ , where  $\langle\theta'|\theta\rangle = \delta(\theta - \theta')$ , or in  $\theta$ 's conjugate basis,  $|\Phi^{\mathcal{K}}\rangle\rangle = \sum_{j,n} \Phi_{j,n} |j\rangle \otimes |n\rangle$ , where  $|n\rangle = \int_0^{2\pi} \exp(in\theta) |\theta\rangle / \sqrt{2\pi}$ . The delta function used above is defined on domain  $S^1$  which satisfies the relation  $\int_0^{2\pi} d\theta \delta(\theta - \theta') f(\theta) = f(\theta')$ . It can also be written as an infinite sum as

$$\delta(\theta - \theta') = \frac{1}{2\pi} \sum_{n \in \mathbb{Z}} e^{in(\theta - \theta')}. \quad (\text{C.4})$$

Our next goal is to find a ‘‘Hamiltonian’’  $\widehat{K}(t)$  that is defined in this enlarged Hilbert space, which governs the state evolution by

$$\frac{\partial}{\partial t} |\Phi^{\mathcal{K}}(t)\rangle\rangle = -i\widehat{K}(t) |\Phi^{\mathcal{K}}(t)\rangle\rangle. \quad (\text{C.5})$$

We want to find a proper definition of  $\widehat{K}(t)$ , such that Eq. (C.5) can somehow reduce to Eq. (C.3). Then, we can use the adiabatic evolution of  $|\Phi^{\mathcal{K}}(t)\rangle\rangle$  to justify the adiabaticity of  $|\psi(t)\rangle\rangle$ 's evolution. Note that now the vector  $|\Phi^{\mathcal{K}}(t)\rangle\rangle$  is by construction periodic in  $\theta$ , which mimics the periodicity of the Floquet states. Meanwhile,  $|\Phi^{\mathcal{K}}(t)\rangle\rangle$  is able to evolve by a non-time-periodic  $\widehat{K}(t)$ . In this way, the incompatibility between the periodicity of the Floquet states and non-periodic Hamiltonian can be resolved.

One choice of  $\widehat{K}(t)$  is

$$\widehat{K}(t) = \int_0^{2\pi} d\theta' \hat{H}'_F(\vec{\lambda}(t), \theta') \otimes |\theta'\rangle\langle\theta'| + \lambda_1 \hat{\mathbb{1}}_{\mathcal{H}} \otimes \hat{n}_\theta, \quad (\text{C.6})$$

where  $\hat{H}(t)$  is the time-dependent Hamiltonian defined in Eq. (C.2), and we define  $\hat{n}_\theta \equiv \sum_{n \in \mathbb{Z}} n |n\rangle\langle n|$ . Now let us check how one vector defined in Hilbert space  $\mathcal{H}$ , namely,

$$|\phi(t)\rangle = \left\langle \theta = \int_0^t \lambda_1(t') dt' \middle| \Phi^{\mathcal{K}}(t) \right\rangle, \quad (\text{C.7})$$

evolves over time. Below, we maintain the definition  $\theta = \int_0^t \lambda_1(t') dt'$ . We first find

$$\frac{\partial}{\partial t} |\phi(t)\rangle = \lambda_1(t) \frac{\partial}{\partial \theta} \left\langle \theta \middle| \Phi^{\mathcal{K}}(t) \right\rangle - i \left\langle \theta \middle| \hat{K}(t) \middle| \Phi^{\mathcal{K}}(t) \right\rangle. \quad (\text{C.8})$$

Above, we have made use of the Schrödinger equation defined in Eq. (C.5). We next evaluate the second term on the right-hand side. It is given by

$$\begin{aligned} \left\langle \theta \middle| \hat{K}(t) \middle| \Phi^{\mathcal{K}}(t) \right\rangle &= \hat{H}(t) \left\langle \theta \middle| \Phi^{\mathcal{K}}(t) \right\rangle + \lambda_1 \left\langle \theta \middle| \hat{n}_\theta \middle| \Phi^{\mathcal{K}}(t) \right\rangle \\ &= \hat{H}(t) |\phi(t)\rangle + \lambda_1 \int_0^{2\pi} d\theta' \left\langle \theta \middle| \hat{n}_\theta \middle| \theta' \right\rangle \left\langle \theta' \middle| \Phi^{\mathcal{K}}(t) \right\rangle. \end{aligned} \quad (\text{C.9})$$

Using the relation

$$\left\langle \theta \middle| \hat{n}_\theta \middle| \theta' \right\rangle = i \frac{\partial}{\partial \theta'} \sum_{n \in \mathbb{Z}} e^{in(\theta - \theta')}, \quad (\text{C.10})$$

and Eq. (C.4), we find

$$\left\langle \theta \middle| \hat{K}(t) \middle| \Phi^{\mathcal{K}}(t) \right\rangle = \hat{H}(t) |\phi(t)\rangle - i \frac{\partial}{\partial \theta} |\phi(t)\rangle. \quad (\text{C.11})$$

Inserting Eq. (C.11) into Eq. (C.8), we find that the first term on the right-hand side is cancelled, which leads to the following result

$$\frac{\partial}{\partial t}|\phi(t)\rangle = -i\hat{H}(t)|\phi(t)\rangle. \quad (\text{C.12})$$

Amazingly,  $|\phi(t)\rangle$  satisfies the Schrödinger equation governed by  $\hat{H}(t)$ . Therefore, we indeed find a way to reduce of evolution in Eq. (C.5) to that in Eq. (C.3). But we need to point out that, in general,  $|\phi(t)\rangle$  is not necessarily normalized if we only require  $|\Phi^{\mathcal{K}}(t)\rangle$  to be normalized. In other words,  $\langle\langle\Phi^{\mathcal{K}}(t)|\Phi^{\mathcal{K}}(t)\rangle\rangle = 1$  does not guarantee  $\langle\phi(t)|\phi(t)\rangle = 1$ . We need to properly set the initial condition for  $\langle\langle\Phi^{\mathcal{K}}(t)|\Phi^{\mathcal{K}}(t)\rangle\rangle$  for  $t = 0$ , such that for any  $\theta$ , the  $\mathcal{H}$ -Hilbert space vector  $\langle\theta|\Phi^{\mathcal{K}}(0)\rangle$  is normalized. We can check that, the proper normalization condition will hold once the initial condition is properly set. [We can prove this by using Eq. (C.7), with an arbitrary offset added to  $\theta(t)$ .]

The operator  $\widehat{K}(t)$  is called the quasi-energy operator [163], because the eigenvalues of the operator  $\widehat{K}(t)$  are identical to the quasi-energy spectrum of the Hamiltonian  $\hat{H}_F(\vec{\lambda}(t), \tau)$ . In fact, the eigenenergies and eigenstates of  $\widehat{K}(t)$  are

$$\epsilon_{j,n} = \epsilon_j + n\lambda_1, \quad \left| \Phi_{j,n}^{\mathcal{K}}(\vec{\lambda}(t)) \right\rangle = \int_0^{2\pi} d\theta' e^{-in\theta'} \left| w_j(\vec{\lambda}(t), \tau = \theta'/\lambda_1(t)) \right\rangle \otimes |\theta'\rangle \langle \theta'|. \quad (\text{C.13})$$

Finally, we apply the adiabatic theorem to the evolution of a vector  $|\Phi^{\mathcal{K}}(t)\rangle$ , and arrive at the central result of the adiabatic Floquet theory. If we consider a truncated  $N$ -level system (for example, we have  $N = 2$  in Chapter 5), we can work out an adiabatic limit for adiabatic evolution, by setting the timescale that parameter set  $\vec{\lambda}$  varies sufficiently slow compared with relevant quasi-energy spacings, all the way along the parameter path  $\vec{\lambda}(t)$ . In this limit, if we

initialize the state in one of the eigenstate of  $\widehat{K}(0)$ , i.e.,

$$\left| \Phi^{\mathcal{K}}(t=0) \right\rangle\rangle = \left| \Phi_{j,0}^{\mathcal{K}}(\vec{\lambda}(0)) \right\rangle\rangle, \quad (\text{C.14})$$

the vector  $|\Phi^{\mathcal{K}}(t)\rangle\rangle$  will adiabatically follow  $|\Phi_{j,0}^{\mathcal{K}}(\vec{\lambda}(t))\rangle\rangle$ , namely,

$$\left| \Phi^{\mathcal{K}}(t) \right\rangle\rangle \approx e^{i\tilde{\chi}_j(t)} \left| \Phi_{j,0}^{\mathcal{K}}(\vec{\lambda}(t)) \right\rangle\rangle. \quad (\text{C.15})$$

The phase is evaluated as

$$\tilde{\chi}_j(t) = - \int_0^t \epsilon_j(t') dt' + i \int_0^t dt' \left\langle \left\langle \Phi_{j,0}^{\mathcal{K}}(\vec{\lambda}(t')) \left| \frac{\partial}{\partial t'} \right| \Phi_{j,0}^{\mathcal{K}}(\vec{\lambda}(t')) \right\rangle \right\rangle. \quad (\text{C.16})$$

Now we relate the evolution of  $|\Phi^{\mathcal{K}}(t)\rangle\rangle$  back to the state evolution of the real physical system, using the relation Eq. (C.7). The initial condition implies that the qubit initial state is  $|\psi(0)\rangle = |w_j(\vec{\lambda}(0), \tau = 0)\rangle\rangle$ , i.e., the system is initiated in the  $j$ th Floquet state of  $\hat{H}_F(\vec{\lambda}(0), \tau)$ . Using Eq. (C.15) and Eq. (C.7), we find the system state

$$|\psi(t)\rangle \approx e^{i\tilde{\chi}_j(t)} \left| w_j \left( \vec{\lambda}(t), \tau = \int_0^t dt' \lambda_1(t') / \lambda_1(t) \right) \right\rangle\rangle. \quad (\text{C.17})$$

However, when  $\mathcal{H}$  has infinite dimensions, we usually do not have a rigorous adiabatic limit since the quasi-energy spectrum become “dense” [176], but in practical cases [46, 155], the experimental results agree well with the theory prediction using a truncated system.

## APPENDIX D

**Born-Oppenheimer Approximation**

In this appendix, we study the application of Born-Oppenheimer approximation in analyzing superconducting qubits [39, 49, 96]. In the context of atomic physics, the condition for applying such approximation is that the nuclei have exceedingly large masses compared with those of the electrons ( $m_N/m_e \sim 10^3$ ). This condition is usually hard to be satisfied by superconducting circuits. In the following, we will present a detailed discussion of the procedures of this approximation and the condition under which the approximation can be applied.

**D.1. General discussion**

We consider a composite system where two quantum objects are weakly coupled to each other. The full system is described by the Hamiltonian <sup>1</sup>

$$\hat{H}_{\text{full}} = \hat{H}_A + \hat{H}_B + \hat{H}_I, \quad (\text{D.1})$$

where  $\hat{H}_{A(B)}$  stands for the Hamiltonian for object  $A(B)$ . The interaction is denoted by  $\hat{H}_I = \eta \hat{O}_A \hat{O}_B$ , where  $\hat{O}_{A(B)}$  is the quantum operator belonging to the object  $A(B)$ , and  $\eta$  denotes the coupling strength. We assume that the energy scales of excitation in these two objects are considerably different – the  $B$  mode has a much higher excitation energy than that of  $A$ . Our intuition is that, since the state of object  $A$  changes much slower than that of  $B$ , the  $B$  mode

---

<sup>1</sup>To avoid introducing another notation, we use the same symbol for  $\hat{H}_A$  and  $\hat{H}_A \otimes \hat{\mathbb{1}}_B$  (similar for  $\hat{H}_B$ ). The readers should be able to understand their exact meaning based on the context.

should evolve adiabatically according to the slow variation of  $\langle \hat{O}_A \rangle$ . We assume that the spectral decomposition of  $\hat{O}_A$  is given by

$$\hat{O}_A = \sum_a \Omega_a |a\rangle \langle a| \otimes \mathbb{1}_B. \quad (\text{D.2})$$

It is reasonable to believe that, if we measure the  $A$  object with  $\hat{O}_A$  as the observable and obtain  $\Omega_a$  as the result, after the measurement we will find the  $A$  object in state  $|a\rangle$  and the  $B$  object in state  $|0_B; a\rangle$ . The latter is the ground state of

$$\hat{H}_{\text{BO},B}(a) = \hat{H}_B + \eta \Omega_a \hat{O}_B. \quad (\text{D.3})$$

Motivated by such intuition, we try choosing a different basis other than the eigenstate of  $\hat{H}_A(B)$  to express  $\hat{H}_{\text{full}}$ , and investigate methods of approximating the Hamiltonian expressed in this basis to simplify the eigenvalue problem. The set of basis states we choose is  $\{|a\rangle \otimes |j_B; a\rangle\}$ , where  $|j_B; a\rangle$  is the  $j_B$ th eigenstate of  $\hat{H}_{\text{BO},B}(a)$  defined in Eq. (D.3), satisfying  $\hat{H}_{\text{BO},B}(a)|j_B; a\rangle = E_{j_B}(a)|j_B; a\rangle$ . In the following, we will use the abbreviation  $|a, j_B; a\rangle \equiv |a\rangle \otimes |j_B; a\rangle$  for convenience. These basis states are normalized as  $\langle a, j_B; a | a', j'_B; a' \rangle = \delta_{a,a'} \delta_{j_B, j'_B}$ , although we should note that  $\langle j_B; a | j'_B; a' \rangle$  in general does not equal to  $\delta_{a,a'} \delta_{j_B, j'_B}$ .

Since we only focus on the low-energy excitations in this system, we are especially interested in the subspace with  $j_B = 0$ . To divide the Hilbert space into subspaces with different  $j_B$ , it is useful to define the projection operator in terms of the new basis states

$$P_{j_B} = \sum_a |a, j_B; a\rangle \langle a, j_B; a|, \quad (\text{D.4})$$

which satisfies

$$\begin{aligned}
 P_{j_B} P_{j'_B} &= \delta_{j_B, j'_B} P_{j_B}, \\
 \sum_{j_B} P_{j_B} &= \sum_a \sum_{j_B} |a, j_B; a\rangle \langle a, j_B; a| = \mathbb{1}.
 \end{aligned} \tag{D.5}$$

The full Hamiltonian is then expanded by

$$\hat{H}_{\text{full}} = \sum_{j_B} \sum_{j'_B} P_{j_B} \hat{H}_{\text{full}} P_{j'_B} = \sum_{j_B} \sum_{j'_B} \hat{H}_{j_B, j'_B}, \tag{D.6}$$

where we define  $\hat{H}_{j_B, j'_B} \equiv \hat{P}_{j_B} \hat{H}_{\text{full}} \hat{P}_{j'_B}$ . Using  $\hat{O}_A |a\rangle = \Omega_a |a\rangle$ , we find

$$\begin{aligned}
 \hat{P}_{j_B} (\hat{H}_B + \hat{H}_I) \hat{P}_{j'_B} &= \hat{P}_{j_B} \sum_a (\hat{H}_B + \eta \Omega_a \hat{O}_B) |a, j'_B; a\rangle \langle a, j'_B; a| \\
 &= \hat{P}_{j_B} \sum_a E_{j'_B}(a) |a, j'_B; a\rangle \langle a, j'_B; a| \\
 &= \delta_{j_B, j'_B} \sum_a E_{j_B}(a) |a, j_B; a\rangle \langle a, j_B; a|.
 \end{aligned} \tag{D.7}$$

This means that part of the Hamiltonian  $\hat{H}_{\text{full}}$  is already subspace diagonal – both  $\hat{H}_B$  and  $\hat{H}_I$  are contained in  $\sum_{j_B} \hat{H}_{j_B, j'_B}$ .

The term that is left over is  $\hat{H}_A$ . We expand  $\hat{H}_A$  as  $\hat{H}_A = \sum_{j_B, j'_B} \hat{H}_{A, j_B, j'_B}$ , where we define

$$\hat{H}_{A, j_B, j'_B} \equiv \hat{P}_{j_B} \hat{H}_A \hat{P}_{j'_B} = \sum_{a, a'} h_{A, aa'} C_{j_B, a, j'_B, a'} |a, j_B; a\rangle \langle a', j'_B; a'|. \tag{D.8}$$

Above, we define  $h_{A,aa'} \equiv \langle a | \hat{H}_A | a' \rangle$ , and  $C_{j_B,a,j'_B,a'} \equiv \langle j_B; a | j'_B; a' \rangle$ . We separate  $\hat{H}_A$  into subspace diagonal and off-diagonal parts, i.e.,

$$\hat{H}_A = \sum_{j_B} \hat{H}_{A,j_B,j_B} + \sum_{j_B \neq j'_B} \hat{H}_{A,j_B,j'_B} = \hat{H}_{A,d} + \hat{H}_{od}. \quad (\text{D.9})$$

For convenience, we further define

$$\hat{H}_d \equiv \hat{H}_B + \hat{H}_I + \hat{H}_{A,d}, \quad (\text{D.10})$$

which collects all the subspace diagonal terms in  $\hat{H}_{\text{full}}$ .

Up to this step, we have not made any approximation. The first approximation we will make is to omit  $\hat{H}_{od}$ . Obviously, such a treatment requires that the coefficients  $h_{A,aa'} C_{j_B,a,j'_B,a'}$  are sufficiently small compared with the relevant detuning in the unperturbed spectrum, such that the coupling terms in  $\hat{H}_{od}$  are only dispersive. To be clear, we assume that we have derived the unperturbed eigenstates  $|j_A, j_B\rangle$  by diagonalizing the unperturbed Hamiltonian  $\hat{H}_d$ . We are allowed to use two separate indices  $j_A$  and  $j_B$  to label these states because  $H_d$  is subspace diagonal, i.e.,  $[\hat{P}_{j_B}, \hat{H}_d] = 0$  for any  $j_B$ , therefore the unperturbed eigenstates should each live in one of the subspaces  $\hat{P}_{j_B}$ . These states satisfy  $\hat{H}_d |j_A, j_B\rangle = E_{j_A,j_B} |j_A, j_B\rangle$  and  $\hat{P}_{j_B} |j_A, j'_B\rangle = \delta_{j_B,j'_B} |j_A, j'_B\rangle$ . Since the  $B$  mode has a much higher energy, it is reasonable to assume  $|E_{j_A,j_B} - E_{j'_A,j'_B}| \gg h_{A,aa'} C_{j_B,a,j'_B,a'}$  whenever  $j_B \neq j'_B$ .<sup>2</sup>

One would of course ask, why don't we neglect  $\hat{H}_I$  in the first place rather than going a long way and still drop some terms? We point out that the terms we omit here can have a much smaller magnitude than those in  $\hat{H}_I$ . To show this, we need to estimate the magnitude

<sup>2</sup>In fact, this condition cannot be satisfied when the  $A$  mode has an infinite number of levels whose energies are not bounded. However, since we usually only care about the low-energy excitation, we can perform a proper truncation on the  $A$  mode's energy levels to avoid such complication.

of coefficients  $h_{A,aa'}C_{j_B,a,j'_B,a'}$ . The magnitude of coefficient  $h_{A,aa'}$  largely depends on the commutation of operators  $\hat{O}_A$  and  $\hat{H}_A$ . A simple but boring scenario is that, if the two operators satisfy  $[\hat{O}_A, \hat{H}_A] = 0$ , we have  $h_{A,aa'} = 0$  for  $a \neq a'$ . And for  $a = a'$ , the coefficient  $C_{j_B,a,j'_B,a'}$  vanishes if  $j_B \neq j'_B$ . This means that  $\hat{H}_{\text{od}}$  vanishes if  $\hat{O}_A$  and  $\hat{H}_A$  commute. Otherwise, we will need to study the specific choice of  $\hat{O}_A$  and  $\hat{H}_A$  to find  $h_{A,aa'}$ .

The coefficient  $C_{j_B,a,j'_B,a'}$  depends on  $\eta$ . Making use of the perturbation theory, we find that to the first order,

$$|C_{j_B,a,j'_B,a'}| \sim \frac{|\eta\Delta\Omega_a\langle j'_B; a|\hat{O}_B|j_B; a\rangle|}{|E_{j_B}(a) - E_{j'_B}(a)|},$$

for  $j_B \neq j'_B$ . Since we have not specified the Hamiltonian and operators, it is difficult to discuss the magnitudes of  $\langle j'_B; a|\hat{O}_B|j_B; a\rangle$ . However, we can tell that from the expression above that the magnitude of the terms we neglect here decrease inversely with the excitation energy in  $B$ . This implies that such an approximation will induce less error if the  $B$  mode's excitation energy is higher.

To complete the Born-Oppenheimer approximation, we have another step to take. We first express  $\hat{H}_d$  in the  $\{|a, j_B; a\rangle\}$  basis

$$\begin{aligned} \hat{H}_d = & \sum_{j_B} \left[ \sum_a E_{j_B}(a) |a, j_B; a\rangle \langle a, j_B; a| \right. \\ & \left. + \sum_{a,a'} h_{A,aa'} C_{j_B,a,j'_B,a'} |a, j_B; a\rangle \langle a', j_B; a'| \right]. \end{aligned} \quad (\text{D.11})$$

To this step, we have almost removed the role of the  $B$  mode, except for the energy  $E_{j_B}(a)$  and  $C_{j_B,a,j'_B,a'}$ . The former in most relevant cases is not difficult to calculate, while the estimation of the latter is more involved. Furthermore, we hope that  $\hat{H}_A$  is almost unaffected after the approximation, while in Eq. (D.11), all matrix elements of  $\hat{H}_A$  are multiplied by the coefficients

$C_{j_B, a, j_B, a'}$ . Further approximation on  $C_{j_B, a, j_B, a'}$  can help us solve these issues. Using the perturbation theory, this coefficient is estimated as

$$|1 - C_{j_B, a, j_B, a'}| \sim \sum_{j'_B \neq j_B} \frac{|\eta \Delta \Omega_a \langle j'_B; a | \hat{O}_B | j_B; a \rangle|^2}{|E_{j_B}(a) - E_{j'_B}(a)|^2}, \quad (\text{D.12})$$

which scales with  $(\eta/|E_{j_B}(a) - E_{j'_B}(a)|)^2$ . Above, we have defined  $\Delta \Omega_a = |\Omega_{a'} - \Omega_a|$ . The difference of  $C_{j_B, a, j_B, a'}$  with 1 is small if  $(\eta/|E_{j_B}(a) - E_{j'_B}(a)|)^2$  is sufficiently small and  $\Delta \Omega_a$  is bounded. In this case, we are allowed to approximate  $C_{j_B, a, j_B, a'}$  by 1. We are also allowed to make this approximation, if  $|1 - C_{j_B, a, j_B, a'}|$  is not sufficiently close to zero for all  $a$  and  $a'$ , but  $h_{A, aa'}$  already approaches zero before  $C_{j_B, a, j_B, a'}$  significantly differ from 1. In this case, replacing  $C_{j_B, a, j_B, a'}$  by 1 will not cause significant error either.

After this replacement, we arrive at the desired Hamiltonian,

$$\begin{aligned} \hat{H}_{\text{BO}} = & \sum_{j_B} \left[ \sum_a E_{j_B}(a) |a, j_B; a\rangle \langle a, j_B; a| \right. \\ & \left. + \sum_{a, a'} h_{A, aa'} |a, j_B; a\rangle \langle a', j_B; a'| \right]. \end{aligned} \quad (\text{D.13})$$

Why is this Hamiltonian good for us? Because if we only focus on the subspace  $\hat{P}_{j_B}$ , the eigenenergies solved for of Hamiltonian  $\hat{P}_{j_B} \hat{H}_{\text{BO}} \hat{P}_{j_B}$  are identical to those of

$$\hat{H}_{\text{eff}, j_B} = \hat{H}_A + E_{j_B}(\hat{a}), \quad (\text{D.14})$$

where we define  $\hat{a} \equiv \sum_a a |a\rangle \langle a|$ , and  $f(\hat{a}) \equiv \sum_a f(a) |a\rangle \langle a|$  for any function  $f(a)$ . The eigenstates of  $\hat{P}_{j_B} \hat{H}_{\text{BO}} \hat{P}_{j_B}$  can also be easily obtained by the eigenstates of  $\hat{H}_{\text{eff}, j_B}$  – if its

$j_A$ th eigenstate is  $|\psi_{j_A}\rangle = \sum_a \psi_{j_A}(a)|a\rangle$ , then the corresponding eigenstate of  $\hat{P}_{j_B} \hat{H}_{\text{BO}} \hat{P}_{j_B}$  is  $|j_A, j_B\rangle = \sum_a \psi_{j_A}(a)|a, j_B; a\rangle$ .

Above, we have focused on the case where the coupling between the two objects is assumed to be the simplest dipole-dipole interaction  $\eta \hat{O}_A \hat{O}_B$ . We can slightly generalize the model a little beyond the simplest linear coupling, by assuming that the interaction takes the form

$$\hat{H}_I = g(\hat{O}_A, \hat{O}_B), \quad (\text{D.15})$$

where  $g(\hat{O}_A, \hat{O}_B)$  is a function of operators  $\hat{O}_A$  and  $\hat{O}_B$  defined by

$$g(\hat{O}_A, \hat{O}_B) = \sum_{a,b} g(\Omega_a, \Omega_b) |a, b\rangle \langle a, b|. \quad (\text{D.16})$$

Above,  $g(x_1, x_2)$  is a real function of variables  $x_1$  and  $x_2$ . Also,  $\Omega_b$  and  $|b\rangle$  denote the eigenvalue and corresponding eigenstate of  $\hat{O}_B$ , which satisfies  $\hat{O}_B |b\rangle = \Omega_b |b\rangle$ . The most important change to the derivation above is probably that we will replace Eq. (D.3) by

$$\hat{H}_{\text{BO},B}(a) = \hat{H}_B + g(\Omega_a, \hat{O}_B). \quad (\text{D.17})$$

The exact definition of  $g(\Omega_a, \hat{O}_B)$  is

$$g(\Omega_a, \hat{O}_B) = \sum_b g(\Omega_a, \Omega_b) |b\rangle \langle b|. \quad (\text{D.18})$$

Now we have described at an abstract level how Born-Oppenheimer approximation is applied and the appropriate condition for making it. In the next section, we will use a concrete example to help the readers understand this method more intuitively.

## D.2. Toy model

In this section, we focus on a concrete example. We assume that the two objects are two harmonic oscillators. Note that such a model can be analytically exactly solved by a Bogoliubov transformation [118]. Our goal is to check how the magnitude of the terms that we neglect scales with the system parameters.

We specify that, in Eq. (D.1)

$$\begin{aligned}\hat{H}_{A(B)} &= 4E_{C_{A(B)}}\hat{n}_{A(B)}^2 + \frac{1}{2}E_{L_{A(B)}}\hat{\varphi}_{A(B)}^2, \\ \hat{H}_I &= \eta\hat{\varphi}_A\hat{\varphi}_B.\end{aligned}\tag{D.19}$$

We assume that the  $B$  mode has a much higher excitation energy, and set  $\omega_B \gg \omega_A$ , where  $\omega_{A(B)} \equiv \sqrt{8E_{C_{A(B)}}E_{L_{A(B)}}}$ . The spectral composition of  $\hat{\varphi}_A$  is given by

$$\hat{\varphi}_A = \int_{-\infty}^{\infty} \varphi_A |\varphi_A\rangle \langle \varphi_A| d\varphi_A.\tag{D.20}$$

Using this concrete model, we first find the specific expressions of  $h_{A,aa'}$  and  $C_{j_B,a,j'_B,a'}$ , to derive the terms we drop in the last section. They are given by

$$\begin{aligned}h_{A,\varphi_A\varphi'_A} &= \langle \varphi_A | \hat{H}_A | \varphi'_A \rangle \\ &= -4E_{C_A} \frac{\partial}{\partial \varphi_A^2} \delta(\varphi_A - \varphi'_A) + \frac{1}{2}E_{L_A} \varphi_A^2 \delta(\varphi_A - \varphi'_A),\end{aligned}\tag{D.21}$$

and

$$C_{j_B,\varphi_A,j'_B,\varphi'_A} = \langle j_B | e^{i\frac{\eta}{E_{L_B}}(\varphi_A - \varphi'_A)\hat{n}_B} | j'_B \rangle,\tag{D.22}$$

where  $|j_B\rangle$  is the  $j_B$ th Fock state of  $\hat{H}_B$ . It is not straightforward to express  $C_{j_B, \varphi_A, j'_B, \varphi'_A}$  explicitly. Interested readers can refer to Ref. [177] for an explicit expression. One exception is that, it is easy to find that, for  $j_B = j'_B = 0$ ,

$$C_{0, \varphi_A, 0, \varphi'_A} = \exp \left[ -\frac{(\eta n^{\text{ZPF}})^2}{2E_{L_B}^2} (\varphi_A - \varphi'_A)^2 \right]. \quad (\text{D.23})$$

With these results, we can evaluate

$$\begin{aligned} \hat{H}_{A, j_B, j'_B} &= \int_{-\infty}^{\infty} d\varphi_A \int_{-\infty}^{\infty} d\varphi'_A \left[ -4E_{C_A} \frac{\partial}{\partial \varphi_A^2} \delta(\varphi_A - \varphi'_A) + \frac{1}{2} E_{L_A} \varphi_A^2 \delta(\varphi_A - \varphi'_A) \right] \\ &\quad \times C_{j_B, \varphi_A, j'_B, \varphi'_A} |\varphi_A, j_B; \varphi_A\rangle \langle \varphi'_A, j'_B; \varphi'_A| \\ &= -4E_{C_A} \int_{-\infty}^{\infty} d\varphi_A \int_{-\infty}^{\infty} d\varphi'_A \delta(\varphi_A - \varphi'_A) \frac{\partial^2}{\partial \varphi_A^2} \left[ C_{j_B, \varphi_A, j'_B, \varphi'_A} |\varphi_A, j_B; \varphi_A\rangle \langle \varphi'_A, j'_B; \varphi'_A| \right] \\ &\quad + \frac{1}{2} \int_{-\infty}^{\infty} d\varphi_A E_{L_A} \varphi_A^2 |\varphi_A, j_B; \varphi_A\rangle \langle \varphi'_A, j'_B; \varphi'_A| \\ &= -4E_{C_A} \int_{-\infty}^{\infty} d\varphi_A \left[ \frac{\partial^2}{\partial \varphi_A^2} C_{j_B, \varphi_A, j'_B, \varphi'_A} \right] |\varphi_A, j_B; \varphi_A\rangle \langle \varphi_A, j_B; \varphi_A| \\ &\quad - 8E_{C_A} \int_{-\infty}^{\infty} d\varphi_A \left[ \frac{\partial}{\partial \varphi_A} C_{j_B, \varphi_A, j'_B, \varphi'_A} \right] \left[ \frac{\partial}{\partial \varphi_A} |\varphi_A, j_B; \varphi_A\rangle \right] \langle \varphi_A, j_B; \varphi_A| \\ &\quad - 4E_{C_A} \int_{-\infty}^{\infty} d\varphi_A C_{j_B, \varphi_A, j'_B, \varphi'_A} \left[ \frac{\partial^2}{\partial \varphi_A^2} |\varphi_A, j_B; \varphi_A\rangle \right] \langle \varphi_A, j_B; \varphi_A| \\ &\quad + \frac{1}{2} \int_{-\infty}^{\infty} d\varphi_A E_{L_A} \varphi_A^2 \delta_{j_B, j'_B} |\varphi_A, j_B; \varphi_A\rangle \langle \varphi_A, j'_B; \varphi_A|. \end{aligned} \quad (\text{D.24})$$

In the expression above, we see the relevance of the derivatives of  $C_{j_B, \varphi_A, j'_B, \varphi'_A}$ . Using Eq. (D.22), we can estimate these derivatives as,

$$\begin{aligned}
\left| \frac{\partial}{\partial \varphi_A} C_{j_B, \varphi_A, j'_B, \varphi'_A} \right| &\sim \left| \frac{\eta n_B^{\text{ZPF}}}{E_{L_B}} \right| \quad (j_B \neq j'_B), \\
\left| \frac{\partial^2}{\partial \varphi_A^2} C_{j_B, \varphi_A, j'_B, \varphi'_A} \right| &\sim \left| \frac{\eta n_B^{\text{ZPF}}}{E_{L_B}} \right|^2 \quad (j_B \neq j'_B), \\
\left| \frac{\partial}{\partial \varphi_A} C_{j_B, \varphi_A, j_B, \varphi'_A} \right| &= 0, \quad (j_B = j'_B), \\
\left| \frac{\partial^2}{\partial \varphi_A^2} C_{j_B, \varphi_A, j_B, \varphi'_A} \right| &\sim \left| \frac{\eta n_B^{\text{ZPF}}}{E_{L_B}} \right|^2, \quad (j_B = j'_B).
\end{aligned} \tag{D.25}$$

Here, we define the zero-point fluctuation by  $n_B^{\text{ZPF}} = (E_{L_B}/32E_{C_B})^{1/4}$ . Therefore, the small parameter in this case scales with  $|\eta E_{C_B}^{-1/4} E_{L_B}^{-3/4}|$ , while the energy scale of the terms we neglect is  $|\eta E_{C_A} E_{C_B}^{-1/4} E_{L_B}^{-3/4}|$ .

After neglecting all undesired terms, we finally show the effective Hamiltonian defined in Eq. (D.14) <sup>3</sup>

$$\begin{aligned}
\hat{H}_{\text{eff}, j_B} &= \hat{H}_A + \left( j_B + \frac{1}{2} \right) \omega_B - \frac{1}{2} \frac{\eta^2}{E_{L_B}} \hat{\varphi}_A^2 \\
&= 4E_{C_A} \hat{n}_A^2 + \frac{1}{2} \left( E_{L_A} - \frac{\eta^2}{E_{L_B}} \right) \hat{\varphi}_A^2 + \left( j_B + \frac{1}{2} \right) \omega_B.
\end{aligned} \tag{D.26}$$

<sup>3</sup>Note that we must have  $\eta^2/E_{L_B} < E_{L_A}$  in the first place. If not, the full potential energy is not positive definite.

## Bibliography

- [1] Y. Makhlin, G. Schön, and A. Shnirman, “*Quantum-State Engineering with Josephson-Junction Devices*”, *Rev. Mod. Phys.* **73**, 357 (2001).
- [2] J. You and F. Nori, “*Superconducting Circuits and Quantum Information*”, *Phys. Today* **58**, 42 (2005).
- [3] M. Kjaergaard, M. E. Schwartz, J. Braumüller, P. Krantz, J. I.-J. Wang, S. Gustavsson, and W. D. Oliver, “*Superconducting Qubits: Current State of Play*”, *Annu. Rev. Condens. Matter Phys.* **11**, 369 (2020).
- [4] A. Blais, A. L. Grimsmo, S. M. Girvin, and A. Wallraff, “*Circuit Quantum Electrodynamics*”, *Rev. Mod. Phys.* **93**, 025005 (2021).
- [5] L. DiCarlo, J. M. Chow, J. M. Gambetta, L. S. Bishop, B. R. Johnson, D. I. Schuster, J. Majer, A. Blais, L. Frunzio, S. M. Girvin, and R. J. Schoelkopf, “*Demonstration of Two-Qubit Algorithms with a Superconducting Quantum Processor*”, *Nature* **460**, 240 (2009).
- [6] R. Barends, J. Kelly, A. Megrant, A. Veitia, D. Sank, E. Jeffrey, T. C. White, J. Mutus, A. G. Fowler, B. Campbell, Y. Chen, Z. Chen, B. Chiaro, A. Dunsworth, C. Neill, P. O’Malley, P. Roushan, A. Vainsencher, J. Wenner, A. N. Korotkov, A. N. Cleland, and J. M. Martinis, “*Superconducting Quantum Circuits at the Surface Code Threshold for Fault Tolerance*”, *Nature* **508**, 500 (2014).
- [7] A. Blais, S. M. Girvin, and W. D. Oliver, “*Quantum Information Processing and Quantum Optics with Circuit Quantum Electrodynamics*”, *Nat. Phys.* **16**, 247 (2020).
- [8] C. D. Bruzewicz, J. Chiaverini, R. McConnell, and J. M. Sage, “*Trapped-Ion Quantum Computing: Progress and Challenges*”, *Appl. Phys. Rev.* **6**, 021314 (2019).
- [9] M Saffman, “*Quantum Computing with Atomic Qubits and Rydberg Interactions: Progress and Challenges*”, *J. Phys. B* **49**, 202001 (2016).

- [10] C. Rigetti, “*Quantum Gates for Superconducting Qubits*”, PhD thesis (Yale University, 2009).
- [11] Y. Y. Gao, M. A. Rol, S. Touzard, and C. Wang, “*A Practical Guide for Building Superconducting quantum devices*”, arXiv:2106.06173 (2021).
- [12] Y. Wu, W.-S. Bao, S. Cao, F. Chen, M.-C. Chen, X. Chen, T.-H. Chung, H. Deng, Y. Du, D. Fan, M. Gong, C. Guo, C. Guo, S. Guo, L. Han, L. Hong, H.-L. Huang, Y.-H. Huo, L. Li, and N. Li *et al.*, “*Strong Quantum Computational Advantage Using a Superconducting Quantum Processor*”, arXiv:2106.14734 (2021).
- [13] G. Ithier, E. Collin, P. Joyez, P. J. Meeson, D. Vion, D. Esteve, F. Chiarello, A. Shnirman, Y. Makhlin, J. Schrieffer, and G. Schön, “*Decoherence in a Superconducting Quantum Bit Circuit*”, Phys. Rev. B **72**, 134519 (2005).
- [14] C. E. Murray, “*Material Matters in Superconducting Qubits*”, arXiv:2106.05919 (2021).
- [15] A. Somoroff, Q. Ficheux, R. A. Mencia, H. Xiong, R. V. Kuzmin, and V. E. Manucharyan, “*Millisecond Coherence in a Superconducting Qubit*”, arXiv:2103.08578, (2021).
- [16] A. P. M. Place, L. V. H. Rodgers, P. Mundada, B. M. Smitham, M. Fitzpatrick, Z. Leng, A. Premkumar, J. Bryon, A. Vrajitoarea, S. Sussman, G. Cheng, T. Madhavan, H. K. Babla, X. H. Le, Y. Gang, B. Jäck, A. Gyenis, N. Yao, R. J. Cava, N. P. de Leon, and A. A. Houck, “*New Material Platform for Superconducting Transmon Qubits with Coherence Times Exceeding 0.3 Milliseconds*”, Nat. Commun. **12**, 1779 (2021).
- [17] C. Wang, X. Li, H. Xu, Z. Li, J. Wang, Z. Yang, Z. Mi, X. Liang, T. Su, C. Yang, G. Wang, W. Wang, Y. Li, M. Chen, C. Li, K. Linghu, J. Han, Y. Zhang, Y. Feng, Y. Song, T. Ma, J. Zhang, R. Wang, P. Zhao, W. Liu, G. Xue, Y. Jin, and H. Yu, “*Transmon Qubit with Relaxation Time Exceeding 0.5 Milliseconds*”, arXiv:2105.09890, 2021.
- [18] N. Earnest, S. Chakram, Y. Lu, N. Irons, R. K. Naik, N. Leung, L. Ocola, D. A. Czaplewski, B. Baker, J. Lawrence, J. Koch, and D. I. Schuster, “*Realization of a  $\Lambda$  System with Metastable States of a Capacitively Shunted Fluxonium*”, Phys. Rev. Lett. **120**, 150504 (2018).
- [19] Y.-H. Lin, L. B. Nguyen, N. Grabon, J. San Miguel, N. Pankratova, and V. E. Manucharyan, “*Demonstration of Protection of a Superconducting Qubit from Energy Decay*”, Phys. Rev. Lett. **120**, 150503 (2018).

- [20] A. Gyenis, P. S. Mundada, A. Di Paolo, T. M. Hazard, X. You, D. I. Schuster, J. Koch, A. Blais, and A. A. Houck, “*Experimental Realization of a Protected Superconducting Circuit Derived from the  $0-\pi$  Qubit*”, PRX Quantum **2**, 010339 (2021).
- [21] Y. Sung, L. Ding, J. Braumüller, A. Vepsäläinen, B. Kannan, M. Kjaergaard, A. Greene, G. O. Samach, C. McNally, D. Kim, A. Melville, B. M. Niedzielski, M. E. Schwartz, J. L. Yoder, T. P. Orlando, S. Gustavsson, and W. D. Oliver, “*Realization of High-Fidelity CZ and ZZ-Free iSWAP Gates with a Tunable Coupler*”, Phys. Rev. X **11**, 021058 (2021).
- [22] Y. Xu, J. Chu, J. Yuan, J. Qiu, Y. Zhou, L. Zhang, X. Tan, Y. Yu, S. Liu, J. Li, F. Yan, and D. Yu, “*High-Fidelity, High-Scalability Two-Qubit Gate Scheme for Superconducting Qubits*”, Phys. Rev. Lett. **125**, 240503 (2020).
- [23] A. Kandala, K. X. Wei, S. Srinivasan, E. Magesan, S. Carnevale, G. A. Keefe, D. Klaus, O. Dial, and D. C. McKay, “*Demonstration of a High-Fidelity CNOT for Fixed-Frequency Transmons with Engineered ZZ Suppression*”, arXiv:2011.07050 (2020).
- [24] J. Preskill, “*Quantum Computing in the NISQ Era and Beyond*”, Quantum **2**, 79 (2018).
- [25] P. Chapman, *Introducing the World’s Most Powerful Quantum Computer*, <https://ionq.com/posts/october-01-2020-introducing-most-powerful-quantum-computer> (visited on 08/03/2021).
- [26] J. M. Martinis, K. B. Cooper, R. McDermott, M. Steffen, M. Ansmann, K. D. Osborn, K. Cicak, S. Oh, D. P. Pappas, R. W. Simmonds, and C. C. Yu, “*Decoherence in Josephson Qubits from Dielectric Loss*”, Phys. Rev. Lett. **95**, 210503 (2005).
- [27] C. Wang, C. Axline, Y. Y. Gao, T. Brecht, Y. Chu, L. Frunzio, M. H. Devoret, and R. J. Schoelkopf, “*Surface Participation and Dielectric Loss in Superconducting Qubits*”, Appl. Phys. Lett. **107**, 162601 (2015).
- [28] J. B. Chang, M. R. Vissers, A. D. Córcoles, M. Sandberg, J. Gao, D. W. Abraham, J. M. Chow, J. M. Gambetta, M. Beth Rothwell, G. A. Keefe, M. Steffen, and D. P. Pappas, “*Improved Superconducting Qubit Coherence Using Titanium Nitride*”, Appl. Phys. Lett. **103**, 012602 (2013).
- [29] Y. Nakamura, Y. A. Pashkin, T. Yamamoto, and J. S. Tsai, “*Charge Echo in a Cooper-Pair Box*”, Phys. Rev. Lett. **88**, 047901 (2002).

- [30] R. C. Bialczak, R. McDermott, M. Ansmann, M. Hofheinz, N. Katz, E. Lucero, M. Neeley, A. D. O’Connell, H. Wang, A. N. Cleland, and J. M. Martinis, “ $1/f$  Flux Noise in Josephson Phase Qubits”, *Phys. Rev. Lett.* **99**, 187006 (2007).
- [31] S. M. Anton, C. Müller, J. S. Birenbaum, S. R. O’Kelley, A. D. Fefferman, D. S. Golubev, G. C. Hilton, H.-M. Cho, K. D. Irwin, F. C. Wellstood, G. Schön, A. Shnirman, and J. Clarke, “*Pure Dephasing in Flux Qubits Due to Flux Noise with Spectral Density Scaling as  $1/f^\alpha$* ”, *Phys. Rev. B* **85**, 224505 (2012).
- [32] D. J. Van Harlingen, T. L. Robertson, B. L. T. Plourde, P. A. Reichardt, T. A. Crane, and J. Clarke, “*Decoherence in Josephson-Junction Qubits Due to Critical-Current Fluctuations*”, *Phys. Rev. B* **70**, 064517 (2004).
- [33] A. P. Sears, A. Petrenko, G. Catelani, L. Sun, H. Paik, G. Kirchmair, L. Frunzio, L. I. Glazman, S. M. Girvin, and R. J. Schoelkopf, “*Photon Shot Noise Dephasing in the Strong-Dispersive Limit of Circuit QED*”, *Phys. Rev. B* **86**, 180504 (2012).
- [34] G. Zhang, Y. Liu, J. J. Raftery, and A. A. Houck, “*Suppression of Photon Shot Noise Dephasing in a Tunable Coupling Superconducting Qubit*”, *npj Quantum Inf.* **3**, 1 (2017).
- [35] G. Catelani, S. E. Nigg, S. M. Girvin, R. J. Schoelkopf, and L. I. Glazman, “*Decoherence of Superconducting Qubits Caused by Quasiparticle Tunneling*”, *Phys. Rev. B* **86**, 184514 (2012).
- [36] K. Serniak, M. Hays, G. de Lange, S. Diamond, S. Shankar, L. D. Burkhardt, L. Frunzio, M. Houzet, and M. H. Devoret, “*Hot Nonequilibrium Quasiparticles in Transmon Qubits*”, *Phys. Rev. Lett.* **121**, 157701 (2018).
- [37] J. Koch, T. M. Yu, J. Gambetta, A. A. Houck, D. I. Schuster, J. Majer, A. Blais, M. H. Devoret, S. M. Girvin, and R. J. Schoelkopf, “*Charge-Insensitive Qubit Design Derived from the Cooper Pair Box*”, *Phys. Rev. A* **76**, 042319 (2007).
- [38] P. Groszkowski, A Di Paolo, A. L. Grimsmo, A. Blais, D. I. Schuster, A. A. Houck, and J. Koch, “*Coherence Properties of the  $0-\pi$  Qubit*”, *New J. Phys.* **20**, 043053 (2018).
- [39] A. D. Paolo, A. L. Grimsmo, P. Groszkowski, J. Koch, and A. Blais, “*Control and Coherence Time Enhancement of the  $0-\pi$  Qubit*”, *New J. Phys.* **21**, 043002 (2019).
- [40] L. B. Nguyen, Y.-H. Lin, A. Somoroff, R. Mencia, N. Grabon, and V. E. Manucharyan, “*High-Coherence Fluxonium Qubit*”, *Phys. Rev. X* **9**, 041041 (2019).

- [41] W. Smith, A. Kou, X. Xiao, U. Vool, and M. Devoret, “*Superconducting Circuit Protected by Two-Cooper-Pair Tunneling*”, npj Quantum Inf. **6**, 8 (2020).
- [42] A. Kamal, J. L. Yoder, F. Yan, T. J. Gudmundsen, D. Hover, A. P. Sears, P. Welander, T. P. Orlando, S. Gustavsson, and W. D. Oliver, “*Improved Superconducting Qubit Coherence with High-Temperature Substrate Annealing*”, arXiv:1606.09262, (2016).
- [43] Q. Guo, S.-B. Zheng, J. Wang, C. Song, P. Zhang, K. Li, W. Liu, H. Deng, K. Huang, D. Zheng, X. Zhu, H. Wang, C.-Y. Lu, and J.-W. Pan, “*Dephasing-Insensitive Quantum Information Storage and Processing with Superconducting Qubits*”, Phys. Rev. Lett. **121**, 130501 (2018).
- [44] B. Pokharel, N. Anand, B. Fortman, and D. A. Lidar, “*Demonstration of Fidelity Improvement Using Dynamical Decoupling with Superconducting Qubits*”, Phys. Rev. Lett. **121**, 220502 (2018).
- [45] Z. Huang, P. S. Mundada, A. Gyenis, D. I. Schuster, A. A. Houck, and J. Koch, “*Engineering Dynamical Sweet Spots to Protect Qubits from  $1/f$  Noise*”, Phys. Rev. Applied **15**, 034065 (2021).
- [46] P. S. Mundada, A. Gyenis, Z. Huang, J. Koch, and A. A. Houck, “*Floquet-Engineered Enhancement of Coherence Times in a Driven Fluxonium Qubit*”, Phys. Rev. Applied **14**, 054033 (2020).
- [47] V. E. Manucharyan, J. Koch, L. I. Glazman, and M. H. Devoret, “*Fluxonium: Single Cooper-Pair Circuit Free of Charge Offsets*”, Science **326**, 113 (2009).
- [48] K. Kalashnikov, W. T. Hsieh, W. Zhang, W.-S. Lu, P. Kamenov, A. Di Paolo, A. Blais, M. E. Gershenson, and M. Bell, “*Bifluxon: Fluxon-Parity-Protected Superconducting Qubit*”, PRX Quantum **1**, 010307 (2020).
- [49] W. C. Smith, M. Villiers, A. Marquet, J. Palomo, M. R. Delbecq, T. Kontos, P. Campagne-Ibarcq, B. Douçot, and Z. Leghtas, “*Magnifying Quantum Phase Fluctuations with Cooper-Pair Pairing*”, arXiv:2010.15488 (2020).
- [50] P. Brooks, A. Kitaev, and J. Preskill, “*Protected Gates for Superconducting Qubits*”, Phys. Rev. A **87**, 052306 (2013).

- [51] J. Bylander, S. Gustavsson, F. Yan, F. Yoshihara, K. Harrabi, G. Fitch, D. G. Cory, Y. Nakamura, J.-S. Tsai, and W. D. Oliver, “*Noise Spectroscopy Through Dynamical Decoupling with a Superconducting Flux Qubit*”, *Nat. Phys.* **7**, 565 (2011).
- [52] F. Yan, S. Gustavsson, J. Bylander, X. Jin, F. Yoshihara, D. G. Cory, Y. Nakamura, T. P. Orlando, and W. D. Oliver, “*Rotating-Frame Relaxation as a Noise Spectrum Analyser of a Superconducting Qubit Undergoing Driven Evolution*”, *Nat. Commun.* **4**, 2337 (2013).
- [53] N. Didier, “*Flux Control of Superconducting Qubits at Dynamical Sweet Spot*”, arXiv:1912.09416 (2019).
- [54] S. S. Hong, A. T. Papageorge, P. Sivarajah, G. Crossman, N. Didier, A. M. Polloreno, E. A. Sete, S. W. Turkowski, M. P. da Silva, and B. R. Johnson, “*Demonstration of a Parametrically Activated Entangling Gate Protected from Flux Noise*”, *Phys. Rev. A* **101**, 012302 (2020).
- [55] N. Didier, E. A. Sete, J. Combes, and M. P. da Silva, “*ac Flux Sweet Spots in Parametrically Modulated Superconducting Qubits*”, *Phys. Rev. Applied* **12**, 054015 (2019).
- [56] J. A. Valery, S. Chowdhury, G. Jones, and N. Didier, “*Dynamical Sweet Spot Engineering via Two-Tone Flux Modulation of Superconducting Qubits*”, arXiv:2104.07835 (2021).
- [57] Y. Nakamura, Y. A. Pashkin, and J. S. Tsai, “*Coherent Control of Macroscopic Quantum States in a Single-Cooper-Pair Box*”, *Nature* **398**, 786 (1999).
- [58] I. Chiorescu, Y. Nakamura, C. J. P. M. Harmans, and J. E. Mooij, “*Coherent Quantum Dynamics of a Superconducting Flux Qubit*”, *Science* **299**, 1869 (2003).
- [59] P. Bertet, I. Chiorescu, G. Burkard, K. Semba, C. J. P. M. Harmans, D. P. DiVincenzo, and J. E. Mooij, “*Dephasing of a Superconducting Qubit Induced by Photon Noise*”, *Phys. Rev. Lett.* **95**, 257002 (2005).
- [60] A. A. Houck, J. A. Schreier, B. R. Johnson, J. M. Chow, J. Koch, J. M. Gambetta, D. I. Schuster, L. Frunzio, M. H. Devoret, S. M. Girvin, and R. J. Schoelkopf, “*Controlling the Spontaneous Emission of a Superconducting Transmon Qubit*”, *Phys. Rev. Lett.* **101**, 080502 (2008).
- [61] H. Paik, D. I. Schuster, L. S. Bishop, G. Kirchmair, G. Catelani, A. P. Sears, B. R. Johnson, M. J. Reagor, L. Frunzio, L. I. Glazman, S. M. Girvin, M. H. Devoret, and R. J.

- Schoelkopf, “*Observation of High Coherence in Josephson Junction Qubits Measured in a Three-Dimensional Circuit QED Architecture*”, Phys. Rev. Lett. **107**, 240501 (2011).
- [62] C. Rigetti, J. M. Gambetta, S. Poletto, B. L. T. Plourde, J. M. Chow, A. D. Córcoles, J. A. Smolin, S. T. Merkel, J. R. Rozen, G. A. Keefe, M. B. Rothwell, M. B. Ketchen, and M. Steffen, “*Superconducting Qubit in a Waveguide Cavity with a Coherence Time Approaching 0.1 ms*”, Phys. Rev. B **86**, 100506 (2012).
- [63] R. Barends, J. Kelly, A. Megrant, D. Sank, E. Jeffrey, Y. Chen, Y. Yin, B. Chiaro, J. Mutus, C. Neill, P. O’Malley, P. Roushan, J. Wenner, T. C. White, A. N. Cleland, and J. M. Martinis, “*Coherent Josephson Qubit Suitable for Scalable Quantum Integrated Circuits*”, Phys. Rev. Lett. **111**, 080502 (2013).
- [64] X. Y. Jin, A. Kamal, A. P. Sears, T. Gudmundsen, D. Hover, J. Miloshi, R. Slattery, F. Yan, J. Yoder, T. P. Orlando, S. Gustavsson, and W. D. Oliver, “*Thermal and Residual Excited-State Population in a 3D Transmon Qubit*”, Phys. Rev. Lett. **114**, 240501 (2015).
- [65] F. Yan, S. Gustavsson, A. Kamal, J. Birenbaum, A. P. Sears, D. Hover, T. J. Gudmundsen, D. Rosenberg, G. Samach, S. Weber, J. L. Yoder, T. P. Orlando, J. Clarke, A. J. Kerman, and W. D. Oliver, “*The Flux Qubit Revisited to Enhance Coherence and Reproducibility*”, Nat. Commun. **7**, 12964 (2016).
- [66] H. Zhang, S. Chakram, T. Roy, N. Earnest, Y. Lu, Z. Huang, D. K. Weiss, J. Koch, and D. I. Schuster, “*Universal Fast-Flux Control of a Coherent, Low-Frequency Qubit*”, Phys. Rev. X **11**, 011010 (2021).
- [67] H. Wang, M. Hofheinz, M. Ansmann, R. C. Bialczak, E. Lucero, M. Neeley, A. D. O’Connell, D. Sank, J. Wenner, A. N. Cleland, and J. M. Martinis, “*Measurement of the Decay of Fock States in a Superconducting Quantum Circuit*”, Phys. Rev. Lett. **101**, 240401 (2008).
- [68] C. Wang, Y. Y. Gao, P. Reinhold, R. W. Heeres, N. Ofek, K. Chou, C. Axline, M. Reagor, J. Blumoff, K. M. Sliwa, L. Frunzio, S. M. Girvin, L. Jiang, M. Mirrahimi, M. H. Devoret, and R. J. Schoelkopf, “*A Schrödinger Cat Living in Two Boxes*”, Science **352**, 1087 (2016).
- [69] S. Rosenblum, P. Reinhold, M. Mirrahimi, L. Jiang, L. Frunzio, and R. J. Schoelkopf, “*Fault-Tolerant Detection of a Quantum Error*”, Science **361**, 266 (2018).

- [70] J. M. Gertler, B. Baker, J. Li, S. Shirol, J. Koch, and C. Wang, “*Protecting a Bosonic Qubit with Autonomous Quantum Error Correction*”, *Nature* **590**, 243 (2021).
- [71] N. Ofek, A. Petrenko, R. Heeres, P. Reinhold, Z. Leghtas, B. Vlastakis, Y. Liu, L. Frunzio, S. M. Girvin, L. Jiang, M. Mirrahimi, M. H. Devoret, and R. J. Schoelkopf, “*Extending the Lifetime of a Quantum Bit with Error Correction in Superconducting Circuits*”, *Nature* **536**, 441 (2016).
- [72] L. Hu, Y. Ma, W. Cai, X. Mu, Y. Xu, W. Wang, Y. Wu, H. Wang, Y. P. Song, C. L. Zou, S. M. Girvin, L.-M. Duan, and L. Sun, “*Quantum Error Correction and Universal Gate Set Operation on a Binomial Bosonic Logical Qubit*”, *Nat. Phys.* **15**, 503 (2019).
- [73] T. W. Larsen, K. D. Petersson, F. Kuemmeth, T. S. Jespersen, P. Krogstrup, J. Nygård, and C. M. Marcus, “*Semiconductor-Nanowire-Based Superconducting Qubit*”, *Phys. Rev. Lett.* **115**, 127001 (2015).
- [74] L. Casparis, T. W. Larsen, M. S. Olsen, F. Kuemmeth, P. Krogstrup, J. Nygård, K. D. Petersson, and C. M. Marcus, “*Gatemon Benchmarking and Two-Qubit Operations*”, *Phys. Rev. Lett.* **116**, 150505 (2016).
- [75] F. Luthi, T. Stavenga, O. W. Enzing, A. Bruno, C. Dickel, N. K. Langford, M. A. Rol, T. S. Jespersen, J. Nygård, P. Krogstrup, and L. DiCarlo, “*Evolution of Nanowire Transmon Qubits and Their Coherence in a Magnetic Field*”, *Phys. Rev. Lett.* **120**, 100502 (2018).
- [76] T. M. Hazard, A. Gyenis, A. Di Paolo, A. T. Asfaw, S. A. Lyon, A. Blais, and A. A. Houck, “*Nanowire Superinductance Fluxonium Qubit*”, *Phys. Rev. Lett.* **122**, 010504 (2019).
- [77] J. I.-J. Wang, D. Rodan-Legrain, L. Bretheau, D. L. Campbell, B. Kannan, D. Kim, M. Kjaergaard, P. Krantz, G. O. Samach, F. Yan, J. L. Yoder, K. Watanabe, T. Taniguchi, T. P. Orlando, S. Gustavsson, P. Jarillo-Herrero, and W. D. Oliver, “*Coherent Control of a Hybrid Superconducting Circuit Made with Graphene-Based van der Waals Heterostructures*”, *Nature Nanotechnology* **14**, 120 (2019).
- [78] E. Kapit, “*The Upside of Noise: Engineered Dissipation as a Resource in Superconducting Circuits*”, *Quantum Sci. and Technol.* **2**, 033002 (2017).

- [79] S. O. Valenzuela, W. D. Oliver, D. M. Berns, K. K. Berggren, L. S. Levitov, and T. P. Orlando, “*Microwave-Induced Cooling of a Superconducting Qubit*”, *Science* **314**, 1589 (2006).
- [80] Z. Leghtas, G. Kirchmair, B. Vlastakis, R. J. Schoelkopf, M. H. Devoret, and M. Mirrahimi, “*Hardware-Efficient Autonomous Quantum Memory Protection*”, *Phys. Rev. Lett.* **111**, 120501 (2013).
- [81] E. Kapit, “*Hardware-Efficient and Fully Autonomous Quantum Error Correction in Superconducting Circuits*”, *Phys. Rev. Lett.* **116**, 150501 (2016).
- [82] K. W. Murch, U. Vool, D. Zhou, S. J. Weber, S. M. Girvin, and I. Siddiqi, “*Cavity-Assisted Quantum Bath Engineering*”, *Phys. Rev. Lett.* **109**, 183602 (2012).
- [83] K. Geerlings, Z. Leghtas, I. M. Pop, S. Shankar, L. Frunzio, R. J. Schoelkopf, M. Mirrahimi, and M. H. Devoret, “*Demonstrating a Driven Reset Protocol for a Superconducting Qubit*”, *Phys. Rev. Lett.* **110**, 120501 (2013).
- [84] R. Lescanne, M. Villiers, T. Peronnin, A. Sarlette, M. Delbecq, B. Huard, T. Kontos, M. Mirrahimi, and Z. Leghtas, “*Exponential Suppression of Bit-Flips in a Qubit Encoded in an Oscillator*”, *Nature Physics* **16**, 509 (2020).
- [85] Z. Leghtas, S. Touzard, I. M. Pop, A. Kou, B. Vlastakis, A. Petrenko, K. M. Sliwa, A. Narla, S. Shankar, M. J. Hatridge, M. Reagor, L. Frunzio, R. J. Schoelkopf, M. Mirrahimi, and M. H. Devoret, “*Confining the State of Light to a Quantum Manifold by Engineered Two-Photon Loss*”, *Science* **347**, 853 (2015).
- [86] H. Breuer and F. Petruccione, “*The Theory of Open Quantum Systems*” (Oxford University Press, New York, 2007).
- [87] S. Kohler, T. Dittrich, and P. Hänggi, “*Floquet-Markovian Description of the Parametrically Driven, Dissipative Harmonic Quantum Oscillator*”, *Phys. Rev. E* **55**, 300 (1997).
- [88] M. Joos, D. Bluvstein, D. M. W. Yuanqi Lyu, and A. B. Jayich, “*Protecting Qubit Coherence by Spectrally Engineered Driving of the Spin Environment*”, arXiv:2101.09654 (2021).
- [89] F. Liu, X. Zhou, and Z.-W. Zhou, “*Memory Effect and Non-Markovian Dynamics in an Open Quantum System*”, *Phys. Rev. A* **99**, 052119 (2019).

- [90] A. Fragner, M. Göppl, J. M. Fink, M. Baur, R. Bianchetti, P. J. Leek, A. Blais, and A. Wallraff, “*Resolving Vacuum Fluctuations in an Electrical Circuit by Measuring the Lamb Shift*”, *Science* **322**, 1357 (2008).
- [91] P. Y. Wen, K.-T. Lin, A. F. Kockum, B. Suri, H. Ian, J. C. Chen, S. Y. Mao, C. C. Chiu, P. Delsing, F. Nori, G.-D. Lin, and I.-C. Hoi, “*Large Collective Lamb Shift of Two Distant Superconducting Artificial Atoms*”, *Phys. Rev. Lett.* **123**, 233602 (2019).
- [92] Y. Nakamura, C. D. Chen, and J. S. Tsai, “*Spectroscopy of Energy-Level Splitting between Two Macroscopic Quantum States of Charge Coherently Superposed by Josephson Coupling*”, *Phys. Rev. Lett.* **79**, 2328 (1997).
- [93] P. Joyez, P. Lafarge, A. Filipe, D. Esteve, and M. H. Devoret, “*Observation of Parity-Induced Suppression of Josephson Tunneling in the Superconducting Single Electron Transistor*”, *Phys. Rev. Lett.* **72**, 2458 (1994).
- [94] V. Bouchiat, D. Vion, P. Joyez, D. Esteve, and M. H. Devoret, “*Quantum Coherence with a Single Cooper Pair*”, *Phys. Scr.* **T76**, 165 (1998).
- [95] D. Vion, A. Aassime, A. Cottet, P. Joyez, H. Pothier, C. Urbina, D. Esteve, and M. H. Devoret, “*Manipulating the Quantum State of an Electrical Circuit*”, *Science* **296**, 886 (2002).
- [96] Y. Lu, S. Chakram, N. Leung, N. Earnest, R. K. Naik, Z. Huang, P. Groszkowski, E. Kapit, J. Koch, and D. I. Schuster, “*Universal Stabilization of a Parametrically Coupled Qubit*”, *Phys. Rev. Lett.* **119**, 150502 (2017).
- [97] S. J. Srinivasan, A. J. Hoffman, J. M. Gambetta, and A. A. Houck, “*Tunable Coupling in Circuit Quantum Electrodynamics Using a Superconducting Charge Qubit with a V-Shaped Energy Level Diagram*”, *Phys. Rev. Lett.* **106**, 083601 (2011).
- [98] P. Mundada, G. Zhang, T. Hazard, and A. Houck, “*Suppression of Qubit Crosstalk in a Tunable Coupling Superconducting Circuit*”, *Phys. Rev. Applied* **12**, 054023 (2019).
- [99] J. Koch, V. Manucharyan, M. H. Devoret, and L. I. Glazman, “*Charging Effects in the Inductively Shunted Josephson Junction*”, *Phys. Rev. Lett.* **103**, 217004 (2009).
- [100] A. Gyenis, A. D. Paolo, J. Koch, A. Blais, A. A. Houck, and D. I. Schuster, “*Moving Beyond the Transmon: Noise-Protected Superconducting Quantum Circuits*”, arXiv:2106.10296 (2021).

- [101] Q. Ficheux, L. B. Nguyen, A. Somoroff, H. Xiong, K. N. Nesterov, M. G. Vavilov, and V. E. Manucharyan, “*Fast Logic with Slow Qubits: Microwave-Activated Controlled-Z Gate on Low-Frequency Fluxoniums*”, Phys. Rev. X **11**, 021026 (2021).
- [102] I. M. Pop, K. Geerlings, G. Catelani, R. J. Schoelkopf, L. I. Glazman, and M. H. Devoret, “*Coherent Suppression of Electromagnetic Dissipation due to Superconducting Quasiparticles*”, Nature **508**, 369 (2014).
- [103] Z. Huang, Y. Lu, E. Kapit, D. I. Schuster, and J. Koch, “*Universal Stabilization of Single-Qubit States Using a Tunable Coupler*”, Phys. Rev. A **97**, 062345 (2018).
- [104] E. Kapit, J. T. Chalker, and S. H. Simon, “*Passive Correction of Quantum Logical Errors in a Driven, Dissipative System: A Blueprint for an Analog Quantum Code Fabric*”, Phys. Rev. A **91**, 062324 (2015).
- [105] S. Shankar, M. Hatridge, Z. Leghatas, K. M. Sliwa, A. Narla, U. Vool, S. M. Girvin, L. Frunzio, M. Mirrahimi, and M. H. Devoret, “*Autonomously Stabilized Entanglement Between Two Superconducting Quantum Bits*”, Nature **504**, 419 (2013).
- [106] P. J. Leek, S. Filipp, P. Maurer, M. Baur, R. Bianchetti, J. M. Fink, M. Göppl, L. Steffen, and A. Wallraff, “*Using Sideband Transitions for Two-Qubit Operations in Superconducting Circuits*”, Phys. Rev. B **79**, 180511 (2009).
- [107] B. Peropadre, D. Zueco, F. Wulschner, F. Deppe, A. Marx, R. Gross, and J. J. García-Ripoll, “*Tunable Coupling Engineering Between Superconducting Resonators: From Sidebands to Effective Gauge Fields*”, Phys. Rev. B **87**, 134504 (2013).
- [108] N. Didier, J. Bourassa, and A. Blais, “*Fast Quantum Nondemolition Readout by Parametric Modulation of Longitudinal Qubit-Oscillator Interaction*”, Phys. Rev. Lett. **115**, 203601 (2015).
- [109] D. C. McKay, S. Filipp, A. Mezzacapo, E. Magesan, J. M. Chow, and J. M. Gambetta, “*Universal Gate for Fixed-Frequency Qubits via a Tunable Bus*”, Phys. Rev. Applied **6**, 064007 (2016).
- [110] P. Bertet, C. J. P. M. Harmans, and J. E. Mooij, “*Parametric Coupling for Superconducting Qubits*”, Phys. Rev. B **73**, 064512 (2006).
- [111] F. Arute, K. Arya, R. Babbush, D. Bacon, J. C. Bardin, R. Barends, R. Biswas, S. Boixo, F. G. S. L. Brandao, D. A. Buell, B. Burkett, Y. Chen, Z. Chen, B. Chiaro, R. Collins, W.

- Courtney, A. Dunsworth, E. Farhi, B. Foxen, and A. Fowler *et al.*, “*Quantum Supremacy Using a Programmable Superconducting Processor*”, *Nature* **574**, 505 (2019).
- [112] J. M. Gambetta, A. A. Houck, and A. Blais, “*Superconducting Qubit with Purcell Protection and Tunable Coupling*”, *Phys. Rev. Lett.* **106**, 030502 (2011).
- [113] S. H. W. van der Ploeg, A. Izmailkov, A. M. van den Brink, U. Hübner, M. Grajcar, E. Il’ichev, H.-G. Meyer, and A. M. Zagoskin, “*Controllable Coupling of Superconducting Flux Qubits*”, *Phys. Rev. Lett.* **98**, 057004 (2007).
- [114] A. Blais, A. M. van den Brink, and A. M. Zagoskin, “*Tunable Coupling of Superconducting Qubits*”, *Phys. Rev. Lett.* **90**, 127901 (2003).
- [115] F. Yan, P. Krantz, Y. Sung, M. Kjaergaard, D. L. Campbell, T. P. Orlando, S. Gustavsson, and W. D. Oliver, “*Tunable Coupling Scheme for Implementing High-Fidelity Two-Qubit Gates*”, *Phys. Rev. Applied* **10**, 054062 (2018).
- [116] Y. Chen, C. Neill, P. Roushan, N. Leung, M. Fang, R. Barends, J. Kelly, B. Campbell, Z. Chen, B. Chiaro, A. Dunsworth, E. Jeffrey, A. Megrant, J. Y. Mutus, P. J. J. O’Malley, C. M. Quintana, D. Sank, A. Vainsencher, J. Wenner, T. C. White, M. R. Geller, A. N. Cleland, and J. M. Martinis, “*Qubit Architecture with High Coherence and Fast Tunable Coupling*”, *Phys. Rev. Lett.* **113**, 220502 (2014).
- [117] P.-M. Billangeon, J. S. Tsai, and Y. Nakamura, “*Circuit-QED-Based Scalable Architectures for Quantum Information Processing with Superconducting Qubits*”, *Phys. Rev. B* **91**, 094517 (2015).
- [118] G. Qin, K. lin Wang, and T. zhong Li, “*General Multimode Squeezed States*”, arXiv:quant-ph/0109020 (2001).
- [119] G. Zhu, D. G. Ferguson, V. E. Manucharyan, and J. Koch, “*Circuit QED with Fluxonium Qubits: Theory of the Dispersive Regime*”, *Phys. Rev. B* **87**, 024510 (2013).
- [120] U. Hohenester, “*Cavity Quantum Electrodynamics with Semiconductor Quantum Dots: Role of Phonon-Assisted Cavity Feeding*”, *Phys. Rev. B* **81**, 155303 (2010).
- [121] X. You, J. A. Sauls, and J. Koch, “*Circuit Quantization in the Presence of Time-Dependent External Flux*”, *Phys. Rev. B* **99**, 174512 (2019).

- [122] G. Burkard, R. H. Koch, and D. P. DiVincenzo, “*Multilevel Quantum Description of Decoherence in Superconducting Qubits*”, Phys. Rev. B **69**, 064503 (2004).
- [123] C. H. van der Wal, A. C. J. ter Haar, F. K. Wilhelm, R. N. Schouten, C. J. P. M. Harmans, T. P. Orlando, S. Lloyd, and J. E. Mooij, “*Quantum Superposition of Macroscopic Persistent-Current States*”, Science **290**, 773 (2000).
- [124] F. Yoshihara, K. Harrabi, A. O. Niskanen, Y. Nakamura, and J. S. Tsai, “*Decoherence of Flux Qubits Due to  $1/f$  Flux Noise*”, Phys. Rev. Lett. **97**, 167001 (2006).
- [125] E. A. Sete, M. J. Reagor, N. Didier, and C. T. Rigetti, “*Charge- and Flux-Insensitive Tunable Superconducting Qubit*”, Phys. Rev. Applied **8**, 024004 (2017).
- [126] M. D. Hutchings, J. B. Hertzberg, Y. Liu, N. T. Bronn, G. A. Keefe, M. Brink, J. M. Chow, and B. L. T. Plourde, “*Tunable Superconducting Qubits with Flux-Independent Coherence*”, Phys. Rev. Applied **8**, 044003 (2017).
- [127] J. M. Martinis, S. Nam, J. Aumentado, K. M. Lang, and C. Urbina, “*Decoherence of a Superconducting Qubit Due to Bias Noise*”, Phys. Rev. B **67**, 094510 (2003).
- [128] C. M. Quintana, Y. Chen, D. Sank, A. G. Petukhov, T. C. White, D. Kafri, B. Chiaro, A. Megrant, R. Barends, B. Campbell, Z. Chen, A. Dunsworth, A. G. Fowler, R. Graff, E. Jeffrey, J. Kelly, E. Lucero, J. Y. Mutus, M. Neeley, C. Neill, P. J. J. O’Malley, P. Roushan, A. Shabani, V. N. Smelyanskiy, A. Vainsencher, J. Wenner, H. Neven, and J. M. Martinis, “*Observation of Classical-Quantum Crossover of  $1/f$  Flux Noise and Its Paramagnetic Temperature Dependence*”, Phys. Rev. Lett. **118**, 057702 (2017).
- [129] A. Kou, W. C. Smith, U. Vool, R. T. Brierley, H. Meier, L. Frunzio, S. M. Girvin, L. I. Glazman, and M. H. Devoret, “*Fluxonium-Based Artificial Molecule with a Tunable Magnetic Moment*”, Phys. Rev. X **7**, 031037 (2017).
- [130] E. S. Fried, P. Sivarajah, N. Didier, E. A. Sete, M. P. da Silva, B. R. Johnson, and C. A. Ryan, “*Assessing the Influence of Broadband Instrumentation Noise on Parametrically Modulated Superconducting Qubits*”, arXiv:1908.11370, (2019).
- [131] A. Frees, S. Mehl, J. K. Gamble, M. Friesen, and S. N. Coppersmith, “*Adiabatic Two-Qubit Gates in Capacitively Coupled Quantum Dot Hybrid Qubits*”, npj Quantum Inform. **5**, 73 (2019).

- [132] J. M. Pirkkalainen, S. U. Cho, J. Li, G. S. Paraoanu, P. J. Hakonen, and M. A. Sillanpää, “*Hybrid Circuit Cavity Quantum Electrodynamics with a Micromechanical Resonator*”, *Nature* **494**, 211 (2013).
- [133] N. Timoney, I. Baumgart, M. Johanning, A. F. Varón, M. B. Plenio, A. Retzker, and C. Wunderlich, “*Quantum Gates and Memory Using Microwave-Dressed States*”, *Nature* **476**, 185 (2011).
- [134] S. Wölk and C. Wunderlich, “*Quantum Dynamics of Trapped Ions in a Dynamic Field Gradient Using Dressed States*”, *New J. Phys.* **19**, 083021 (2017).
- [135] Y.-C. Yang, S. N. Coppersmith, and M. Friesen, “*Achieving High-Fidelity Single-Qubit Gates in a Strongly Driven Charge Qubit with 1/f Charge Noise*”, *npj Quantum Inf.* **5**, 12 (2019).
- [136] J. R. Petta, A. C. Johnson, J. M. Taylor, E. A. Laird, A. Yacoby, M. D. Lukin, C. M. Marcus, M. P. Hanson, and A. C. Gossard, “*Coherent Manipulation of Coupled Electron Spins in Semiconductor Quantum Dots*”, *Science* **309**, 2180 (2005).
- [137] F. H. L. Koppens, K. C. Nowack, and L. M. K. Vandersypen, “*Spin Echo of a Single Electron Spin in a Quantum Dot*”, *Phys. Rev. Lett.* **100**, 236802 (2008).
- [138] H. Bluhm, S. Foletti, I. Neder, M. Rudner, D. Mahalu, V. Umansky, and A. Yacoby, “*Dephasing Time of GaAs Electron-Spin Qubits Coupled to a Nuclear Bath Exceeding 200  $\mu$ s*”, *Nat. Phys.* **2**, 109 (2011).
- [139] A. Safavi-Naini, P. Rabl, P. F. Weck, and H. R. Sadeghpour, “*Microscopic Model of Electric-Field-Noise Heating in Ion Traps*”, *Phys. Rev. A* **84**, 023412 (2011).
- [140] N. Daniilidis, S. Narayanan, S. A. Möller, R. Clark, T. E. Lee, P. J. Leek, A. Wallraff, S. Schulz, F. Schmidt-Kaler, and H. Häffner, “*Fabrication and Heating Rate Study of Microscopic Surface Electrode Ion Traps*”, *New J. Phys.* **13**, 013032 (2011).
- [141] M. Brownnutt, M. Kumph, P. Rabl, and R. Blatt, “*Ion-Trap Measurements of Electric-Field Noise near Surfaces*”, *Rev. Mod. Phys.* **87**, 1419 (2015).
- [142] M. Constantin and C. C. Yu, “*Microscopic Model of Critical Current Noise in Josephson Junctions*”, *Phys. Rev. Lett.* **99**, 207001 (2007).

- [143] M. Mück, M. Korn, C. G. A. Mugford, J. B. Kycia, and J. Clarke, “*Measurements of  $1/f$  Noise in Josephson Junctions at Zero Voltage: Implications for Decoherence in Superconducting Quantum Bits*”, Appl. Phys. Lett. **86**, 012510 (2005).
- [144] K. Khodjasteh and D. A. Lidar, “*Fault-Tolerant Quantum Dynamical Decoupling*”, Phys. Rev. Lett. **95**, 180501 (2005).
- [145] L. Cywinski, R. M. Lutchyn, C. P. Nave, and S. Das Sarma, “*How to Enhance Dephasing Time in Superconducting Qubits*”, Phys. Rev. B **77**, 174509 (2008).
- [146] L. Viola, E. Knill, and S. Lloyd, “*Dynamical Decoupling of Open Quantum Systems*”, Phys. Rev. Lett. **82**, 2417 (1999).
- [147] G. S. Uhrig, “*Keeping a Quantum Bit Alive by Optimized  $\pi$ -Pulse Sequences*”, Phys. Rev. Lett. **98**, 100504 (2007).
- [148] E. L. Hahn, “*Spin Echoes*”, Phys. Rev. **80**, 580 (1950).
- [149] H. Y. Carr and E. M. Purcell, “*Effects of Diffusion on Free Precession in Nuclear Magnetic Resonance Experiments*”, Phys. Rev. **94**, 630 (1954).
- [150] S. Meiboom and D. Gill, “*Modified Spin-Echo Method for Measuring Nuclear Relaxation Times*”, Rev. Sci. Instrum. **29**, 688 (1958).
- [151] L. Viola and E. Knill, “*Robust Dynamical Decoupling of Quantum Systems with Bounded Controls*”, Phys. Rev. Lett. **90**, 037901 (2003).
- [152] J. Jing, P. Huang, and X. Hu, “*Decoherence of an Electrically Driven Spin Qubit*”, Phys. Rev. A **90**, 022118 (2014).
- [153] A. Y. Smirnov, “*Decoherence and Relaxation of a Quantum Bit in the Presence of Rabi Oscillations*”, Phys. Rev. B **67**, 155104 (2003).
- [154] S.-K. Son, S. Han, and S.-I. Chu, “*Floquet Formulation for the Investigation of Multiphoton Quantum Interference in a Superconducting Qubit Driven by a Strong ac Field*”, Phys. Rev. A **79**, 032301 (2009).
- [155] C. Deng, J.-L. Orgiazzi, F. Shen, S. Ashhab, and A. Lupascu, “*Observation of Floquet States in a Strongly Driven Artificial Atom*”, Phys. Rev. Lett. **115**, 133601 (2015).

- [156] J. Hausinger and M. Grifoni, “*Dissipative Two-Level System Under Strong ac Driving: A Combination of Floquet and Van Vleck Perturbation Theory*”, Phys. Rev. A **81**, 022117 (2010).
- [157] J. Stehlik, Y.-Y. Liu, C. Eichler, T. R. Hartke, X. Mi, M. J. Gullans, J. M. Taylor, and J. R. Petta, “*Double Quantum Dot Floquet Gain Medium*”, Phys. Rev. X **6**, 041027 (2016).
- [158] S. Ashhab, J. R. Johansson, A. M. Zagoskin, and F. Nori, “*Two-Level Systems Driven by Large-Amplitude Fields*”, Phys. Rev. A **75**, 063414 (2007).
- [159] M. P. Silveri, J. A. Tuorila, E. V. Thuneberg, and G. S. Paraoanu, “*Quantum Systems Under Frequency Modulation*”, Rep. Prog. Phys. **80**, 056002 (2017).
- [160] J. Li, M. P. Silveri, K. S. Kumar, J. M. Pirkkalainen, A. Vepsäläinen, W. C. Chien, J. Tuorila, M. A. Sillanpää, P. J. Hakonen, E. V. Thuneberg, and G. S. Paraoanu, “*Motional Averaging in a Superconducting Qubit*”, Nat. Commun. **4**, 1420 (2013).
- [161] T. R. Tan, J. P. Gaebler, R. Bowler, Y. Lin, J. D. Jost, D. Leibfried, and D. J. Wineland, “*Demonstration of a Dressed-State Phase Gate for Trapped Ions*”, Phys. Rev. Lett. **110**, 263002 (2013).
- [162] G. Mikelsons, I. Cohen, A. Retzker, and M. B. Plenio, “*Universal Set of Gates for Microwave Dressed-State Quantum Computing*”, New J. Phys. **17**, 053032 (2015).
- [163] S. Guérin, “*Complete Dissociation by Chirped Laser Pulses Designed by Adiabatic Floquet Analysis*”, Phys. Rev. A **56**, 1458 (1997).
- [164] Y.-C. Yang, S. N. Coppersmith, and M. Friesen, “*High-Fidelity Entangling Gates for Quantum-Dot Hybrid Qubits Based on Exchange Interactions*”, Phys. Rev. A **101**, 012338 (2020).
- [165] D. K. Weiss, A. C. Y. Li, D. G. Ferguson, and J. Koch, “*Spectrum and Coherence Properties of the Current-Mirror Qubit*”, Phys. Rev. B **100**, 224507 (2019).
- [166] U. Vool and M. Devoret, “*Introduction to Quantum Electromagnetic Circuits*”, Int. J. Circ. Theor. Appl. **45**, 897 (2017).
- [167] L. S. Theis, F. Motzoi, S. Machnes, and F. K. Wilhelm, “*Counteracting Systems of Diabaticities Using DRAG Controls: The Status After 10 Years*”, EPL **123**, 60001 (2018).

- [168] N. Leung, M. Abdelhafez, J. Koch, and D. Schuster, “*Speedup for Quantum Optimal Control from Automatic Differentiation Based on Graphics Processing Units*”, Phys. Rev. A **95**, 042318 (2017).
- [169] P Aliferis, F Brito, D. P. DiVincenzo, J Preskill, M Steffen, and B. M. Terhal, “*Fault-Tolerant Computing with Biased-Noise Superconducting Qubits: A Case Study*”, New J. Phys. **11**, 013061 (2009).
- [170] S. Puri, L. St-Jean, J. A. Gross, A. Grimm, N. E. Frattini, P. S. Iyer, A. Krishna, S. Touzard, L. Jiang, A. Blais, S. T. Flammia, and S. M. Girvin, “*Bias-Preserving Gates with Stabilized Cat Qubits*”, Sci. Adv. **6**, eaay5901 (2020).
- [171] S. Haroche and J.-M. Raimond, “*Quantum Computing: Dream or Nightmare?*”, Phys. Today **49**, 51 (1996).
- [172] J. Preskill, “*Quantum Computing 40 Years Later*”, arXiv:2106.10522 (2021).
- [173] D. Zeuch, F. Hassler, J. J. Slim, and D. P. DiVincenzo, “*Exact Rotating Wave Approximation*”, Ann. Phys. **423**, 168327 (2020).
- [174] C. Creffield, “*Location of Crossings in the Floquet Spectrum of a Driven Two-Level System*”, Phys. Rev. B **67**, 165301 (2003).
- [175] H. P. Breuer and M. Holthaus, “*Adiabatic Processes in the Ionization of Highly Excited Hydrogen Atoms*”, Z. Phys. D **11**, 1 (1989).
- [176] D. W. Hone, R. Ketzmerick, and W. Kohn, “*Time-Dependent Floquet Theory and Absence of an Adiabatic Limit*”, Phys. Rev. A **56**, 4045 (1997).
- [177] A Wunsche, “*Displaced Fock States and Their Connection to Quasiprobabilities*”, J. Eur. Opt. Soc. B **3**, 359 (1991).